



DISSERTATION

Energy Measurement with the ATLAS Electromagnetic Calorimeter at the Per Mill Accuracy Level

ausgeführt zum Zwecke der Erlangung des akademischen Grades eines Doktors der
technischen Wissenschaften unter der Leitung von

UNIV.-PROF. DIPL.-ING. DR. TECHN. CHRISTIAN FABJAN
E141
ATOMINSTITUT

eingereicht an der Technischen Universität Wien
Fakultät für Physik

von

DIPL.-ING. FLORIAN TEISCHINGER

Matrikelnummer: 0030835
Unterfladnitz 38
8181 St. Ruprecht/Raab

Wien, im Februar 2014

Kurzfassung

Das ATLAS-Experiment wurde entwickelt um die Proton-Proton Kollisionen am Large Hadron Collider (LHC) zu studieren. Es ist in mehrere Subdetektoren unterteilt, um die Eigenschaften aller Teilchen, die in den Proton-Proton Kollisionen produziert werden, zu messen. In den letzten drei Jahren wurden rund 20×10^{14} solcher Kollisionen mit Schwerpunktsenergien von 7 TeV und 8 TeV aufgezeichnet.

Die Energiemessung erfolgt in einem Flüssig-Edelgas-Kalorimeter mit Bleiabsorbern, das in vier hintereinanderliegenden Schichten segmentiert ist. Im Gegensatz dazu misst der innere Spurendetektor den Impuls von geladenen Teilchen.

Das Hauptthema dieser Arbeit war die absolute Energiemessung des elektromagnetischen Kalorimeters und die Verbesserung der Messgenauigkeit. Um die Energieskala des elektromagnetischen Kalorimeters zu extrahieren, wurde eine Methode entwickelt, die sich das Verhältnis der gemessenen Energie im elektromagnetischen Kalorimeter zur Impulsskala des inneren Spurendetektors zu Nutze macht.

Mehrere Effekte, die zu einer wesentlichen Verbesserung der Messgenauigkeit der extrahierten Energieskala beitragen, wurden untersucht. Mit dem vorgestellten Kalibrationsverfahren konnte die Linearität des Kalorimeters zum ersten Mal in ATLAS gemessen werden. Energieverlust auf Grund von Material vor dem Kalorimeter wurde untersucht. Der Unterschied in der Entwicklung des elektromagnetischen Schauers zwischen Monte-Carlo Simulationen und Kollisionsdaten wurde gezeigt. Die Uniformität der Energiemessung im gesamten Detektorvolumen als Funktion der Anzahl von gleichzeitiger Kollisionen mehrerer Teilchen und ihrer zeitlichen Entwicklung wurde gemessen. Die Messgenauigkeit der Energieskala relativ zu den in den verschiedenen Schichten gemessenen Energien wurde abgeschätzt.

Eine der physikalisch wichtigsten, grundlegendsten Messungen im Standardmodell der Teilchenphysik ist die Bestimmung der Masse der W -Bosonen. Um die Masse des W -Bosons zu messen, ist eine Linearität in der Messung der Elektronenenergie in einem Bereich von 20 bis 80 GeV entscheidend. Der Einfluss der Energieskala und der Linearität abgeleitet aus den Ergebnissen der Kalibration auf die Messung der Masse des W -Bosons wurde untersucht. Das Ziel war es Messunsicherheiten zu bestimmen, die eine Messung der W -Boson Masse mit einer Genauigkeit kleiner als 0.02% ermöglichen.

Abstract

The ATLAS experiment is designed to study the proton-proton collisions produced at the Large Hadron Collider (LHC) at CERN. It is made up of various sub-detectors to measure the properties of all the particles produced at the proton-proton collision. Over the last three years of running around 20×10^{14} collisions of proton data have been recorded.

Liquid argon (LAr) sampling calorimeters are used for all electromagnetic calorimetry and for hadronic calorimetry in the end-caps. The Inner Detector, on the other hand, measures the transverse momentum of charged particles down to a momentum of 0.5 GeV/c.

This thesis deals with the absolute measurement of the energy in the electromagnetic calorimeter and the improvement of the systematic uncertainties. A method using the ratio of the energy E in the calorimeter and the momentum measurement p in the Inner Detector (E/p) was used to extract the energy scale of the electromagnetic LAr calorimeter for electrons and positrons.

To investigate and further reduce the systematic uncertainties of the extracted energy scale correction, several effects were studied. The calorimeter's linearity had to be measured - for the first time in ATLAS - in five regions of the detector. Energy loss due to material effects upstream of the calorimeter had to be investigated. Differences in the shower development between MC simulation and data, along with its energy dependence, were shown. The uniformity of the energy response was measured with respect to time, pile-up and detector geometry. The uncertainties on the energy scale relative to the different sampling energies in the calorimeter had to be estimated.

One very important, fundamental measurement within the Standard Model of particle physics is the measurement of the mass of the W boson. To measure the mass of the W boson the linearity of the electron energy measurement in a region from 20 to 80 GeV is crucial. Using the derived energy scale and linearity from the E/p ratio the impact on the W mass measurement was shown. The goal was to estimate uncertainties for this measurement, which aims to reach an accuracy smaller than 0.02%.

Acknowledgements

I want to thank Prof. Christian Fabjan for supervising my thesis in such an open and encouraging way. His valuable remarks guided me through these three years here at CERN.

I thank Dr. Martin Aleksa who crucially contributed with his enormous knowledge on calorimetry on a daily basis to my work. I also want to thank Dr. Maarten Boonekamp for cross-checking my results and providing his support on behalf of the e/γ calibration group, as well as Dr. Nenad Vranjes for his support on my analysis on the W boson mass.

Many thanks to the people working in ATLAS, especially from the Liquid Argon and e/γ working groups, where informal input and feedback to my work was given during weekly meetings.

I would like to thank CERN, the European Organization for Nuclear Research, as well, along with the ATLAS collaboration for providing all the material used during my work and presented in this thesis.

Moreover I would like to thank the Austrian Ministry of Science with its financial support in the "CERN Austrian Doctoral Student Program". Without this program my work here at CERN would have not been possible.

Contents

1	The ATLAS Experiment at the LHC	3
1.1	The Large Hadron Collider	3
1.2	The ATLAS Detector	6
1.2.1	The Inner Detector	8
1.2.2	Calorimeters	9
1.2.3	Muon Spectrometer	11
1.2.4	Trigger and Data Acquisition	14
1.3	Physics Program	16
1.3.1	Higgs Searches	16
1.3.2	Supersymmetry	18
1.3.3	Standard Model	19
1.3.4	Exotics	20
1.3.5	Heavy Ions	21
2	The ATLAS Liquid Argon Calorimeter	23
2.1	Overview	23
2.2	Electromagnetic Calorimetry	23
2.2.1	Interaction of Charged Particles with Matter	23
2.2.2	Interaction of Photons with Matter	25
2.2.3	Physics of the Electromagnetic Cascade	27
2.3	The ATLAS Electromagnetic Calorimeter	28
2.3.1	General Design	28
2.3.2	Barrel Calorimeter	30
2.3.3	End-cap Calorimeter	30
2.3.4	Presampler	32
2.3.5	Accordion, Absorber and Cryogenic System	32
2.3.6	Granularity of the Samplings	34
2.3.7	From the Energy Deposit to the Signal	34
2.3.8	Calorimeter Resolution	37
3	Reconstruction Software and Monte Carlo Simulation	41
3.1	Overview	41
3.2	Reconstruction Software	41
3.3	Monte Carlo Simulation in 2011 and 2012	44
3.4	Data in 2011 and 2012	44

3.4.1	Pile-up and Data Taking Conditions	46
3.5	MC Simulation and Data Samples	46
3.5.1	MC simulation samples	46
3.5.2	Data samples	49
3.5.3	General Selection Cuts	49
4	Electron Reconstruction and Identification	51
4.1	Electron Track Reconstruction	51
4.2	Electron Reconstruction	54
4.3	Electron Identification	55
4.4	Electron Trigger	58
4.5	Electron Isolation	58
4.6	Missing Transverse Energy	59
5	Calibration of the EM Calorimeter	61
5.1	Overview	61
5.2	Electronics Calibration at the Cell Level	62
5.2.1	Impact of Pile-up on the Cell Energy	63
5.3	Cluster Level Calibration	65
5.4	In-situ Calibration using Physics Objects - Data-driven Calibration	68
5.4.1	Energy Scale	70
5.4.2	Resolution	74
5.5	Contribution of this thesis	75
6	Ratio of Calorimeter Energy and Inner Detector momentum, E/p	77
6.1	Overview	77
6.2	Event Selection	78
6.3	The E/p Distribution and Fitting Methods	81
6.3.1	Crystal Ball Model	82
6.3.2	Convolution Model	84
6.4	Systematic Uncertainties of the Convolution Model	93
6.4.1	MC Closure Test	93
6.4.2	Systematics due to Additional Material	95
6.4.3	Parameter Extraction	95
6.4.4	Systematic Error on the Momentum Measurement	96
6.4.5	Summary	98
6.5	Results	99
6.5.1	Energy Scales	99
6.5.2	E/p tails	100
7	Uniformity and Stability	103
7.1	Overview	103
7.2	Uniformity	103
7.2.1	Comparing $Z \rightarrow e^+e^-$ and $W^\pm \rightarrow e^\pm \nu$ in narrow η Bins	105
7.2.2	Comparing $Z \rightarrow e^+e^-$ and $W^\pm \rightarrow e^\pm \nu$ in narrow ϕ Bins	108
7.2.3	Uniformity and Constant Term	115

7.2.4	2D Uniformity in η and ϕ	120
7.3	Stability	122
7.3.1	Stability of Energy Response versus Relative Location in the Bunch Train in 2011 Data	122
7.3.2	Stability of Energy Response versus Time and Pile-up	125
7.4	Summary	127
8	Linearity of Energy Response	129
8.1	Overview	129
8.2	Results	130
9	Lateral Leakage	133
9.1	Overview	133
9.2	Method description	133
9.3	Numbers of Bunches in Front - Out of Time Pile-Up	134
9.4	Results	136
10	Passive Material Determination	141
10.1	Overview	141
10.2	Averaging using ϕ -Periodicity	142
10.3	Estimation of Passive Material Using Shower Shapes	143
10.3.1	$0.25 < \eta < 0.3$	144
10.3.2	$0.6 < \eta < 0.8$	145
10.3.3	$ \eta \sim 1.7$	145
10.3.4	$ \eta \sim 1.85$	145
10.4	Material Information in E/p Tailfractions	145
10.5	Efficiency Problem at $ \eta \sim 1.7$	149
10.6	Towards a Data-Driven Material Description	152
11	Layer Calibration	157
11.1	Overview	157
11.2	Extraction of the Presampler Scale	158
11.3	Layer Calibration E_1 and E_2	162
11.3.1	Electrons	162
11.3.2	Muons	165
11.4	Results	166
12	Conclusion on the Final Energy Scale Correction	169
13	Measurement of the W Boson Mass	175
13.1	Overview	175
13.2	The Templates Method	176
13.3	Event Selection	178
13.4	Impact of Non-Linearity on the W mass measurement	178
14	Conclusions	181

A	The $Z \rightarrow e^+e^-$ Invariant Mass Peak	183
B	Energy Scale from the $Z \rightarrow e^+e^-$ Lineshape	185
C	Intermodule Widening Effect	187
D	Event Selection and Used Tags	191
D.1	Monte Carlo Sample Generation	191
D.2	Data Sample	191
D.3	General Selection Cuts	191
D.4	Ratio of Calorimeter Energy and Inner Detector momentum, E/p	194
D.5	Linearity of Energy Response	194
D.6	Lateral Leakage	194
D.7	W Mass Measurement	195
	Curriculum Vitae	203

Introduction

As of March 2010 the ATLAS experiment at the LHC at CERN has been recording collisions of protons at unprecedented energies. The broad physics program ranges from Standard Model precision measurements, to the test of models beyond the Standard Model and to model independent searches for unknown particles and phenomena.

High energy physics is investigating very short lived particles that eventually decay to light leptons or hadronic final states. They are produced in particle collisions and recorded by large detectors. Most of these particles decay even before they can interact with the detector. In order to analyze them they need to be identified by their decay products. Actual hits in the detector are caused by baryons and mesons, by muons (μ^+, μ^-), photons (γ), electrons (e^-) and positrons (e^+)¹. To examine any particle or process, a precise identification of these decay products is imperative. Physics analyses extensively rely on the three last-mentioned μ , γ and e and sprays of collimated particles, so-called jets.

In many physics analyses the electromagnetic (EM) calorimetry plays an important role. Many processes manifest themselves through photons and electrons in the final states, where the energy and position of electrons, photons and jets, as well as missing energy of the event are measured. The Higgs discovery channels such as $H \rightarrow \gamma\gamma$, $H \rightarrow 4e$, as well as possible discovery of exotic particles, such as Z' or W' and precision measurements (e.g. W boson mass) put the most stringent constraints on the EM calorimeter:

- The electromagnetic energy scale, which determines the scale between the deposited energy measured in the EM calorimeter and the initial energy of the penetrating particle, must be controlled at the level of 0.05% for many standard model measurements. A competitive W mass measurement needs an even smaller scale uncertainty at the 0.01% level.
- Invariant mass resolution at the 1% level for particles decaying into 2 γ or 2 e .

In order to achieve this performance the description of the calorimeter in Monte Carlo has to be extremely accurate and many effects need to be understood and corrected at the per mill level. This thesis addresses this necessary understanding of the ATLAS electromagnetic calorimeter through several studies that are outlined in the text.

¹For reasons of simplicity the term electron stands from now on for electrons and positrons, unless explicitly stated otherwise.

The thesis starts with a very brief introduction of the LHC in Chapter 1 and the ATLAS detector describing its sub-detectors and its physics program (Chapter 2). This introduction will be followed by a general overview of the data distribution and datasets used in this thesis (Chapter 3). After describing the complex electron reconstruction process (Chapter 4), the calibration strategy for the LAr electromagnetic calorimeter will be outlined in Chapter 5.

Results for the calibration of the LAr electromagnetic calorimeter using the 2011 and 2012 Run 1 datasets will be presented:

- Electron Energy Calibration in Chapter 6
- Uniformity of the energy response in η and ϕ in Chapter 7
- Linearity of the energy measurement in Chapter 8
- Leakage out of the reconstructed cluster in Chapter 9
- Material determination in front and inside the calorimeter in Chapter 10
- Sampling layer inter-calibration in Chapter 11

Chapter 12 concludes on the final energy scale correction based on the findings described in the previous chapters. In the final chapter, Chapter 13, the impact of the obtained electron energy calibration and its linearity on the W mass measurement will be presented.

Chapter 1

The ATLAS Experiment at the LHC

The Large Hadron Collider (LHC), located on the French-Swiss border near Geneva, the world's most powerful particle accelerator, is designed to collide either protons, of up to 7 TeV per nucleon, or lead nuclei, of up to 2.76 TeV per nucleon in a 26.7 km ring of superconducting magnets. The LHC started operation with proton beams colliding successfully in November 2009. The actual collisions take place at four interaction points along the ring. Four giant particle detectors sit on each point and two smaller ones close by. Among those the largest is the ATLAS (A Toroidal LHC ApparatuS) experiment.

Material taken for this chapter comes from various Technical Design Reports and Papers. References to this material are stated in the beginning of each section or within a paragraph using the square shaped brackets.

1.1 The Large Hadron Collider

The LHC [1] is a proton-proton accelerator and collider installed in a tunnel approximately 100 m under the surface. The accelerator consists of eight arcs and eight straight sections of superconducting magnets. The operation of two beams of equally charged particles, one clockwise, the other counter-clockwise, necessitates two opposite magnetic dipole fields to bend the particles on a circular path. For the LHC, a design has been realised where both beams circulate in two adjacent pipes. The collider has been designed for a center of mass energy of 14 TeV. To reach this energy, protons are accelerated in a number of successive accelerators with increasing energy until they are injected into the LHC ring at 450 GeV. The LHC has been designed to reach an instantaneous luminosity of $L = 10^{34} \text{ cm}^{-2} \text{ s}^{-1}$. This high luminosity is delivered to the two multi-purpose experiments ATLAS and CMS. There is also a low luminosity experiment LHCb, dedicated to B-physics and designed for $L = 10^{32} \text{ cm}^{-2} \text{ s}^{-1}$. The LHC is also capable of colliding lead ions at a design energy of $\sqrt{s} = 2.76 \text{ TeV}$. These collisions are recorded by the two multi-purpose detectors and the ALICE experiment, designed specifically for the analysis of Pb-Pb collisions and intended to study the quark-gluon-plasma.

There are three smaller experiments, namely TOTEM which aims to measure total cross sections, elastic scattering, and diffractive processes, LHCf, which intends to measure neutral

pions to help explaining the origin of ultra-high-energy cosmic rays and MoEDAL (in planning phase).

The LHC operated at 3.5 TeV per beam in 2010 and 2011 and at 4 TeV per beam in 2012. It operated for two months in 2013 colliding protons with lead nuclei. On February 14, 2013 it went into shutdown for upgrades to increase the beam energy to 6.5 TeV per beam, with start of operation planned for early 2015. A summary of different LHC achievements is shown in Table 1.1 and an overview of the different pre-accelerators and detectors at the LHC is given in Figure 1.1.

	Run 1			Run 2	Run 3
year	2010	2011	2012	2015 - 2017	2019 - 2021
Center of mass energy \sqrt{s} (TeV)	7	7	8	13-14	14
Luminosity L ($\text{cm}^{-2}\text{s}^{-1}$)	$2 \cdot 10^{32}$	$3.5 \cdot 10^{33}$	$7.6 \cdot 10^{33}$	$1 \cdot 10^{34}$	$2.2 \cdot 10^{34}$
Luminosity (integrated) L_{int} (fb^{-1})	0.48	5.2	20.7	75 - 100	300
Bunch spacing (ns)	150	75/50	50	25	25

Table 1.1: *Summary of LHC achievements in proton-proton runs and future program. Currently, between Run 1 and Run 2, a maintenance shutdown (LS 1) is on-going. During the break between Run 2 and Run 3 another shutdown (LS 2) is foreseen in which a new linear collider will replace a LHC pre-accelerator.*

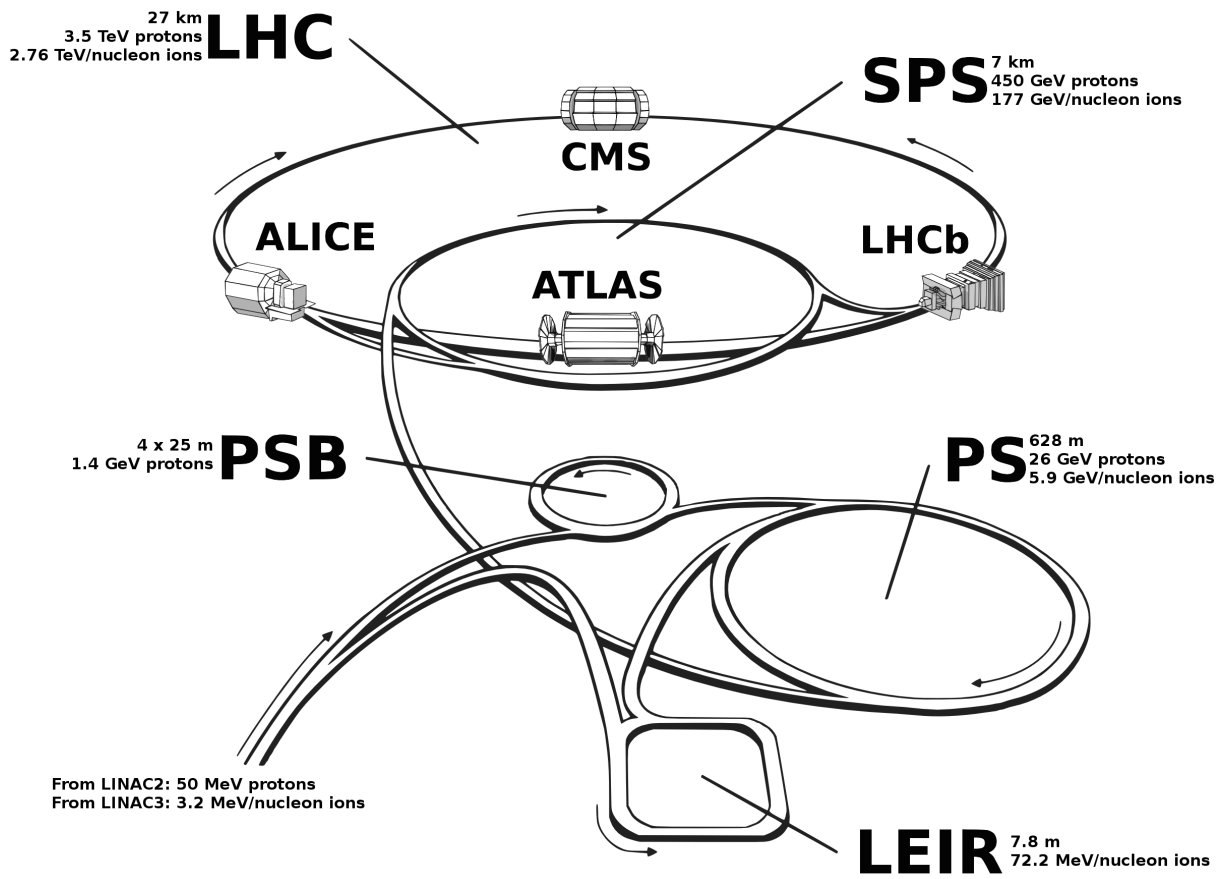


Figure 1.1: Cut-away view of the LHC and its pre-acceleration steps. Taken from Ref. [2].

1.2 The ATLAS Detector

The ATLAS [3] experiment has been designed to record the particles produced in the proton-proton (or heavy ion) collisions delivered by the LHC. A cut-away view of the detector is given in Figure 1.2.

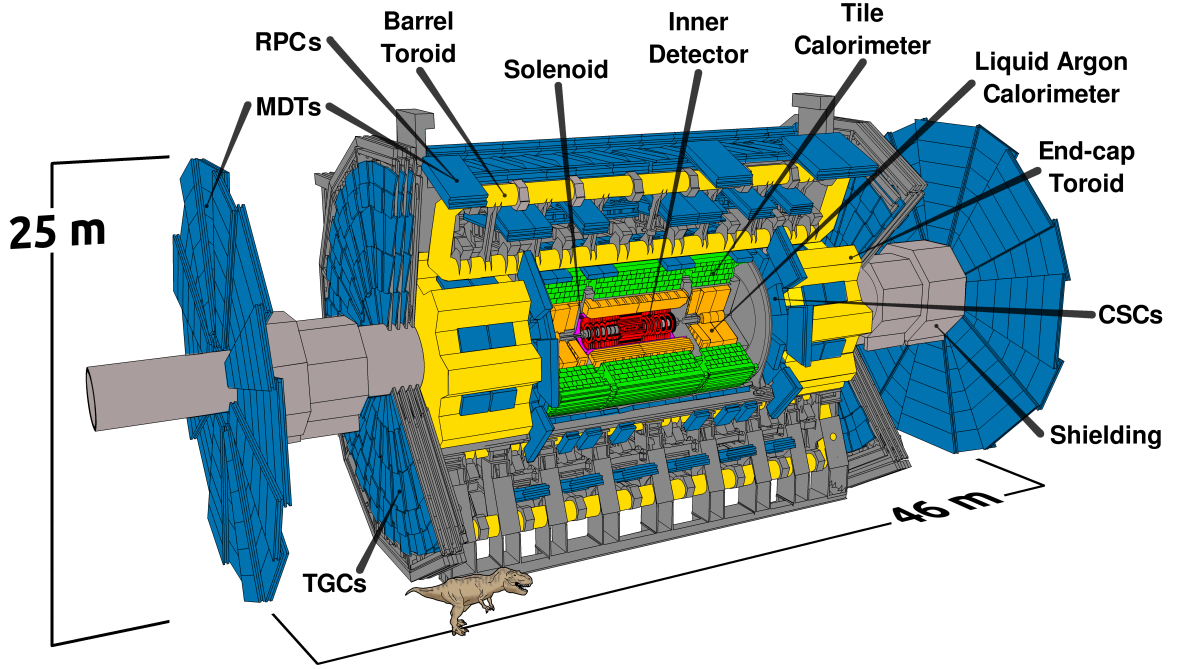


Figure 1.2: *Cut-away view of the ATLAS detector. Taken from Ref. [2].*

It is assembled in several layers around the nominal interaction point and symmetric in forward and backward direction along the beam pipe w.r.t. the interaction point. The inner detector consists of three tracking sub-systems and is embedded in a superconducting solenoid magnet that produces a magnetic field of $B \approx 2$ T. The combination of magnetic field and tracking system allows for the momentum measurement of charged particles. Around it, the calorimeter system is built as a cylindrical barrel with two end-caps. It is divided into an electromagnetic (EM) and a hadronic calorimeter part, designed according to their purpose of providing a high resolution measurement of electrons and photons through electromagnetic showers and an adequate resolution measurement for hadronic particles. The detector is completed by the muon spectrometer, consisting of another magnetic system with a barrel and two end-cap toroid magnets, producing a field of $B \approx 0.2$ to 3.5 T respectively, and a number of different muon chambers made of drift tubes assembled inside and around the toroids. In order to record the collisions, the event rate has to be reduced from 40 MHz to about 500 Hz. This is achieved by a three-level trigger system.

The nominal interaction point is taken as the origin of a right-handed coordinate system with the z -axis defined by the beam direction. Perpendicular to it is the x - y plane, with the x -axis

pointing towards the center of the LHC ring and the y -axis pointing upwards. With that, the azimuth and polar angles ϕ and θ are measured from the positive x -axis counter-clockwise in the x - y -plane and from the z -axis, respectively. Throughout this thesis, further quantities will be used repeatedly: the pseudorapidity η , defined as

$$\eta = -\ln \left[\tan \left(\frac{\theta}{2} \right) \right], \quad (1.1)$$

and the distance in pseudorapidity-azimuth-angle-space ΔR

$$\Delta R = \sqrt{\Delta \eta^2 + \Delta \phi^2}. \quad (1.2)$$

The observable p_T is the component of momentum in the transverse (x - y) plane

$$p_T = p \cdot \sin(\theta) \quad (1.3)$$

The transverse energy (E_T) is defined as

$$E_T = E \cdot \sin(\theta) \quad (1.4)$$

where E is the (calorimeter cell) energy and again θ is the angle between the beam direction and the direction of the vector pointing from the interaction vertex to the calorimeter (cell).

In accelerator physics, luminosity (L) is the ratio of the number of events detected (N) in a certain time (t) to the interaction cross section (σ):

$$L = \frac{1}{\sigma} \frac{dN}{dt}. \quad (1.5)$$

It has the dimension of events per time per area, and is usually expressed in units of $\text{cm}^{-2} \cdot \text{s}^{-1}$. L depends on the beam parameters, such as beam width and particle flow rate, as well as the target properties. A related quantity is integrated luminosity (L_{int}), which is the integral of the luminosity with respect to time:

$$L_{\text{int}} = \int L dt. \quad (1.6)$$

The luminosity and integrated luminosity are useful values to characterize the performance of a particle accelerator. In particular, all collider experiments aim to maximize their integrated luminosities, as the higher the integrated luminosity, the more data is available to analyze.

In high energy physics the unit barn (symbol b) is used to express cross sections of scattering processes and as a measure of the probability of interaction between particles. A barn is a unit of area and defined as 10^{-28} m^2 and is approximately the cross sectional area of a uranium nucleus. The “inverse femtobarn” (fb^{-1}) [4] is a measurement of particle collision events per femtobarn of target cross section, and is the conventional unit for time-integrated luminosity. In a particle accelerator two streams of particles, with cross sectional areas measured in femtobarns, are directed to collide over a period of time. The total number of collisions is directly proportional to the integrated luminosity of the collisions measured over this time. Therefore, the collision count can be calculated by multiplying the integrated luminosity by the sum of the cross section for those collision processes. This count is then expressed as inverse femtobarns for the time period (e.g. 100 fb^{-1} in two months). Inverse femtobarns are often quoted as an indication of particle collider productivity.

1.2.1 The Inner Detector

The Inner Detector (ID) [5] is designed for high resolution measurements of the momentum of charged particles and the reconstruction of primary and secondary vertices. It consists of three independent but complementary sub-detectors: the Pixel detector, the Semiconductor Tracker (SCT) and the Transition Radiation Tracker (TRT). The different parts are depicted in Figure 1.3.

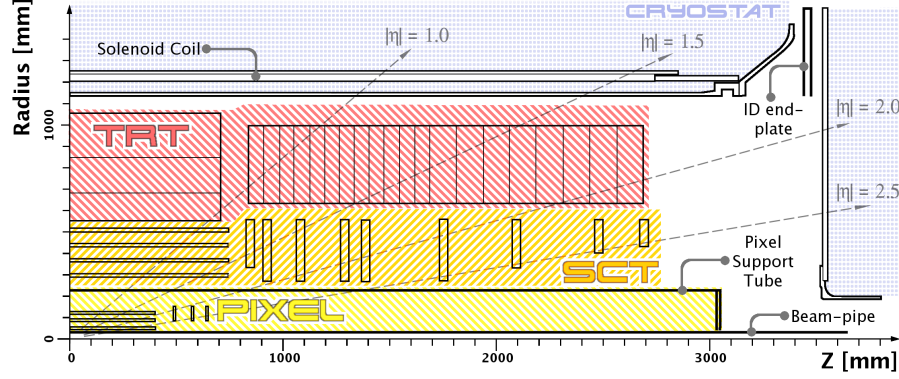


Figure 1.3: Sketch of the inner detector. Taken from Ref. [2].

The Pixel detector comes in three cylindrical silicon layers and three end-cap discs on each side. The nominal pixel size is $50 \times 400 \mu\text{m}^2$. It constitutes the sub-detector with the highest spatial resolution and the highest number of readout channels. The layer closest to the beam pipe is referred to as the b-layer since through its proximity to the beam pipe it reaches the highest resolution and plays an important role in the identification of jets from b -quarks. The SCT consists of a barrel part of four layers and a total of nine discs in the end-cap region, again on each side, with silicon strip detectors. For a three-dimensional measurement of the trajectory of a particle each layer has two silicon strips that are oriented under a 40 mrad angle. Both systems are commonly referred to as silicon trackers. They span a pseudorapidity range of $|\eta| < 2.5$. Beyond that no track reconstruction is possible. Without the possibility of track reconstruction, electrons cannot reliably be distinguished from photons above a pseudorapidity of $|\eta| > 2.5$.

The third part of the inner detector is the TRT, a combination of tracking and transition radiation detector. It consists of straw drift tubes, 4 mm in diameter, that are interleaved with polyimide fibres in the barrel and foils in the end-cap as a transition radiation element. The straws are filled with a xenon-based gas mixture. A tungsten wire is used as an anode for the drift tube. The barrel straws are divided in two in the middle at $\eta = 0$. They are read out at each end and in the center. The TRT front-end electronics can discriminate between signals from tracking hits from minimum-ionising particles and transition radiation hits (that yield higher signal amplitudes) by using separate low and high thresholds. It covers a range of up to $|\eta| < 2.0$ with a gap for the readout at $|\eta| < 0.1$. The tubes are aligned parallel to the beam pipe in the barrel and radially in the end-caps. The TRT has only limited resolution in η but measures the important ϕ -coordinate accurately.

The amount of material a particle has to pass in order to penetrate the inner detector and reach the electromagnetic calorimeter is given in Figure 1.4 in units of radiation length. In addition to the ID material, it has to traverse the solenoid magnet and the cryostat walls to reach the Electromagnetic Calorimeters. Figure 1.4 includes the solenoid. By passing through the material, electrons lose a considerable fraction of their energy by Bremsstrahlung; large fractions of photons convert to electron-positron pairs - becoming a background for genuine electrons.

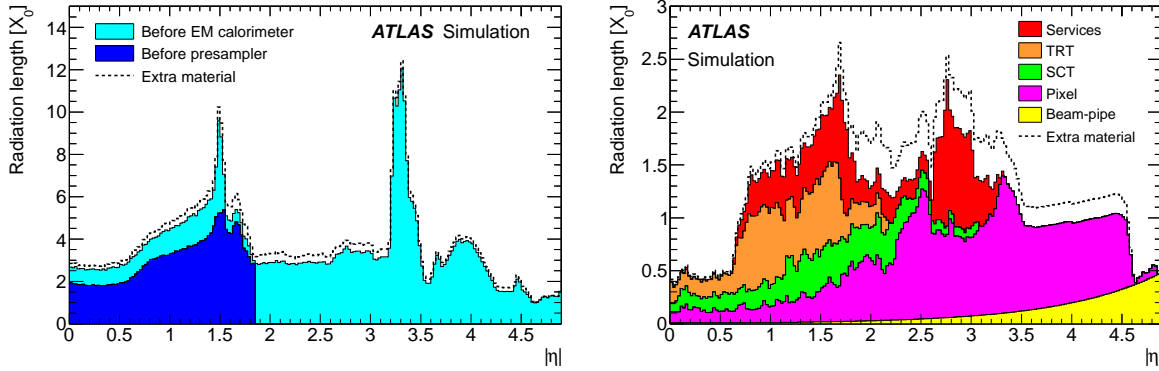


Figure 1.4: Amount of material, in units of radiation length X_0 , traversed by a particle as a function of η : (left) material in front of the Presampler detector and the EM calorimeter, and (right) material up to the ID boundaries. The contributions of the different detector elements, including the services and thermal enclosures, are shown separately by filled color areas. The primary vertex position has been smeared along the beamline. Taken from Ref. [6].

1.2.2 Calorimeters

Electromagnetic Calorimeter

The calorimeters cover a range $|\eta| < 4.9$ using different techniques for the measurement of the energy of electrons, photons, and jets. An overview is given in Figure 1.5. The electromagnetic calorimeter [7] (EM) is a lead-liquid-argon calorimeter and provides a three-dimensional subdivision (granularity).

It is designed for a high-resolution measurement of the energy of electrons and photons. It is divided into a barrel and two end-cap parts, covering $|\eta| < 1.475$ and $1.375 < |\eta| < 3.2$, respectively. The cells consist of alternating layers of accordion-shaped lead absorbers, readout electrodes and liquid argon as a sampling material. The accordion structure provides symmetry in ϕ without azimuth cracks. The calorimeter is made up of three longitudinal layers in the barrel and end-caps ($|\eta| < 2.5$) and two for $|\eta| > 2.5$ with different granularity. The distribution of material in front of the EM calorimeter is shown in Figure 1.4. This amount of material, the way it is distributed in space, and the presence of a magnetic field, combine to require a Presampler, in order to correct for the energy lost in front of the calorimeter.

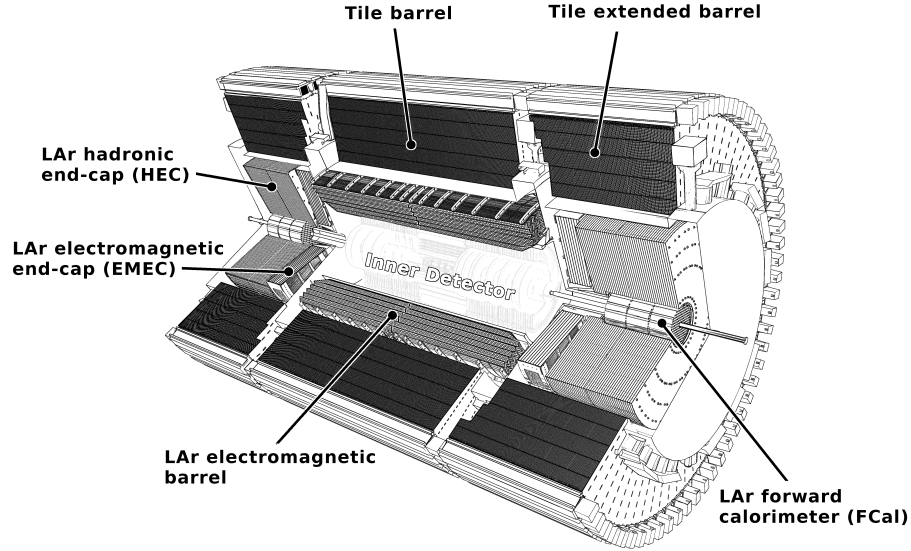


Figure 1.5: *Cut-away view of the calorimeter system. Taken from Ref. [2].*

The barrel (end-cap) Presampler feature a 1 cm (5 mm) liquid argon active layer instrumented with electrodes roughly perpendicular (parallel) to the beam axis. In the transition region between barrel and end-cap, around $|\eta| = 1.4$, the situation is particularly critical, and a scintillator layer, between the two cryostats, is used to recover mainly the jet energy measurement. This also improves the electron and photon measurement. Beyond a pseudorapidity of 1.8, the Presampler is no longer necessary given the more limited amount of dead material and the higher energy of particles for a given p_T .

The front layer, also called strip layer, has a very fine granularity in η and only very limited resolution in ϕ . The size of the cells is $\Delta\eta \times \Delta\phi = 0.0031 \times 0.1$ for $|\eta| < 1.8$ and coarser beyond that. The middle layer amounts to the largest part of the whole system and has almost equal granularity in η and ϕ with cells of size $\Delta\eta \times \Delta\phi = 0.025 \times 0.025$. The electromagnetic calorimeter is completed by the back layer that has the same granularity as the middle layer in ϕ , but only half the granularity in η . All three accordion layers and the Presampler are summed to $\Delta\eta \times \Delta\phi = 0.1 \times 0.1$ trigger towers used for the L1 calorimeter trigger.

Hadronic Calorimeter

Hadronic showers usually penetrate the material further and are absorbed in the consecutive hadronic calorimeter, which surrounds the electromagnetic calorimeter. The ATLAS hadronic calorimeter is a sampling calorimeter, too. In the barrel region it is made of steel absorbers and scintillating tiles. In the end-caps it consists of two independent wheels per end-cap of copper plates that are interleaved with liquid-argon gaps.

Forward Calorimeter

The forward region is covered by the Forward Calorimeter (FCAL) in the pseudorapidity range of $3.1 < |\eta| < 4.9$. As already mentioned, electrons outside the acceptance of the tracking system are not discussed in this thesis. The forward calorimeter contributes to the measurement of the missing transverse energy MET.

The FCAL is, again, a liquid argon sampling calorimeter consisting of three layers, the first with copper, and the other two with tungsten as the absorber material.

1.2.3 Muon Spectrometer

The muon spectrometer [8] forms the outer shell of the ATLAS detector and occupies by far the largest part of its volume. It is located on the outside of the calorimeter modules and covers the space between approximately 4.5 m and 11 m in radius and 7 m and 23 m longitudinally on both sides of the interaction point. The total volume is approximately $16\,000\text{ m}^3$. A 3D view of the ATLAS detector in the underground cavern (Figure 1.6) shows the arrangement of the muon chambers around the magnet. The magnet creates a toroidal field in air with field values of typically 0.5-2 Tesla.

In the barrel region ($|\eta| < 1$) the field is provided by eight superconducting coils forming the barrel toroid (BT). Each of these coils is 25.6 m long and extends from 5 m to 10 m in radius. In the forward region ($1.4 < |\eta| < 2.7$) the field is generated by the end-cap toroids (ECT), inserted on both ends into the inner bore of the BT. Each ECT consists of eight coils and is contained in a single 10.7 m diameter cryostat. The BT and ECT coils are rotated in the azimuthal direction by 22.5° with respect to each other. In the intermediate pseudorapidity range ($1.0 < |\eta| < 1.4$) the magnetic field is a superposition of the barrel and the end-cap fields.

In the barrel the muon chambers are arranged in three concentric cylinders around the beam axis. The end-cap chambers form four disks on each side of the interaction point, concentric around the beam axis (Figure 1.7).

The chambers are placed such that particles which originate at the interaction point traverse three chamber stations. The position of these stations has been chosen to take optimum advantage of the magnetic field configuration. Wherever possible, the chambers measure the sagitta of the curved tracks in three positions: at the inner field boundary, close to the field maximum, and at the outer field boundary. In the end-cap region ($|\eta| > 1.4$) this is not possible since the magnetic volume is almost completely enclosed in the ECT. Instead, the deflections of the tracks that have traversed the ECT are measured taking advantage of a large lever arm between the two outer measurement stations. Two separate systems with distinct functionality are used:

- Trigger: Resistive Plate Chambers (RPC) in the barrel region and Thin Gap Chambers (TGC) for the end-caps covering the spectrometer acceptance up to $|\eta| = 2.4$. Both types of chambers generate fast signals with a time resolution of a few nanoseconds which are used for level-1 triggering and bunch crossing identification. A spatial resolution of 5-

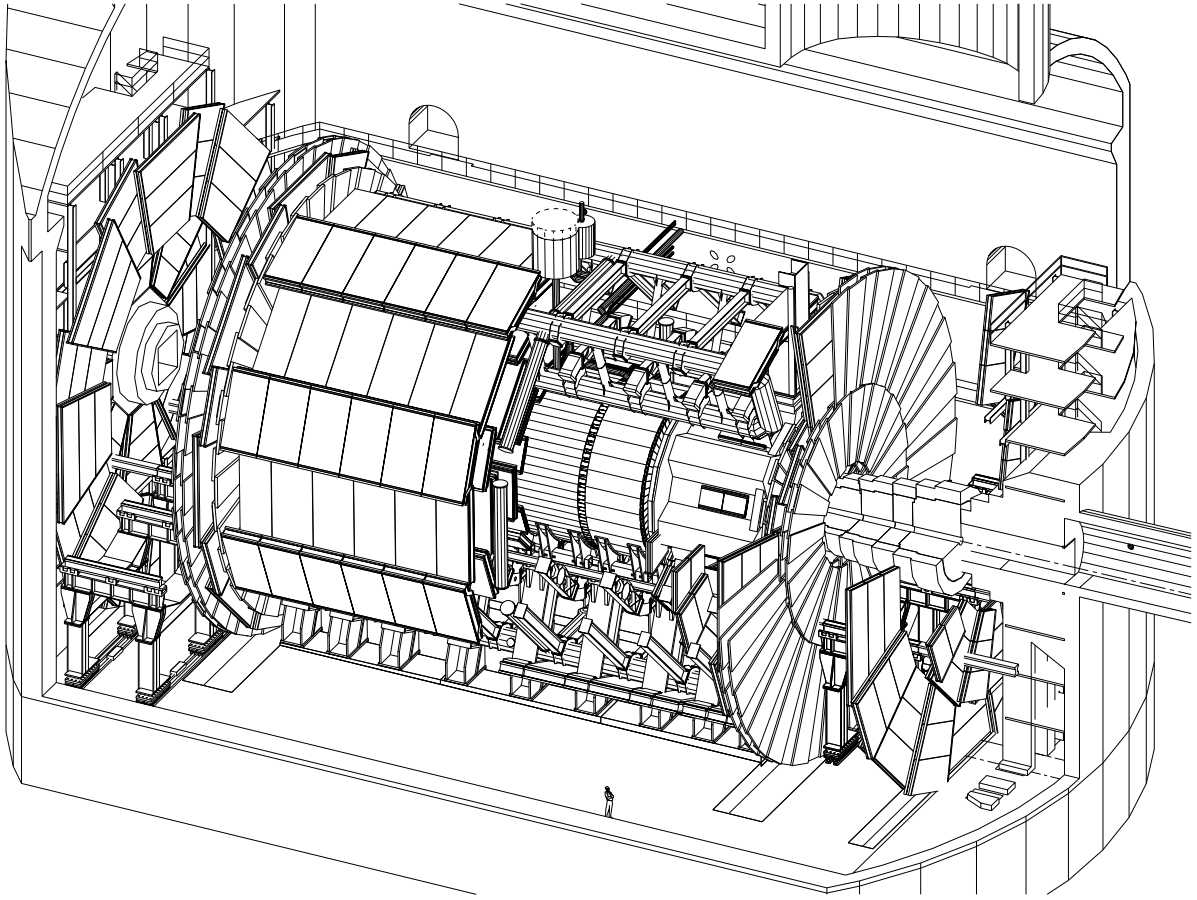


Figure 1.6: 3-D view of the ATLAS detector in the underground hall. The muon chambers (only partly shown) are arranged in three layers around the inner detector and the calorimeter in the space between 5 and 10 m in radius and 7 and 23 m distance from the interaction point. Taken from Ref. [8].

20 mm is adequate for these chambers. It is used in the pattern recognition algorithm and provides the only measurement of the track coordinate in the non-bending plane.

- Precision measurement: Monitored Drift Tube chambers (MDT) for 99.5% of the area and Cathode Strip Chambers (CSC) for the remaining very small forward area where particle fluxes are highest. Although small in physical size, this area covers a large range in pseudorapidity ($|\eta| = 2 - 2.7$). The precision chambers measure the track coordinates in the bending plane with high precision. For the MDTs no information on the non-bending coordinate and on the bunch crossing time is available. The CSCs, however, do measure both quantities.

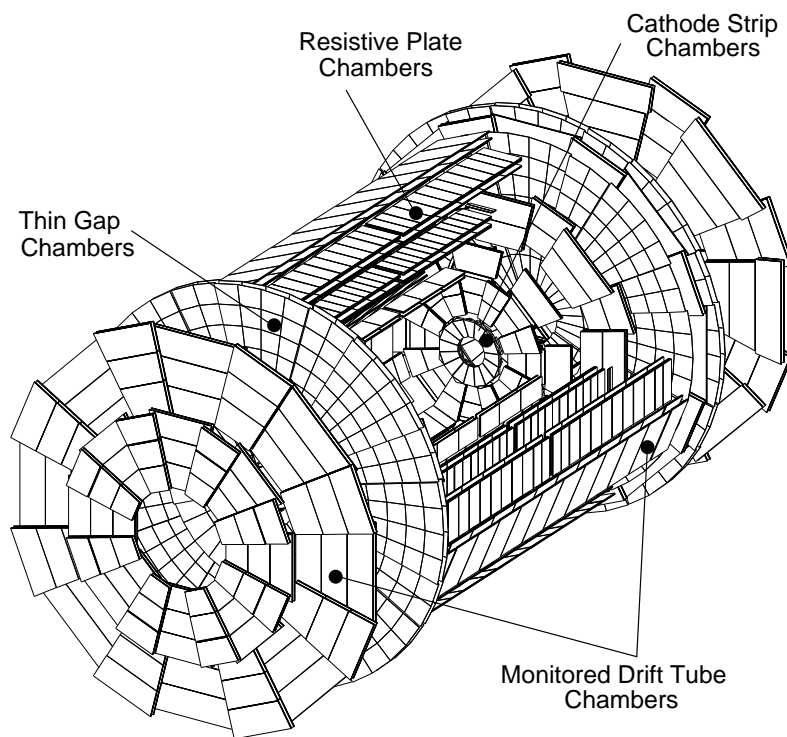


Figure 1.7: 3-D view of the muon system, indicating where the different chamber technologies are used. Taken from Ref. [8].

1.2.4 Trigger and Data Acquisition

At nominal operating conditions, bunches of 1011 protons cross each other at 40 MHz, resulting in ~ 25 proton-proton interactions per bunch crossing (events) at the center of ATLAS. Nevertheless, only a small fraction of this ~ 1 GHz event rate results in interesting physics processes. The Trigger and Data Acquisition (TDAQ) system of ATLAS [9] has to select a manageable rate of such events for permanent storage and further analysis. The amount of information to be recorded is about 1.6 MB per event and keeping ~ 500 events/s. To reduce the ~ 40 MHz event rate a three-level trigger system was developed where, at each level, different selection criteria are applied. If an event gets accepted - meaning passing all the three levels - the complete detector information is read out and data are sent for local TDAQ storage to the Sub-Farm Output (SFO) nodes. From there, the data are transmitted to the central mass storage facility at CERN (see Figure 1.8).

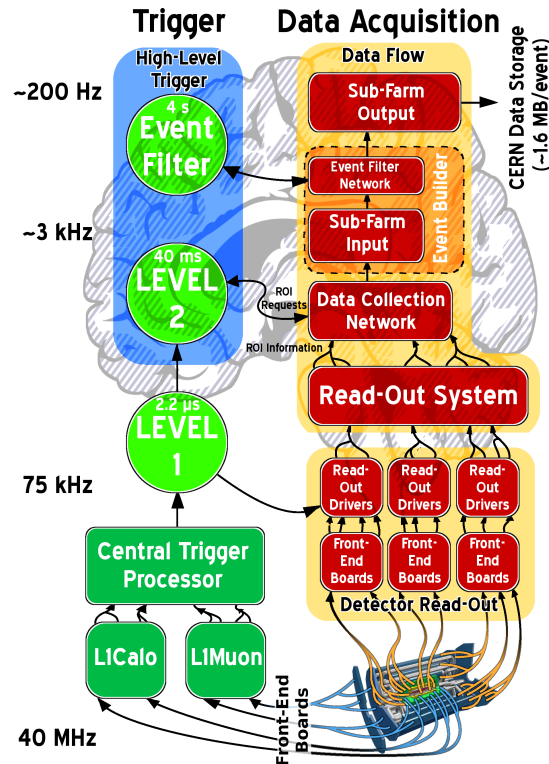


Figure 1.8: The schematic data flow of the ATLAS detector. Taken from Ref. [2].

First Level Trigger

The first level trigger L1 looks for high E_T objects, large missing transverse energy and total transverse energy. It uses only a subset of the detector with reduced granularity and simplified algorithms. These are used to define one or more Regions of Interest (RoIs) in $\eta \times \phi$ that are passed to the higher level triggers. At this stage the event rate is reduced to ~ 75 kHz.

Second Level Trigger

At second level, L2, the RoIs are further analyzed, using all detector sub-systems at full granularity but, again, with simplified algorithms. The event rate is reduced to ~ 3.5 kHz.

Event Filter

For an event that passed L2 the full information is passed to the last trigger level, a processing farm called event filter (EF). At EF level, offline-like algorithms as given in Chapter 4 are used, further reducing the event rate to the designated 300 Hz. The event filter processing uses farms of processors acting on the full-event data. The complicated selection criteria of the off-line analysis will be used in a real-time environment.

Examples of trigger algorithms - for electrons in that case - are given in Chapter 3, along with an explanation of their important role.

1.3 Physics Program

This section will describe the physics goals set by the ATLAS collaboration for Run 1. The major physics discoveries for each program will be stated. The work presented in this thesis was important for several of these discoveries, moreover the obtained results will be used in the future Run 2 data taking phase to further improve the precision of these analyses.

1.3.1 Higgs Searches

The Standard Model (SM) of particle physics [10, 11] has been tested by many experiments over the last four decades and has been shown to successfully describe high energy particle interactions. However, the mechanism that breaks electroweak symmetry in the SM had not been verified experimentally for a long time, prior to the start of the LHC.

This mechanism [12] which gives mass to massive elementary particles, implies the existence of a scalar particle, the SM Higgs boson. The search for the Higgs boson, its discovery and measuring its properties such as couplings to other particles, was an important part of the Large Hadron Collider [13] (LHC) physics program during the last three years.

In the past, indirect limits on the SM Higgs boson mass of $m_H < 158$ GeV at 95% confidence level (CL) have been set using global fits to precision electroweak results. Direct searches at LEP [14], the Tevatron [15, 16, 17] and the LHC [18, 19] had previously excluded, at 95% CL, a SM Higgs boson with mass below 600 GeV, apart from some mass regions between 116 GeV and 127 GeV.

Both, the ATLAS and CMS collaborations reported excesses of events in their 2011 datasets of proton-proton (pp) collisions at center of mass energy at the LHC, which were compatible with SM Higgs boson production and decay in the mass region 124-126 GeV with significances of 2.9 [18] and 3.1 [19] standard deviations (σ).

Searches for the Standard Model Higgs boson have been performed in the $H \rightarrow ZZ(\star) \rightarrow 4l$, $H \rightarrow \gamma\gamma$, and $H \rightarrow WW(\star) \rightarrow e\nu\mu\nu$ channels with the ATLAS experiment at the LHC using 5.8-5.9 fb⁻¹ of pp collision data recorded during April to June 2012 at a center of mass energy of 8 TeV. These results are combined with earlier results [19], which are based on an integrated luminosity of 4.6-4.8 fb⁻¹ recorded in 2011 at a center of mass energy of 7 TeV, except for the $H \rightarrow ZZ(\star) \rightarrow 4l$ Figure 1.9 and $H \rightarrow \gamma\gamma$ Figure 1.10 channels, which have been updated with the improved analyses [20].

The Standard Model Higgs boson is excluded at 95% CL in the mass range 111-559 GeV except for the narrow region 122-131 GeV. In this region, an excess of events with significance 5.9 σ is observed. The excess is driven by the two channels with the highest mass resolution, $H \rightarrow ZZ(\star) \rightarrow 4l$ and $H \rightarrow \gamma\gamma$, and the equally sensitive but low-resolution $H \rightarrow WW(\star) \rightarrow l\nu l\nu$. Taking into account the entire mass range of the search, 110-600 GeV the global significance of the excess is 5.1 σ .

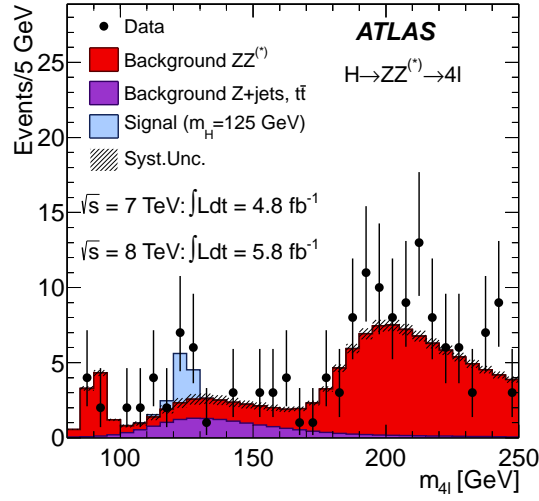


Figure 1.9: The distribution of the four-lepton invariant mass, $m_{4\ell}$, for the selected candidates, compared to the background expectation in the 80–250 GeV mass range, for the combination of the $\sqrt{s} = 7$ TeV and $\sqrt{s} = 8$ TeV data. The signal expectation for a SM Higgs with $m_H = 125$ GeV is also shown. Taken from Ref. [20].

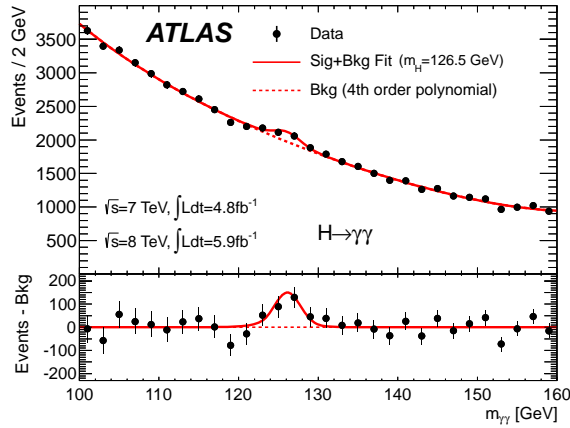


Figure 1.10: The distributions of the invariant mass of diphotons after all selections for the combined 7 TeV and 8 TeV data sample. Top: The result of a fit to the data of the sum of a signal component fixed to $m_H = 126.5$ GeV and a background component described by a fourth-order (Bernstein) polynomial is superimposed. Bottom: The residual of the data with respect to the respective fitted background component is displayed. Taken from Ref. [20].

The obtained results provide conclusive evidence for the discovery of a new particle with mass 126.0 ± 0.4 (stat) ± 0.4 (syst) GeV [20], showing properties consistent with those expected for the SM Higgs. In recognition for this discovery the Nobel Prize in Physics 2013 was awarded to the physicists who described this mechanism of symmetry breaking in 1964, Francois Englert and Peter Higgs.

1.3.2 Supersymmetry

Many extensions of the Standard Model of particle physics predict the presence of strongly interacting particles on the TeV scale that decay to weakly interacting descendants. In the context of R-parity-conserving supersymmetry (SUSY) the strongly interacting parent particles are the partners of the quarks (squarks, q^-) and gluons (gluinos, g^-) and are produced in pairs. The lightest supersymmetric particle (LSP) is stable, providing a candidate that can contribute to the relic dark matter density in the universe. If they are kinematically accessible, the squarks and gluinos could be produced in the proton-proton interactions at the Large Hadron Collider (LHC).

Events would be characterised by significant missing transverse momentum from the unobserved weakly interacting descendants, and by a large number of jets from emissions of quarks and/or gluons.

A search - presented in [21] - for new particles decaying to large numbers (seven or greater) of jets, missing transverse momentum and no isolated electrons or muons are done in various SUSY analyses. The results were interpreted in the context of various simplified supersymmetry-inspired models where gluinos are pair produced, as well as a mSUGRA/CMSSM model. No evidence is found for physics beyond the Standard Model so far.

A summary of the achieved results for SUSY searches can be found in Figure 1.11.

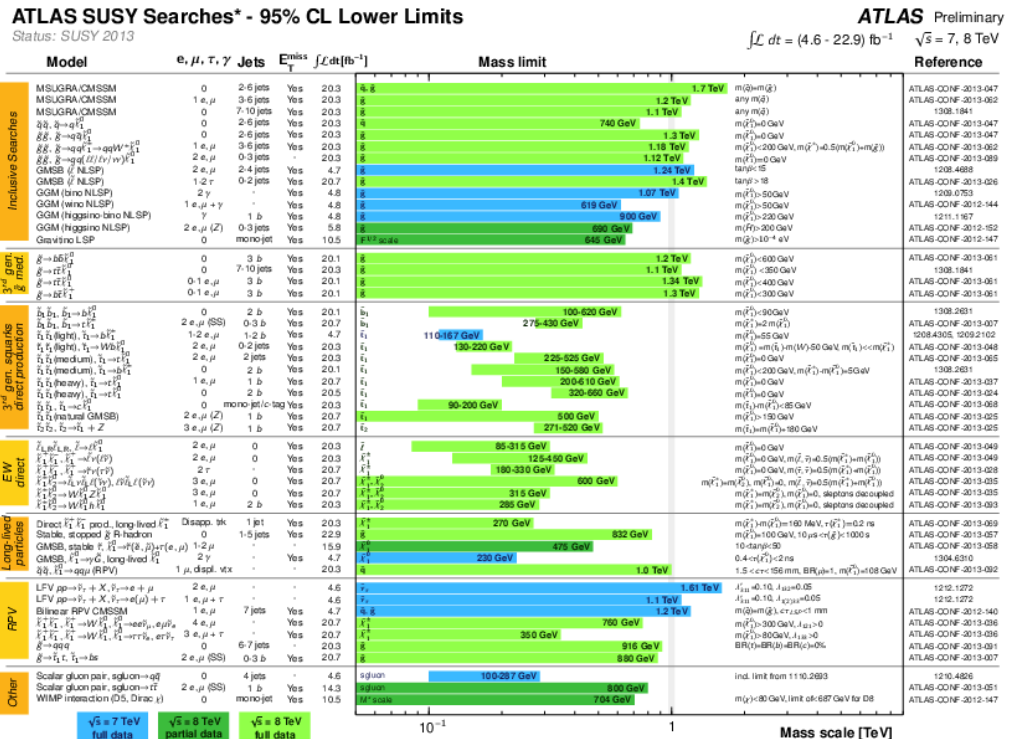


Figure 1.11: Mass reach of ATLAS searches for Supersymmetry. Only a representative selection of the available results is shown. Taken from Ref. [22].

1.3.3 Standard Model

The ATLAS detector was not just built to discover new physics but also to perform precise measurements of the Standard Model.

The mass of the top quark is a fundamental parameter of the Standard Model of particle physics. One of the latest public results [23] measures the top quark mass in dileptonic top quark pair decays in pp collisions at $\sqrt{s} = 7$ TeV. This event topology is characterised by the presence of two charged leptons, at least two neutrinos and several jets, two of which originate from bottom quarks. The top quark mass is measured to be 173.09 ± 0.64 (stat) ± 1.50 (syst) GeV.

Another important aspect for the Standard Model Physics Program in ATLAS is the comparison of existing event generators and the predictions of perturbative QCD calculations at next-to-next-to-leading order with the measured data. Results of such a comparison are presented in [24]. High-mass Drell-Yan differential cross section in proton-proton collisions at a center of mass energy of 7 TeV were measured. Based on an integrated luminosity of 4.9 fb^{-1} , the differential cross section in the $Z \rightarrow \gamma^* \rightarrow e^+e^-$ channel is measured with the ATLAS detector as a function of the invariant mass, M_{ee} , in the range $116 < M_{ee} < 1500$ GeV, for a region in which both the electron and the positron have transverse momentum $p_T > 25$ GeV and pseudorapidity $\eta < 2.5$.

Figure 1.12 shows a summary of several Standard Model total production cross section measurements compared to the corresponding theoretical expectations. The W and Z vector-boson inclusive cross sections were measured with 35 pb^{-1} of integrated luminosity from the 2010 dataset. All other measurements were performed using the 2011 dataset or the 2012 dataset. The top quark pair production cross section at 7 TeV is based on a statistical combination of measurements in the single-lepton, dilepton and all-hadronic channels using up to 1.0 fb^{-1} of data.

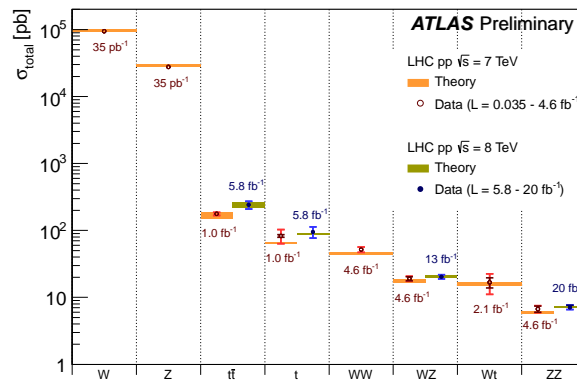


Figure 1.12: Summary of several Standard Model total production cross section measurements. Theoretical expectations were calculated at NLO or higher. The luminosity used for each measurement is indicated close to the data point. Taken from Ref. [22].

1.3.4 Exotics

Also for Exotic Physics searches ATLAS has a designated program. A recent public paper [25] presents the search for microscopic black holes in a like-sign dimuon final state in proton-proton collisions at $\sqrt{s} = 8$ TeV. The data correspond to an integrated luminosity of 20.3 fb^{-1} . Using a high track multiplicity requirement, 0.6 ± 0.2 background events from Standard Model processes are predicted and none observed. This result is interpreted in the context of low-scale gravity models and 95% CL lower limits on microscopic black hole masses are set for different model assumptions.

A summary of the achieved results for exotic physics searches can be found in Figure 1.13.

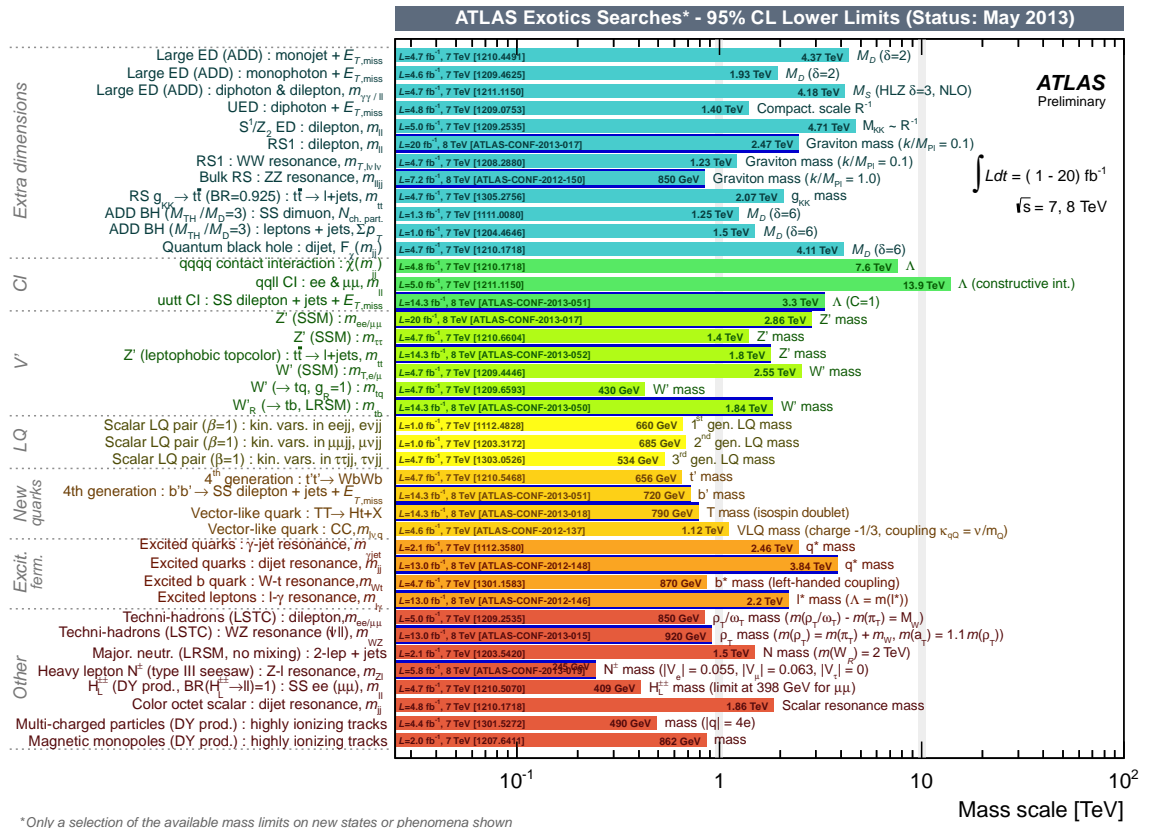


Figure 1.13: Mass reach of ATLAS searches for new phenomena other than Supersymmetry. Only a representative selection of the available results is shown. Dark blue lines indicate 8 TeV data results. Taken from Ref. [22].

1.3.5 Heavy Ions

During heavy ion runs at the end of the year 2011 and 2012 observations have been made of a centrality-dependent dijet asymmetry in the collisions of lead ions at the Large Hadron Collider. In a sample of lead-lead events with a per-nucleon center of mass energy of 2.76 TeV, selected with a minimum bias trigger, jets are reconstructed in fine-grained, longitudinally segmented electromagnetic and hadronic calorimeters. The transverse energies of dijets in opposite hemispheres were observed to become systematically more unbalanced with increasing event centrality leading to a large number of events which contain highly asymmetric dijets (see Figure 1.14. This was the first observation of an enhancement of events with such large dijet asymmetries, not observed in proton-proton collisions, which may point to an interpretation in terms of strong jet energy loss in a hot, dense medium [26].

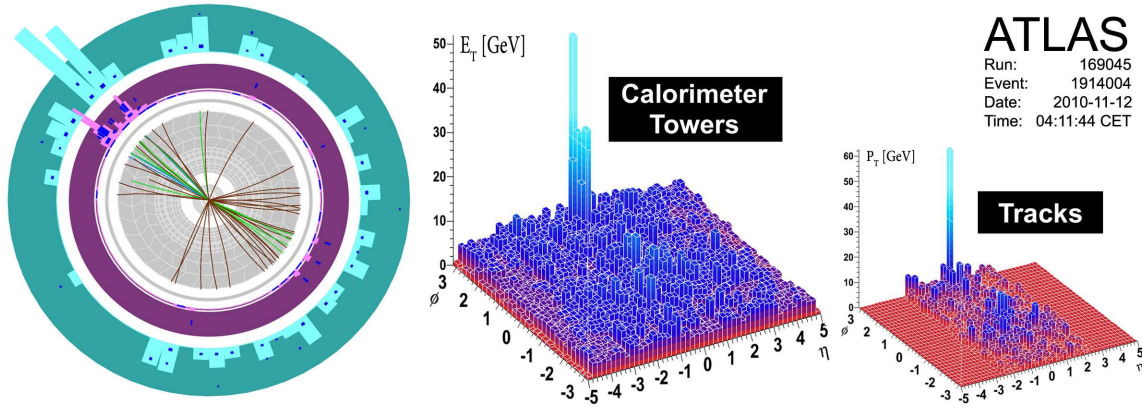


Figure 1.14: *Event display of a highly asymmetric dijet event, with one jet with $E_T > 100$ GeV and no evident recoiling jet, and with high energy calorimeter cell deposits distributed over a wide azimuthal region. By selecting tracks with $p_T > 2.6$ GeV and applying cell thresholds in the calorimeters ($E_T > 700$ MeV in the electromagnetic calorimeter, and $E > 1$ GeV in the hadronic calorimeter) the recoil can be seen dispersed widely over azimuth. Taken from Ref. [26].*

Chapter 2

The ATLAS Liquid Argon Calorimeter

2.1 Overview

This chapter explains general concepts of calorimetry in modern high energy physics, such as the physics behind the calorimetric measurement, the conceptual design ideas and requirements for an experiment at a hadron collider. All these aspects will be used to further explain the ATLAS Liquid Argon Calorimeters in the addition to the introduction in Chapter 1.

2.2 Electromagnetic Calorimetry

The essential concept of calorimetry [27] is to measure the total energy of electrons and photons via total absorption. Two basic principles are used:

- Incoming particles interact with the calorimeter material and produce secondary and tertiary particles, called particle showers. The shower composition and dimension depend on the particle type and the detector material
- The energy of the particle traversing the calorimeter is deposited in form of heat, ionization or excitation of atoms (e.g. scintillation such Cherenkov light)

The ATLAS electromagnetic calorimeter is built to measure the energy of electrons and photons, part of the energy of jets and contribute to the measurement of missing E_T .

The next two section will describe the interaction of charged particles (Section 2.2.1) and photons (Section 2.2.2) with matter.

2.2.1 Interaction of Charged Particles with Matter

When a charged particle enters a medium it will interact with the electrons and nuclei in the medium and will lose energy as it penetrates into the medium. The interaction can be generally thought of as collisions between the charged particle and the atomic electron or the nucleus. Two main processes are responsible for electromagnetic energy loss of high energetic charged particles when passing through matter:

- Ionization: The incoming particle interacts with the atom in the media and transfers enough energy to produce a free electron.
- Bremsstrahlung: The incoming particle is decelerated by interacting with the (mostly nuclear) Coulomb field and radiates photons

The total energy loss can modelled by:

$$\left(\frac{dE}{dx}\right)_{tot} = \left(\frac{dE}{dx}\right)_{ion} + \left(\frac{dE}{dx}\right)_{brem} \quad (2.1)$$

In many materials, at energies above 100 MeV the principal source of energy loss of electrons is Bremsstrahlung (see Figure 2.1).

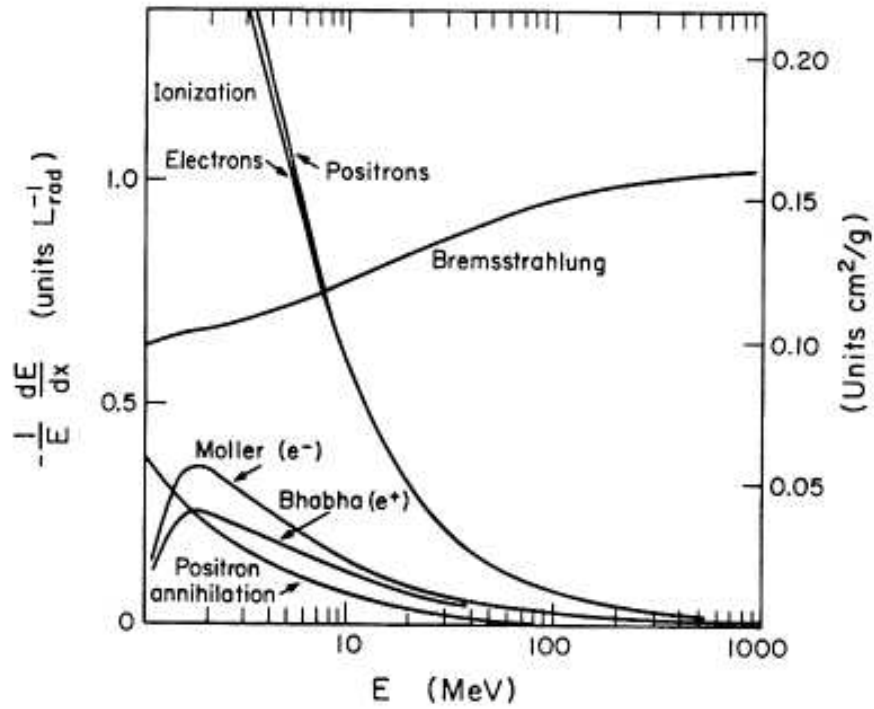


Figure 2.1: Energy loss $\frac{dE}{dx}$ of electrons and positrons versus Energy (MeV) in lead.

The characteristic length for the energy loss of high energetic charged particles is defined as the radiation length X_0 : an electron passing one X_0 has only $1/e$ of it's primary energy left (i.e. $\sim 37\%$). The energy loss through Bremsstrahlung can be calculated using Equation 2.2, [28] and [29]:

$$\frac{dE}{dx} = 4\alpha N_A \frac{Z^2}{A} r_e^2 \cdot E \ln \frac{183}{Z^{1/3}} = \frac{E}{X_0}$$

with

$$X_0 = \frac{A}{4\alpha N_A \frac{Z^2}{A} r_e^2 \cdot E \ln \frac{183}{Z^{1/3}}} \quad (2.2)$$

$$\rightarrow E = E_0 e^{-x/X_0}$$

where Z is the atomic number, A the atomic mass of the matter that is transversed, N_A is Avogadro's number, $r_e = \frac{e^2}{m_e c^2}$ the classical electron radius and $\alpha \approx 1/137$ is the fine structure constant.

The critical energy E_c is defined where the ionization process and Bremsstrahlung are equal:

$$\left(\frac{dE}{dx}\right)_{ion} = \left(\frac{dE}{dx}\right)_{brem} \quad (2.3)$$

An approximate formula for E_c is given by

$$E_c \approx \frac{1600 m_e c^2}{Z} \quad (2.4)$$

The radiation length X_0 is often approximated by the following formula:

$$X_0 = \frac{716.4A}{Z(Z+1) \ln \frac{287}{\sqrt{Z}}} [g \text{ cm}^2] \quad (2.5)$$

Another quantity used to describe the transverse development of an electromagnetic shower in a material is the Molière radius. It is defined such that a cylinder of a radius equal to the Molière radius contains on average 90% of the shower energy and can be calculated by the following expression:

$$R_M \approx E_s \cdot \frac{X_0}{E_c} \quad (2.6)$$

in which E_s - the scale energy - is defined as $m_e c^2 \sqrt{4\pi/\alpha}$. Since the Molière radius can be approximated by the ratio of the radiation length and the critical energy, the Z dependence cancels out in a first approximation. As a consequence shower development in different materials can have non-intuitive differences in the longitudinal (X_0) and lateral (R_M) shower development. Comparing copper ($Z=29$) with lead ($Z=82$): the radiation length between those 2 materials differs by a factor of three (compare Table 2.1) whereas the Molière radii are similar. This means that it takes three times as much copper as lead to contain the shower but the lateral development in copper is even narrower.

A listing of materials and their critical energy E_c as well as their radiation length X_0 and their Molière radius r_M can be found in Table 2.1. Cu, Pb and Ar are materials used for the absorbers and electrodes in the ATLAS electromagnetic calorimeter (see Section 2.3).

2.2.2 Interaction of Photons with Matter

In contrast to the interaction of charged particles in matter, photons are totally absorbed or scattered at relatively large angles. The following effects describe the interactions in different energy ranges (compare different cross sections in Figure 2.2):

- Photoelectric effect: photon is absorbed liberating an atomic electron
- Compton effect: interaction of the photon with a quasi-free atomic electron

material	E_c [MeV]	X_0 [cm]	R_M [cm]
Cu	24.8	1.43	1.5
Pb	9.51	0.56	1.6
Ar (liquid)	30.5	14.2	9.5
Fe	21	1.76	1.7
air	102	30050	-
plastic	100	42.9	-
water	92	36.1	10.6

Table 2.1: E_c , X_0 and R_M for different materials.

- Pair creation: this process corresponds to an absorption of a photon (in the nuclear or electron field) producing a $e^+ e^-$ pair.

As seen in Figure 2.2 the dominant process at high energies is pair production. The cross section can be approximated by [29]

$$\sigma = \frac{7 A}{9 X_0 N_A} \quad (2.7)$$

which means that a high energy photon ($> MeV$) interacts, on average, after passing a length of $\frac{9}{7}X_0$ through matter (A is the atomic mass, X_0 the radiation length and N_A Avogadro's number). The probability of converting into a $e^+ e^-$ pair after $\frac{9}{7}X_0$ is $1 - 1/e$ and the probability of not converting is $1/e$.

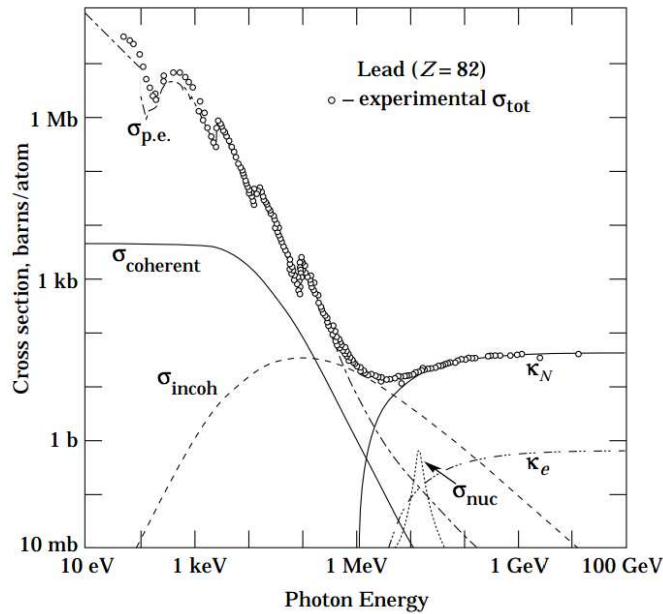


Figure 2.2: Total cross section of photons in lead for different photon energies: σ_{coh} for the coherent Rayleigh scattering, σ_{incoh} for Compton scattering and κ_n , κ_e for the pair production in a nuclear (n) and electron (e) field. Taken from Ref. [30]

2.2.3 Physics of the Electromagnetic Cascade

As described in Section 2.2.1 and Section 2.2.2 at high energies (above a few MeV already) photons interact with matter primarily via pair production and high-energy electrons and positrons primarily emit photons via Bremsstrahlung. The radiation length X_0 is the characteristic relation between energy loss and length of traversed matter (absorber material) for these effects. It was shown that it is the mean distance over which a high-energy electron loses all but $1/e$ of its energy by Bremsstrahlung and $7/9$ of the mean free path for pair production by a high energy photon.

High-energy electrons, positrons or photons cause a cascade of pair production and Bremsstrahlung when penetrating a block of material, as in a calorimeter. This process is called the electromagnetic cascade or shower (see Figure 2.3).

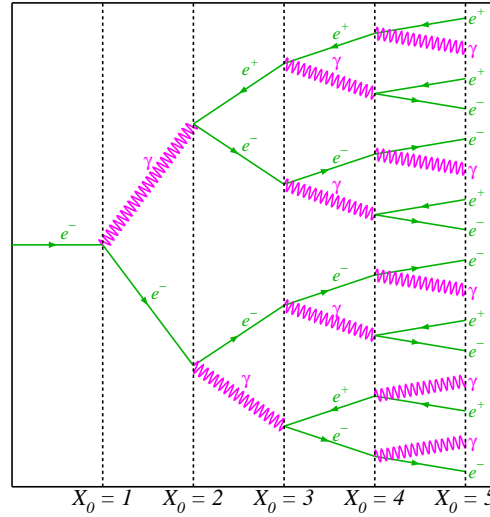


Figure 2.3: *The electromagnetic shower development for a high-energetic electron in radiation length X_0 . The shower development for incoming photons is very similar. Taken from Ref. [31].*

As demonstrated in the previous sections, the shower development is governed by the radiation length. The "shower depth" can be approximated by

$$X = X_0 \frac{\ln(E_0/E_c)}{\ln 2} \quad (2.8)$$

where X_0 is the radiation length of the matter, and E_c is the critical energy. The shower depth increases logarithmically with the energy. The mean longitudinal profile of the energy deposition in electromagnetic cascades is reasonably well described by a gamma distribution [32]:

$$\frac{dE}{dt} = E_0 b \frac{b t^{a-1} e^{-b t}}{\Gamma(a)} \quad (2.9)$$

where $t = X/X_0$, E_0 is the initial energy and a and b are parameters to be fitted with Monte Carlo or experimental data.

2.3 The ATLAS Electromagnetic Calorimeter

The calorimeter plays a central role in ATLAS. In the difficult high luminosity LHC environment, the calorimeter is designed to trigger on and to provide precision measurements of electrons, photons, tau leptons, jets, and missing energy.

In the following Sections the The ATLAS Electromagnetic (EM) Calorimeter will be discussed based on the JINST detector paper [33].

The Liquid Argon sampling calorimeter technique, with accordion-shaped electrodes, is used for all electromagnetic calorimetry covering the pseudorapidity interval $|\eta| < 3.2$. The overall layout inside the cryostat is shown in Figure 2.4.

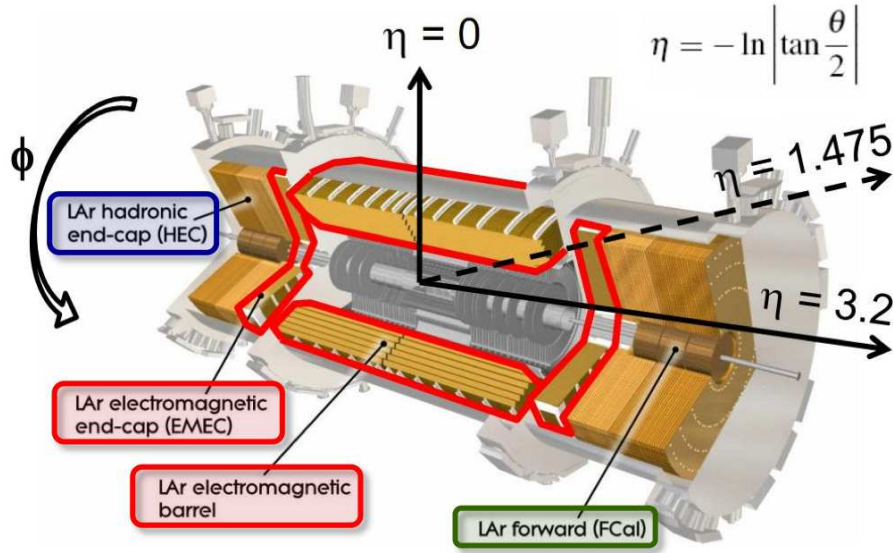


Figure 2.4: *Perspective view of the LAr Calorimeter showing the four different parts it consists of. Taken from Ref. [7].*

The central cryostat contains the barrel electromagnetic calorimeter and the 2 T superconducting solenoid. Each end-cap cryostat houses an electromagnetic and two hadronic wheels, and one forward calorimeter. The central cryostat, which houses the tracking system in its inner cavity, is supported by the barrel Tile calorimeter. In the extended barrel tile calorimeters support each of the two end-cap cryostats. The design of calorimeter is presented in Section 2.3.1 The Tile calorimeter is not a subject of this chapter and thesis in general but was briefly discussed in Chapter 1.

2.3.1 General Design

The ATLAS Liquid Argon (LAr) [7] calorimeter is a sampling calorimeter using liquid argon as the active material and lead, copper or tungsten as the passive absorber. The energy is measured in three different longitudinal layers (samplings) and is pre-sampled in an extra layer to account

for energy loss in the material in front of the calorimeter. The LAr calorimeter, as seen in Figure 2.4, consists of four parts:

- electromagnetic Barrel (EMB), electromagnetic Endcap (EMEC),
- hadronic Endcap (HEC) and the forward calorimeter (FCal)

It covers an overall pseudorapidity region of $|\eta| < 4.9$ using over 182 000 read-out channels. A special accordion structure for the absorber material was chosen to ensure uniformity in ϕ (no cracks) as shown in Figure 2.5. This geometry also allows the calorimeters to have several active layers in depth. The absorbers are emerged in a Liquid Argon bath at an operating temperature of 88K (-185C).

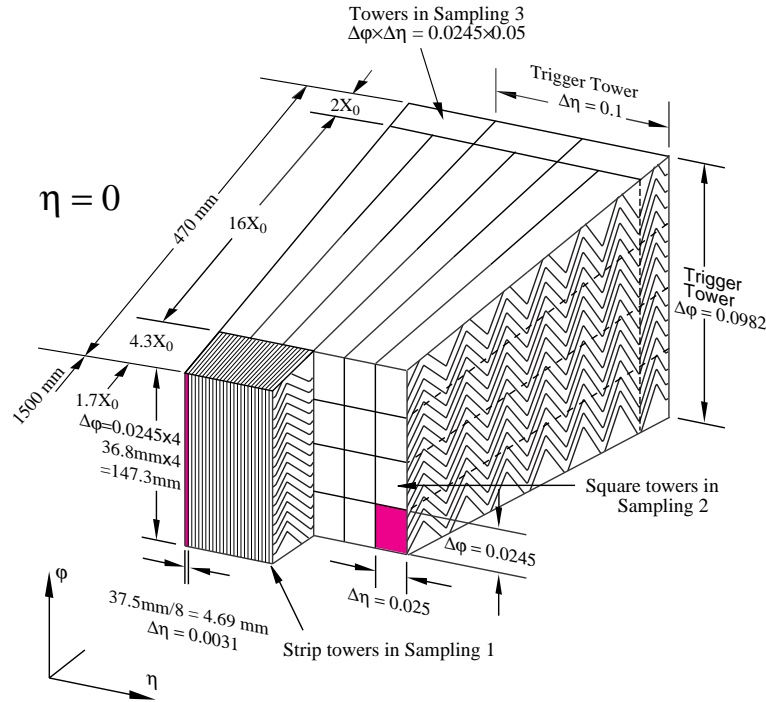


Figure 2.5: Sketch of the accordion structure of the EM calorimeter. The size of the 3 sampling layers (Strips - Middle - Back) and their granularity in η and ϕ . Taken from Ref. [7].

2.3.2 Barrel Calorimeter

A cross section of the the barrel calorimeter system in its cryostat is shown in Figure 2.6. The full cryostat is 6.8 m long, with an outer radius of 2.25 m, and an inner radius of 1.15 m. The vessels are made of aluminum with vacuum insulation. The solenoid, sharing the vacuum insulation, has 44 mm thickness and amounts to $0.63 X_0$.

Inside the liquid argon vessel, the calorimeter consists of two identical half-barrels, with a gap of a few millimetres in between. Each half-barrel consists of 1024 lead-stain-less-steel absorbers with copper-polyimide multilayer readout electrodes in between. To the interaction point pointing readout cells are defined in η . Each calorimeter half-barrel had been divided into 16 modules for fabrication and connection purposes.

The barrel calorimeter system covers the pseudorapidity range $0.0 < |\eta| < 1.3$.

2.3.3 End-cap Calorimeter

As for the barrel, the end-cap cryostats are built out of aluminum, and are vacuum insulated. The outer radius of the cylindrical warm shell is the same as the barrel (2.25 m), and the length of one cryostat is 3.17 m. Figure 2.6 shows a perspective view of an end-cap cryostat.

In the end-caps, the amplitude of the accordion waves scales with the radius. Given the practical limitations in fabrication of the absorber plates, they are arranged like the spokes of a wheel. Each end-cap wheel consists of two concentric wheels, the large one spanning the pseudorapidity interval from 1.4 to 2.5, and the small one from 2.5 to 3.2. The boundary between the two wheels is located at $|\eta| = 2.5$ and matches the boundary of the rapidity range covered by the tracking system $|\eta| < 2.5$. The corresponding gap is 3 mm wide and mainly filled with low density material. There are 768 plates in the large wheel (3 consecutive planes are grouped together to form a readout cell of 0.025 in ϕ) and 256 in the small wheel. The total pseudorapidity coverage is $1.375 < |\eta| < 3.2$.

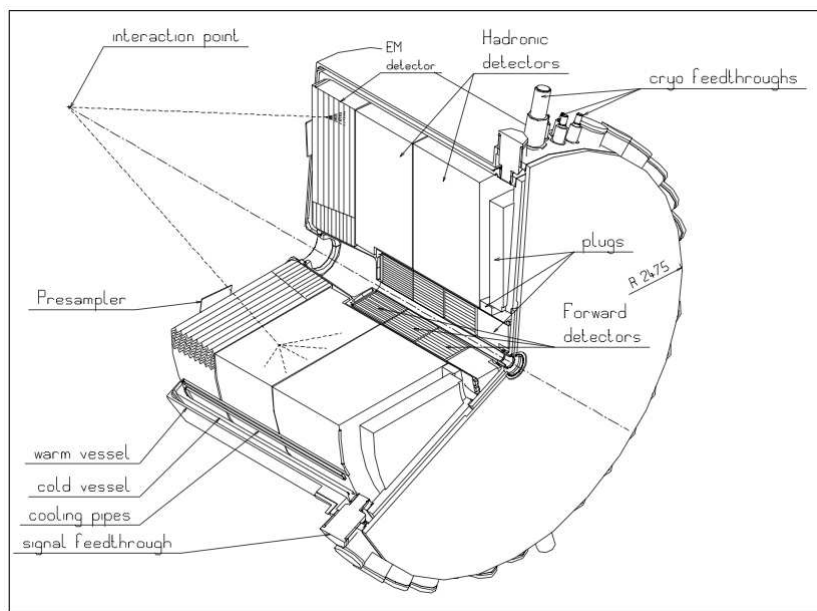
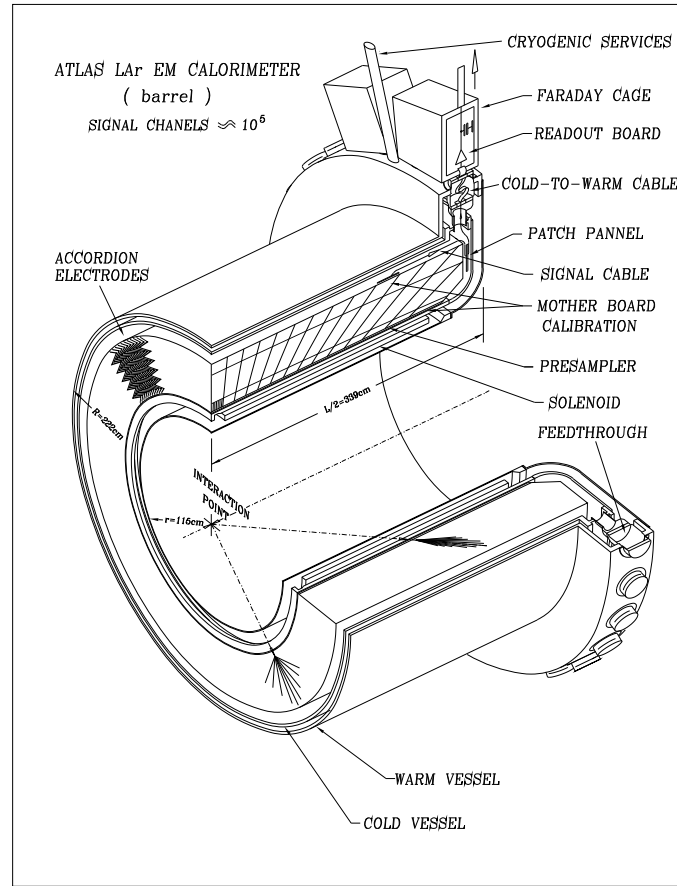


Figure 2.6: Perspective view of one half of the barrel cryostat and the end-cap cryostat. Taken from Ref. [7].

2.3.4 Presampler

As one can see in Figure 1.4, the amount of material in front of the calorimeter necessitates a Presampler (PS) device to correct for energy loss in this passive material. The Presampler is a 1 cm (5 mm) liquid argon active layer instrumented with electrodes roughly perpendicular (parallel) to the beam axis up to a pseudorapidity $|\eta| < 1.37$. Due to the impact of more material in front of the calorimeter in the transition region between the two cryostats, of $1.37 < |\eta| < 1.52$, the Presampler plays a very important role. Above $|\eta| = 1.8$, the Presampler is no longer necessary given the limited amount of dead material and the higher energy of particles for a given p_T . The Presampler is made of 32 sectors in ϕ , and two sectors are fixed to one calorimeter module.

2.3.5 Accordion, Absorber and Cryogenic System

The absorbers in the *barrel* have an accordion shape (see Figure 2.7).

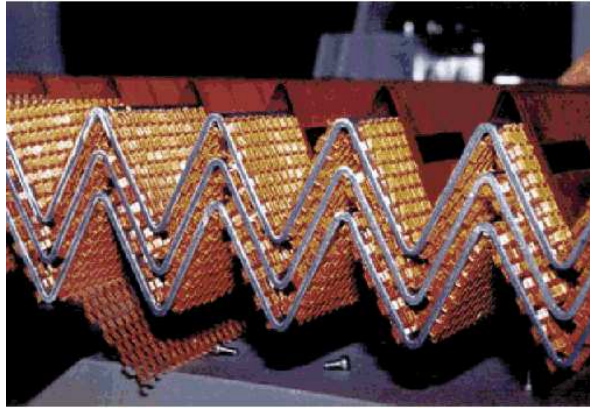


Figure 2.7: *The copper electrode is sitting on top of three lead (+ stainless steel) absorbers separated by light kapton spacers. Taken from Ref. [7].*

The absorber material is a lead/steel sandwich of about 2.2 mm thickness per absorber and 46 kg (the overall weight per half-barrel is about 55 tons). Two lead thicknesses (1.53 mm for $0.0 < \eta < 0.8$, 1.13 mm for $0.8 < \eta < 1.4$) have been chosen to ensure a depth of at least $22 X_0$ ¹. The decrease in lead thickness after $\eta = 0.8$ limits the decrease of the sampling fraction at higher η . The folding angles decrease with increasing radius, in order to leave an approximately constant gap between two neighbours (4.5 mm). Three read-out electrode, made out of copper, are centered in this gap separated by light kapton honeycomb spacers. This defines the two liquid argon gaps of 2.1 mm. High voltage (2000 V) is applied on the read-out electrodes which creates an electric field in these gaps. The currents induced by ionizing electrons passing these gaps are then read-out. There are three compartments (layers) in depth. Strips in the front compartment are read from the front face, whereas the middle and back compartments are read from the back face.

¹Including the material in front

As in the barrel, in the *end-cap* the absorbers and electrodes are accordion-shaped. The absorbers are made of lead plates clad with two layers of 0.20 mm thick stainless steel to ensure absorber rigidity and smooth surface for high voltage. The lead plates are 1.7 mm thick in the outer wheel and 2.2 mm in the inner wheel. The total active thickness of an end-cap calorimeter is larger than $24 X_0$, except for $|\eta| < 1.475$. It increases from 24 to $38 X_0$ when $|\eta|$ runs from 1.475 to 2.5, and from 26 to $36 X_0$ for $2.5 < |\eta| < 3.2$. The readout electrodes are flexible large size printed boards and consist of three conductive layers (copper) insulated by polyimide sheets (kapton). The two outer layers hold a high voltage potential to drift the ionization charge created by charged particles in the liquid argon gap between the absorbers and electrodes. Contrary to the barrel part, the drift gap is not constant, but is a function of the radius (R). In the outer wheel it varies from 2.8 mm at $R=200$ cm to 0.9 mm at $R=60$ cm. In the inner wheel it varies from 3.1 mm at $R = 70$ cm to 1.8 mm at $R = 30$ cm. The detector signal is proportional to the sampling fraction and the drift velocity, and inversely proportional to the liquid argon gap thickness.

The temperature of the liquid argon between the absorbers and electrodes has to be held constant at approximately 88.5 K. The purity has to be guaranteed well below 2 ppm (volume) of oxygen equivalent. The three liquid argon cryostats are operated by a cryogenic system. It is also used for cooling down and warming up the cryostats.

2.3.6 Granularity of the Samplings

The middle layer (second sampling) absorbs most of the particle's energy. The energy in the barrel is measured in quadratic cells (squares) of 0.025 in both pseudorapidity η and azimuth ϕ ($2\pi/256$). The first sampling is a set of narrow strip towers of a granularity of $0.025/8$ (0.003125) (in the barrel, in the end-cap 0.003125 - 0.1) in η . The third sampling is arranged in larger towers of 0.050 (in barrel and end-cap) in η and 0.0025 in ϕ . The fine granularity in η enables a measurement of the angle of the incoming particle and hence the primary vertex. The high granularity of the first calorimeter layer contributes to the high jet rejection capability needed to obtain a very pure $\gamma\gamma$ spectrum.

The number of samplings and the granularity in each of the samplings are summarized in Table 2.2 and visualized in Figure 2.5.

The depth of the first sampling ends up to be $6 X_0$ (including dead material and Presampler). The end of the second (main) sampling is $24 X_0$. The depth of the back sampling varies from 2 to $12 X_0$ (for η less than about 0.6 the depth of the second sampling is limited to $22 X_0$, in order to have at least $2 X_0$ in the third sampling).

$ \eta $ region	0 to 1.4	1.4 to 1.8	1.8 to 2.0
Presampler	0.025×0.1	0.025×0.1	
Sampling 1 (Layer 1) (Strips)	0.003125×0.1	0.003125×0.1	0.004×0.1
Sampling 2 (Layer 2) (Middle)	0.025×0.025	0.025×0.025	0.025×0.025
Sampling 3 (Layer 3) (Back)	0.050×0.025	0.050×0.025	0.050×0.025
Readout channels	110 208	25 600	12 288

$ \eta $ region	2.0 to 2.5	2.5 to 3.2
Presampler		
Sampling 1 (Layer 1) (Strips)	0.006×0.1	0.1×0.1
Sampling 2 (Layer 2) (Middle)	0.025×0.025	0.1×0.1
Sampling 3 (Layer 3) (Back)	0.050×0.025	
Readout channels	24 064	1792

Table 2.2: Granularity for the different samplings in the liquid argon calorimeter in pseudorapidity and azimuth direction ($\eta \times \phi$).

2.3.7 From the Energy Deposit to the Signal

Electrodes are grouped to readout cells inside the cryostat. Coaxial cables bring the signals of the cells (signal, monitoring, calibration) from the liquid argon cold volume to the front-end crates located outside of the barrel and end-cap cryostats at room temperature (signal feed-through) [33].

Crates, housing the front-end electronics, are mounted near the feed-throughs containing several electronic boards:

- The calibration board: injecting known pulses through precision resistors on the mother boards inside the cryostat to simulate as accurately as possible energy deposits in the

calorimeters.

- Front-end boards (FEB) process the raw calorimeter signals and digitise them.
- Tower-builder boards: signals are time aligned and summed up into trigger towers ($\Delta\eta \times \Delta\phi = 0.1 \times 0.1$) sent to the L1 trigger processor
- Front-end crate-controller boards receive the LHC clock, the L1 trigger accept signal to synchronize the front-end electronics
- Additional boards process information from sensors such as the liquid argon temperature

58 front-end crates are used in the LAr calorimeter system: up to 28 FEBs and two calibration boards, trigger-tower builder and front-end crate controller board. Each FEB processes up to 128 calorimeter channels, and a total of 1524 FEBs are used to read out the 182.468 channels of LAr calorimetry.

The incident electrons create EM showers in the lead absorber and the active liquid argon gaps. The secondary electrons create electron/ion pairs in the liquid argon. Ionized electrons and the ions drift in the electric field (2 kV for 2 mm gaps in barrel) and induce a signal (current) of triangular shape with a drift time of about 450 ns proportional to the energy deposited. These signals are summed up per cell and passed via 114 feed-throughs to the front-end electronics outside of the cryostat. After amplification, shaping (splitting the signal into three overlapping linear gain scales in ratios 1/10/100 to optimize the signal to noise ratio) and sampling (every 25 ns) in the front-end boards, the signals are stored in a capacitive array pipeline and are prepared for the trigger inputs (see Figure 2.8). Further on in the tower builder boards, the analogue signals are time aligned and kept in a pipeline storage. They are only digitized after being accepted a L1 trigger which operates at a read-out with 40 MHz in 12 bit. Further explanation on the calibration of the the cell energy will be given in Section 5.2.

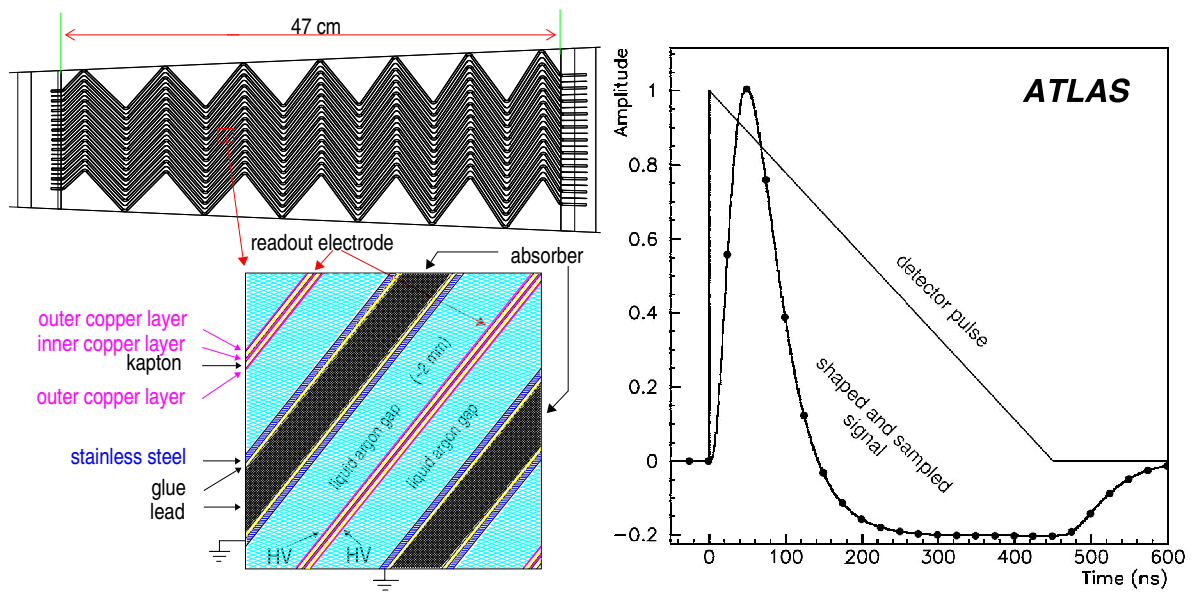


Figure 2.8: Working principle from the energy deposition to the final signal. Left: Signal induced due to drift of ions and electrons in LAr gaps between the accordion shaped absorbers. Right: Amplitude versus time for triangular pulse of the current in a LAr barrel electromagnetic cell and of the FEB output signal after shaping. Also indicated are the sampling points every 25 ns. Taken from Ref. [33].

2.3.8 Calorimeter Resolution

The calorimeter resolution σ_E (see Figure 2.9) can be parametrized using the following equation [34]:

$$\frac{\sigma_E}{E} = \frac{a}{\sqrt{E}} \oplus \frac{b}{E} \oplus c \quad (2.10)$$

where a , b and c are η -dependent parameters:

- a is the sampling term which corresponds to the stochastic nature of an EM shower,
- b is the noise term and describes the contribution of electronic noise of the read out electronics. It depends on the cluster size, typical values are 200 - 300 MeV.
- and c is the constant term arising from spatial inhomogeneities of the LAr calorimeter structure or of dead material.

The symbol \oplus indicates that the two terms are added quadratically.

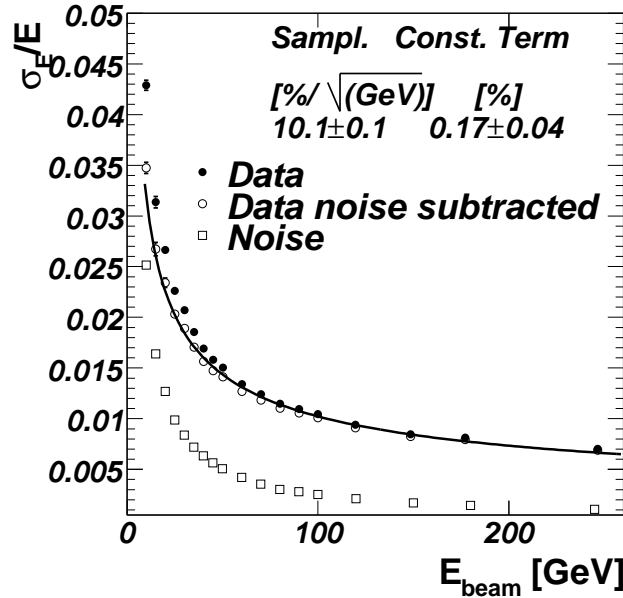


Figure 2.9: The relative energy resolution for a particular cell of the ATLAS Barrel LAr electromagnetic calorimeter as a function of electron beam energy, measured in the test beam. Equation 2.10 without the noise term is fitted to the obtained points. The open squares indicate the subtracted noise contribution. Taken from Ref. [34]

Sampling Term

The sampling term a covers stochastic fluctuations of the electromagnetic cascade during energy deposition. It is the leading term in the resolution for low or medium energy electrons. It can be measured using the J/ψ width where $J/\psi \rightarrow e^+e^-$ provides low energy electrons whose energy measurement resolution is completely dominated by a . The sampling term spreads mostly from 10% to 15% with η .

The sampling term depends on the choice of the material used for the absorber and the active material as well as the thickness of the sampling layers. The sampling fluctuations can be reduced by increasing the sampling fraction f_{samp} :

$$f_{\text{samp}} = \frac{E_{\text{mip}}^{\text{active}}}{E_{\text{mip}}^{\text{active}} + E_{\text{mip}}^{\text{absorber}}} \quad (2.11)$$

where $E_{\text{mip}}^{\text{active}}$ and $E_{\text{mip}}^{\text{absorber}}$ denote the energy deposited by a minimum ionizing particle in the active and in the absorber material. This means that increasing the amount of active material for the shower development reduces the sampling fraction and hence the sampling term. Most calorimeters with a resolution better than $10\%/\sqrt{E}$ have a large sampling fraction exceeding 20%.

Example of the sampling term of the ATLAS calorimeter versus $|\eta|$ for electrons and photons as calculated in Monte Carlo Simulations can be seen in Figure 2.10.

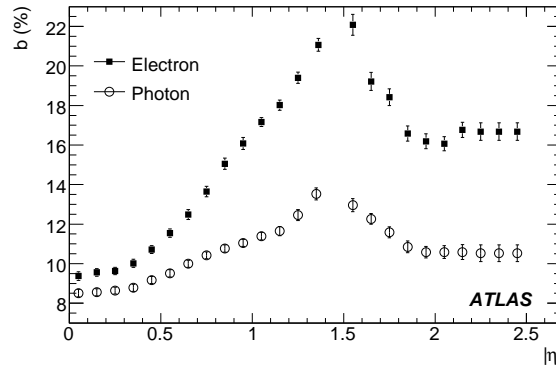


Figure 2.10: Sampling term of the ATLAS calorimeter versus $|\eta|$ for electrons and photons as calculated in MC simulations. Taken from Ref. [22].

Noise Term

This contribution to the energy resolution comes from the electronic noise of the readout chain and depends on the detector technique and on the features of the readout circuit (detector capacitance, cables, etc.). Techniques like signal shaping and optimal filtering are used to optimize the signal to noise ratio in these detectors. Nevertheless, a fundamental limitation remains. This can be described by the relation $Q = \sqrt{4kTR\delta F}$ (where Q is the equivalent noise charge, k the Boltzmann constant, T the temperature, R the equivalent noise resistance of the preamplifier and δF the bandwidth), which shows that the noise increases when one wants to operate at high rate. The noise contribution to the energy resolution increases with decreasing energy of the incident particles and at energies below a few GeV may become dominant. Therefore, the noise equivalent energy is usually required to be much smaller than 100 MeV per channel. In sampling calorimeters the noise term can be decreased by increasing the sampling fraction, because the larger the sampling fraction, the larger the signal from the active medium and therefore the higher the signal-to-noise ratio.

Since the noise term (including pile-up noise and electronics noise) can be measured with pedestal runs and zero-bias triggers, the J/ψ width can be used to compare the sampling term in MC with the measured one.

Constant Term

The constant term includes contributions which do not depend on the energy of the particle. Non-uniformities of the calorimeter response caused by instrumental effects contribute an additional smearing to the measured energy and manifest themselves in the constant term. Non-uniformities can originate from the detector geometry (for instance if the absorber and active layers have irregular shapes), from imperfections in the detector's mechanical structure and readout system, from temperature gradients, from the detector aging, from radiation damage, etc. These non-uniformities can be cured (to a large extent) if they exhibit a periodic pattern, as is the case if they are related to the detector geometry. On the other hand, other effects such as mechanical imperfections are randomly distributed and therefore more difficult to correct. With the increasing energy of present accelerators, the constant term becomes more and more the dominant contribution to the energy resolution at high particle energies of electromagnetic calorimeters. Tight construction tolerances are therefore imposed on the mechanics and readout system of modern calorimeters, for instance LHC calorimeters. Typically the constant term of an electromagnetic calorimeter should be kept at the level of one percent or smaller. This is particularly true for homogeneous calorimeters, because of their small stochastic term.

The constant term of the ATLAS LAr calorimeter for both years 2011 and 2012 will be discussed and further explained in Section 7. For both years higher constant terms in data than expected from MC simulations (Figure 2.11) lead to precise investigations of non-uniformities of the energy response to uncover the problem.

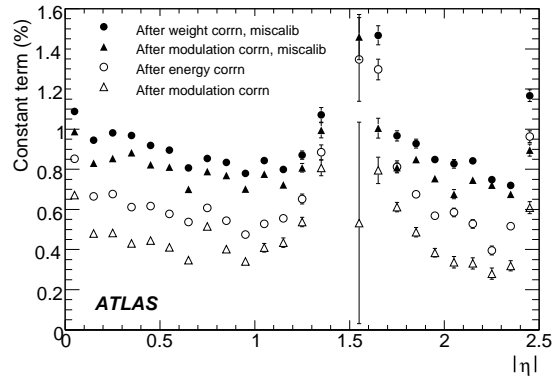


Figure 2.11: *Constant term versus $|\eta|$ of the ATLAS calorimeter calculated with MC simulations. Taken from Ref. [22].*

Chapter 3

Reconstruction Software and Monte Carlo Simulation

3.1 Overview

This chapter introduces the ATLAS Reconstruction Software ATHENA which is used to reconstruct raw data coming from the detector's hardware (such as the energy deposited by an electron in the LAr EM calorimeter) to a full event. Not only data produced in pp-collisions is processed with this software but also data from Monte Carlo Simulations - to test, predict, correct and compare with "real" data. This is a very important feature for all physics and calibration efforts (see Section 3.5). Data from real or simulated collisions are stored in different data containers and distributed all over the world via the Worldwide LHC Computing Grid (WLCG or simply just GRID).

Data taking conditions for both years will also be presented Section 3.4.

3.2 Reconstruction Software

ATHENA is the Atlas Control and Reconstruction Framework based on the common Gaudi architecture [35] and the data analysis framework ROOT [36].

This software contains libraries and executables to develop and run physics applications, from trigger selection, to event reconstruction, simulation, and analysis. It is organized in so-called packages or services to manage the large amount of raw data produced: a service to manage time-varying conditions and detector data (store them in a database), a toolkit to simulate and analyze the overlay of multiple collisions during the detector sensitive time (pile-up). Athena components are configured via python scripts. The scripting interface allows to fully configure any Athena component and modify its configuration.

A common - for all sub-detector and analysis groups - 4-momentum interface is developed to ensure easy maintenance over a long period of time and coherence between event reconstruction and physics analysis - ATLAS Event Data Model (EDM). Moreover EDM allows the use of

common software between on-line data processing and offline reconstruction.

The EDM is defined by several hundred data objects, usually containers of physics entities such as cells, tracks or particles. To access these data objects from ATHENA a service called StoreGate is used. The full detector geometry and conditions during runs are stored in a common database and are accessible through StoreGate.

The size of each data object depends on the container, as mentioned before, stored inside the object. To reduce the size of the objects and adapt them to certain needs, three different formats are defined. These formats are again containers holding data object information per pp-collision (event). The difference between the three formats is the amount of information available inside the container. Starting from a raw event with an average size of $\sim 1.6\text{MB}$ the largest format is the Event Summary Data (ESD) of a size of $\sim 500\text{kb/event}$ to Analysis Object Data (AOD) of a size of $\sim 100\text{kb/event}$. The last format is the Derived Physics Data (DPD) - of the size of few kb/event - not containing any data objects anymore but a set of predefined variables and its values (chosen by the final user or analysis group) per event, such as the basic electron attributes for example: el_cl_E , el_cl_eta , el_cl_phi (reconstructed electron cluster energy, η and ϕ position) or $el_trackpt$, $el_trackphi$, $el_tracketa$ (reconstructed track momentum, η and ϕ position). AODs are centrally produced by a given set of selection criteria. The last step, the DPD creation, is in the responsibility of a single user or a group, see Figure 3.1.

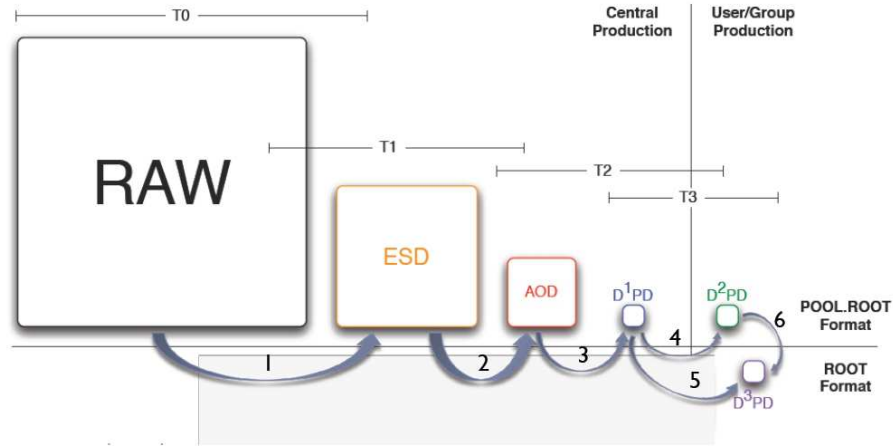


Figure 3.1: Data ending up in different containers and different storage spaces on the GRID. The difference between the three containers is the amount of information available. Until step 4 data is handled central. Just for the last step the single user or analysis group is responsible. Taken from Ref. [37].

To filter out unnecessary information the following techniques are used:

- Skimming: Selection of events, only selected events passing certain criteria are stored.
- Trimming: Removal of the data object's container.
- Thinning: Removal of individual objects from a container.

- Slimming: Removal of parts of a data object's container.

To overcome network and storage limitations, the different containers are distributed all over the world to different computing centers, called Tier. These computing centers are connected with each other in a computing grid called the Worldwide LHC Computing Grid (WLCG) [38](see Figure 3.2). The WLCG is the largest scientific computing grid in the world. It involves over 170 computing centers in 36 countries.

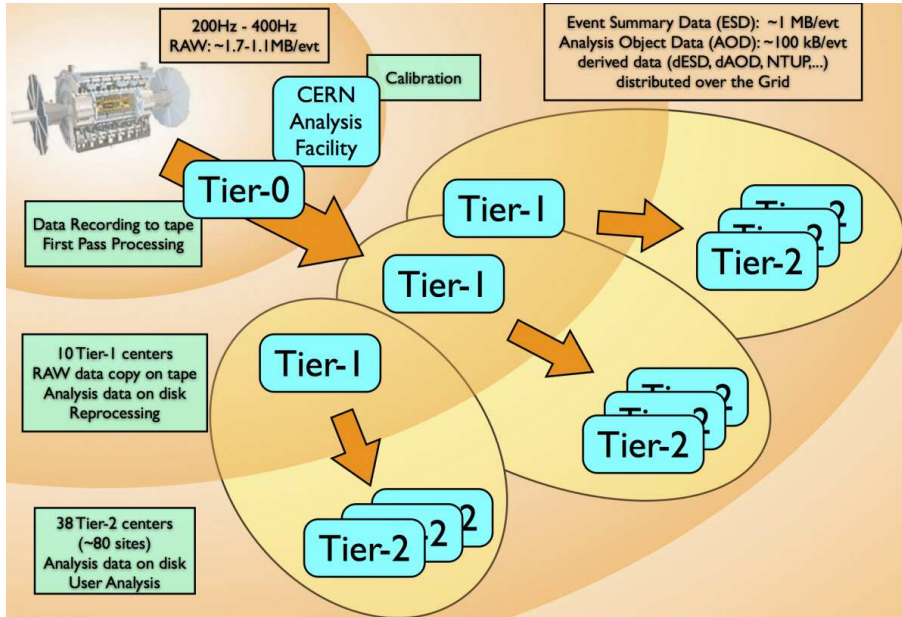


Figure 3.2: Top left is the ATLAS detector showing the data distribution over the grid to the different Tier sites. On the top right the size per collision (event; 'evt') for the different container can be seen. Taken from Ref. [37].

3.3 Monte Carlo Simulation in 2011 and 2012

The results presented in this dissertation are based on the data taken by ATLAS in 2011 and 2012 as well as the corresponding samples from Monte Carlo simulations. Several sources of high- E_T and isolated electrons are exploited to quantify the absolute scale, uniformity and linearity of the EM calorimeter. The Z resonance is the primary technique used to extract the EM calorimeter absolute scale. $W^\pm \rightarrow e^\pm \nu$ decays on the other hand provide a high number of isolated electrons, and are exploited for the energy scale extraction as well as for uniformity and linearity measurements.

W and Z production is simulated using the PYTHIA [39] and POWHEG [40] event generators interfaced with PHOTOS [41] for QED final state radiation. Interactions between the final state particles and the detector are simulated with GEANT4 [42] and classified as nominal MC samples. As these samples were produced ahead of the actual data taking, the simulated level of pileup (see Section 3.4.1), parametrized as the average number of interactions per bunch crossing, $\langle \mu \rangle$, only approximately matches that of the actual data. This is corrected by reweighting, in each sample, the simulated $\langle \mu \rangle$ distribution to match the data. Similarly, the simulated primary vertex z distribution was corrected to match the data. To investigate the impact of additional or lost material w.r.t. data during simulation there are samples where more material in terms of X_0 is added to different detector layers. These samples are known as distorted geometry samples. A summary of the samples used and corresponding statistics is given in Section 3.5.

3.4 Data in 2011 and 2012

The ATLAS detector recorded 5.2 fb^{-1} of data from 7 TeV pp collisions, running from March to October 2011 with a data taking efficiency of 89.9% for the whole detector and 96.9% for the Liquid Argon Calorimeter. From April to December 2012, 21.3 fb^{-1} of 8 TeV pp collision data were recorded with an ATLAS overall efficiency of 95.5% when LAr calorimeter efficiency reached 99.1%. Figure 3.3 (a) shows the integrated luminosity evolution in 2011 and 2012.

The production cross sections for $W^\pm \rightarrow e^\pm \nu$ and $Z \rightarrow e^+ e^-$ for both years, 2011 (7TeV) and 2012 (8TeV), can be found in Table 3.1.

[nb]	7 TeV	8 TeV
$\sigma(W^+ \rightarrow e^+ \nu)$	$6.01 \pm 0.016(\text{stat}) \pm 0.072(\text{sys})$	$7.10 \pm 0.04(\text{stat}) \pm 0.26(\text{sys}) \pm 0.31(\text{lumi})$
$\sigma(W^- \rightarrow e^- \nu)$	$4.14 \pm 0.014(\text{stat}) \pm 0.057(\text{sys})$	$4.94 \pm 0.03(\text{stat}) \pm 0.19(\text{sys}) \pm 0.22(\text{lumi})$
$\sigma(W^\pm \rightarrow e^\pm \nu)$	$10.207 \pm 0.021(\text{stat}) \pm 0.121(\text{sys})$	$12.04 \pm 0.05(\text{stat}) \pm 0.37(\text{sys}) \pm 0.53(\text{lumi})$
$\sigma(Z \rightarrow e^+ e^-)$	$0.937 \pm 0.006(\text{stat}) \pm 0.009(\text{sys})$	$1.10 \pm 0.02(\text{stat}) \pm 0.05(\text{sys}) \pm 0.05(\text{lumi})$

Table 3.1: Latest $W^\pm \rightarrow e^\pm \nu$ and $Z \rightarrow e^+ e^-$ inclusive production cross sections measurements. Taken from Ref. [43] and [44].

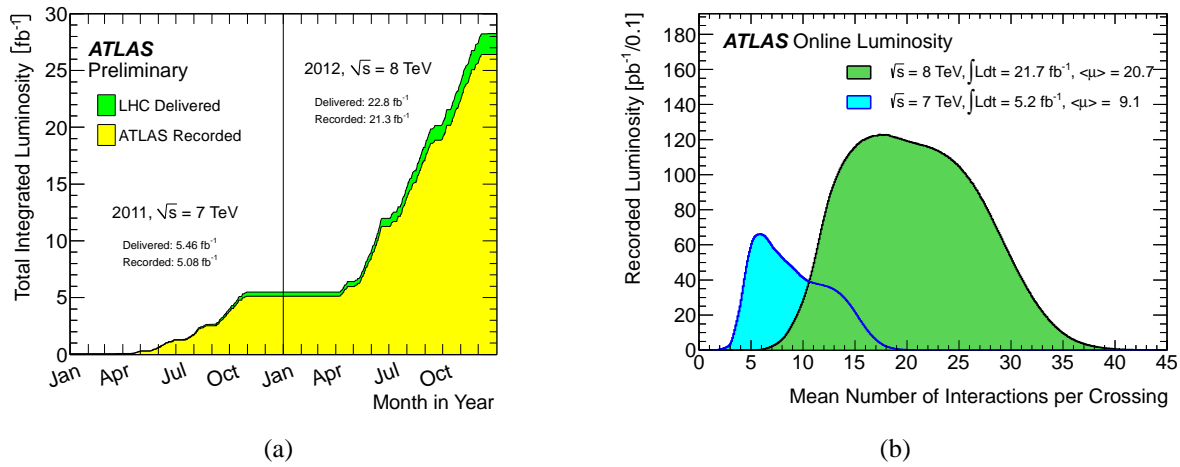


Figure 3.3: (a) Cumulative luminosity versus time delivered to (green), and recorded by (yellow) ATLAS during stable beams and for pp collisions in 2011 ($\sqrt{s} = 7 \text{ TeV}$) and 2012 ($\sqrt{s} = 8 \text{ TeV}$). The delivered luminosity accounts for the luminosity delivered from the start of stable beams until the LHC requests ATLAS to put the detector in a safe standby mode to allow a beam dump or beam studies. The recorded luminosity reflects the DAQ inefficiency. (b) Luminosity-weighted distribution of the mean number of interactions per bunch crossing during 2011 and 2012 data taking. The integrated luminosities and the mean μ values are given in the figure. The mean number of interactions per bunch crossing corresponds to the mean of the poisson distribution on the number of interactions per bunch crossing calculated for each bunch. Taken from Ref. [45].

3.4.1 Pile-up and Data Taking Conditions

Pile-up describes the fact that many soft underlying interactions are hiding below the hard interaction, which usually fires the trigger of this event. Each of these soft underlying events adds additional particles to the event of interest. Due to finite integration times in the sub detectors, these additional events might even come from neighbouring bunch crossings. As these have different effects on the different sub detectors, these events are subdivided into two classes:

- in-time pile-up means that the additional collisions happen during the same bunch crossing as the hard scattering which triggers the event.
- out-of-time pile-up means that the additional collisions come from other bunch crossings than the hard scattering which triggers the event. Depending on the technology of the subsystem, a different number of events before or after the bunch crossing of the hard scatter can contribute. The LAr EM calorimeter, for example, has longer integration times (around 600 ns) relative to the bunch spacing (25 ns and 50 ns) and is therefore more affected by the out-of-time pile-up.

A typical pile-up interaction adds additional tracks to the event, depending on transverse momentum thresholds, quality requirements, etc. The amount of pile-up is characterized by the variable $\langle \mu \rangle$ which denotes the average number of pile-up events overlayed over the hard scatter.

From the electron energy calibration point of view, the major challenge in 2012 was to cope with high and heterogeneous pile-up conditions from run to run. In 2012, pile-up rose by a factor of ~ 3 w.r.t. to the preceding year. A comparison of the pile-up distribution in 2011 and 2012 data taking can be seen in Figure 3.3 (b).

3.5 MC Simulation and Data Samples

Section 3.5.1 and 3.5.2 explain the data and MC samples used for the work done in this thesis. In order to get as many signal electrons as possible by reducing possible background, most of the studies presented in this thesis follow the same electron selection criteria, which will be explained in Section 3.5.3.

3.5.1 MC simulation samples

For 2011 three different sets of MC simulation samples were produced, namely MC11a,b,c. To generate physics events PYTHIA and POWHEG were used, whereas in 2012 only one MC simulation, namely MC12, was needed. A nominal geometry configuration was used to simulate the actual material as well as a distorted material configuration. The difference in percent of additional X_0 compared nominal MC can be seen in Figure 3.4. For reasons of simplicity the term “MC simulation” stands from now on for the full chain of MC simulation (event generation - detector simulation and reconstruction) unless explicitly stated otherwise.

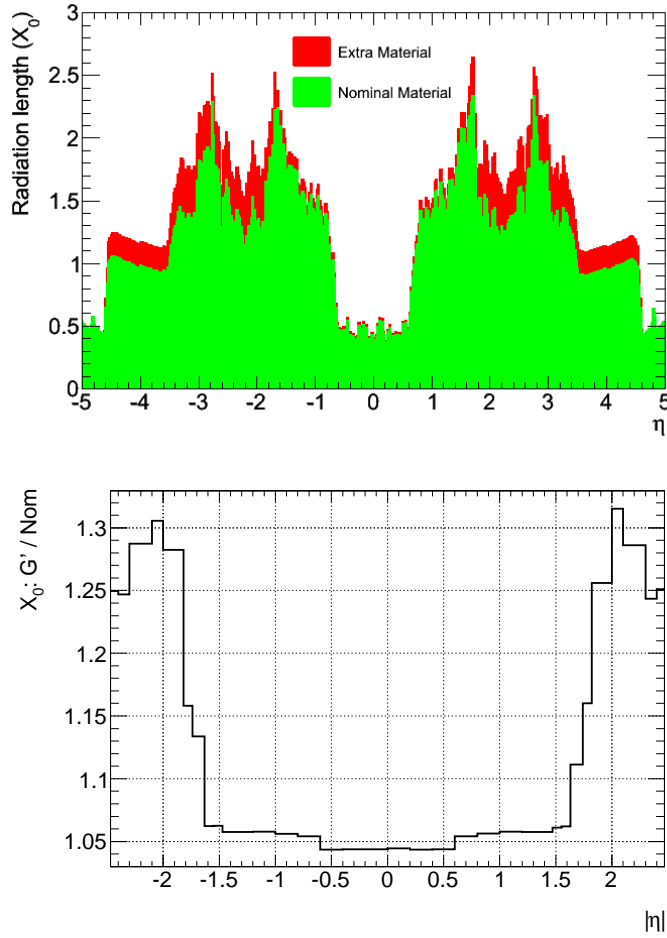


Figure 3.4: *Difference in X_0 of the nominal MC sample (green) to the distorted material sample (G') in red. As seen, for a region $|\eta| < 1.5$ about 5% X_0 was added in the inner detector and up to $1.5 < |\eta| < 2.0$ up until 30% X_0 . Taken from Ref. [46].*

The distorted geometry configuration G' includes additional material in front of the calorimeter for the following layer: 5% of whole ID, 20% of pixel services, 20% of SCT services, +15% X_0 at end of the SCT/TRT end-caps and +15% X_0 at the ID endplate. The location of the additional material is illustrated in Figure 3.5.

A summary of the events generated for both years can be found in Appendix D. The reconstruction and simulation software is in constant development and published in releases. To link a software releases with a given reconstruction or simulation process, so-called tags are used. To track the tag history, tags are stored in a database. A summary of the tags used for the MC production in 2011 and 2012 can be found in the Appendix D, Table D.2.

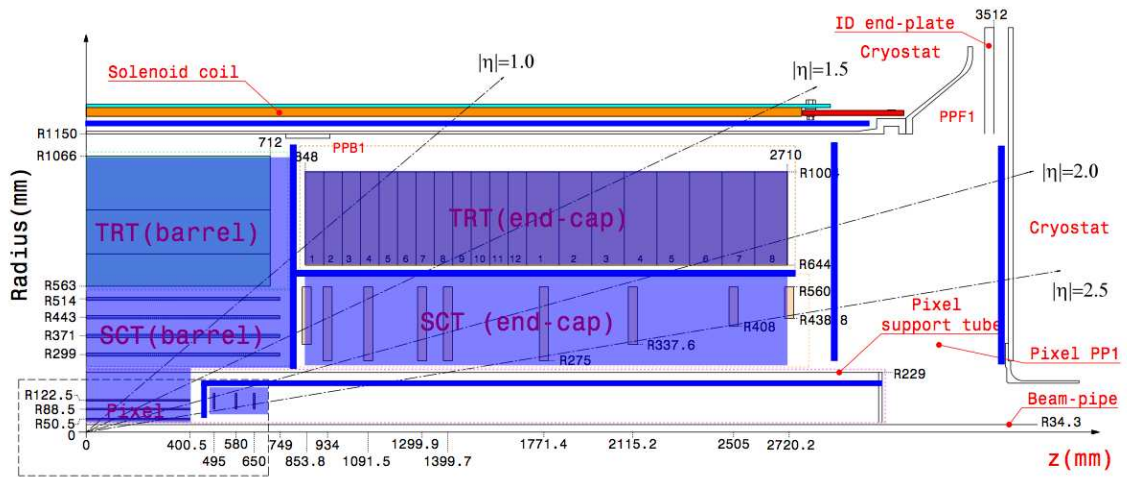


Figure 3.5: Graphical representation of additional material in front of the the EM calorimeter in the distorted geometry MC sample. Parts where material was added are marked in blue. Taken from Ref. [46].

3.5.2 Data samples

The data taking of the ATLAS experiment is divided into data periods. Each period consists of several runs of data taking which can last minutes up to days. For each run specific conditions (eg the reconstruction software release) are stored in a database and linked to the run number, again, with tags. Moreover in the e/γ calibration group dedicated mini n-tuples¹ are used for the calibration analyses. These mini n-tuples are basically a set of variables inherited from the official e/γ DPD. An overview of the different data taking tags and calibration n-tuples versions can be found in Appendix D, Table D.3.

3.5.3 General Selection Cuts

The event selection passes several cuts adapted to the needs of the analysis or studies. For the calibration studies done within this thesis a general cut-flow for electrons coming from $Z \rightarrow e^+e^-$ and $W^\pm \rightarrow e^\pm \nu$ can be given.

$Z \rightarrow ee$ events are selected requiring exactly two oppositely charged electrons, satisfying the medium (Chapter 4) identification criterion, $E_T^e > 27$ GeV, and $|\eta| < 2.47$. The invariant mass of the pair should be within $80 < M_{ee} < 100$ GeV.

More subject to jet backgrounds than Z decays are electrons coming from $W^\pm \rightarrow e^\pm \nu$. The electrons are required to pass tight identification requirement (more explanation will be given in Chapter 4). The reconstructed kinematics should satisfy $p_T^e > 30$ GeV and $|\eta| < 2.47$, excluding the barrel-end-cap transition region $1.37 < |\eta| < 1.52$. Furthermore, the missing transverse energy should satisfy $E_T^{miss} > 30$ GeV, and the transverse mass requirement is $M_T = \sqrt{2p_T^e E_T^{miss}(1 - \cos \Delta\phi)} > 60$ GeV.

The selection process performs in two steps. Loose selection criteria are applied, when selecting events from the official e/γ DPD, to small calibration n-tuples, including the variables most relevant for the calibration. On top of the calibration baseline cuts additional selection cuts were applied, in order to reduce the background, clean up the signal electrons and be consistent with the current Standard Model analyses (see Appendix D, Table D.4 for electrons coming from $W^\pm \rightarrow e^\pm \nu$ decays and Table D.5 for electrons coming from $Z \rightarrow e^+e^-$ decays).

Most of the studies presented with 2011 data, if not indicated otherwise, are using the full 2011 dataset, which contains a total integrated luminosity of 4.9 fb^{-1} and the official ATLAS MC2011c simulation sample. For the 2012 results, a dataset of 12 fb^{-1} of total integrated luminosity is used. The number of Z and W events after applied cuts, as presented in Appendix D, can be found in Table 3.2.

¹A n-tuple is a matrix (with rows and columns) of numbers (or ROOT objects). Each row reflects one event of a pp collision. The columns contain observables such as the electron energy, momentum, charge or fired trigger.

	MC	data
$W^\pm \rightarrow e^\pm \nu$ 2011	$40 \cdot 10^6$	—
after cut step 1	$11.2 \cdot 10^6$	$32.01 \cdot 10^6$
after cut step 2	$5.62 \cdot 10^6$	$13.92 \cdot 10^6$
$W^\pm \rightarrow e^\pm \nu$ 2012	$40 \cdot 10^6$	—
after cut step 1	$11.2 \cdot 10^6$	$51.26 \cdot 10^6$
after cut step 2	$5.62 \cdot 10^6$	$22.05 \cdot 10^6$
$Z \rightarrow ee$ 2011	$10 \cdot 10^6$	—
after cut step 1	$5.15 \cdot 10^6$	$2.75 \cdot 10^6$
after cut step 2	$3.02 \cdot 10^6$	$1.62 \cdot 10^6$
$Z \rightarrow ee$ 2012	$10 \cdot 10^6$	—
after cut step 1	$5.15 \cdot 10^6$	$4.15 \cdot 10^6$
after cut step 2	$3.02 \cdot 10^6$	$2.43 \cdot 10^6$

Table 3.2: Number of residual $W^\pm \rightarrow e^\pm \nu$ and $Z \rightarrow e^+ e^-$ events, after applying the cuts mentioned before, for specific datasets and years.

Chapter 4

Electron Reconstruction and Identification

As discussed in Section 3 all recorded data are reconstructed by the ATHENA offline reconstruction software. To collect as many signal events as possible but rejecting at the same time background, various steps are needed. These steps can be summarized as efficient triggers, optimized reconstruction algorithms and an efficient particle identification.

This chapter gives an introduction to the reconstruction algorithms used to fully reconstruct an electron. The first section addresses the reconstruction of the track parameters from the inner detector Section 4.2. To describe the fully reconstructed electron object further stages will be discussed: starting with the actual electron candidate reconstruction (Section 4.2), electron identification (Section 4.3), the electron trigger (Section 4.4) and concluding on additional requirements (Section 4.5) needed to get a clean signal when using $W^\pm \rightarrow e^\pm \nu$ (or $Z \rightarrow e^+ e^-$ samples).

Electron reconstruction outside the precision of region $|\eta| < 2.5$, will not be discussed in this thesis.

4.1 Electron Track Reconstruction

Electron tracks are a basic ingredient for the reconstruction of electrons. The direction of the curvature in the magnetic field is used to determine the charge of a particle and thus allows to distinguish electrons from positrons.

Hits in the inner detector are used to reconstruct charged-particle tracks. The Seeding of the tracks is done by a combination of hits in the three pixel layers and the first SCT layer. These seeds are extrapolated in a fitting procedure to the outer SCT layers to become full tracks. Tracks are then associated with hits in the TRT where finally the full information of the inner detector is used to reconstruct final track.

These final tracks are matched to energy deposits in the calorimeter, called cluster, to build electron candidates and then to provide information for particle identification. Nevertheless this track-cluster matching is affected by Bremsstrahlung losses. The radiated photons do not leave a track in the inner detector but deposit energy in the calorimeters. To combine the cluster

in the calorimeter with the track in the inner detector several techniques are used in the ATLAS reconstruction. More on that will be explained in the next section.

The intrinsic track reconstruction proceeds in two steps: pattern recognition and track fitting. On top of the standard pattern recognition [47], which uses a π^\pm hypothesis, a modified pattern recognition algorithm (based on a Kalman fitter-smoother formalism [48]) is run. This allows track candidates above 1 GeV¹ to have a Bremsstrahlung energy loss of maximally 30% at each material surface. Track candidates are then fitted first with a π^\pm hypothesis. In case of a high χ^2 , caused by large energy losses, the electron hypothesis is applied by the updated ATLAS Global χ^2 Track Fitter [49]. The track fitting procedure using the electron hypothesis that allows for energy loss is unfortunately only available in 2012 data.

The electron reconstruction scheme used for the 2010 and 2011 publications of ATLAS results uses the same tracking algorithm for all charged particles. All tracks are fitted using a π^\pm particle hypothesis to estimate the material effects. The lack of special treatment for Bremsstrahlung losses resulted in inefficiencies in reconstructing the electron trajectory and contributed to the degradation of the estimated track parameters. This effect increases with the amount of material encountered by the particle. Consequently, this effect depends strong on the electron's pseudorapidity.

In the 2012 electron energy reconstruction, Bremsstrahlung losses (and the resulting alteration of the track curvature) were taken into account. Bremsstrahlung losses induced by material in the inner detector are described by using a Gaussian sum filter (GSF) [50] approach. The estimated electron track parameters are highly improved with respect to 2011 reconstruction. The impact of the GSF algorithm on the reconstructed electron's track parameters (p/q), where p is the track momentum and q the charge of the associated particle, is compared to the 2011 reconstruction algorithm output in Figure 4.1.

Measuring the electron energy response using E/p with the new GSF algorithm has a direct impact since, in E/p , the momentum measurement plays a major role in the tails and in the width of the corresponding distribution.

¹The transverse momentum lower threshold for tracks with pion hypothesis is 400 MeV.

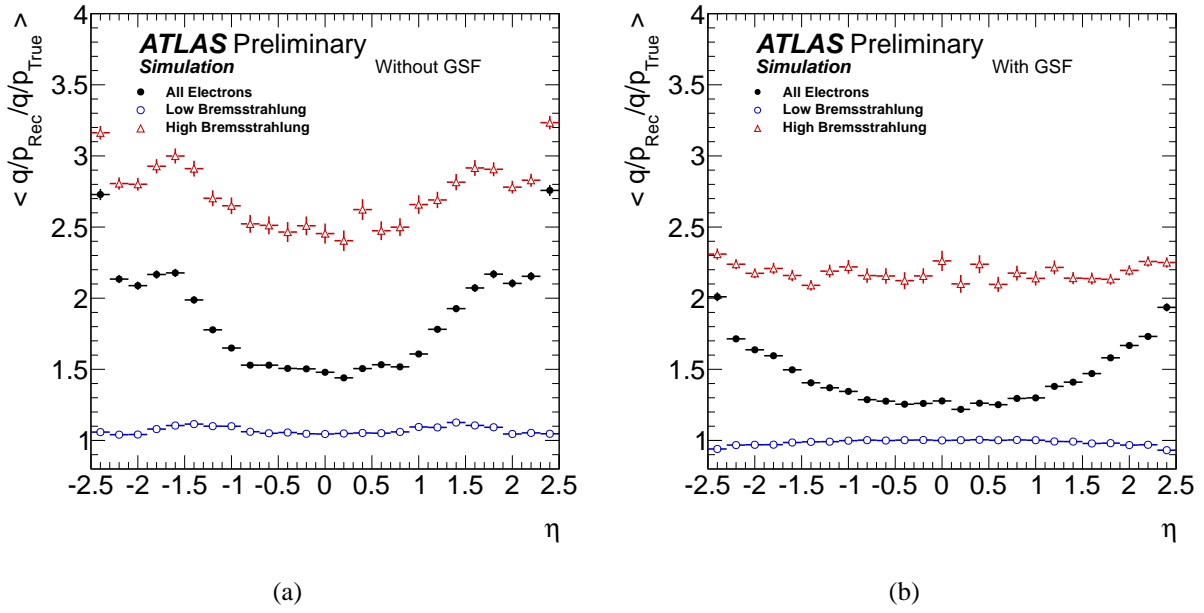


Figure 4.1: Mean value of the ratio of the reconstructed over the true electron inverse momentum times charge (q/p) as a function of pseudorapidity for single electrons. The electrons are selected to have a transverse momentum between 7 and 80 GeV. Electrons that lose less than (open points) and more than (open triangles) 20% of their energy due to Bremsstrahlung in the silicon detector and surrounding infrastructure are shown. (a) is without and (b) is with the GSF refitting applied. Electrons that suffer significant Bremsstrahlung losses dominate the high pseudorapidity regions. This explains the larger dependence with pseudorapidity when all the electrons are averaged (solid points).

4.2 Electron Reconstruction

An electron is reconstructed if at least one track can be matched to a cluster in the accordion, i.e. a certain number of LAr cells grouped together. The electromagnetic cluster is computed using a 3×7 (5×5) sliding window in $\eta \times \phi$ middle layer cell units in the barrel (end-caps). From their last measured point tracks are further extrapolated to the second calorimeter layer. The one with the smallest $\Delta R = \sqrt{\Delta\eta^2 + \Delta\phi^2}$ is considered the best match.

According to Equation 5.2 (which will be explained in Section 5.3) the full cluster energy is then determined by summing four different contributions:

- the estimated energy deposit in the material in front of the EM calorimeter,
- the measured energy deposit in the calorimeter cluster,
- the estimated external energy deposit outside the cluster (lateral leakage), and
- the estimated energy deposit beyond the EM calorimeter (longitudinal leakage).

The four terms are parametrised as a function of the measured cluster energies in the Presampler detector, where it is present, and in the three EM calorimeter longitudinal layers based on the detailed simulation of the energy deposition in both active and inactive material in the relevant detector systems. A good description of the detector in the MC simulation is therefore essential in order to correctly reconstruct the electron energy. With the in-situ calibration methods several discrepancies in the MC description of the calorimeter have been identified.

Objects reconstructed in the ways mentioned above are labelled as electron candidate. The four-momentum of the final electron candidate is computed using information from both the final cluster and the best track matched to the original seed cluster. The energy is given by the cluster energy. The ϕ and η directions are taken from the corresponding track parameters at the vertex, except for TRT-only tracks for which the cluster ϕ and η directions are used.

The sample of electron candidates is still highly contaminated with photon conversions. Dedicated cuts to reject the latter are applied in the electron identification.

4.3 Electron Identification

Not all objects built by the electron reconstruction algorithms are isolated signal electrons. Background objects include hadronic jets as well as background electrons from photon conversions and heavy flavor hadron decays. In order to reject as much of these backgrounds as possible, while keeping the efficiency for signal electrons high, electron identification in ATLAS is based on discriminating variables, which are combined into menus with varying background rejections. Both, kinematic cuts and multivariate analysis (MVA)² techniques are employed.

In the central high precision region of $|\eta| < 2.47$, which is within the coverage of the ID, a number of variables are used to discriminate against the different background sources. Among those, there are variables which describe the longitudinal and transverse shapes of the electromagnetic showers in the calorimeters, the properties of the tracks in the ID, as well as the matching between tracks and energy clusters. These variables are detailed in Table 4.1.

Three different identification menus were defined in both years, 2011 and 2012: *loose++*, *medium++* and *tight++*. Each of these identification menus is defining cuts on the different discrimination variables. The menus are subsets of each other, where for each set the tightness of cuts is increased or more variables are added. The *loose++* menu uses variables from the middle layer of the calorimeter, the energy leakage into the hadronic calorimeter, the pixel and SCT tracking system and a matching of a track to the cluster in η . The *medium++* menu is based on the *loose++* menu but tightens its cuts on the shower development and requires additional information from the TRT. The *tight++* menu is based on the *medium++* menu but cuts on the ratio of cluster energy to track momentum (E/p), and track related variables, such as the quality of track-cluster matching. Table 4.2 summarizes which variables are used for the different menus.

²The MVA based identification variables were not used for the studies presented in this thesis, thus they are not be explained.

Type	Description	Name
Hadronic leakage	Ratio of E_T in the first layer of the hadronic calorimeter to E_T of the EM cluster (used over the range $ \eta < 0.8$ and $ \eta > 1.37$)	R_{Had1}
	Ratio of E_T in the hadronic calorimeter to E_T of the EM cluster (used over the range $ \eta > 0.8$ and $ \eta < 1.37$)	R_{Had}
Third layer of EM calorimeter	Ratio of the energy in the third layer to the total energy	f_3
Middle layer of EM calorimeter	Lateral shower width, $\sqrt{(\sum E_i \eta_i^2)/(\sum E_i) - ((\sum E_i \eta_i)/(\sum E_i))^2}$, where E_i is the energy and η_i is the pseudorapidity of cell i and the sum is calculated within a window of 3×5 cells	$W_{\eta 2}$
	Ratio of the energy in 3×3 cells over the energy in 3×7 cells centered at the electron cluster position	R_ϕ
	Ratio of the energy in 3×7 cells over the energy in 7×7 cells centered at the electron cluster position	R_η
Strip layer of EM calorimeter	Shower width, $\sqrt{(\sum E_i (i - i_{\text{max}})^2)/(\sum E_i)}$, where i runs over all strips in a window of $\Delta\eta \times \Delta\phi \approx 0.0625 \times 0.2$, corresponding typically to 20 strips in η , and i_{max} is the index of the highest-energy strip	W_{stot}
	Ratio of the energy difference between the largest and second largest energy deposits in the cluster over the sum of these energies	E_{ratio}
	Ratio of the energy in the strip layer to the total energy	f_1
Track quality	Number of hits in the B-layer (discriminates against photon conversions)	n_{Blayer}
	Number of hits in the pixel detector	n_{Pixel}
	Number of total hits in the pixel and SCT detectors	n_{Si}
	Transverse impact parameter	d_0
	Significance of transverse impact parameter defined as the ratio of d_0 and its uncertainty	σ_{d_0}
TRT	Total number of hits in the TRT	n_{TRT}
	Ratio of the number of high-threshold hits to the total number of hits in the TRT	F_{HT}
Track-cluster matching	$\Delta\eta$ between the cluster position in the strip layer and the extrapolated track	$\Delta\eta_1$
	$\Delta\phi$ between the cluster position in the middle layer and the extrapolated track	$\Delta\phi_2$
	Defined as $\Delta\phi_2$, but the track momentum is rescaled to the cluster energy before extrapolating the track to the middle layer of the calorimeter	$\Delta\phi_{\text{Res}}$
	Ratio of the cluster energy to the track momentum	E/p
Conversions	Veto electron candidates matched to reconstructed photon conversions	!isConv

Table 4.1: Definition of electron discriminating variables taken from [6].

Name	Cut-based		
	<i>loose++</i>	<i>medium++</i>	<i>tight++</i>
$R_{\text{Had}(1)}$	✓	✓	✓
f_3		✓	✓
$W_{\eta 2}$	✓	✓	✓
R_{η}	✓	✓	✓
R_{ϕ}			
W_{stot}	✓	✓	✓
E_{ratio}	✓	✓	✓
n_{Blayer}		✓	✓
n_{Pixel}	✓	✓	✓
n_{Si}	✓	✓	✓
d_0		✓	✓
σ_{d_0}			
n_{TRT}		✓	✓
F_{HT}		✓	✓
$\Delta\eta_1$	✓	✓	✓
$\Delta\phi_2$			✓
$\Delta\phi_{Res}$			
E/p			✓
$!isConv$			✓

Table 4.2: *The electron identification menus taken from [6].*

4.4 Electron Trigger

The ATLAS trigger is built of three different levels. Each level reduces the detector's output rate significantly. Due to high event rates, limitations in the event information and the lack of computing power, full reconstruction and particle identification cannot be with the trigger. Hence slimmed down algorithms, with similar characteristics to the full offline reconstruction, are used to preselect possible electron candidates.

At the first level - L1 - so-called trigger towers of $\Delta\eta \times \Delta\phi = 0.1 \times 0.1$ are used in the LAr calorimeter to spot regions-of-interest (RoI). 4×4 trigger towers are grouped together to measure the energy deposited in a 2×2 region. To pass the trigger, the energy has to surpass the L1 threshold that is set to a few GeV depending on the final filter step threshold.

The next level is the L2 trigger where cells are clustered according to the RoI. As in the offline reconstruction, the energy deposit in the accordion is used to calculate the final energy in a 3×7 (barrel) or 5×5 (end-cap) window. At this level, algorithms are used to find tracks starting from the inner silicon detectors extending to the TRT.

The last stage in the trigger chain is the event filter (EF). Here, a slim track reconstruction and close-to-offline electron identification are used to select events. Examples of single electron trigger, depending on the year, are: *e20_medium*, *e22_medium* and *e22vh_medium1*). The suffix *e* stands for electron, the two digits for the required final (transverse) energy and *vh* denotes an η dependent threshold as well as a hadronic leakage requirement.

Trigger rates for different single electron triggers and their individual levels are illustrated in Table 4.3. On top of the trigger selections there are a various number of corrections and cuts applied offline that cannot be applied at trigger level.

Trigger	L1 Rate (Hz)	L2 Rate (Hz)	EF Rate (Hz)
<i>e20_medium</i>	7300	273	50
<i>e22_medium</i>	5700	273	45
<i>e22vh_medium1</i>	3600	150	22

Table 4.3: *Example of trigger rates for the individual levels as measured in 2011.*

4.5 Electron Isolation

In order to further reject hadronic jets faking electrons, in addition to the identification cuts described above, most analyses require electrons to pass an isolation cut.

The two main principles are:

- Calorimeter based isolation :

The calorimetric isolation variable $E_T^{\text{cone}\Delta R}$ is defined as the sum of the transverse energy

deposited in the calorimeter cells in a cone of ΔR around the electron, excluding the contribution of the electron itself. It is corrected for energy leakage from the electron to the isolation cone and for the effect of pile-up.

- Track based isolation:

The track isolation variable $P_T^{\text{cone}\Delta R}$ is the sum of the transverse momentum of the tracks in a cone of ΔR around the electron, excluding the track of the electron itself. The tracks considered in the sum must come from the primary vertex and be of good quality; i.e. they must have at least four hits in the pixel and silicon strip detectors in total.

In the following chapters the first type of isolation is used for selecting electrons from $W^\pm \rightarrow e^\pm \nu$ decays. Furthermore, these cones will be of major importance in Section 9 where energy deposition outside the cluster (energy leakage) is measured in different isolation cones.

4.6 Missing Transverse Energy

In studies where electrons from $W^\pm \rightarrow e^\pm \nu$ decays are used, the properties of the reconstructed electron are of major importance, along with the energy of the neutrino. However, neutrinos generally escape without producing any signal in any detectors. The only way of measuring neutrinos, and other only weakly interacting particles, is by relying on momentum conservation. Since the vector sum of the momenta of all produced particles must be in the plane perpendicular to the beam³, any non-zero vector sum is denoted with E_T^{miss} and defined as:

$$E_x^{\text{miss}} = -\sum_i E_i \sin \theta_i \cos \phi_i \quad (4.1)$$

$$E_y^{\text{miss}} = -\sum_i E_i \sin \theta_i \sin \phi_i \quad (4.2)$$

$$E_T^{\text{miss}} = \sqrt{(E_x^{\text{miss}})^2 + (E_y^{\text{miss}})^2} \quad (4.3)$$

where E_i , θ_i and ϕ_i are the cell energy, the polar angle and the azimuthal angle, respectively.

E_T^{miss} is reconstructed over the range $|\eta| < 4.5$ using only calorimeter information. Due to the high granularity of the calorimeter, noise suppression for E_T^{miss} reconstruction is crucial. This leads to a limiting of the number of cells used for reconstruction. To group cells together, so-called three-dimensional topological clusters (topoclusters) [51] need to be defined.

For a better reconstruction of E_T^{miss} and its resolution, energy lost in the dead material in front of and between the calorimeters needs to be taken into account. Consequently, a dedicated calibration scheme corrects for the different calorimeter response to hadrons and electrons/photons and for losses in inactive materials [52].

³The crossing angle of the two LHC beams creates a very small and negligible momentum in the positive y direction.

Chapter 5

Calibration of the EM Calorimeter

5.1 Overview

The precise determination of the electron energy scale of the EM calorimeter, which relates the deposited energy to the initial energy of the penetrating particle, is essential both for SM measurements and for searches of the SM Higgs boson or other new phenomena. Physics processes of prime interest at the LHC produce electrons from a few GeV to several TeV and therefore the estimation of the EM calorimeter's linearity is of major importance. Many of the physics processes, such as Higgs boson production, have small cross sections and suffer from large background, typically from jets of hadrons. Therefore an excellent electron identification capability is needed. As discussed in Chapter 4, the electron reconstruction is able to face this challenge by using a powerful combination of detector technologies: silicon detectors, a transition radiation tracker and a longitudinally layered electromagnetic calorimeter system with fine lateral segmentation. The same applies for the calibration of the electron energy with which the energy scale is determined. The goal of the calibration procedure is to precisely estimate the initial energy of the particles.

This chapter describes the different steps needed to calibrate the EM calorimeter as well as the overall in-situ calibration strategy for the electron energy scale (and resolution). This chapter will be followed by several chapters explaining the measurement itself and presenting improvements on the uncertainties of this measurement.

In general, the calibration of the EM calorimeter's energy scale is a three-step process. The first step is the electronics calibration at the cell level which is described in Section 5.2. The electronics calibration is followed by the calibration on the cluster level. Cells are subsequently summed into clusters, as explained in Chapter 4. Electromagnetic clusters then need to be calibrated, which constitutes the second calibration step. Section 5.3 explains the so-called calibration hits method and a novel method based on a multivariate analysis (MVA) technique. The last step is the so-called in-situ calibration, where the energy scale of fully reconstructed electrons is determined. A scale correction is obtained by comparing data to simulation, using the invariant mass of two electrons around the Z peak or the ratio of the energy response to the momentum (E/p) as a reference. This is described in Section 5.4.

An overview describing the various contributions of this thesis to different calibration steps will be given in the last Section 5.5.

5.2 Electronics Calibration at the Cell Level

The first step of the energy calibration begins at the level of the read out electronics (Front-end boards (FEBs)). For each of the 1524 FEBs there are 128 read-out channels.

The triangular pulse induced by the drift of the electrons in the LAr gaps is shaped and sampled every 25 ns (usually five samples but up to 32 samples are possible in special runs) while the collisions during Run 1 occurred every 50 ns, this is illustrated in Figure 5.1.

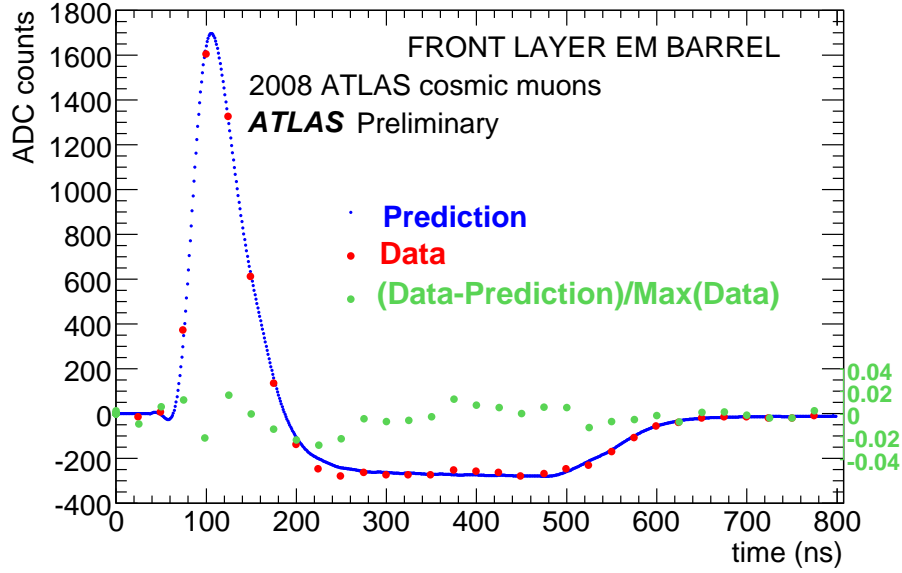


Figure 5.1: The ionization pulse shape, sampled every 25 ns (32 times), in the second layer of the EM Barrel for a time window of 800 ns. Red points: data points; blue points: shape predictions extracted from calibration runs. Taken from Ref. [45].

The total pulse length is ≈ 450 ns¹. The LAr ionisation pulse shape is characterized by a zero-value integral, a large amplitude peak structure during 100 ns followed by a long negative tail. This means that each point of the LAr pulse receives an average contribution of several preceding collisions.

The calibration of the cell energy is obtained by pulsing each channel through the calibration boards. The electronics calibration signal is fast (electromagnetic showers induce signals with rise time of 1 ns or less), and has a decay time comparable to the drift time in the gap. To get an accurate electronics calibration, the signal resembles the physics signal. The calibration system

¹The exact value of the length of the ionisation signal depends on the location of the cell in the calorimeter and is defined by the LAr gap size and the applied HV.

sends voltage pulses to precision resistors located close to calorimeter cells.

On the front-end boards the signal of the cell is passed through a pre-amplifier, a signal shaper and is sampled by a 12 bit ADC (Analog-to-Digital-Converter) with three different gains. The final reconstructed energy per cell, as read out by the reconstruction software, and its calibration chain (from analog signal to the final raw energy) can be written as Equation 5.1:

$$E_{\text{cell}} = F_{\mu\text{A} \rightarrow \text{MeV}} \cdot F_{\text{DAC} \rightarrow \mu\text{A}} \cdot \frac{1}{\frac{M_{\text{phys}}}{M_{\text{cali}}}} \cdot R \left[\sum_{j=1}^{N_{\text{samples}}} a_j (s_j - p) \right] \quad (5.1)$$

where

- $F_{\mu\text{A} \rightarrow \text{MeV}}$ is a factor is converting the signal in MeV
- the factor $F_{\text{DAC} \rightarrow \mu\text{A}}$ is coming from the calibration board
- the factor $\frac{1}{\frac{M_{\text{phys}}}{M_{\text{cali}}}}$ scales the physics signal to the calibration signal
- R is the factor obtained by calibration runs and transforms ADC to DAC
- a_j , s_j and p are optimal filtering coefficients [53] computing the peak of the shaped ionization signal by minimizing the electronics noise contributions.

5.2.1 Impact of Pile-up on the Cell Energy

The impact of pile-up (pile-up is described in detail in Section 3.4.1) on the measurement of the cell energy is primarily due to energy deposited in the EM calorimeter by particles produced in the numerous soft interactions taking place at each bunch crossing. However, the mean energy in any calorimeter cell, and its fluctuations, depend in a critical way on the details of the calorimeter signal treatment. The main parameters reflecting pile-up are the particle multiplicity distribution and the spectrum of the momentum measured in transverse plane (p_T). With the signal shape as described in Figure 5.1 the average signal in any calorimeter cell is zero, except for settling effects at the beginning and end of a bunch train.

Due to high- p_T tails (and the signal shape), the most probable value of the average signal is not precisely zero. Depending on the conditions of the collision its typical value is about -50 MeV in an EM cluster (three cells in pseudorapidity, times five cells in azimuth, defined in the second sampling). This kind of pedestal is continuously measured by taking random triggers interspersed with physics triggers.

The root mean square (RMS) of the energy deposit is directly proportional to the overall pile-up, summing all the bunch crossings contributing to the signal. It was shown in Ref. [7] that in an EM cluster (3×5 in $\Delta\eta \times \Delta\phi$) the RMS of the transverse energy deposition is typically about 300 MeV. A pile-up value like this contributes significantly to the calorimeter resolution. An obvious way to reduce it is to make the signal response faster (peaking time $t_p(\Delta)$ shorter). In doing so, one increases the accepted bandwidth, and thus the thermal noise.

The interplay of pile-up and thermal noise as a function of shaping time is shown in Figure 5.2. The shaping is chosen to give the optimum response (minimal sum for electronics and pile-up noise) when measuring at the peak luminosity. At lower luminosities (down to $10^{33}\text{cm}^{-2}\text{s}^{-1}$) digital filtering, using five samples around the peak of the pulse shape, allows to maintain at optimum performance. The same shaping time is used for the calorimeter trigger signal. For larger clusters, the pile-up increases typically linear with the area.

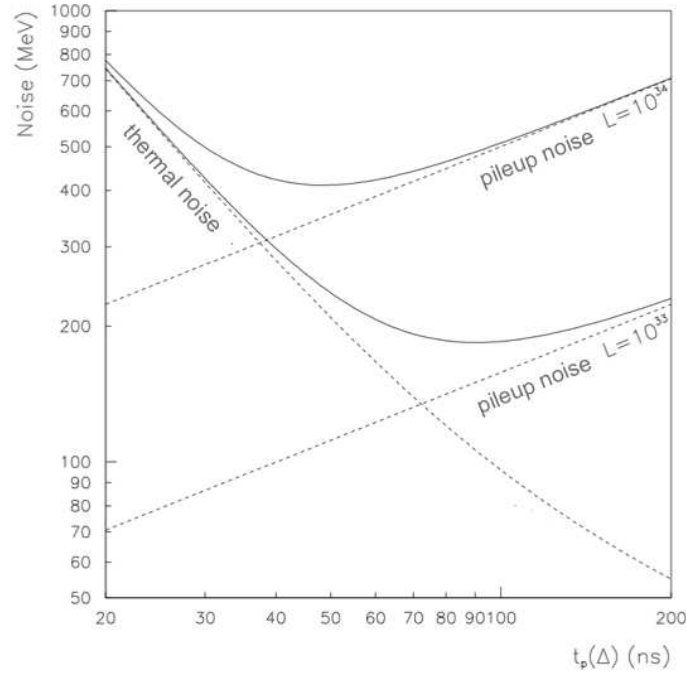


Figure 5.2: *Optimization of the shaping time for high and low luminosity. Taken from Ref. [7].*

5.3 Cluster Level Calibration

The cluster level calibration aims to attribute the correct particle energy to each cluster. Two methods have been established:

- Calibration Hits method
- MVA calibration

Both methods differentiate between electrons, converted photons and unconverted photons.

The *calibration hits method* [54] estimates the energy of the particle starting from the energy measured in the calorimeter layers and applying correction for four effects: the energy lost in front of the calorimeter, the energy lost outside the cluster, the longitudinal leakage and the cluster sampling fraction.

The parameters are obtained from MC simulation as so-called calibration hits, recovering the actual energy lost in dead material. The aim is to correct for this loss, hence a very accurate MC description is needed.

The particle energy E is reconstructed with the following formula, which consists of a term to calibrate the Presampler energy and a second one to calibrate the accordion energy:

$$\begin{aligned}
 E = & \underbrace{a(E_{\text{acc}}^{\text{true}}, |\eta|) + b(E_{\text{acc}}^{\text{true}}, |\eta|) \times E_{\text{PS}}^{\text{raw}} + c(E_{\text{acc}}^{\text{true}}, |\eta|) \times (E_{\text{PS}}^{\text{raw}})^2}_{\text{Calibrated Presampler energy}} \\
 & + \underbrace{f_{\text{samp}}(X, |\eta|) \times f_{\text{lat}}(X, |\eta|) \times f_{\text{long}}(X, |\eta|) \times f_{\text{mod}}(|\eta|, \phi) \times E_{\text{acc}}^{\text{raw}}}_{\text{Calibrated accordion energy}}
 \end{aligned} \tag{5.2}$$

The Presampler energy is calibrated by adding up three factors: an offset a , depending on η and the true energy deposited in the accordion ($E_{\text{acc}}^{\text{true}}$), and two factors including the raw Presampler energy ($E_{\text{PS}}^{\text{raw}}$) corrected by the slopes b and c . a , b and c are optimised in dedicated MC simulation studies, as described in Ref. [54]. The quadratic term is only included for $1.5 < |\eta| < 1.8$. The region beyond $|\eta| > 1.8$ is outside the Presampler acceptance, and $E_{\text{PS}}^{\text{raw}}$ is replaced by the longitudinal barycenter of the shower (X). In general, X is calculated from the Presampler, for $|\eta| < 1.8$, and the three accordion layers. It is expressed in radiation lengths.

The raw accordion energy, $E_{\text{acc}}^{\text{raw}}$, is corrected for the shower depth dependent calorimeter sampling fraction, for energy deposited outside the cluster (lateral leakage), which was used to define $E_{\text{acc}}^{\text{raw}}$, and for energy deposited behind the LAr calorimeter (longitudinal leakage). The correction factors as a function of $|\eta|$ and X , denoted f_{samp} , f_{lat} and f_{long} respectively, are obtained with MC simulation, as described in References [6, 54]. Finally, $f_{\text{mod}}(|\eta|, \phi)$ is a correction for the energy modulation depending on the impact point inside a cell, and reflects the alternance of lead absorbers and LAr gaps as a function of azimuth, as well as the finite cluster size for electrons and photons and hence a η and ϕ dependent lateral leakage.

The different coefficients and correction factors of Equation 5.2, from now on referred to as *calibration constants*, are optimized separately for electrons and photons, from samples simulated at different fixed energy points between 5 GeV and 1 TeV.

The performance for electrons is quantified in terms of linearity and resolution of the energy reconstruction. These parameters are computed from the mean and width of a Gaussian fit to the reconstructed energy response function in an interval of $[-1\sigma, 2.5\sigma]$. The σ and the mean are obtained iteratively.

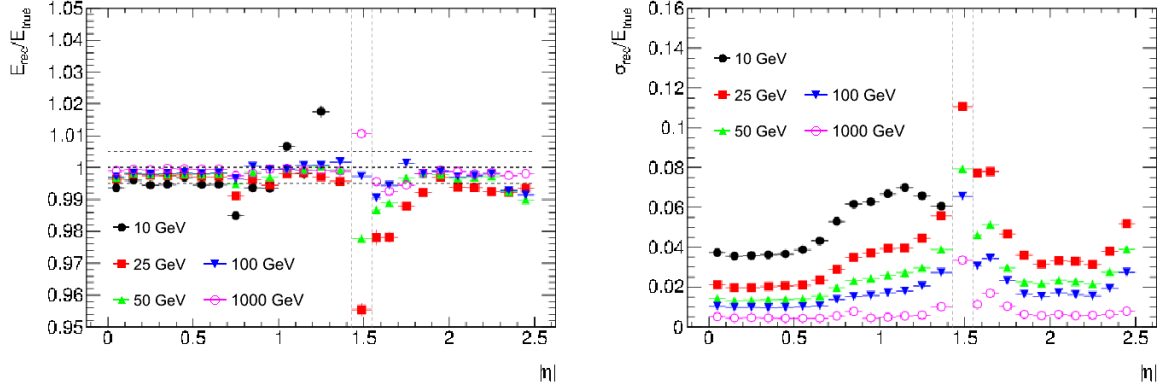


Figure 5.3: *Quantification of the electron performance after the cluster level calibration. η -dependence of the energy response for different energies (linearity) (left) and resolution (right). The detector responses are calculated from pure MC simulations using the ratio of the reconstructed energy with the MC truth energy ($E_{\text{rec}}/E_{\text{true}}$).*

Figure 5.3 shows the linearity and resolution of the response as a function of pseudorapidity. The deviation from linearity is less than 1% for electrons with $E \geq 50$ GeV over the full pseudorapidity range. For lower energy electrons, a degradation of the linearity is observed around $|\eta| \sim 1.7$ and at high η . The fractional energy resolution is shown as a function of $|\eta|$ for different energies. The resolution deteriorates as a function of the number of radiation lengths in front of the EM calorimeter. This effect is particularly visible for the lower-energy electrons and is due to the combined effect of the Bremsstrahlung radiation and the magnetic field. Typical resolution values for electrons with $E = 100$ GeV are 1% for $|\eta| < 0.8$, 2% for $0.8 < |\eta| < 1.8$, and 1.5% for $|\eta| > 1.8$.

A new approach based on *multivariate analysis* (MVA) techniques to correct the energies of electrons and photons, measured in the ATLAS electromagnetic calorimeter, is being developed. This MVA calibration method is intended to replace the calibration hits method in the future.

Both approaches derive the corrections using detailed MC simulations of the ATLAS detector response to electrons in a wide energy range. The goal of the calibration procedure is to estimate the initial energy of the particles, identifying and, if possible, removing any dependence of the response on quantities like the impact position on the calorimeter, the shower profile and

many others.

In the calibration hits method some of these quantities - namely the energy lost in front of the accordion, the lateral and longitudinal leakage - are parametrized as a function of the longitudinal barycenter of the shower (shower depth). This parametrization is done independently in each region in pseudorapidity and for a few energies of the particles. Any possible correlations between these quantities are ignored. With the multivariate technique, it is possible to take into account the correlations between the input variables. The MVA calibration should therefore improve the energy resolution, when these correlations are significant.

One additional reason to adapt to a MVA calibration is the simplicity to derive a new set of corrections that can be done within a few days or even hours. This is extremely convenient in case of changes in the detector simulation or the geometry description. Furthermore, this scheme allows to introduce an arbitrary number of variables. Adding new variables is the most promising way to improve the MVA calibration.

In this thesis the calibration hits methods is used for the cluster level calibration.

5.4 In-situ Calibration using Physics Objects - Data-driven Calibration

The calibration scheme summarized in Section 5.3 transforms the energies measured in the reconstructed calorimeter cluster into an estimate of the true incident electron or photon energy. The calibration constants are derived from the simulation, and hence rely on correct intercalibration of the different calorimeter layers, on the correct modelling of the signal collection in the LAr gaps, on accurate simulation of the energy fraction deposited outside the calorimeter cluster, and on proper modeling of the passive material upstream of the calorimeter. The absolute scale of the calorimeter response is set in-situ² by comparing

- the energy of the theoretically well known $Z \rightarrow e^+e^-$ and $J/\psi \rightarrow e^+e^-$ resonances
- the ratio of the energy response in the calorimeter and the momentum measured in the inner detector (E/p) using electrons from $W^\pm \rightarrow e^\pm \nu$ or $Z \rightarrow e^+e^-$ decays

in data and simulation (see Figure 5.4). A review of experimental measurements for calibration relevant parameters are illustrated in Table 5.1.

	Mass	Width	selected decay mode and branching fraction
J/ψ	$3096.916 \pm 0.011 \text{ MeV}$	$92.9 \pm 2.8 \text{ keV}$	$\text{hadrons} : 87.7 \pm 0.5\%$ $\gamma g g : 8.8 \pm 1.1\%$ $e^+e^- : 5.94 \pm 0.06\%$ $\mu^+\mu^- : 5.93 \pm 0.06\%$
W^\pm	$80.385 \pm 0.015 \text{ GeV}$	$2.085 \pm 0.042 \text{ GeV}$	$\text{hadrons} : 67.6 \pm 0.27\%$ $e^+\nu : 10.75 \pm 0.13\%$ $\mu^+\nu : 10.57 \pm 0.15\%$
Z	$91.1876 \pm 0.0021 \text{ GeV}$	$2.4952 \pm 0.0023 \text{ GeV}$	$\text{hadrons} : 69.91 \pm 0.06\%$ $\mu^+\mu^- : 3.366 \pm 0.007\%$ $e^+e^- : 3.363 \pm 0.004\%$

Table 5.1: *Experimental measurements [29] (world average) of the main decay parameters, which are relevant for calibration purposes. For W^\pm only W^+ modes are shown, W^- modes are charge conjugates of those.*

The difference between data and simulation in a given region i is parametrised by

$$E_i^{\text{data}} = (1 + \alpha_i) E_i^{\text{MC}} \quad (5.3)$$

where E^{MC} is the true electron energy, E^{data} is the energy measured by the calorimeter after applying the MC-based corrections obtained from the Calibration Hits method, and α_i measures the residual miscalibration. It should be noted that these corrections α_i only correct the overall energy scale. In case the MC simulation is not accurate, one or more of the above ingredients are imperfectly simulated, additional corrective terms, like generally position or energy dependence, are required and will be discussed in the following.

²In-situ refers to the calibration of actual physics objects measured with the ATLAS detector.

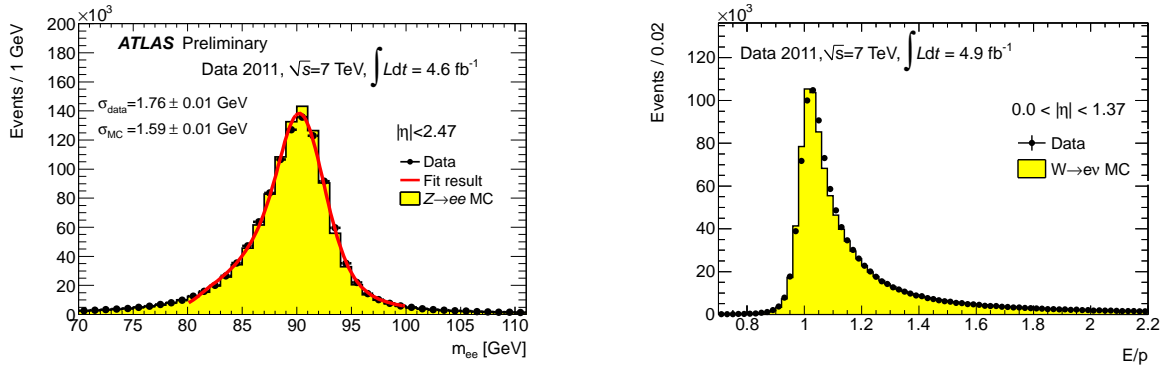


Figure 5.4: Left: The simulated position of the Z mass peak compared to the observed one for 2011 data. Right: The ratio E/p for electrons selected in the barrel EM calorimeter in $W^\pm \rightarrow e^\pm \nu$ events. E/p is close to unity, with a significant tail at large values due to Bremsstrahlung occurring in the inner detector. These distributions (here bins integrated in η) are corrected by scaling the detector response (α_η).

The Z resonance in combination with E/p defines the energy scale correction along η , $\alpha(\eta)$, and is considered as the baseline in-situ calibration method. Since the experimental distribution of the di-electron invariant mass or the shape of the E/p distribution depend strongly on the pseudorapidity η of the electrons, mainly due to the material in front of the calorimeter, the energy scale correction is produced for different regions in η .

The electromagnetic calorimeter plays an important role to study $H \rightarrow \gamma\gamma$ and Higgs decays with leptonic final states, but also many high precision measurements from the Standard Model, such as the mass of the W boson. To achieve a mass measurement with a precision of the level of a few times 10^{-4} , the absolute scale (and its linearity) and the resolution of the calorimeter have to be understood at least with the same level of precision. The goal is an overall calibration with an accuracy on the per mill level.

The calibration strategies for the energy scale and the resolution will be introduced in the following subsections to prepare the reader for the upcoming chapters (Chapter 6 to Chapter 12) in which each of the topics will be described in detail.

5.4.1 Energy Scale

The absolute energy scale is not sufficiently well known from first principles and test beam measurements. High cross section processes, that are well understood, are therefore used to calculate the η -dependent scale correction α .

The well known mass peaks of $Z \rightarrow e^+e^-$ and $J/\psi \rightarrow e^+e^-$ can be used to improve considerably the knowledge of the electron energy scale and to establish the linearity of the response of the EM calorimeter. An alternative strategy to determine the electron energy scale is to study the ratio of the energy E measured by the EM calorimeter and the momentum p measured by the inner detector, E/p . This technique gives access to a larger number of reconstructed electrons coming from $W^\pm \rightarrow e^\pm \nu$ decays but depends on the knowledge of the momentum scale measured by the inner detector. The measurements of the electron energy scale and its uncertainties are using $J/\psi \rightarrow e^+e^-$ and $Z \rightarrow e^+e^-$ decays or the E/p ratio of $Z \rightarrow e^+e^-$ and $W^\pm \rightarrow e^\pm \nu$ events.

First attempts to extract the energy scale correction as a function of η started with the first data arriving in 2010 [6]. Despite the low number of reconstructed electrons in the dataset, containing about 40 pb^{-1} of integrated luminosity, the electron energy scale could already be determined in bins of pseudorapidity with a precision of 0.5-1.6% in the central region and 2-3% in the forward regions. The energy scale correction as a function of η and its uncertainties for the 2010 dataset is shown in Figure 5.5.

The accuracy and granularity (see Figure 5.5) benefit from the much larger number of reconstructed electrons available in 2011 and 2012. Two-dimensional measurements in (E_T, η) space with finer η granularity and (η, ϕ) space can be obtained allowing a more precise identification of the sources of the different E_T -dependent difference in MC and data.

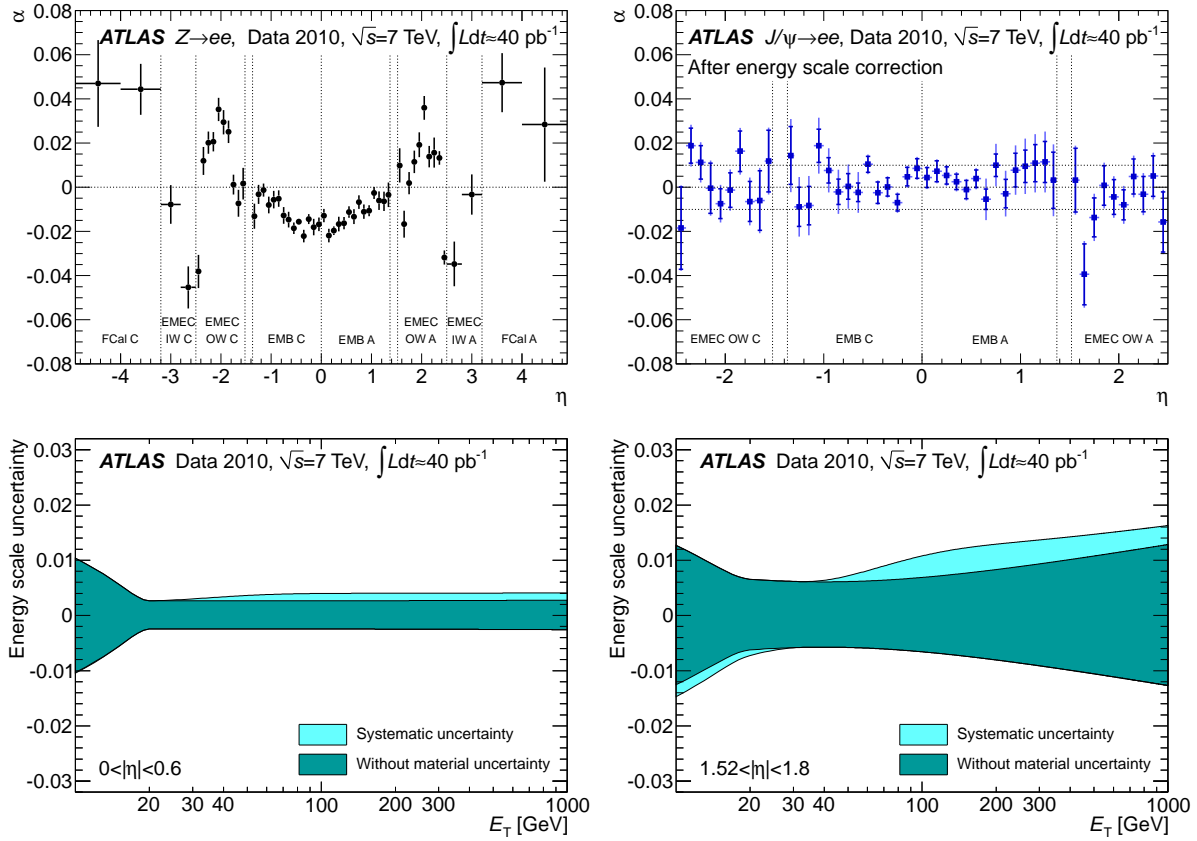


Figure 5.5: Top row: The 2010 energy scale correction α as a function of the pseudorapidity of the electron cluster derived from fits (left) to $Z \rightarrow e^+e^-$ and (right) to $J/\psi \rightarrow e^+e^-$ using the 2010 dataset; The uncertainties of the $Z \rightarrow e^+e^-$ measurement are statistical only. Bottom row: Total systematic uncertainty on the electron energy scale extracted in 2010; (left) for the region $|\eta| < 0.6$ which has the smallest uncertainty and (right) for $1.52 < |\eta| < 1.8$ which has the largest uncertainty. The uncertainty is also shown without the contribution due to the amount of additional material in front of the EM calorimeters. For the year 2011 and 2012 the uncertainties became substantially smaller (see Chapter 12). Taken from Ref. [6].

Different sources of systematic uncertainties affect the electron energy scale measurement. The reduction of these uncertainties is of major importance, which is driven by needs of the physics program.

- **Linearity**

Electrons from different decays have different E_T spectra (e.g. $Z \rightarrow e^+e^-$ with a mean value around 45 GeV and around 40 GeV for $W^\pm \rightarrow e^\pm \nu$). Thus, the energy scale correction α needs to be extracted in different E_T regimes. The procedure to extract the linearity of the scale correction is described in Chapter 8. It will also be shown that different effects contribute to the linearity, such as lateral leakage or the layer calibration.

- **Lateral Leakage**

The electron shower is larger than the cluster used. Energy deposition outside the “sliding window” cluster therefore occurs, the so-called lateral leakage of energy. This has to be corrected for in the cluster level calibration. However, known differences in the shower width between data and MC simulation can lead to inadequate corrections (Chapter 9).

- **Additional Material**

Imperfect knowledge of the material in front of the EM calorimeter affects the electron energy measurement. The energy deposited in any additional material is neither measured, nor accounted for in the MC-based energy calibration. This impact will be corrected in average by the α scale correction. However, it will certainly depend on the particle energy and type. Material effects are discussed in Chapter 10.

- **Presampler Energy Scale**

The sensitivity of the calibration to the measured Presampler energy is significant because it is used to correct for energy lost upstream of the active EM calorimeter. Since the in-situ calibration only fixes one overall scale (the overall energy measured in the Presampler and the accordion), it has to rely on correct relative scales between the Presampler and the accordion. The Presampler energy scale can be derived from the ratio of Presampler energies in data and Monte Carlo, estimated from electrons from W and Z decays. However, this ratio is strongly influenced by the amount of material in front of the EM calorimeter. This effect has to be disentangled from the measurement of the energy scale (Chapter 11).

- **Layer Calibration**

Cells belonging to different sampling layers in the EM calorimeters may have slightly different energy scales due to cross-talk and uncertainties arising from the electronic calibration, as well as the inaccuracies in the geometry and electric field modeling of the detector. It will be shown in Chapter 11, how to extract the energy scale relative to the middle layer for cells in the strip layer. This is done using a method measuring the electron energy response (as well as muons) in data w.r.t. to MC along the middle and strip layer.

- **Non-linearities in the Readout Electronics and Differences between the electronic Gains**

As explained in Section 5.2 the read-out electronics is calibrated on a regular basis. However, small non-linearities are estimated to be typically 0,1% [6]. In addition, it was found that the differences between high gain and medium gain cause an additional systematic error of about 0.1% [55].

- **Requirements on Calorimeter Operating Conditions**

Possible bias on the electron energy measurement changing with pile-up conditions and over time needs to be taken into account for defining the systematic uncertainties (Chapter 7).

- **Possible Biases of the Methods**

The biases of the different methods used is assessed by repeating the fit procedures on simulated data in MC closure tests. Since the simulated, pseudo data is perfectly known, the obtained results of the fit should not differ from the expected results. Any deviation between the obtained and the expected result - the so-called non-closure - indicates an intrinsic bias of a method itself and is either resolved in specific studies or added as an additional uncertainty.

The overall systematic uncertainty on the electron energy scale is a function of E_T and η . It is crucial to investigate these effects in detail to further reduce the systematic uncertainty needed to realize the full physics potential of the LHC. This is the subject of the following chapters (Chapter 6 to Chapter 12).

5.4.2 Resolution

Extracting the energy resolution function from data, as described in Section 2.3.8, is another goal in the overall calibration strategy:

$$\frac{\sigma_E}{E} = \frac{a}{\sqrt{E}} \oplus \frac{b}{E} \oplus c \quad (5.4)$$

Assuming that a is known (comparing the MC and data J/ψ width, where $J/\psi \rightarrow e^+e^-$ provides low energy electrons whose energy measurement resolution is completely dominated by a) and measuring the total noise (electronics noise and pile-up noise) parameter b in minimum bias runs³, extraction of the constant term c becomes possible. In data the constant term is measured using the width of the Z peak with the following relation:

$$c_{\text{data}} = \sqrt{2 \cdot \left(\left(\frac{\sigma}{m_Z} \right)_{\text{data}}^2 - \left(\frac{\sigma}{m_Z} \right)_{\text{MC}}^2 \right) + c_{\text{MC}}^2} \quad (5.5)$$

where c_{MC} reflects a local constant term implemented in MC simulation of about 0.5%. This local constant term originates from known locally uniform construction tolerances. c_{data} is an effective constant term composed of the calorimeters local constant term and a contribution originating from non-uniformities of the detector response.

To demonstrate the azimuthal (and also η , but this is mostly corrected by the energy scale corrections) uniformity, both the dielectron invariant mass distributions of $Z \rightarrow e^+e^-$ events and the E/p distributions of $W^\pm \rightarrow e^\pm \nu$ events in bins of granularity of a calorimeter cell are used (Chapter 7). Non-uniformities need to be investigated and corrected, if possible.

The goal is to achieve an effective constant term (which intrinsically is the quadratic sum of the local constant term and a non-uniformity component) of less or around 0.5 - 1% for most of the EM calorimeter, which is a requirement driven by physics needs.

³A minimum-bias run contains only randomly triggered events. The measured energy hardly contains (if ever) signal events and hence reflects the total noise.

5.5 Contribution of this thesis

To all of the topics mentioned, the work described in this thesis made major contributions.

The η dependent energy scale correction α was extracted for different regions in η using a model which parametrizes the individual detector response functions, calorimeter response and the momentum measurement of the inner detector in MC. This model is called “Convolution Model” and will be explained in detail in Chapter 6. The individual parameterizations are then convoluted to a function which can be fitted to the E/p distribution. This function was applied to E/p from MC, as a closure test, and on data, to extract the scale correction α . The obtained scale correction was compared to the scale correction extracted with the Z peak method and was made available to the various analysis groups.

To measure the contribution of non-uniformity (Chapter 7) to the constant term the energy response was investigated in fine η and ϕ regions using E/p from $W^\pm \rightarrow e^\pm \nu$ and $Z \rightarrow e^+ e^-$ decays.

The stability in time of the energy response of the LAr calorimeter for the full 2011 and 2012 datasets was measured, as well as the stability against pile-up (Chapter 7). Electrons from $W^\pm \rightarrow e^\pm \nu$ (using E/p) and $Z \rightarrow e^+ e^-$ decays (using the invariant mass) were used.

Furthermore, the linearity of the energy response was measured using the Convolution Model with the electrons from $W^\pm \rightarrow e^\pm \nu$ and $Z \rightarrow e^+ e^-$ decays (Chapter 8). Further investigations on the measured non-linearity (on the per mill level) were accomplished. Part of the non-uniformities could be traced back to an inaccurate out-of-cluster correction, identified by comparing the energy deposits in energy cones around the reconstructed cluster in data and MC. The observed difference of the leakage between data and MC could produce similar non-linearities (Chapter 9). A correction to this effect was provided.

Tail fraction in E/p as well as electron shower shapes (using electrons from $W^\pm \rightarrow e^\pm \nu$ and $Z \rightarrow e^+ e^-$ decays) were used to find regions where the simulation failed to describe the actual material in the detector (Chapter 10). A data-driven geometry description, based on the material studies presented in this thesis, for an improved detector simulation and MC sample production was initiated.

E/p was used (amongst others) to distinguish miscalibrations in the first layer from miscalibrations in the second layer (Chapter 11). The impact of the layer calibration on the measured non-linearity was tested, by correcting the energy with the obtained corrections and comparing to the non-corrected case. This correction was provided to the analysis groups and is used in the upcoming physics results of ATLAS.

A summary of all the discovered corrections and its uncertainties will be given in Chapter 12. The results were presented in various talks as well as at the Higgs seminar in July 2012, where the ATLAS spokesperson Fabiola Gianotti gave the talk on the Higgs searches results of ATLAS [56].

Chapter 6

Ratio of Calorimeter Energy and Inner Detector momentum, E/p

6.1 Overview

This chapter follows up on the calibration strategy presented in Chapter 5, which contains the in-situ measurement of the EM energy scale and resolution along pseudorapidity and the estimation of its uncertainties.

The objective of the presented work is to complement the Z peak (see Appendix B) method on deriving the energy scale correction used for the 2011 and 2012 datasets and improve the measurements done with the 2010 dataset [6].

One complementary way to obtain information about the energy scale (and derive its correction) of the electromagnetic calorimeter is comparing the calorimetric energy measurement of the electrons with the momentum measurement performed by the inner detector using their ratio, namely E/p . Different ways of analysing the E/p distributions have been investigated, as illustrated in Section 6.3.1.

In Section 6.3.2 a method is introduced to obtain high precision fit functions used to extract the energy scale and the calorimeter linearity from fits to E/p distributions. Complementarily, a simple Crystal Ball function, parameterizing the E/p distribution, was as well applied to extract the energy scale.

It will be shown that, to achieve a precision at the per mill level, the fit functions must describe the E/p distributions with high precision. Discrepancies in the tails of the distributions are found to systematically bias the obtained results.

6.2 Event Selection

For the E/p studies presented here e^\pm from $W^\pm \rightarrow e^\pm \nu$ (and $Z \rightarrow e^+ e^-$) decays were used. This study uses non calibrated electrons, identified with: *tight* ++. The Monte Carlo samples used were from the MC11c and MC12 reprocessing produced in PYTHIA (a list of reconstruction tags is given in Appendix D).

The data used are from the full 2011 data set corresponding to a total integrated luminosity of 4.9 fb^{-1} , with $13.9 \cdot 10^6 W^\pm \rightarrow e^\pm \nu$ and $1.62 \cdot 10^6 Z \rightarrow e^+ e^-$ events after all cuts. For 2012 data set a total integrated luminosity of 12.0 fb^{-1} , corresponding to $22.05 \cdot 10^6 W^\pm \rightarrow e^\pm \nu$ and $2.43 \cdot 10^6 Z \rightarrow e^+ e^-$ events after all cuts.

The results discussed in this section are based on the e/γ calibration n-tuples and the baseline selections given in Table 6.1. These selections reduce the sample by a factor four.

cut1	Trigger	if run < 186873: <i>EF_e20_medium</i>
	Trigger	if run < 188902: <i>EF_e22_medium</i>
	Trigger	and run \geq 186873: <i>EF_e22vh_medium1</i> or <i>EF_e45_medium1</i>
cut2	Electron object quality (<i>el_OQ</i>) applied	
cut3	Electron author: 1 or 3 (to avoid electrons from conversions)	
cut4	$E_T^{\text{el}}(\text{el_et}) > 25 \text{ GeV}$	
cut5	Electron identification: <i>medium</i> ++	
cut6	$E_T^{\text{miss}}(\text{LocHadTopo}) > 25 \text{ GeV}$	
cut7	$m_T > 40 \text{ GeV}$	

Table 6.1: $W^\pm \rightarrow e^\pm \nu$ baseline selections in the calibration n-tuples.

On top of the calibration baseline cuts additional selection cuts were applied (as used in the W boson mass analysis), in order to reduce the background, clean up the signal electrons and be consistent with the current SM analyses (see Table 6.2). This leads to a further reduction by a factor 2.5 of signal events. A data-MC comparison after applying all the cuts is shown in Figure 6.1, where the typical agreement for the bulk regions is of a few percent inclusive in η with some outliers in the tails.

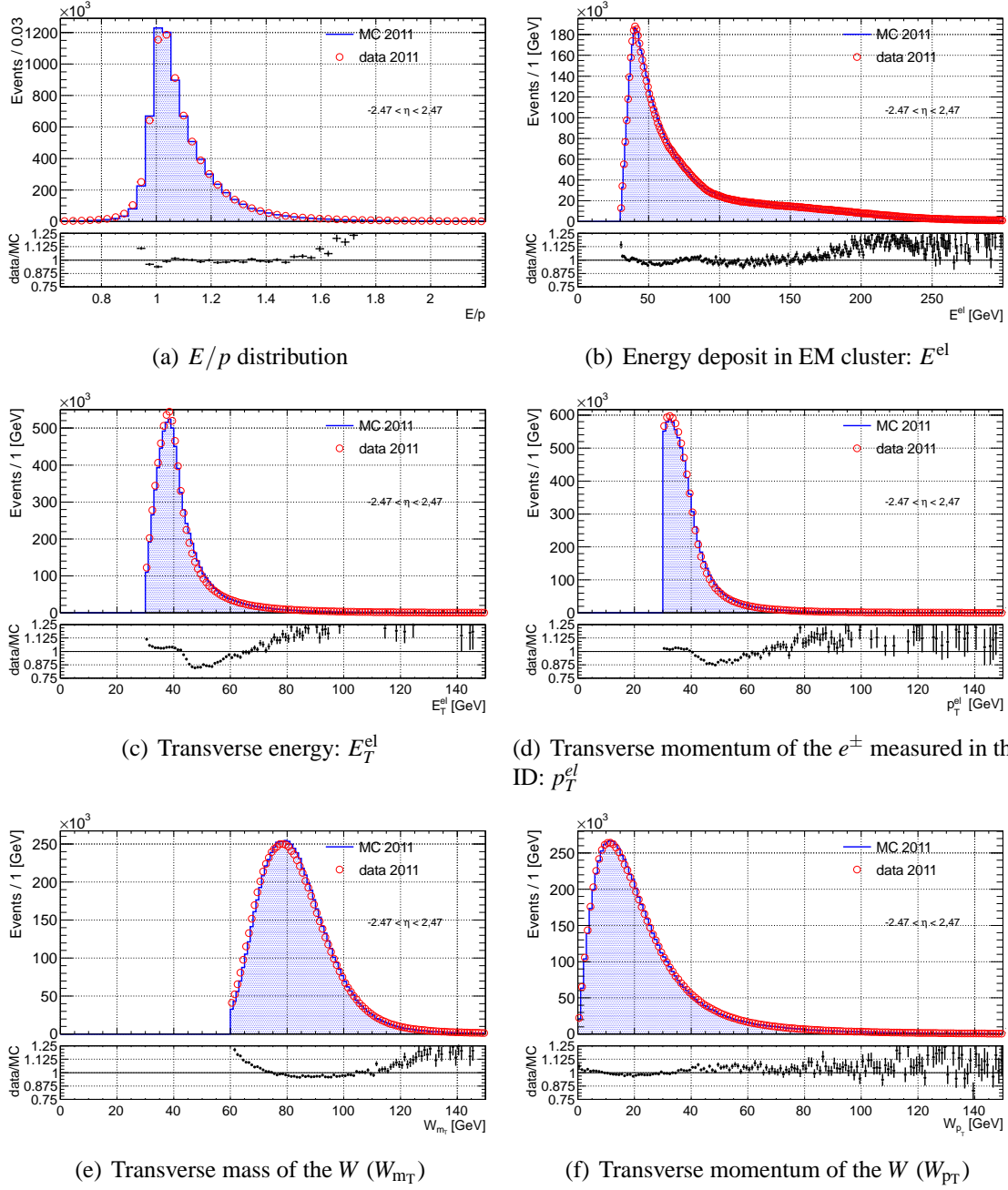


Figure 6.1: The E/p and various kinematic distributions for both data and MC inclusive in η are shown. The top part of each plot represents an overlay of MC with data, whereas the bottom part is the ratio of both. The typical agreement between data and MC is at the level of a few percent for signal regions with outliers in the tails.

cut1	GRL (use certified runs only)
cut2	Electron identification: <i>tight</i> + +
cut3	$E_{T\text{cone30}}^{\text{el}} < 6 \text{ GeV}$
cut4	$E_T^{\text{el}} > 30 \text{ GeV}$
cut5	$p_T^{\text{el}} > 30 \text{ GeV}$
cut6	$E_T^{\text{miss}} (\text{LocHadTopo}) > 30 \text{ GeV}$
cut7	$m_T > 60 \text{ GeV}$

Table 6.2: List of cuts applied for the $W^\pm \rightarrow e^\pm \nu$ selection on top of the calibration n -tuples baseline cuts.

6.3 The E/p Distribution and Fitting Methods

The distributions of E/p are expected to have a peak around one. The peak position is not only heavily impacted by the calibration of the calorimeter (which needs to be established) but also influenced by the alignment of the ID, the material distribution inside the ID (leading to Bremsstrahlung) and effects related with the track fitting. These effects lead to substantial tails at $E/p \gg 1$ and to a lesser degree at $E/p < 1$. It is therefore impossible to compare the mean of the distribution, but methods have been developed to extract well defined parameters of these distributions.

In general, the energy calibration assumes that the ID momentum scale is ad hoc better known as the energy scale (upper limit of the momentum bias of about 0.1% at $p_T = 40$ GeV [57]). As described in Chapter 4, positions of signals (hits) recorded in ID detector elements are used to reconstruct the trajectories of charged particles inside the ID and ultimately to estimate their kinematic parameters. Any detector misalignment add to the uncertainty on the hit position and consequently on the reconstructed track parameters. Therefore, it is important to know the positions of all the ID detector elements within the detector volume as accurately as possible. The alignment procedure determines these positions and corrects any misalignment before any reliable physics measurements (or electron calibration studies) are performed. The misalignment is charge dependent but affect positrons and electrons in the same amount. The energy calibration does not distinguish between electrons and positrons, therefore any residual misalignment cancels out.

The information of the magnetic field strength within the ID volume is used to reconstruct the momentum. Any insufficient knowledge of the magnetic field would lead to a wrong momentum reconstruction. To account for that, the magnetic field in the ID has been measured during dedicated precision measurement campaign [58]. The resulting field residuals were less than 0.5mT, and the systematic error on the measurement of the track sagitta due to the field uncertainty was estimated to range from $2 \cdot 10^{-4}$ to $12 \cdot 10^{-4}$, depending on the track rapidity.

As already mentioned in Chapter 4, in 2012 the shape of the E/p distribution changed with respect to 2011 due to the GSF Bremsstrahlung recovery of the momentum measurement (see [50]). With this new reconstruction, tails for $E/p > 1$ appear less dominant than in 2011 and the distribution itself coming closer to unity (see Figure 6.2).

In order to obtain the energy scale (from data and MC) and its correction (when comparing data to MC) two fitting methods are used, namely:

- **Crystal Ball Model** : It is the basic method used in most studies to be consistent with the calibration done in 2010 [6]. It aims to extract and compare the most probable value (MPV) of the distribution.
- **Convolution Model** : This, more sophisticated model, aims to extract directly the energy scale of E/E_0 (E_0 being the true electron energy) assuming a correct scale of p_0/p . Since also tail parameters can be fitted, it is possible to estimate the material in front of the calorimeter.

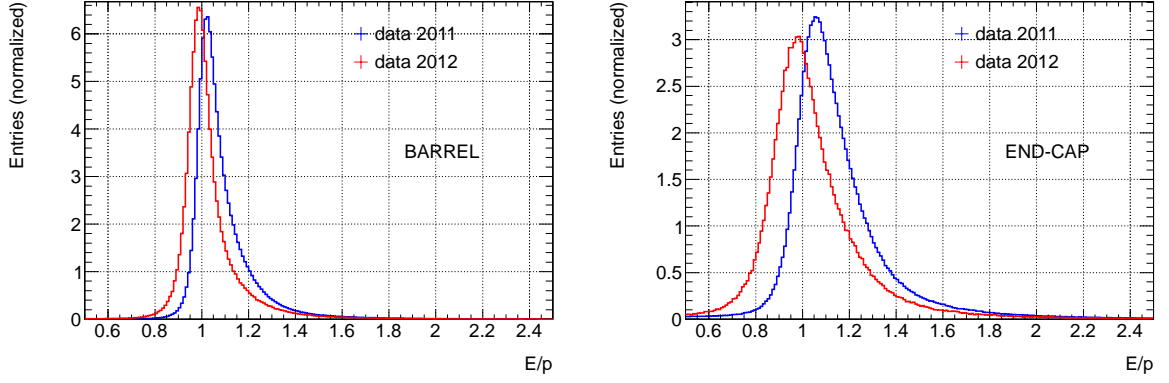


Figure 6.2: A comparison of E/p distributions in 2011 (blue) and 2012 (red) showing less dominant tails for $E/p > 1$ in 2012 compared to 2011. The 2012 distribution benefits from the improved GSF Bremsstrahlung track fitting as demonstrated by the overall shift of the distribution towards 1.

6.3.1 Crystal Ball Model

In order to extract the energy scale from the E/p distribution a Crystal Ball function [59] f_{CB} is fitted to the E/p distribution (see Figure 6.3).

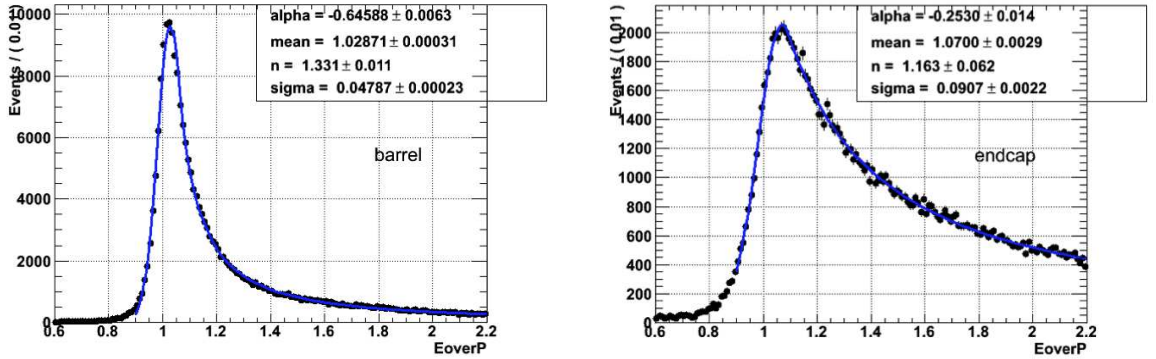


Figure 6.3: Examples of E/p distribution for e^\pm from W decays and their Crystal Ball fits with two different η regions, $0.0 < |\eta| < 1.37$ and $1.52 < |\eta| < 2.47$.

The obtained most probable value (MPV) reflects the energy scale. The Crystal Ball function, named after the Crystal Ball Collaboration, is a probability density function commonly used to model various processes in high energy physics. It consists of a Gaussian core part and a power-law low-end tail below a certain threshold. These two parts are spliced together (through two coefficients A and B) that the function value and its first derivative are continuous. The Crystal Ball function f_{CB} is given by:

$$f_{CB}(x; \mu, \sigma, \alpha, n) = N \cdot \begin{cases} \exp\left(-\frac{(x-\mu)^2}{2\sigma^2}\right), & \text{for } \frac{x-\mu}{\sigma} > -\alpha \\ A \cdot \left(B - \frac{x-\mu}{\sigma}\right)^{-n}, & \text{for } \frac{x-\mu}{\sigma} \leq -\alpha \end{cases} \quad (6.1)$$

where

$$A = \left(\frac{n}{|\alpha|} \right)^n \exp \left(-\frac{|\alpha|^2}{2} \right) \quad (6.2)$$

$$B = \frac{n}{\alpha} - |\alpha| \quad (6.3)$$

N is the normalization factor and α , n , μ and σ are parameters.

This was the basic method used for checking consistency with the 2010 calibration. The core of the distribution is described by a Gaussian which width is determined by the electron energy resolution and electron momentum resolution. The upper tail is mainly due to the Bremsstrahlung occurring in the inner detector. An early energy loss by Bremsstrahlung leads to an underestimation of the momentum in the track fit but usually a large fraction of those Bremsstrahlung photons are contained in the 3×7 cluster, and therefore the energy is nevertheless measured correctly.

In order to stabilize fit results, the region $E/p \in [0.9, 2.2]$ was used in all fits. The energy scale corrections $\alpha_{E/p}^{CB}$ are calculated from the MPV of the Crystal Ball fits in data and MC:

$$\alpha_{E/p}^{CB} = \frac{MPV_{E/p}^{DATA}}{MPV_{E/p}^{MC}} - 1 \quad (6.4)$$

where *DATA* refers to the 2011 or 2012 datasets and *MC* to the simulated distributions.

The Crystal Ball model is also used in Chapter 7 to measure the uniformity of the energy response in (η, ϕ) plane and its stability versus time and pile-up.

Systematics

The systematic uncertainties coming from the choice of the *fit range* as well as the parameter space was investigated in [6]. The default fit range was chosen to be $[0.9, 2.2]$. Within several different fit ranges, it is shown in [6], that fit results are stable within 0.1%. However, good fits rely on the exact modeling of the E/p distribution in MC. Insufficient simulated tails can very easily lead to a systematic shift of the extracted scales. This error is correlated in rapidity and estimated to be 0.5%. The Crystal Ball method is therefore only used for a relative comparison, but is not well suited to extract the energy scale correction.

Possible effects of a residual *misalignment in the ID* and therefore the momentum measured in E/p , as well as the presence of additional material in front of the calorimeter have been considered and tested in [6]. Effects seen are constant in η and estimated to be around 0.1%. Similar studies have been performed with the Convolution Model (see Section 6.3.2) and lead to very similar results.

6.3.2 Convolution Model

The second fitting approach is the so-called Convolution Model. With this method it is possible to intercalibrate the energy scale of the EM calorimeter and the momentum scale of the ID. The intercalibration is performed by investigating the ratio of E/p for electrons, i.e. the ratio of the energy E measured by the EM calorimeter and the momentum p measured by the ID. The basic idea is to extract from a fit to the E/p distribution a relative scale (relative to the other response function) and a relative width of one of the two single detector response functions:

- Response function of the electromagnetic calorimeter - E/E_0 (ratio of the electron energy after detector smearing to the true energy)
- Response function of the Inner Detector - p_0/p (ratio of the true momentum to the momentum measured after the detector smearing)

In order to achieve this, the E/p distribution has to be parametrized through the two individual detector response functions. This parametrization is a convolution of the two separate functions fitting E/E_0 and p_0/p . Since E/E_0 and p_0/p describe not necessarily uncorrelated random variables, their correlation also has to be taken into account for the E/p parametrization. Since the knowledge of the true (without detector smearing) energy (E_0) and the true momentum (p_0) is necessary to obtain a description of their correlations, the correlations are modeled in MC only.

The parametrization for E/p is then fitted to the observed E/p distribution. Since it is build upon the individual detector response functions, the fit parameters obtained from the E/p fit reflect the properties of the individual detector response functions. This chapter is devoted to the extraction of the relative scale of the EM response function. Since the momentum scale and the width (resolution) of the ID has been measured very precisely [57], the obtained relative scale and width reflect the energy scale and the resolution of the EM calorimeter.

The intercalibration is done in the following steps:

1. Derive parameterizations for the individual detector response functions, i.e. E/E_0 and p_0/p .
2. Calculate correlation between E/E_0 and p_0/p .
3. Model E/p by convoluting E/E_0 and p_0/p and taking their correlation into account.
4. The parameterization for E/p is fitted to the observed E/p distribution. All parameters except the parameter for the relative scale and the width are kept fix to their values obtained in step 1).

This method has been developed during the analysis of the ATLAS combined testbeam [60] and has been further adapted to ATLAS data in the following.

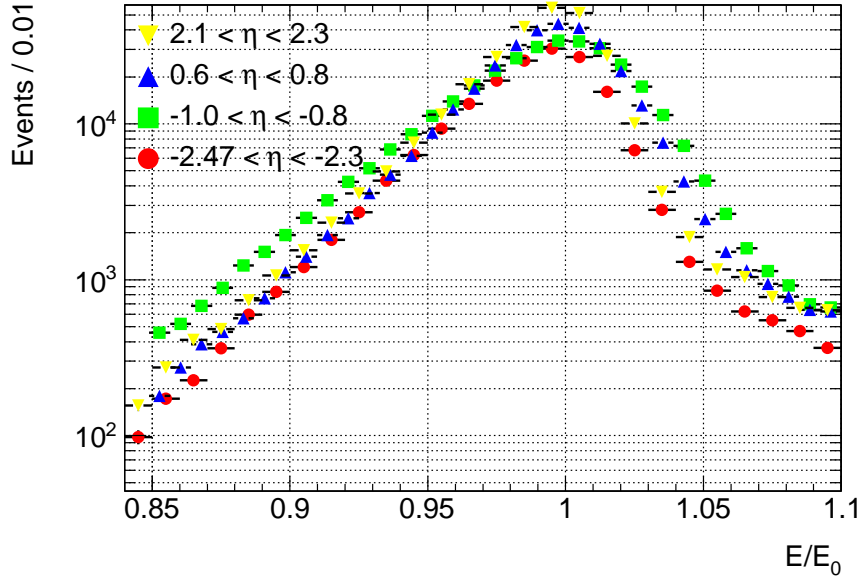


Figure 6.4: E/E_0 distributions for electrons coming from $W \rightarrow e\nu$ for different η regions. It can be seen that the negative tail (i.e. $E/E_0 < 1$) is approximately exponential. This exponential shape is due to energy loss in front of the EM calorimeter.

Modeling E/E_0

The energy response of the EM calorimeter to a particle with a given momentum is not a Gaussian, showing a tail towards lower energies (see Figure 6.4). This tail comes from energy deposits due to Bremsstrahlung in the material upstream of the calorimeter. These energy deposits should be partly corrected by the Presampler, however the tail is not completely removed and therefore has to be taken into account for modeling the energy distribution.

Motivated by Figure 6.4 one can make the following Ansatz to model the exponential part of the negative tail (the background driven parts of the tails will be discussed afterwards), where μ_E is the parameter for the energy scale and τ_E describes the slope of the negative tail:

$$f_e(e; \mu_E, \tau_E) = c \frac{1}{\tau_E \mu_E \left(\frac{1}{e^{\tau_E}} - 1 \right)} \exp\left(\frac{e}{\tau_E \mu_E} \right), e < \mu_E \quad (6.5)$$

The detector resolution (without the energy loss in upstream material) can be modeled with a Gaussian function. The expected value for the Gaussian is set to 0, whereas the variance σ_E reflects the detector resolution:

$$D(x; \sigma_E) = \frac{1}{\sqrt{2\pi}\sigma_E} \exp\left(\frac{-x^2}{2\sigma_E^2} \right) \quad (6.6)$$

The convolution of 6.5 with 6.6 will be used to describe the energy response of the calorimeter:

$$\begin{aligned}
 E(e; \mu_E, \sigma_E, \tau_E) &= \int_0^{\mu_e} f_e(x; \mu_e, \tau_E) D(e-x; \sigma_E) dx \\
 &= N \cdot \frac{\exp\left(\frac{\sigma_E^2 + 2\mu_E \tau_E e}{2\mu_E^2 \tau_E^2}\right) \left(\operatorname{Erfc}\left[\frac{\sigma_E^2 + \mu_E \tau_E (-\mu_E + e)}{\sqrt{2}\mu_E \sigma_E \tau_E}\right] - 1\right)}{2\tau_E \left(\exp\left(\frac{1}{\tau_E}\right) - 1\right)} \quad (6.7)
 \end{aligned}$$

N is the normalization factor and is set in the following to 1¹.

Additional tails in the E/E_0 distribution, mainly driven due to background events, need to be modeled. Their description is based on a "Crystal Ball-like-Ansatz" by adding power-law terms to (6.7) in positive and negative directions by introducing two cut-off parameters α_E and β_E and two exponents n_E and m_E .

$$E_{\text{tail-}}(e; \mu_E, \sigma_E, n_E) = A^- \cdot \left(B^- - \frac{e - \mu_E}{\sigma_E}\right)^{-n_E}, \text{ for } -\frac{e - \mu_E}{\sigma_E} \leq \alpha_E \quad (6.8)$$

$$E_{\text{tail+}}(e; \mu_E, \sigma_E, m_E) = A^+ \cdot \left(B^+ + \frac{e - \mu_E}{\sigma_E}\right)^{-m_E}, \text{ for } \frac{e - \mu_E}{\sigma_E} \geq \beta_E \quad (6.9)$$

where A^- , B^- and A^+ , B^+ need to fulfill the following continuity conditions² on Eq. (6.7):

$$E(\alpha_E; \mu_E, \sigma_E, \tau_E, n_E) = E_{\text{tail-}}(\alpha_E; \mu_E, \sigma_E, n_E) \quad (6.10)$$

$$E'(\alpha_E; \mu_E, \sigma_E, \tau_E, n_E) = E'_{\text{tail-}}(\alpha_E; \mu_E, \sigma_E, n_E) \quad (6.11)$$

For the positive tail $E_{\text{tail+}}$ in E/E_0 the same continuity conditions need to be fulfilled for $e = \beta_E$.

The overall function describing E/E_0

For a proper description of E/E_0 the final function can be summarized:

$$E(e; \mu_E, \sigma_E, \tau_E, \alpha_E, n_E, \beta_E, m_E) = \begin{cases} \frac{A^-}{(B^- - \frac{e - \mu_E}{\sigma_E})^{n_E}}, & \text{for } -\frac{e - \mu_E}{\sigma_E} \leq \alpha_E \\ N \cdot \frac{\exp\left(\frac{\sigma_E^2 + 2\mu_E \tau_E e}{2\mu_E^2 \tau_E^2}\right) \left(\operatorname{Erfc}\left[\frac{\sigma_E^2 + \mu_E \tau_E (-\mu_E + e)}{\sqrt{2}\mu_E \sigma_E \tau_E}\right] - 1\right)}{2\tau_E \left(\exp\left(\frac{1}{\tau_E}\right) - 1\right)}, & \text{for } -\frac{e - \mu_E}{\sigma_E} > \alpha_E \text{ and } \frac{e - \mu_E}{\sigma_E} < \beta_E \\ \frac{A^+}{(B^+ + \frac{e - \mu_E}{\sigma_E})^{m_E}}, & \text{for } \frac{e - \mu_E}{\sigma_E} \geq \beta_E \end{cases} \quad (6.12)$$

Figure 6.5 shows typical fits to the E/E_0 distribution. It can be seen that the shape of the E/E_0 distribution changes with η depending on the material in front of the calorimeter. To have one perfect fitting function for different regions in the detector a certain flexibility of the shape is needed (especially towards lower and higher values of E/E_0). The two added power-law terms to (6.7), introduce such a flexibility to the function and simultaneously preserves the physics motivation.

¹The part $\int_{\mu_e}^{\infty}$ is zero since Equation 6.5 is zero for $e > \mu_E$

²The two functions (and its first derivatives) evaluated on the connection point should have the same value.

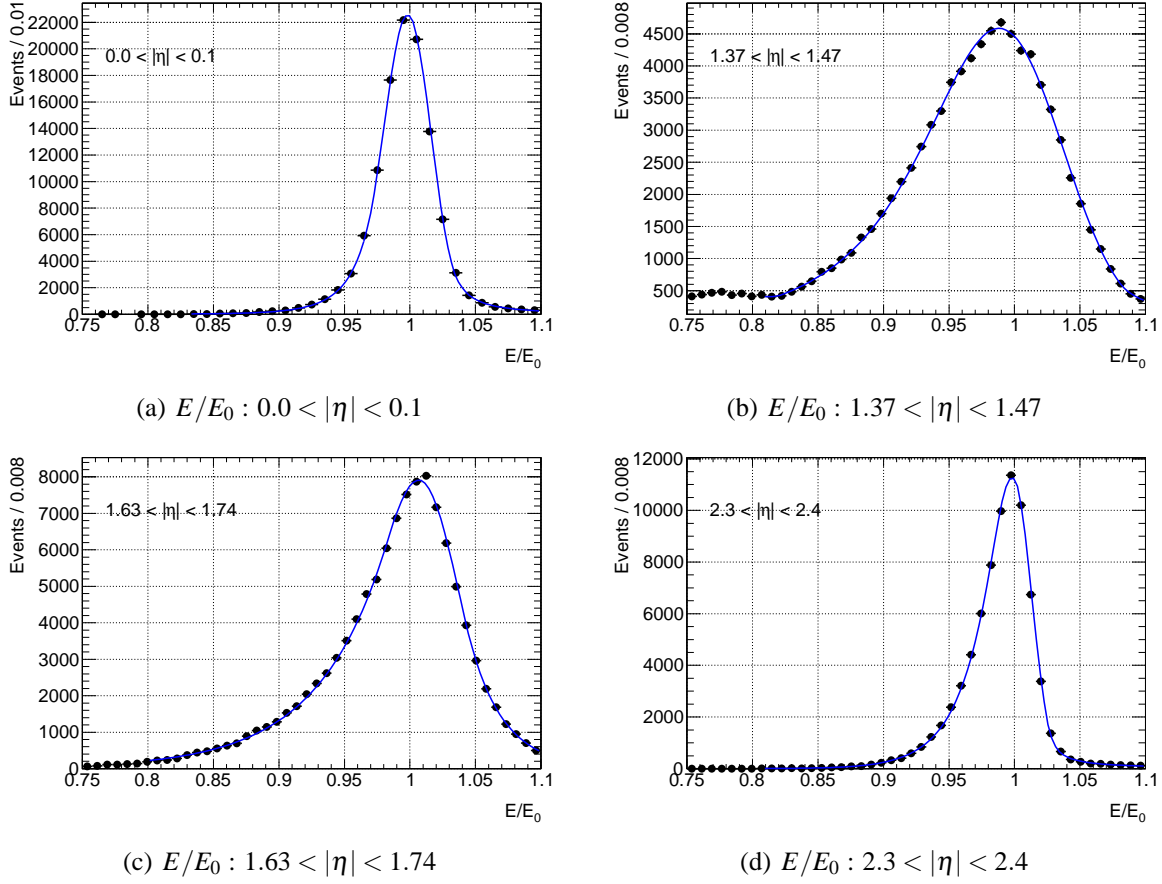


Figure 6.5: MC distributions of E/E_0 fitted with the function in Eq. 6.12 for different η regions are shown. For the crack and the transition regions (see Figure 6.5(b) and 6.5(c)) E/E_0 is broader due to more material in front of the detector (the ID has almost $2 X_0$ at $\eta \sim 1.7$. In the cracks there are regions with up to $4 X_0$ in front of the active calorimeter) hence higher Bremsstrahlung loss. For other regions of the detector (see Figure 6.5(a) and 6.5(d)) the E/E_0 distributions are rather narrow.

Modelling p_0/p

The Crystal Ball function f_{CB} is reminded here:

$$f_{CB}(x; \mu, \sigma, \alpha, n) = N \cdot \begin{cases} \exp\left(-\frac{(x-\mu)^2}{2\sigma^2}\right), & \text{for } \frac{x-\mu}{\sigma} > -\alpha \\ A \cdot \left(B - \frac{x-\mu}{\sigma}\right)^{-n}, & \text{for } \frac{x-\mu}{\sigma} \leq -\alpha \end{cases} \quad (6.13)$$

where

$$A = \left(\frac{n}{|\alpha|}\right)^n \exp\left(-\frac{|\alpha|^2}{2}\right) \quad (6.14)$$

$$B = \frac{n}{\alpha} - |\alpha| \quad (6.15)$$

N is the normalization factor and α , n , μ and σ are parameters. The p_0/p distribution (see Figure 6.6) is modelled using a Crystal Ball function, denoted as $Q(q; \mu_q, \sigma_q, \alpha_q, n_q)$, where

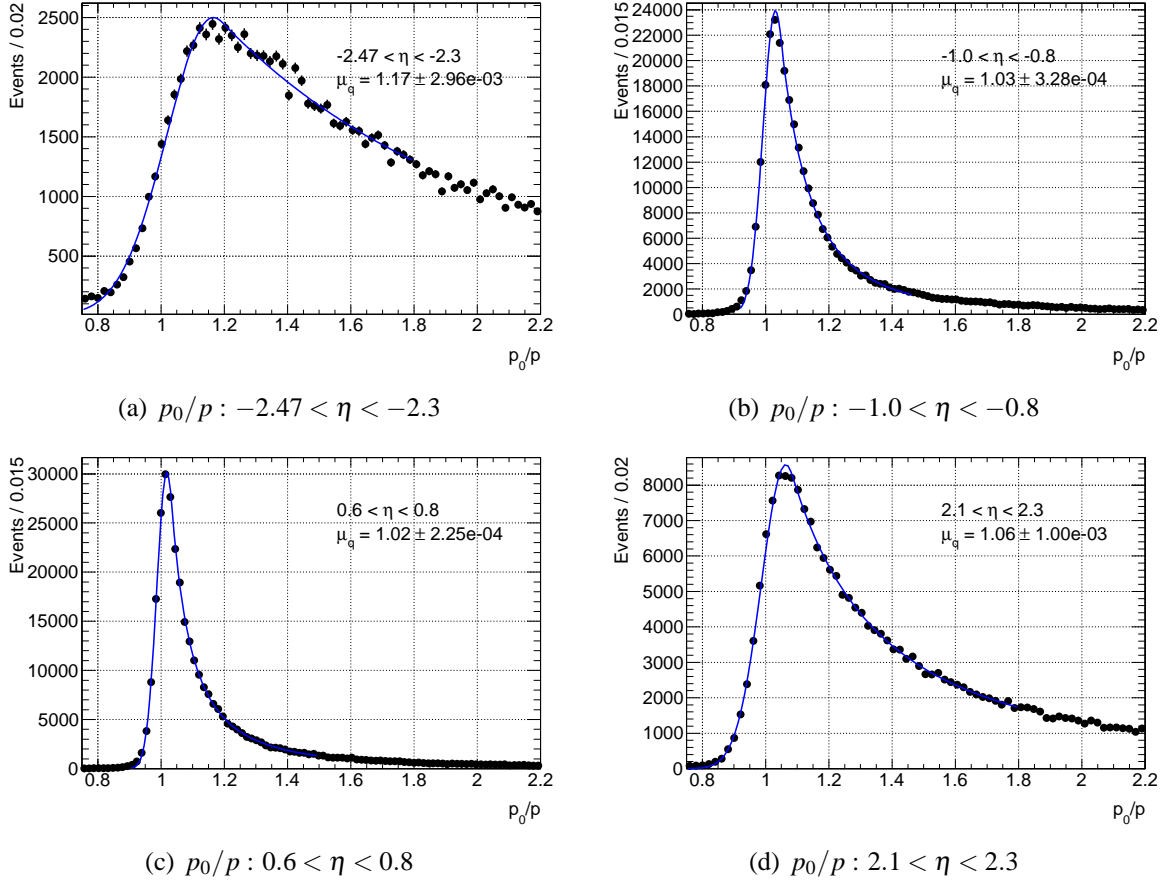


Figure 6.6: Distributions of p_0/p with the Crystal Ball fit for different η regions are shown. For low η bins the p_0/p distributions are well described by a simple Crystal Ball function (see Figure 6.6(b) and 6.6(c)). For higher η bins (last few bins, for example see Figure 6.6(a) and 6.6(d)) the Crystal Ball fit is heavily impacted by the tails and the extracted most probable value (μ_q) is associated with a larger error.

$\alpha = -\alpha_q$, with the tail added on the left side of the distribution.

Modeling E/p

The variables to be measured are e and q . E/p will then be described by the product $r = e \cdot q$ with a distribution $R(r)$. $R(r)$ is a probability integral transform, which holds the single distributions of the measured variables e and q . It is given by the following integral:

$$R(r) = \int_{-\infty}^{\infty} f_{(E,Q)} \left(\frac{r}{w}, w \right) \frac{1}{w} dw \quad (6.16)$$

The joint distribution can be rewritten as:

$$f_{E,Q}(e, q; \mu_e, \sigma_e, \tau_e, \alpha_e, n_e, \beta_e, m_e, \mu_q, \sigma_q, \alpha_q, n_q) = E(e; \mu_e, \sigma_e, \tau_e, \alpha_e, n_e, \beta_e, m_e) Q(q; \mu_q, \sigma_q, \alpha_q, n_q) C(e, q) \quad (6.17)$$

where $C(e, q)$ represent the correlations between e (E/E_0) and q (p_0/p) (see Section 6.3.2). Inserting (6.17) into (6.16) leads to

$$R(r; \mu_e, \sigma_e, \tau_e, \alpha_e, n_e, \beta_e, m_e, \mu_q, \sigma_q, \alpha_q, n_q) = \int_{-\infty}^{\infty} E\left(\frac{r}{w}; \mu_e, \sigma_e, \tau_e, \alpha_e, n_e, \beta_e, m_e\right) Q(w; \mu_q, \sigma_q, \alpha_q, n_q) C\left(\frac{r}{w}, w\right) \frac{1}{w} dw \quad (6.18)$$

Correlation

Assuming that there is no correlation between E/E_0 (e) and p_0/p (q), $C(e, q)$ in (6.18) is set to one. This should be the case for high energy electrons where the impact of Bremsstrahlung on the momentum measurement is small. In order to achieve a precision for the relative scale at the per mill level, however, the correlation between E/E_0 and p_0/p has to be taken into account. The continuous function $C(e, q)$ can be approximated by discrete values for bins in e and q . $C(e, q)$ is determined from Monte Carlo simulations by performing the division bin wise:

$$C(e, q) = \frac{f_{E,Q}(e, q)}{E(e) Q(q)} \quad (6.19)$$

Figure 6.7 shows the distribution of correlations between E/E_0 (e) and p_0/p (q). Three different regions can be distinguished:

- I $E < E_0$ and $p < p_0$ ($E/E_0 < 1, p_0/p > 1$): The momentum measurement of the electrons is too low due to Bremsstrahlung loss in the ID. The Bremsstrahlung photons are outside the reconstructed cluster, therefore also the energy measurement is underestimating the real energy. Since it is Bremsstrahlung causing both inaccuracies those event have a large correlation factor.
- II $E \approx E_0$ and $p < p_0$ ($E/E_0 \approx 1, p_0/p > 1$): a correlation factor > 1 can also be found for electrons with a underestimated momentum in the ID but their photons, radiated due to Bremsstrahlung, deposit their energy in the cluster. The energy measurement hence is correct.
- III $E < E_0$ and $p \approx p_0$ ($E/E_0 < 1$ and $p_0/p \approx 1$): it is highly unlikely that the momentum is measured correctly, if the reconstructed energy of electrons underestimates the real energy. Most of those tails are due to outliers in the E/E_0 distribution. Those events have a correlation factor < 1 .

Fitting E/p

To summarize the scale extraction and the resolution extraction from a fit to the final E/p distribution with Equation 6.18 the following steps need to be processed within the Convolution Model:

- a fit to E/E_0 with eq. 6.12
- a fit to p_0/p with eq. 6.13
- calculate correlation factors as described in eq. 6.19.

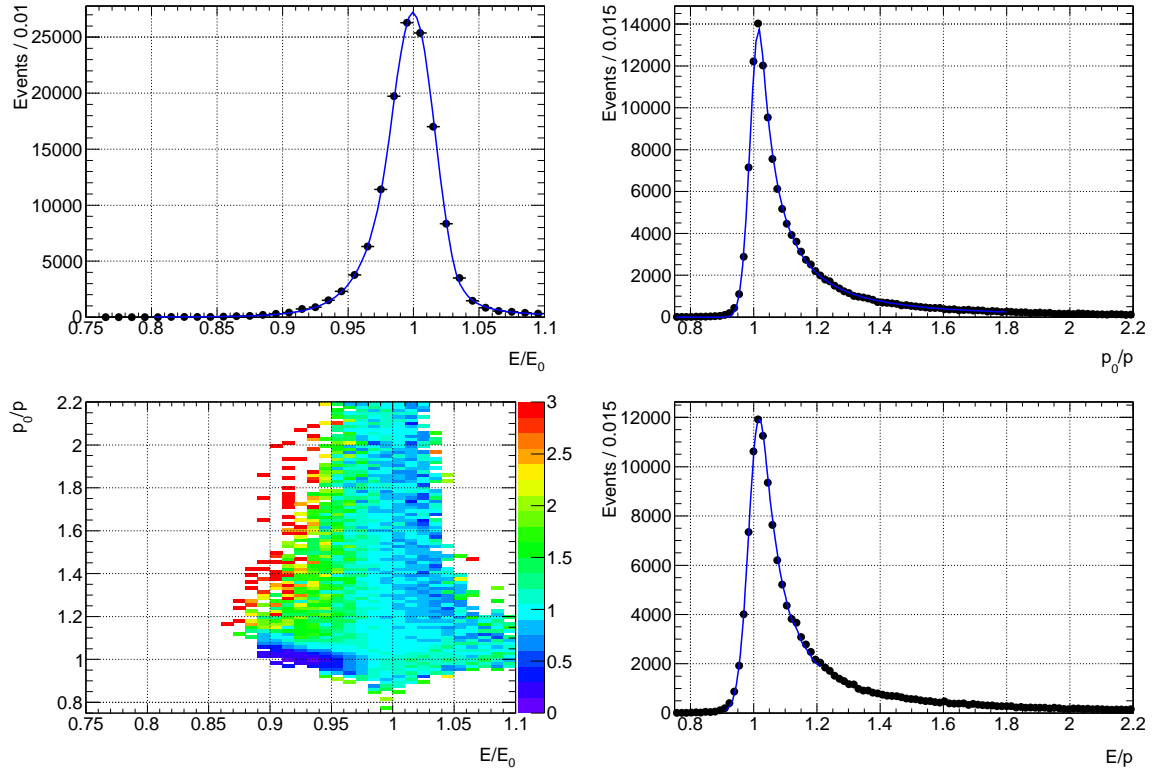


Figure 6.7: Breakdown of the individual fits which contribute to the final fit function describing E/p distribution is shown for $[0.7 < \eta < 0.8]$. Content of plots (from left to right): fit on E/E_0 , fit on p_0/p , description of the correlations between E and p (the color code is the value $C(e, q)$ obtained with Equation 6.19), final fit to the E/p . Here, all fits are performed on MC distributions.

The final function $R(r; \mu_e, \sigma_e, \tau_e, \alpha_e, n_e, \beta_e, m_e, \mu_q, \sigma_q, \alpha_q, n_q)$ fitting E/p is determined by $11 + 1$ parameters, where 7 are resulting from the fit to E/E_0 (i.e: $\mu_e, \sigma_e, \tau_e, \alpha_e, n_e, \beta_e$) and the latter four from the fit to p_0/p (i.e: $\mu_q, \sigma_q, \alpha_q, n_q$) and one additional parameter accounts for the normalisation. To extract the energy scale (μ_e) and the resolution (σ_e) from R , nine parameter are fixed as they result from their single fits to MC. As already mentioned, the correlations between E and p , as they are applied in R , are as well taken from MC (see Equation 6.19). An overview of used fit ranges and obtained values are shown in Table 6.3.

This method relies extensively on a correct description of data with MC (see MC data comparisons in Figure 6.1). In the following it will be shown how inaccuracies in MC can cause (small) systematic errors.

The final energy scale correction $\alpha_{E/p}^{\text{ConvMod}}$ is calculated in η (and ϕ) bins. Figure 6.7 shows all single fits in one η bin (ϕ integrated). For each bin a (energy scale correction) factor

$$\alpha_{E/p}^{\text{ConvMod}} = \frac{\mu_e^{(E/p)}}{\mu_e^{(E/E_0)_{\text{MC}}}} - 1 \quad (6.20)$$

is defined, where $\mu_e^{(E/E_0)_{\text{MC}}}$ refers to the parameter fitted from the E/E_0 distributions in MC and $\mu_e^{(E/p)}$ is the value extracted from the fit to the E/p distribution of the data sample (or MC sample for closure test).

Tests have been done to extract μ_E together with σ_E and μ_p together with σ_p while each time fixing all the other parameters. Due to the difference in the track fitting (GSF was used in 2012, see Section 4.1) the optimal procedure (smallest non-closure) actually is different for 2011 and 2012. For 2011 a combined fit of (μ_e, σ_e) is chosen, for 2012 a combined fit of (μ_e, σ_p) is chosen.

Variable	Fit Range	Obtained Value ($\eta \approx 0.6$)	Obtained Value ($\eta \approx 1.6$)
E/E_0			
μ_e	0.95 - 1.05	1.00551	1.02058
σ_e	0.008 - 0.1	0.01620	0.02758
τ_e	0.009 - 0.1	0.00953	0.01784
α_e	0.0001 - 50.0	1.4608	10.3542
n_e	0.0 - 40.0	19.2432	38.97542
β_e	0.0001 - 40.0	1.25653	0.19556
m_e	0.0 - 40.0	3.94916	35.57469
p_0/p			
μ_q	0.85 - 1.3	1.01918	1.06572
σ_q	0.01 - 1.0	0.03225	0.0607
α_q	-19 - 0.1	-0.23157	-0.22092
n_q	0.0 - 5.0	1.80299	3.19873
E/p			
$\mu_e^{E/p}$	$\pm 1\%$ of μ_e		
$\sigma_e^{E/p}$	$\pm 35\%$ of σ_e		
$\sigma_q^{E/p}$	$\pm 35\%$ of σ_q		

Table 6.3: Overview of fit ranges used for different variables in the Convolution Model. The obtained values for 2 η regions are given respectively for E/E_0 and p_0/p from MC simulations.

6.4 Systematic Uncertainties of the Convolution Model

Several systematic errors, such as uncertainties on the method itself, uncertainties due to additional material in front of the calorimeter or uncertainties of the momentum measurement in the ID, have been investigated and will be presented in the following. A summary of all the systematic effects will be given in Section 6.4.5.

6.4.1 MC Closure Test

To estimate the systematic errors of the Convolution Model method as well as the accuracy, a MC closure test was made. For each bin in η $\alpha_{E/p}^{\text{ConvMod}}$ is calculated. For the closure test all parameters but the relative energy scale (μ_e) and the resolution of either the calorimeter (σ_e) or the inner detector (σ_p) are fixed to its MC value. The nominal MC sample is split into two parts: 2/3 of the number of electrons is used to calculate the correlations, the rest serves as pseudo-data, on which R is fitted to E/p . Figure 6.8 shows $\alpha_{E/p}^{\text{ConvMod}}$ as a function of 25 η bins within $|\eta| < 2.47$, fitting μ_e and σ_e .

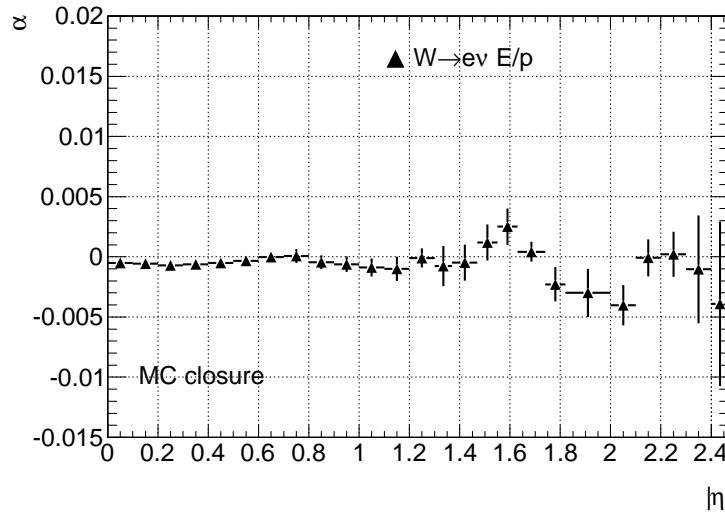


Figure 6.8: $\alpha_{E/p}^{\text{ConvMod}}$ from the MC closure test in 25 η bins for $|\eta| < 2.47$ ($\Delta\eta \approx 0.1$). To achieve results in this fine binning in η for the closure test (the nominal MC sample is split into 2/3 to calculate the correlations and 1/3 left as pseudo data), absolute values in η are taken.

The presented results are pretty stable for $|\eta| < 2$ (with the exception of the transition region between barrel and end-caps around $|\eta| \approx 1.5$) and the MC closure is within 0.1%. For the regions $|\eta| > 2$ the non-closure is at the level of $\sim 0.5\%$. This offset can be explained due to problems with a proper description of the Crystal Ball fit on p_0/p in the end-caps, as well as the low number of electrons in the MC simulation, to generate correlation factors in this region.

The MC closure test suggests that the energy scale extraction is possible with an accuracy of 0.1% for $|\eta| < 1.4$ and 0.3% for $1 < |\eta| < 2.5$ (with the exceptions of a few bins at

$|\eta| \approx 1.7 - 2.1$).

In the following the full distance of the α to 0 in the MC closure test are taken as systematic error and are included in the error bars.

6.4.2 Systematics due to Additional Material

To estimate the uncertainty of the effect of *additional material in front* the energy scale was extracted with the Convolution Model using a distorted MC sample (G'). The exact distribution of additional material in the distorted material MC sample can be found in Chapter 3.

The following four cases (see Figure 6.9) with G' and nominal MC samples for the correlation factor calculation are considered to estimate the systematic error due to a wrong material description:

- Correlations are calculated on nominal MC, R is fitted to a E/p distribution generated with an additional material in front of the detector using the distorted G' MC sample. ($Corr_{nom} - E/p_{G'}$)
- Correlations are calculated with the distorted G' MC sample, R is fitted to the nominal MC E/p distribution ($Corr_{G'} - E/p_{nom}$)
- The nominal MC sample is split into 2/3 to calculate the correlations and the remaining 1/3 are used to generate the E/p distribution - conventional MC closure test as explained before ($Corr_{nom} - E/p_{nom}$)
- The distorted MC sample G' is split into 2/3 to calculate the correlations and R is fitted to the E/p distribution generated with the remaining 1/3 ($Corr_{G'} - E/p_{G'}$)

The black and the red points in Figure 6.9 show the results for the first two cases: if additional material in front of the EM calorimeter appears in data (here represented by distorted material MC sample G'), the extracted energy scale (here represented by the scale correction α since it is pure MC) increases w.r.t the nominal closure test. This increase comes from missing information of additional material in the calculation matrix. On the other hand, if there is too much material in front of the EM calorimeter in MC (in this test represented by the distorted material MC sample G') than it appears to be in data (pseudo data represented by nominal MC), the extracted energy scale decreases. This effect is symmetric for equal amounts of material meaning that the direction (positive or negative) changes depending if material is missing in MC simulation (and hence the correlation matrix) or in collision data.

Comparing the last two cases (blue and green points in Figure 6.9), it can be seen that the Convolution Model is able to extract the energy scale in both cases with an accuracy smaller than one per-mill in the barrel and better than five per-mill in the end-cap.

6.4.3 Parameter Extraction

In the final energy scale (and resolution) extraction only μ_e and σ_e in R (see Equation 6.18) are chosen to be free parameters in the fit to the E/p distribution. As already mentioned before, the obtained μ_e represents the energy scale and μ_e the resolution. To estimate a possible uncertainty on the energy scale (or resolution) extraction based on the chosen free parameters in R two different MC closure test were performed:

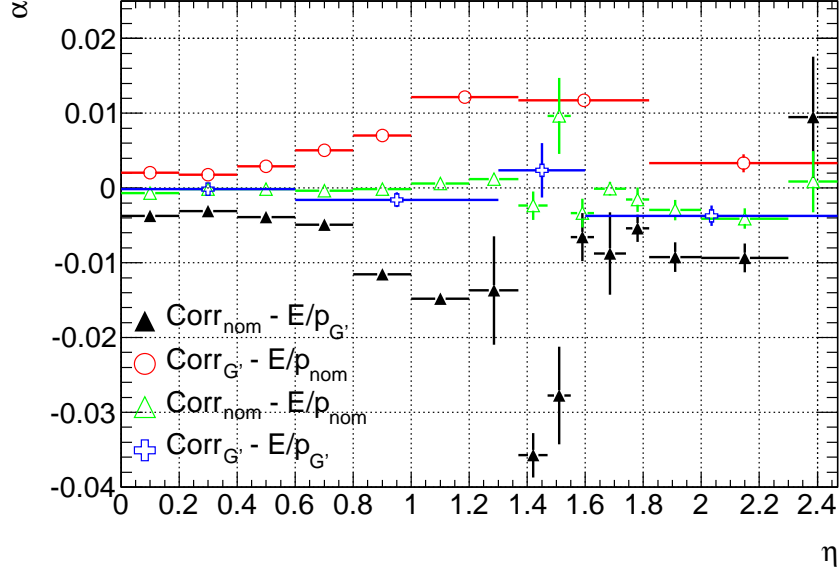


Figure 6.9: Considering four cases in a MC on MC test using G' and nominal MC samples to calculate the correlation factors and generate the E/p distribution with which α is extracted. The blue and green points show a MC closure test on nominal and distorted material MC. Black points: the nominal material description was used to generate the two detector response functions (and its correlations) but E/p was generated with an additional material in front of the detector. The red points show the inverse scenario: the two detector response functions (and its correlations) are generated with additional material in front of the detector but E/p with the nominal MC. The shown error bars are the errors returned by the fit procedure.

1. either μ_e or σ_e is a free parameter
2. both, μ_e or σ_e , are free parameters in the fit (as shown in Figure 6.8)

The obtained results on the *parameter extraction* are shown in Figure 6.10. As one can see on the left plot, the difference between the extracted values for the energy scale is within the error bars and no additional systematic error is needed.

For the resolution σ_E , a significant non-closure is observed (μ_e and σ_e are free parameters), which is only slightly improved when extracting the resolution only (σ_e is the only free parameter in R). One cause of that are in-accuracies in low-statistic bins of the correlation matrix.

6.4.4 Systematic Error on the Momentum Measurement

Residual *misalignment of the ID* causes wrong momentum measurement. Most of the misalignment modes would have opposite effects on positively and negatively charged particles. Although some mis-alignment modes exist that impact both positively and negatively charged particles in the same way, it has been shown [57] that these residual misalignment is in the order of 10^{-4} , when averaging over the azimuthal angle ϕ . Figure 6.11 shows the charge dependence of the extracted α . The difference between the W^+ and the W^- sample is found to

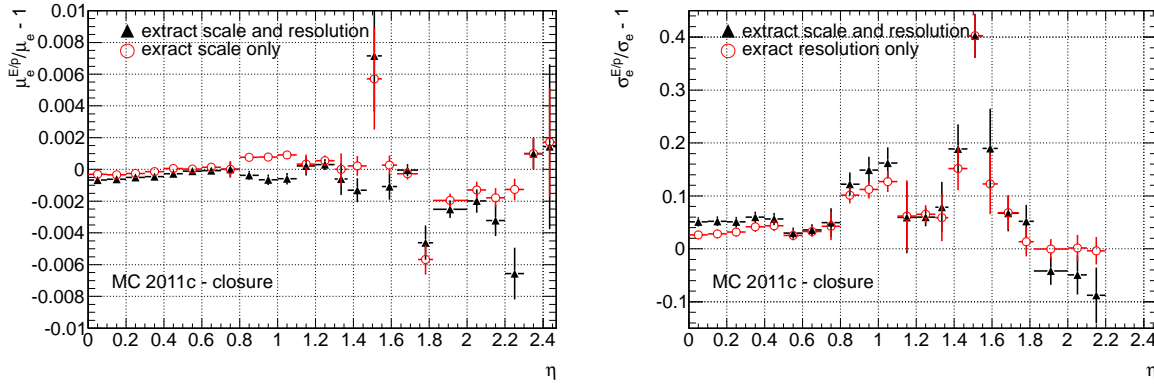


Figure 6.10: *MC closure for the extraction of single parameters (red) gives the same result (within the error bars) as for the parallel scale/resolution extraction (black). Left: closure test on μ_e ; Right: closure test on σ_e . For μ_e the non-closure is on the sub per mill and fairly negligible, whereas the non-closure for σ_e is on the percent level.*

be $< 0.2\%$ for $|\eta| < 1$ and $< 0.5\%$ above (apart from the transition region around $|\eta| = 1.4$). The difference observed between the results obtained with W^\pm and Z are likely due to the different electron p_T distributions of the two samples which suggests a small non-linearity of the energy response which will be discussed later.

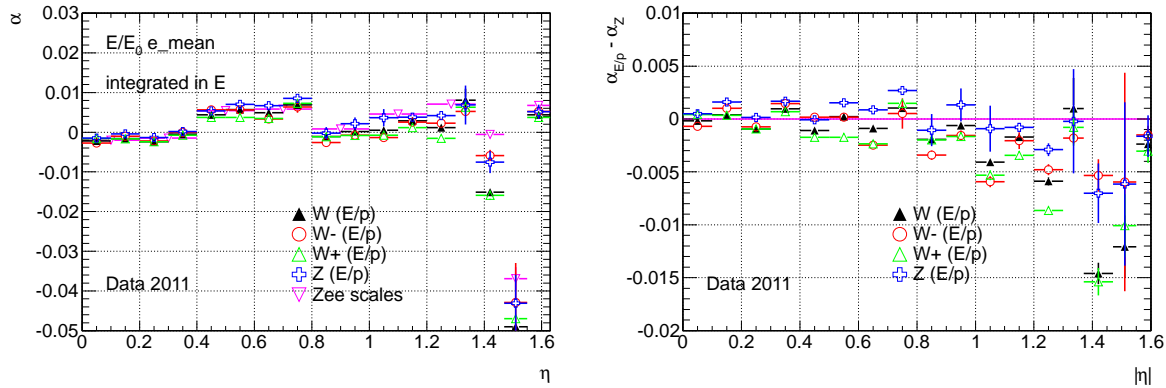


Figure 6.11: *Left: The energy scale correction for different samples and with both electrons and positrons using the E/p distribution in all cases but 1, i.e. purple open triangle being the corrections calculated with the Z peak. A residual misalignment would appear as a difference in the extracted scale corrections. Right: Difference of the scale corrections from E/p to corrections calculated with the Z peak.*

It was shown in [57] that averaging in ϕ will establish the correct momentum scale despite the presence of small mis-alignemt modes impacting both charges in the same way. However, this would increase the width σ of the p_0/p distributions by about 0.9%. This effect was tested by smearing $1/p$ in the MC E/p distribution with a Gaussian of $\sigma_{\text{Gauss}} = 0.009$ but generating the detector response functions (and its correlations) with nominal MC. The energy scale (and resolution) is extracted for that case and the resulting scale (and resolution) correction α is

compared to the nominal MC closure along η (see Figure 6.12).

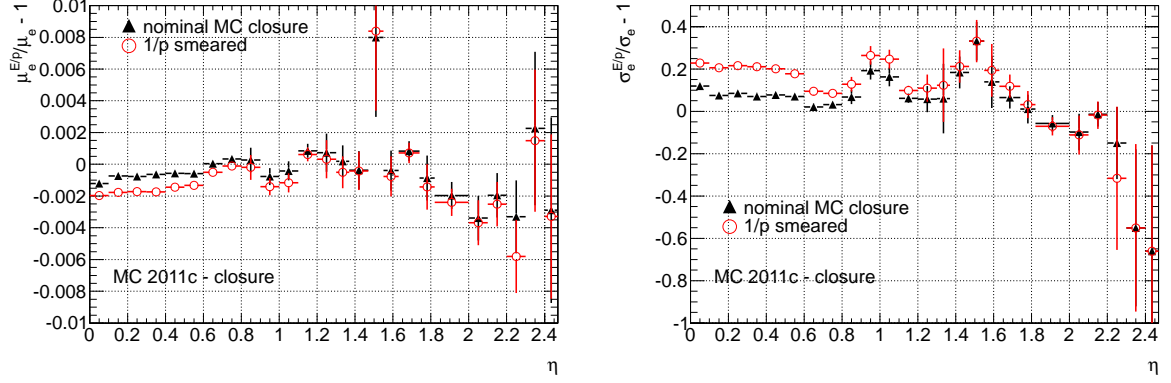


Figure 6.12: *Left: Comparing the effect on the scale correction α after smearing $1/p$ in E/p with a Gaussian (red open points) with the nominal MC closure (black points). A systematic effect of up to 0.1% is observed for $|\eta| < 1.1$. Right: Same as left but in the case for the resolution. The red open points (smearing $1/p$ in E/p with a Gaussian) show an expected shift to higher levels since the larger width of the E/p distributions coming from the smearing of p/p_0 is being accounted for by a larger σ_E .*

Considering a possible residual misalignment in the ID ($\sigma_{\text{Gauss}} = 0.009$) a slight systematic error of up to one per mill up to $|\eta| < 1.1$ can be observed. This effect is washed-out for $\eta > 1.1$, since there the nominal E/p distributions have already a large width.

6.4.5 Summary

On top of the statistical error due to the number of $Z \rightarrow e^+e^-$ or $W^\pm \rightarrow e^\pm \nu$ used for the different analyses, different systematic uncertainties contribute to the energy scale extraction with the Convolution Model and were discussed in the last sections. A summary of the different uncertainties is presented in Table 6.4.

source	barrel	transition region	end-caps
MC closure	$\pm 0.08\%$	$\pm 0.5\%$	$\pm 0.3\%$
Additional material (G')	$\pm 0.3\%$	$\pm 1.2\%$	$\pm 1\%$
Parameter extraction	$\pm 0.05\%$	$\pm 0.3\%$	$\pm 0.3\%$
Momentum measurement	$\pm 0.1\%$	$\pm 0.05\%$	$\pm 0.01\%$
Overall (without additional material)	$\pm 0.14\%$	$\pm 0.58\%$	$\pm 0.42\%$

Table 6.4: *Break down of different systematic uncertainties of the energy scale extraction using the Convolution Model.*

6.5 Results

This section presents results for the extraction of the energy scale correction α using E/p applying the methods mentioned before. It will be shown that the measurements from E/p agree on the per mill level with the measurement from the Z peak.

6.5.1 Energy Scales

To extract the energy scale corrections with electrons from $W^\pm \rightarrow e^\pm \nu$ using E/p (with the methods explained before) the data sample is divided into 34 bins in η . The $|\eta|$ bin boundaries are as follows (in positive and negative η direction the same binning is used):

Barrel:

$$\{0.0, 0.2, 0.4, 0.6, 0.8, 1.0, 1.2, 1.37, 1.47\}$$

End-cap:

$$\{1.55, 1.63, 1.74, 1.82, 2.0, 2.1, 2.3, 2.4, 2.47\}$$

For the 2011 dataset the parameter μ_e and σ_e of R were chosen as free parameters for the extraction of the energy scale in E/p . The MC closure test was performed, as seen on the left plot in Figure 6.13, with a precision on a sub per mill level excluding the transition region between the barrel and the end-cap calorimeter. A fast jump of material along η can be found in this region. The non-closure would be less dramatic when using finer bins in η in that specific region. Unfortunately, the MC simulation does not provide a sufficient number of reconstructed electrons to generate correlation matrices with high accuracy in finer η binning as done in this closure test. As a common analysis strategy the region $1.37 < |\eta| < 1.52$ is excluded for most of the analyses done with ATLAS data.

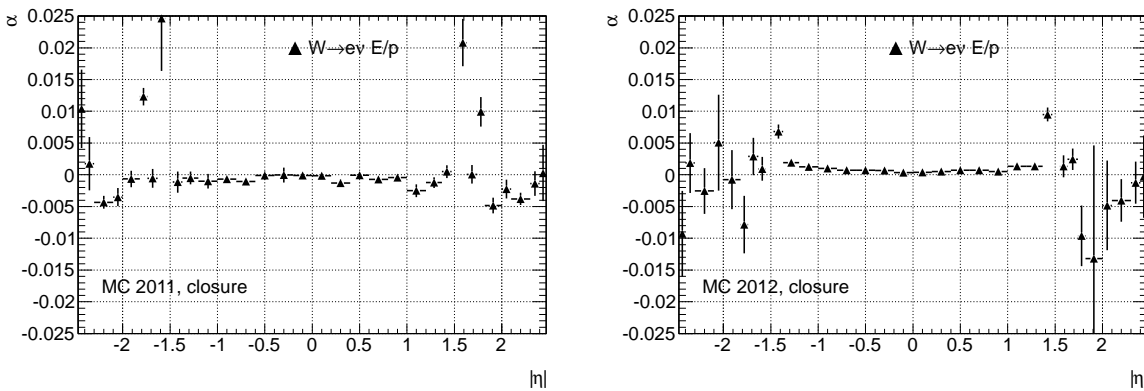


Figure 6.13: *MC closure tests; Left: Fit of the energy scale and resolution (μ_e and σ_e) in E/p , while fixing the other parameter to the MC value for 2011 MC. Right: Fit of the energy scale and the momentum resolution (μ_e and σ_p) for 2012 MC.*

For the 2012 dataset the parameter μ_e and σ_p of R were chosen as free parameters for the extraction of the energy scale in E/p . The MC closure test was performed, as seen on the

right plot in Figure 6.13, with a precision on a sub per mill level excluding the transition region between the barrel and the end-cap calorimeter. The reason of choosing σ_p instead of σ_e , as done in 2011, comes from the difference of the track fitting algorithm used in these two years. As explained in Section 4.1, a Gaussian Sum Filter (GSF) was used for the track fit taking Bremsstrahlung losses induced by material in the Inner Detector into account. The new track fitting results in narrower E/p distributions. A dependence on the correct momentum resolution description in MC simulation (w.r.t. data) is given, as is a perfectly calculated correlation matrix needed when fitting a R to E/p . Since the accuracy of the correlation matrix in MC simulation is limited due to a maximum number of generated electrons, σ_p was chosen as the second free parameter to account for limits in the correlation matrix and in the MC description of the momentum resolution.

The final energy scale correction for 2011 as a function of η of the Convolution Model compared to the Crystal Ball model and the Z peak can be seen in Figure 6.14. For the barrel the scale correction extracted with the Convolution Model is absolutely compatible with the scale correction from the Z peak ³, for the central region $|\eta| < 1$. The Crystal Ball scale correction shows a global shift. This shift comes from the fact that even small discrepancies in the tails of the E/p distribution can lead to a substantial shift in the extracted scale. As discussed in Section 6.3.1, the results from the Crystal Ball fits are only shown for comparison, but they are not suited to extract an absolute scale. The discrepancies between the extracted scales correction for $|\eta| > 1$ come from the fact that the amount of material and its uncertainties in front of the EM calorimeter increases substantially there, as shown in Figure 6.9. Each of the methods is affected differently by additional material in front of the calorimeter.

To obtain the energy scale correction versus η for the 2012 MC and dataset the same procedures were applied. For the energy scales extracted with the Convolution Model the same two setups as for 2011 were used: fit the energy scale and inner detector resolution (μ_e and σ_p) or fit the energy scale and calorimeter resolution (μ_e and σ_e). As discussed in Section 6.3.2 for 2011 a better MC closure is obtained for fitting μ_e and σ_e and for 2012 μ_e and σ_p . The results for 2012 when fitting (μ_e and σ_e) can be seen on the top plot in Figure 6.15. A global shift w.r.t. the energy scale correction obtained from the Z peak of about one per mill can be observed in this setup. The bottom plot of Figure 6.15 shows the final results for the 2012 dataset.

6.5.2 E/p tails

The E/p tails are sensitive to passive material in front of the calorimeter. A study of the tails in E/p is subject of Chapter 10.

³The method of extracting the energy scales using the Z peak is explained in Appendix B

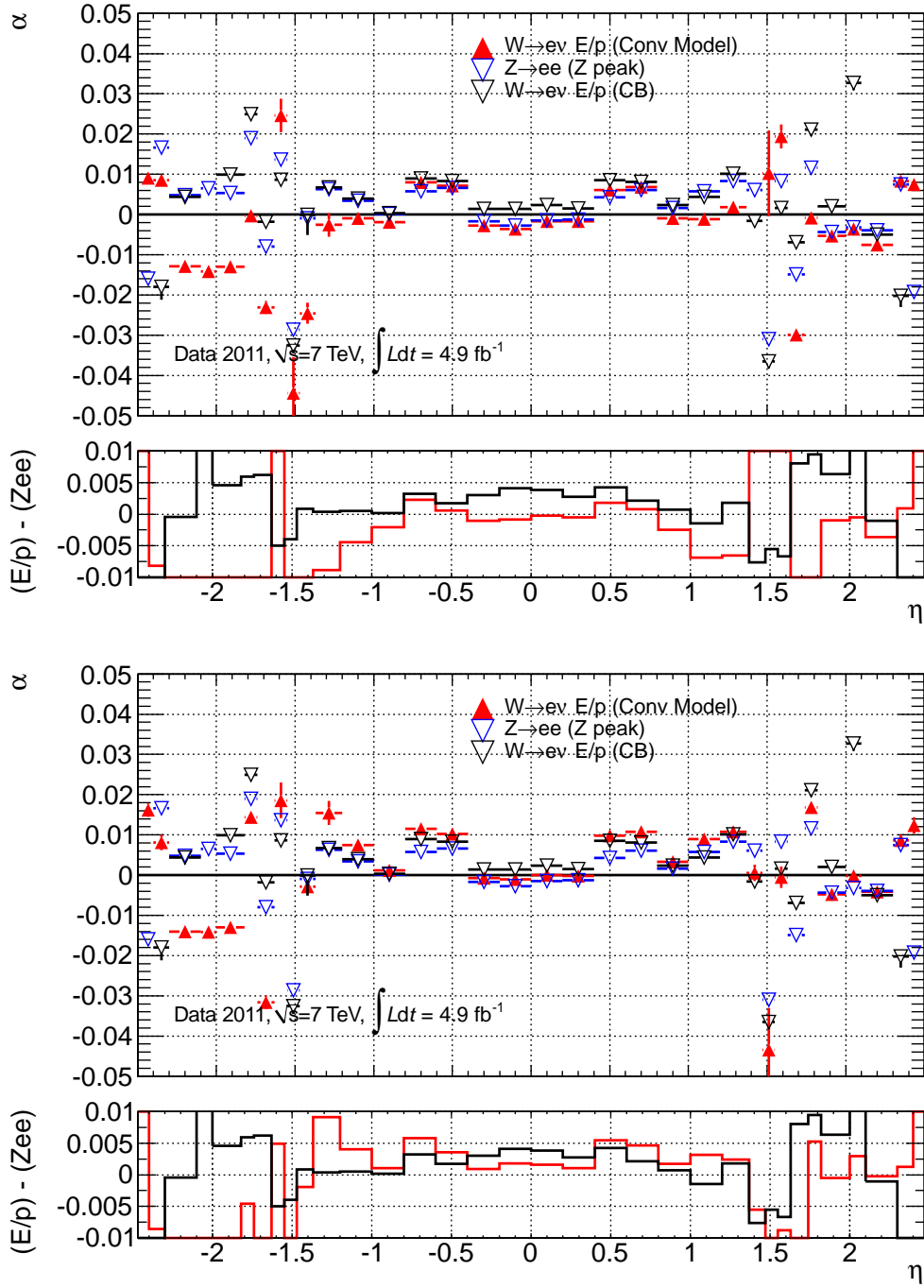


Figure 6.14: Energy scale correction for 2011 data; Red triangles are the measurements from the Convolution Model, Black open triangles are the results from the Crystal Ball fits, Blue triangle are the scales from the Z peak; Top and bottom plot differ between each other for the setup used in the Convolution Model; Top: Fit the energy scale and resolution (μ_e and σ_e) in E/p , while fixing the other parameter to the MC value. Bottom: Fit to the energy scale and the momentum resolution (μ_e and σ_p)

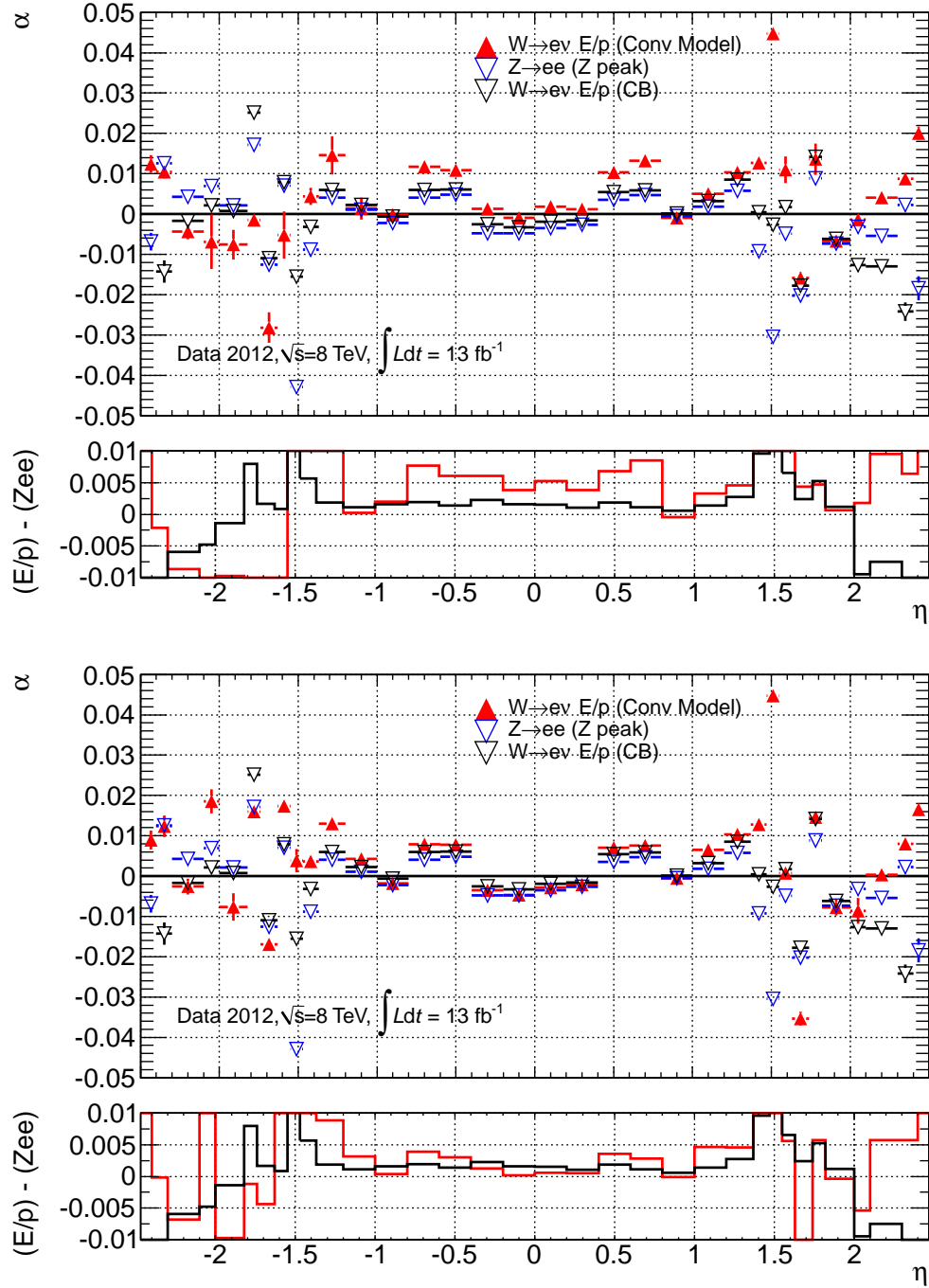


Figure 6.15: Energy scale correction for 2012 data; Black open triangles are the results from the Crystal Ball fits, Blue triangles are the scales from the Z peak, Red triangles are the measurements from the Convolution Model; Top: fit (μ_e and σ_e) in the Convolution Model; Bottom: fit (μ_p and σ_p);

Chapter 7

Uniformity and Stability

7.1 Overview

This chapter demonstrates the outstanding performance of the ATLAS electromagnetic calorimeter in terms of stability versus time and pileup conditions and spatial uniformity in the (η, ϕ) plane. Some of the analysis procedures which were developed and used during the past two years and which contributed to this exceptional performance, will now be discussed in further detail.

The uniformity of the energy response in η and ϕ is investigated using electron samples (see Section 7.2). Then, a study of the stability of the energy response versus time and pile-up and relative location in the bunch train will be presented (see Section 7.3).

The uniformity and stability is measured using E/p distributions for electrons and positrons from $W^\pm \rightarrow e^\pm \nu$ (and $Z \rightarrow e^+ e^-$) events from ATLAS data. The most probable value (MPV) of the E/p distribution is obtained from a Crystal ball fit (as presented in Section 6.3.1) to the E/p distribution.

A complementary method uses the invariant mass peak of $Z \rightarrow e^+ e^-$ events. The method is discussed in Appendix A. The position of the Z peak is only an indirect measurement of the energy response since the second electron comes from a random region. It will be shown that non-uniformities along η (or ϕ) are usually a factor of about two smaller compared to the measurement with a single electron, such as in E/p .

7.2 Uniformity

As described in Section 5.4 non-uniformities in the energy response contribute to the calorimeter's constant term. The energy resolution function is parametrized as

$$\frac{\sigma_E}{E} = \frac{a}{\sqrt{E}} \oplus \frac{b}{E} \oplus c \quad (7.1)$$

η range	Effective constant term, c_{data}
$ \eta < 1.37$	$1.2\% \pm 0.1\% \text{ (stat)} \begin{smallmatrix} +0.5\% \\ -0.6\% \end{smallmatrix} \text{ (syst)}$
$1.52 < \eta < 2.47$	$1.8\% \pm 0.4\% \text{ (stat)} \pm 0.4\% \text{ (syst)}$
$2.5 < \eta < 3.2$	$3.3\% \pm 0.2\% \text{ (stat)} \pm 1.1\% \text{ (syst)}$
$3.2 < \eta < 4.9$	$2.5\% \pm 0.4\% \text{ (stat)} \begin{smallmatrix} +1.0\% \\ -1.5\% \end{smallmatrix} \text{ (syst)}$

Table 7.1: Measured effective constant term c_{data} from the observed width of the $Z \rightarrow e^+e^-$ peak for different calorimeter η regions for the 2010 dataset. The systematic uncertainty includes uncertainties on the sampling term and on the fit procedure (uncertainties on pile-up were found to be negligible). Taken from Ref. [6].

where c is the constant term obtaining contributions which do not depend on the energy of the particle. It results mostly from instrumental effects that cause variations of the energy response and add an additional smearing to the measured energy of the particle distributed over large calorimeter areas. In the test beam setup, four different modules of the ATLAS EM barrel LAr calorimeter were studied in the energy range from 10 to 245 GeV. The sampling term (a) of the energy resolution was found to be $10\% \cdot \sqrt{\text{GeV}}$, the local¹ constant term along η in average about 0.35% but below 0.5% [61, 62]. Uniformity studies done in the same test beam showed a non-uniformity of about 0.6% [62], leading to a constant term of about 0.7%. Based on these test beam measurements a local constant term of about 0.5% is implemented in MC simulations. In data an effective constant term c_{data} is extracted from the width of the Z peak:

$$c_{\text{data}} = \sqrt{2 \cdot \left(\left(\frac{\sigma}{m_Z} \right)_{\text{data}}^2 - \left(\frac{\sigma}{m_Z} \right)_{\text{MC}}^2 \right) + c_{\text{MC}}^2} \quad (7.2)$$

where c_{MC} is the constant term implemented in MC simulations. c_{data} is composed of the calorimeter's local constant term and a contribution originating from non-uniformities of the detector response.

During a dedicated study measuring the effective constant term with the first data in-situ in 2010 [6] (Table 7.1), it was found that the measured constant term was larger then expected from test beam measurements.

One of the main purposes of the uniformity study presented here is to investigate the impact of the non-uniformities of the energy response along η and ϕ on the constant term of the energy resolution. The uniformity has been studied using both the di-lepton invariant mass distribution from $Z \rightarrow e^+e^-$ events (Z peak) and the E/p ratio for electrons coming from $W^\pm \rightarrow e^\pm \nu$ events which benefits of a large number of electrons. Three characteristics, coming from both methods, need to be taken into account and will manifest themselves in the results presented in this chapter:

1. Concerning the Z peak method: since the invariant mass peak is influenced by the scales of two electrons, the non-uniformities in η and ϕ (location is determined by the electron with the higher p_T) are less pronounced than those measured with E/p of single electrons.

¹Originating from construction tolerances

Hence, the E/p method is more sensitive - usually reflected by a factor of two² in the size of the effect - than the Z peak method to localized non-uniformities in the energy response.

2. E/p in contrast is measured by two different detectors, the inner detector and the calorimeter. The results with the E/p method are a combination of effects arising from these two detectors and therefore do not necessarily agree with what is observed by the Z peak which is only measured by the calorimeter. The impact of such an effect can clearly be seen for measurements in the end-cap regions, where E/p is strongly affected by a poor track measurement quality manifesting in large fluctuations which are not related to non-uniformities of the energy measurement.
3. As the two methods provide very different numbers (Z peak at around 91 GeV and E/p ratio around one), their comparison requires normalizing these values. Consequently, for each method, the numerical output is divided by its average value of the full dataset.

The optimal granularity to measure non-uniformities of the energy response would be at the level of one cell in η and ϕ . Unfortunately data and MC simulation do not provide enough electrons for such a measurement, therefore one can only measure a uniformity with sufficient granularity in one direction (η or ϕ) by averaging the other. The goal is to combine the obtained results and to estimate its impact on the constant term. The size of the uniformity is expressed by the root mean square (RMS) of the measured energy response in a given region.

7.2.1 Comparing $Z \rightarrow e^+e^-$ and $W^\pm \rightarrow e^\pm\nu$ in narrow η Bins

In this subsection, the $Z \rightarrow e^+e^-$ and $W^\pm \rightarrow e^\pm\nu$ data samples are used to investigate the dependence of the calorimeter energy scale as a function of η with a very fine granularity.

Granularity of the Study

The uniformity in η is measured in narrow bins with the size of a cell of the second layer of the EM calorimeter ($\Delta\eta = 0.025$) while the measurement is integrated over ϕ . The obtained ratio of data over MC for both methods is closely related to the energy scale correction α (see Chapter 6). In the following, the energy scales extracted with the two methods are compared and their differences discussed.

As seen in Figure 7.1 both methods agree within the errors with each other indicating common non-uniformities with a typical size of $\pm 2\%$, as mentioned before. Both methods reveal common structures in the following areas:

- $|\eta| \sim 0.6$: an overestimation of the energy can be observed ($\sim 1\%$)
- $|\eta| \sim 1.68$: a negative α is measured with both methods ($\sim 3\%$)
- $|\eta| > 2.4$: a negative α is measured with both methods, $\sim 6\%$ for W.

²The factor of two is a consequence of Equation B.1 where two energy scales contribute to the invariant mass.

An overall non-uniformity for this narrow η binning in percentage of deviation is observed for the two cases:

- $\sim 1.1\%$ for E/p from $W \rightarrow e\nu$
- $\sim 0.7\%$ for $Z \rightarrow e^+e^-$ invariant mass

A detailed summary of all non-uniformities in η exceeding 1% are listed in Table 7.2.

$ \eta $ range	observation
0.5 – 0.7	higher energy in data mainly seen by the E/p method
1.2 – 1.3	small region with higher energy in data
1.3 – 1.37	small region with higher energy in data
1.52 – 1.55	end of crack, energy scale very different between data/MC
1.55 – 1.65	significant bump only on negative η region
1.65 – 1.75	presence of extra material in data (will be discussed in Chapter 10)
1.75 – 1.85	higher energy in data
2.0 – 2.1	higher energy in data
2.4 – 2.47	substantial decrease of energy scale (end of the end-cap/electrode). Large effect in the E/p method but unreliable fits in this forward region.

Table 7.2: A summary of structures (see Fig.7.1) observed in narrow η bins.

For calibration purposes a new binning in $|\eta|$ has been proposed. It should deal with the structures seen in both methods as well as with the HV sectors and overcome problems within the calibration along η . The new binning is :

$$\{0, 0.2, 0.4, 0.6, 0.8, 1.0, 1.2, 1.37, 1.47, 1.55, 1.63, 1.74, 1.82, 2.0, 2.1, 2.3, 2.4, 2.47\}$$

The binning is symmetrical in the negative η region and has been used for the energy scale correction (α) discussed in Chapter 6.

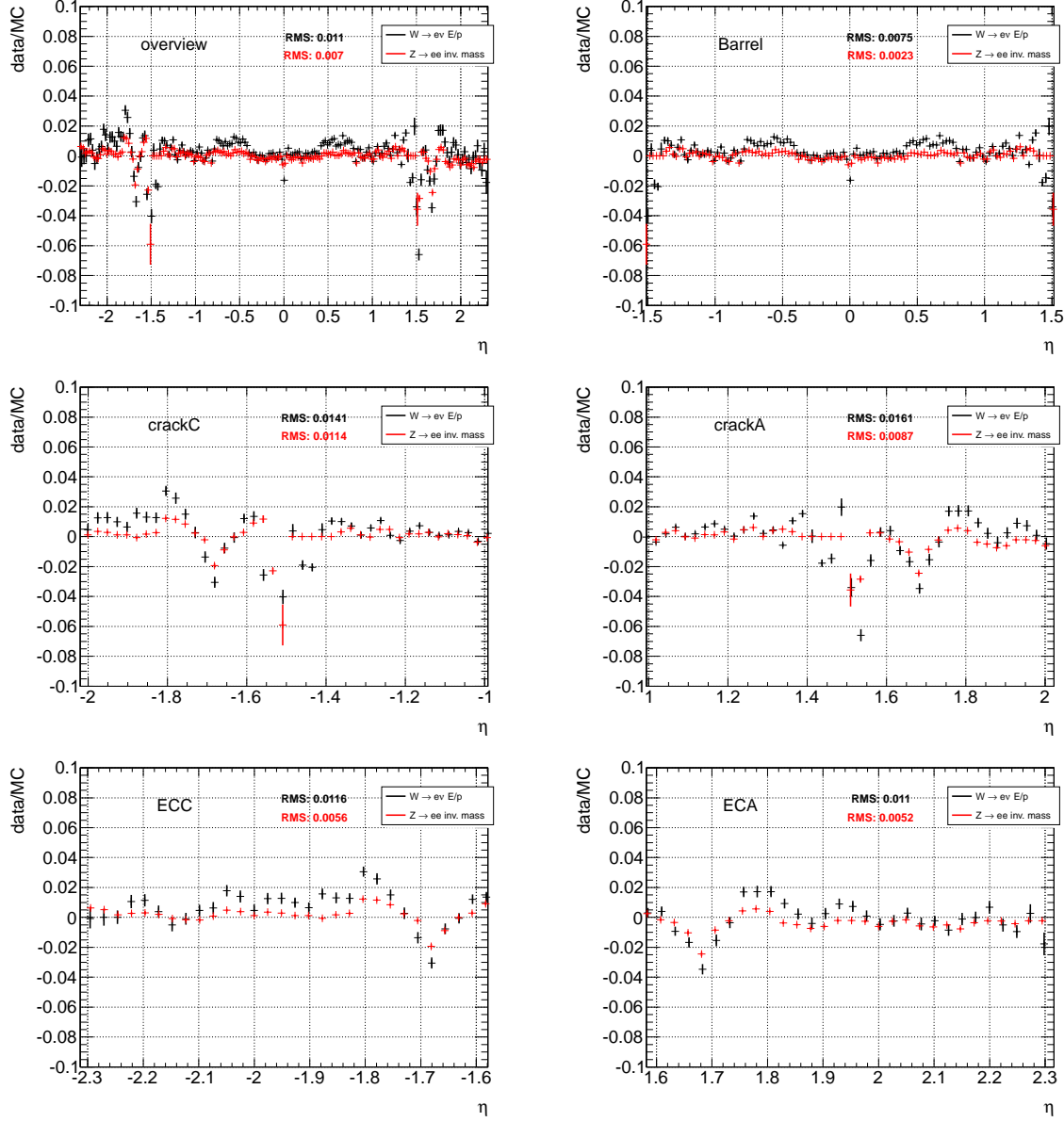


Figure 7.1: Energy scale dependence with a granularity of one cell per η bin - ϕ integrated. The overview plot is followed by five zooms in different η regions. These plots are done before applying the η dependent scale correction α as discussed in Chapter 6.

7.2.2 Comparing $Z \rightarrow e^+e^-$ and $W^\pm \rightarrow e^\pm\nu$ in narrow ϕ Bins

The energy response uniformity in ϕ has been scrutinized for both 2011 and 2012 datasets since non-uniformity along this variable is a possible explanation for the large constant term seen in data [6]. For this purpose, each dataset was binned in narrow ϕ bins of the size of a single cell of the second layer of the calorimeter ($\Delta\phi = 0.025$) and in six bins in η : [-2.4,-1.6], [-1.3,-0.8], [-0.8,0], [0,0.8], [0.8,1.3], [1.6,2.4] (excluding the transition region between barrel and end-caps).

As in the previous section, the E/p method with $W^\pm \rightarrow e^\pm\nu$ events and the $Z \rightarrow e^+e^-$ invariant mass method have been implemented in two ways: either using the normalized output of each method versus ϕ or looking at the ratio between data and MC simulation.

Results for 2011 Data

Results for the energy response uniformity in ϕ for 2011 data are shown in Figure 7.2.

The pattern of a deviation from one in the barrel with the two methods suggests that the effect is likely to the periodicity of the calorimeter modules. The electromagnetic calorimeter is divided in 16 modules in the barrel and eight modules in each end-cap. In the barrel, each module is subdivided into 16 cells of size $\Delta\phi = 0.025$. The center of the first module is located at $\phi = 0$ and its two edges at $\phi = \pm 0.2$. These plots demonstrate that each intermodule connection generates a larger liquid argon gap than anywhere else and hence reduce the energy response. This so-called Intermodule Widening effect is a limitation to the energy measurement and its correction is being provided offline for the full Run 1 dataset.

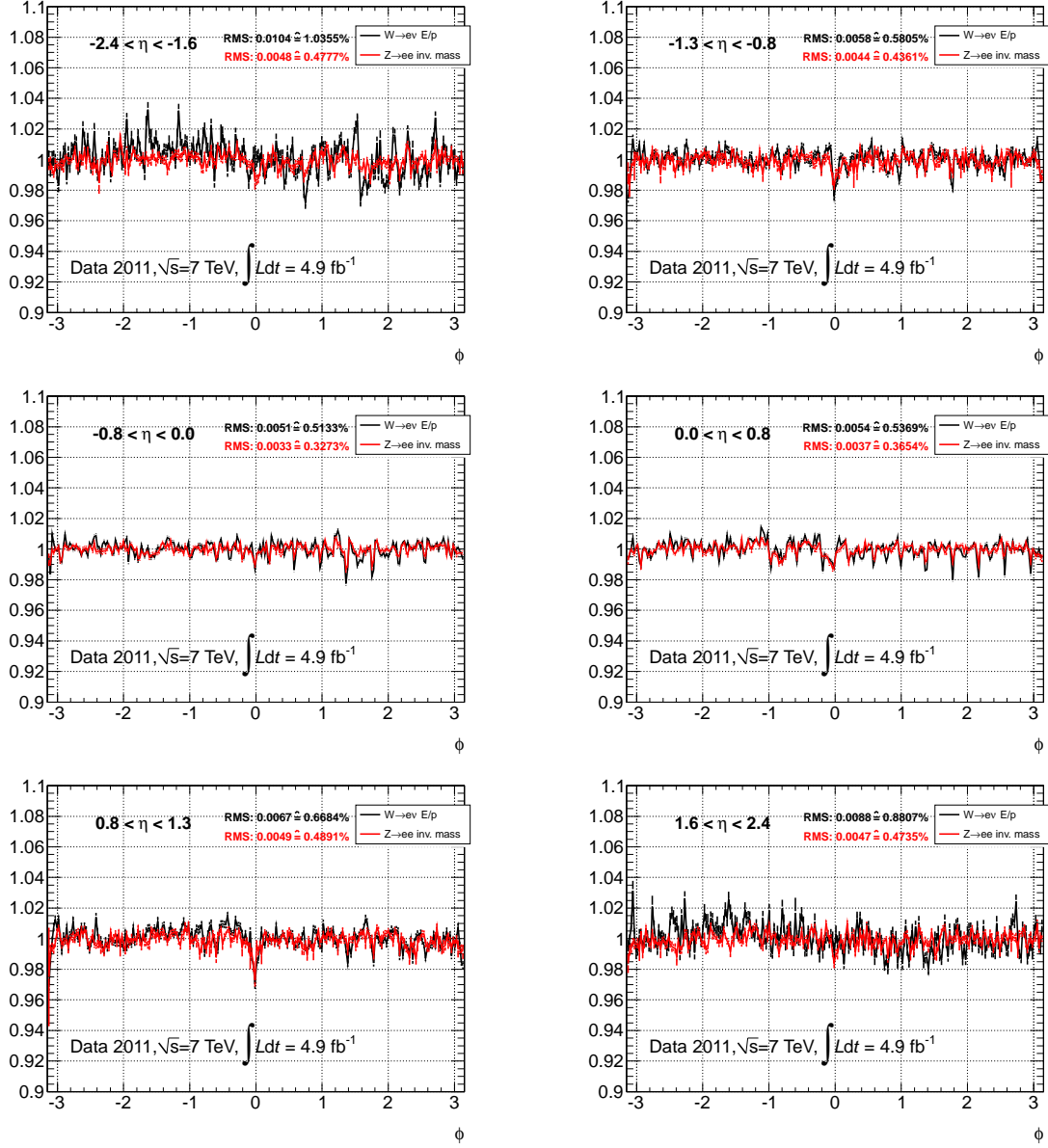


Figure 7.2: Uniformity in data in narrow ϕ bins for different η bins. Clear structures with periodicity $\Delta\phi \sim 0.4$ can be seen in the region $|\eta| < 0.8$. They correspond to the Intermodule Widening effect. A correction for this effect was developed and applied in the following.

Correcting for the Intermodule Widening Effect

A software tool has been provided and used to correct for the effect mentioned before. The correction procedure is explained in Appendix C. Applying these corrections on E/p and on the Z invariant mass, the periodical structures along ϕ become less pronounced (see Figure 7.3) and the non-uniformities decrease.

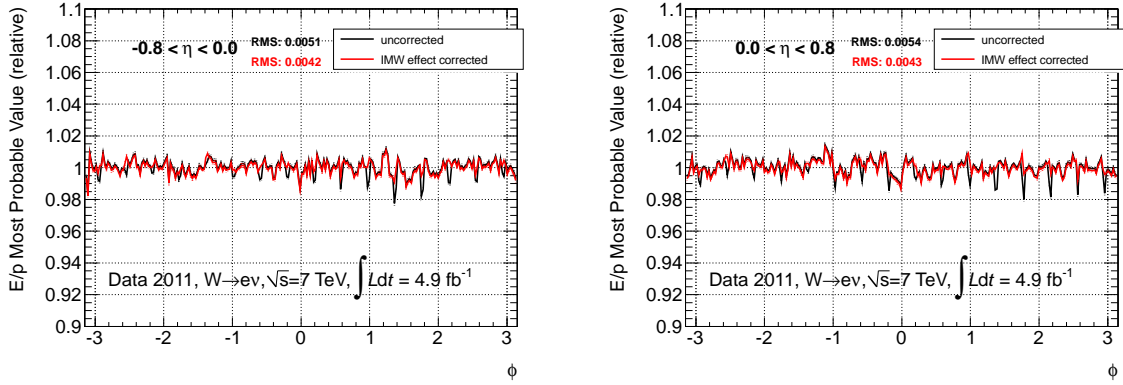


Figure 7.3: Intermodule Widening effect corrections in 2011 data showing the E/p most probable value (normalized to one) versus ϕ for $-0.8 < \eta < 0.8$ and the improvement of the RMS.

Table 7.3 summarizes the corresponding quantitative results:

method	before Correction ($0.0 < \eta < 1.3$)	after Correction ($0.0 < \eta < 1.3$)
E/p	0.51%-0.67%	0.42%-0.66%
$Z \rightarrow e^+e^-$	0.33%-0.5%	0.28%-0.48%

Table 7.3: This table shows the impact of the Intermodule Widening Effect on the ϕ -uniformity in data. The numbers are taken from Figure C.4 (in Appendix C)

The average improvement due to the Intermodule Widening effect correction is $\sim 12\%$ for the E/p case and $\sim 9\%$ for the Z invariant mass case. Again, the expected difference between E/p and the $Z \rightarrow e^+e^-$ invariant mass in the non-uniformities that can be observed, comes from the averaging effect of the second electron in the Z peak method.

To measure the constant term, as it will be presented in Section 7.2.3, the difference between data and MC in the ϕ uniformity after Intermodule Widening effect correction needs to be examined. This data/MC comparison can be seen in Figure 7.4.

A summary of the non-uniformities seen along ϕ on the data over MC ratio extracted from $Z \rightarrow e^+e^-$ invariant mass fit and from the E/p ratio with $W^\pm \rightarrow e^\pm \nu$ events after the Intermodule Widening Effect correction is given in Table 7.4.

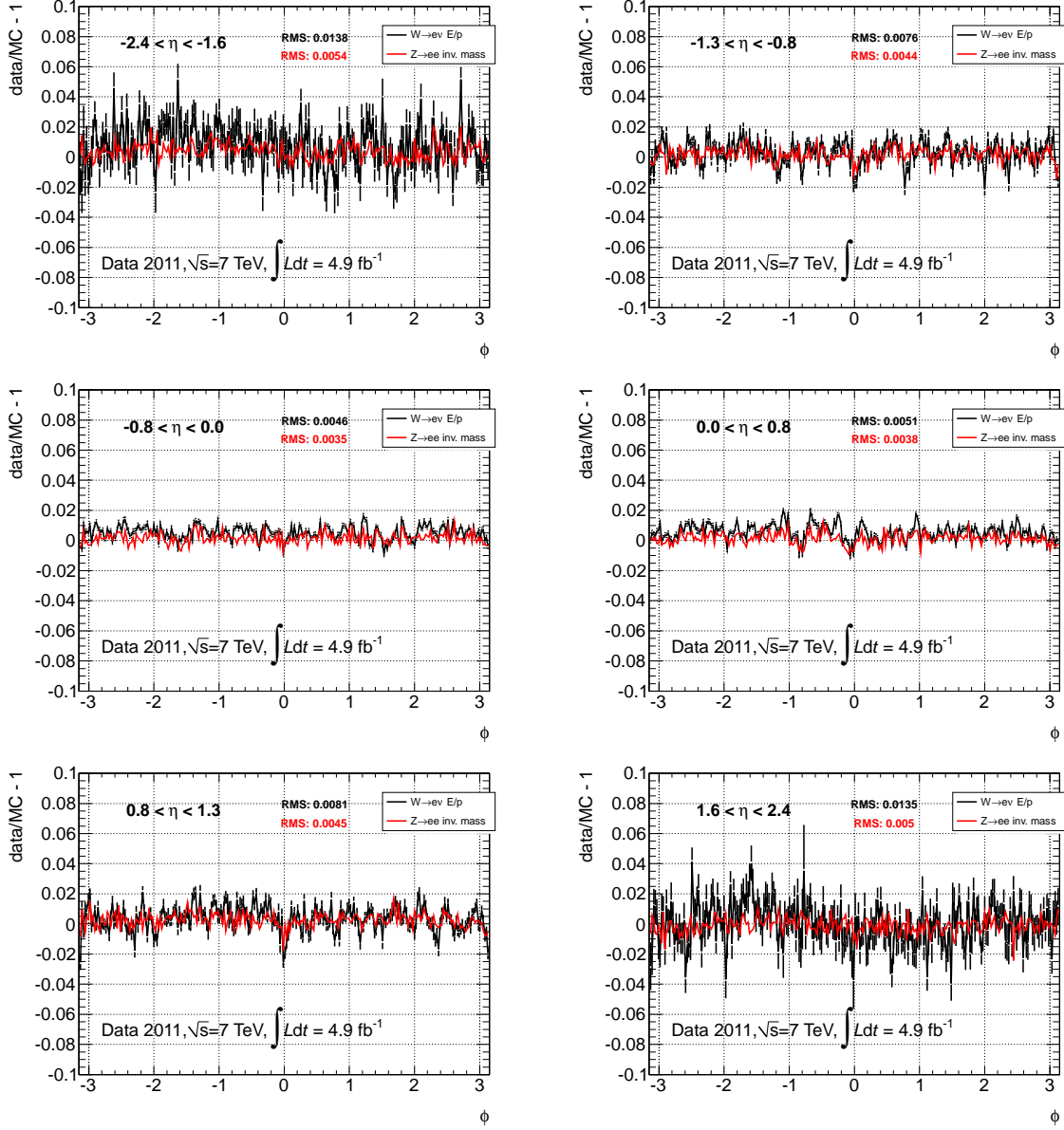


Figure 7.4: Uniformity of the data/MC ratio in narrow ϕ bins after Intermodule Widening effect correction. The quoted RMS gives an estimate on the contribution to the constant term. These results will be used to evaluate the constant term in Section 7.2.3

η range	ϕ	Observation
all η bins	$-\pi, 0, \pi$	Drop in the energy response in data coming from a wrong description of ID rails in MC (with not enough material in MC) located from $0.6 < \eta < 1.8$.
$0.0 < \eta < 0.8$	-0.8	A structure is seen - dead FEBS in third sampling of the calorimeter, are located at $(\eta, \phi) \sim (0.5, -0.8)$.
$0.8 < \eta < 1.3$	-0.9, 0.9	Oscillations seen.
$1.6 < \eta < 2.4$	along ϕ	A large oscillation is seen (periodicity $\sim 2\pi$). The scale between data and MC is larger in negative than in positive ϕ . One candidate to explain this would be a mechanical sagging effect of the electrodes and absorbers in the end-cap.

Table 7.4: *Summary of non-uniformities (as seen Figure 7.4) in data compared to MC observed in narrow ϕ bins after the Intermodule Widening effect is corrected.*

Results for 2012 Data

Due to the new GSF track reconstruction used for 2012 data, the E/p distribution changed significantly with respect to 2011, as shown in Figure 6.2. A big difference in the distribution due to the better treatment of Bremsstrahlung in the track fit can be seen.

The position of the Z peak was compared to the E/p measured points. Due to the larger number of reconstructed electrons in 2012, it was possible to use $Z \rightarrow e^+e^-$ events also for the E/p method. A comparison between the two methods can be found in Figure 7.5.

From the studies done with 2011 data (Figure 7.2) it was known that the RMS obtained from E/p is on average about twice as large as the RMS obtained with the Z peak. This is due to the fact that only the leading p_T electron is used for the spatial assignment in η and the second electron washes out the structures. In 2012 this effect is seen only for the barrel regions but in the end-caps a discrepancy between the two methods is found. This is so far not understood and currently under investigation. Nevertheless, most of the structures are shown to be the same in both years.

The obtained RMS and a comparison of the the two years can be found in Table 7.5 by taking the RMS of Figure 7.2 and Figure 7.5. These results are not corrected for the Inter Module Widening effect. The RMS values obtained with the Z peak are very similar between the two years and even improve from 2011 to 2012. A slight improvement is expected since the error bars of the individual points are reduced in 2012. The reduction comes from the much larger number of reconstructed electrons and hence a smaller statistical error. This is not observed in the results of the E/p method. The difference between the two methods is not understood yet, but it is likely that part of the effect observed with E/p is due to the track fit.

η range	2011 (E/p)	2012 (E/p)	2011 (Z peak)	2012 (Z peak)
$-2.4 < \eta < -1.6$	1.0355%	1.3485%	0.4777%	0.355%
$-1.3 < \eta < -0.8$	0.5805%	0.7914%	0.4361%	0.3143%
$-0.8 < \eta < 0.0$	0.5133%	0.5857%	0.3273%	0.2868%
$0.0 < \eta < 0.8$	0.5369%	0.6381%	0.3654%	0.3103%
$0.8 < \eta < 1.3$	0.6684%	0.8747%	0.4891%	0.3404%
$1.6 < \eta < 2.4$	0.8807%	1.3075%	0.4735%	0.3375%

Table 7.5: Summary of the RMS measured with E/p and the Z peak by comparing the 2011 (Figure 7.2) with the 2012 uniformity (Figure 7.5). An increase in the RMS of the ϕ uniformity between 2011 and 2012 measured with E/p can be observed, which is not understood at the moment. The RMS measured with the Z peak on the contrary improves between 2011 and 2012, partly due to a higher number of reconstructed electrons in the 2012 dataset w.r.t. to the 2011 dataset.

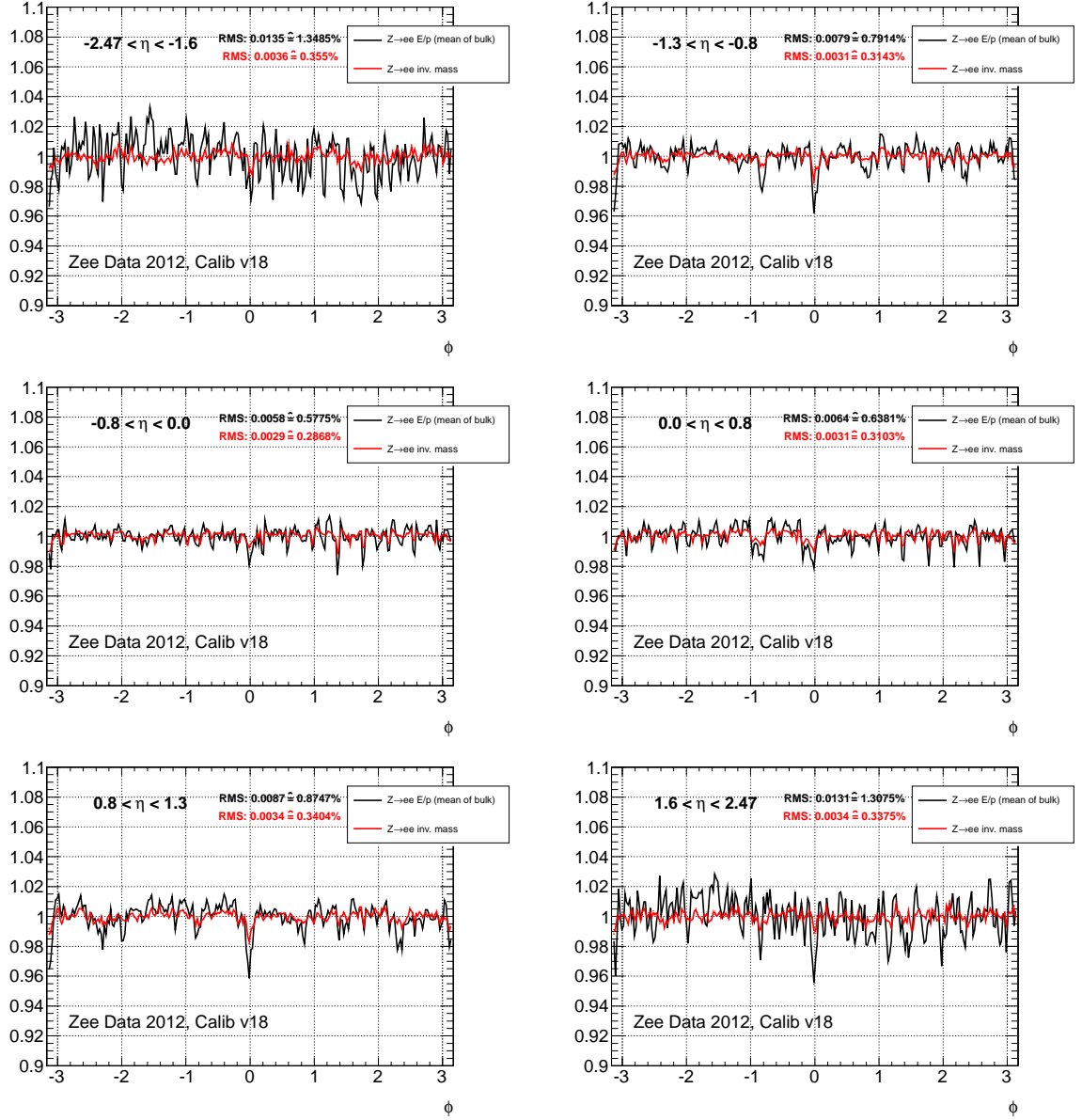


Figure 7.5: This figure compares the results obtained from the two methods, Z peak and E/p, for the 2012 dataset. The RMS of E/p is twice as large (as expected) on average w.r.t. the RMS of the Z peak in the barrel regions. In the end-caps a discrepancy between the two methods is observed and is currently under investigation.

7.2.3 Uniformity and Constant Term

The constant term (see Figure 7.6) measured with collision data was larger than expected from test beam measurements.

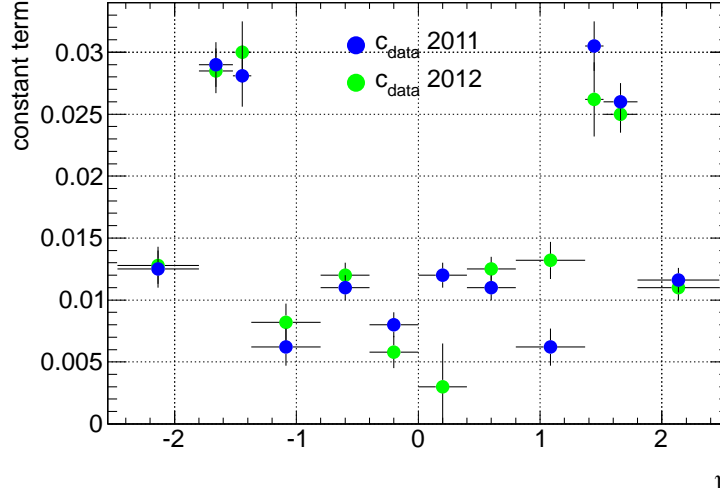


Figure 7.6: Constant term c_{data} (Equation 7.2) for the year 2011 in blue and the year 2012 in green is shown here. The results are obtained from the Z peak width for both years. One can see a difference between the two years in various regions of η but also a difference to the expected constant term from test beam results (0.7%). To investigate this difference, studies on uniformity of the energy response in η and ϕ were performed. Taken from Ref. [46].

A dedicated study will be presented here, to estimate a contribution of the non-uniformities in ϕ (and η) to the constant term. This study is a pure MC study but is based on the results from collision data obtained with the uniformity study. The measured non-uniformities (Figure 7.4) of the 2011 dataset are implemented in the MC energy reconstruction and the resolution as a function of energy (as described in Chapter 2) is calculated for different regions in η .

To further also simulate non-uniformities in η , the reconstructed energy is, on top of the ϕ non-uniformities, smeared with a Gaussian distribution using different widths: $\sigma \in [0.5\%, 1\%, 1.5\%]$.

To measure the constant term, the sample has to be divided into different energy bins (see Section 2.3.8). Here, the following binning in E_T (on top of the six bins in η as described in Section 7.2.2) is applied:

$$E_T \in [30, 32, 34, 37, 40, 43, 48, 55, 60, 70, 90, 120, 250]$$

The ratio $E_{\text{reco}}/E_{\text{truth}}$ of the reconstructed energy and the true energy, measures the impact of the detector smearing on the actual true energy used at generation level. This ratio is calculated for the different measured non-uniformities along η and E_T . Finally, it is fitted with a Gaussian function in range $\in [-1\sigma, 2.5\sigma]$. The extracted width of the Gaussian function corresponds to a σ_E/E of the resolution function (see Figure 7.7) in MC.

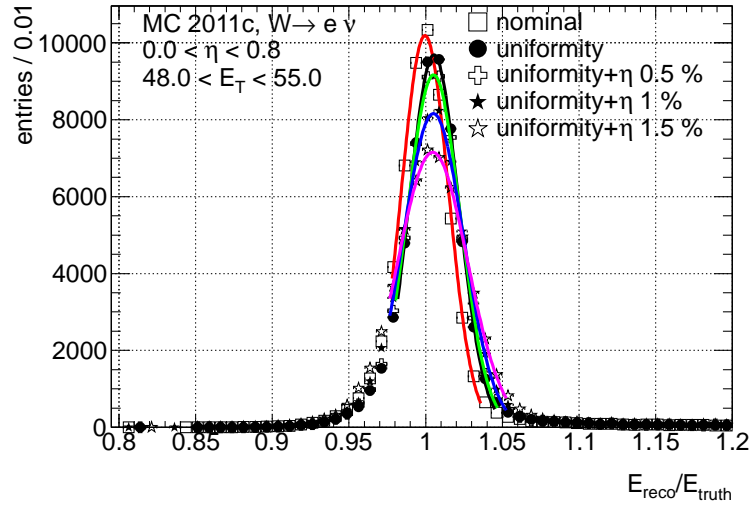


Figure 7.7: E_{reco}/E_{truth} for one bin in η for different non-uniformities in the nominal E_{reco} .

Each plot in Figure 7.8 corresponds to a specific region in η . For each region in η the resolution functions for different measured non-uniformities are shown and σ_E/E is obtained as described before from a fit to E_{reco}/E_{truth} . Each color belongs to a different variation of the reconstructed energy: red points are values obtained from nominal MC, black points correspond to the measured non-uniformity in ϕ , the other colors represent an additional non-uniformity in η . The resolution function, as described in Chapter 2, is then fitted for the different cases. The constant term is extracted from the fit.

The sampling and noise terms are obtained from nominal MC simulations and not free parameters in the fit. As expected, the constant term becomes larger with worse ϕ and η uniformity.

η range	c (nominal MC)	c (ϕ uniformity)
$-2.47 < \eta < -1.6$	-	$1.66 \cdot 10^{-2} \pm 2.88 \cdot 10^{-9}$
$-1.6 < \eta < -1.3$	-	$2.06 \cdot 10^{-2} \pm 7.26 \cdot 10^{-8}$
$-1.3 < \eta < -0.8$	$5.10 \cdot 10^{-3} \pm 1.51 \cdot 10^{-7}$	$9.72 \cdot 10^{-3} \pm 2.12 \cdot 10^{-8}$
$-0.8 < \eta < 0.0$	$5.27 \cdot 10^{-3} \pm 9.21 \cdot 10^{-8}$	$7.64 \cdot 10^{-3} \pm 7.93 \cdot 10^{-9}$
$0.0 < \eta < 0.8$	$5.34 \cdot 10^{-3} \pm 9.28 \cdot 10^{-8}$	$7.99 \cdot 10^{-3} \pm 7.27 \cdot 10^{-9}$
$0.8 < \eta < 1.3$	$5.65 \cdot 10^{-3} \pm 1.35 \cdot 10^{-7}$	$1.05 \cdot 10^{-2} \pm 2.01 \cdot 10^{-8}$
$1.3 < \eta < 1.6$	-	$2.23 \cdot 10^{-2} \pm 6.54 \cdot 10^{-8}$
$1.6 < \eta < 2.47$	-	$1.60 \cdot 10^{-2} \pm 2.87 \cdot 10^{-9}$

η range	c (ϕ uniformity, $\eta \pm 0.5\%$)	c (ϕ uniformity, $\eta \pm 1.0\%$)	c (ϕ uniformity, $\eta \pm 1.5\%$)
$-2.47 < \eta < -1.6$	$1.77 \cdot 10^{-2} \pm 2.74 \cdot 10^{-9}$	$2.06 \cdot 10^{-2} \pm 2.41 \cdot 10^{-9}$	$2.40 \cdot 10^{-2} \pm 2.61 \cdot 10^{-9}$
$-1.6 < \eta < -1.3$	$2.16 \cdot 10^{-2} \pm 6.95 \cdot 10^{-8}$	$2.46 \cdot 10^{-2} \pm 6.39 \cdot 10^{-8}$	$2.73 \cdot 10^{-2} \pm 6.03 \cdot 10^{-8}$
$-1.3 < \eta < -0.8$	$1.11 \cdot 10^{-2} \pm 2.02 \cdot 10^{-8}$	$1.48 \cdot 10^{-2} \pm 1.68 \cdot 10^{-8}$	$1.93 \cdot 10^{-2} \pm 1.67 \cdot 10^{-8}$
$-0.8 < \eta < 0.0$	$9.45 \cdot 10^{-3} \pm 6.95 \cdot 10^{-9}$	$1.36 \cdot 10^{-2} \pm 5.74 \cdot 10^{-9}$	$1.80 \cdot 10^{-2} \pm 6.54 \cdot 10^{-9}$
$0.0 < \eta < 0.8$	$9.70 \cdot 10^{-3} \pm 6.91 \cdot 10^{-9}$	$1.37 \cdot 10^{-2} \pm 5.65 \cdot 10^{-9}$	$1.80 \cdot 10^{-2} \pm 6.44 \cdot 10^{-9}$
$0.8 < \eta < 1.3$	$1.17 \cdot 10^{-2} \pm 1.89 \cdot 10^{-8}$	$1.53 \cdot 10^{-2} \pm 1.58 \cdot 10^{-8}$	$1.93 \cdot 10^{-2} \pm 1.54 \cdot 10^{-8}$
$1.3 < \eta < 1.6$	$2.19 \cdot 10^{-2} \pm 6.63 \cdot 10^{-8}$	$2.55 \cdot 10^{-2} \pm 5.80 \cdot 10^{-8}$	$2.85 \cdot 10^{-2} \pm 5.50 \cdot 10^{-8}$
$1.6 < \eta < 2.47$	$1.72 \cdot 10^{-2} \pm 2.79 \cdot 10^{-9}$	$2.03 \cdot 10^{-2} \pm 2.49 \cdot 10^{-9}$	$2.38 \cdot 10^{-2} \pm 2.65 \cdot 10^{-9}$

Table 7.6: *Extracted constant terms obtained from the fits in Figure 7.8.*

The extracted constant terms along η are summarized in Figure 7.9 and Table 7.6. Due to the kinematics of the W boson decay there is less data in higher η regions for low energies. Therefore the extraction of the constant term is not quite as accurate with the $W^\pm \rightarrow e^\pm \nu$ sample. Finer granularity in η and electrons with lower p_T (such as electrons from $J/\psi \rightarrow e^+ e^-$) would be needed for an accurate description. Nevertheless, for $|\eta| < 1.37$ the results are very stable and accurate due to the fact that an expected constant term of 0.5% in nominal MC is extracted.

The left plot in Figure 7.10 shows a fit of the different constant terms as a function of different non-uniformities with a polynomial of second degree: 0 stands for a ϕ non-uniformity only, 0.5% means a 0.5% non-uniformity in η on top of the ϕ non-uniformity etc. For each measured value of the constant term in data along η (Figure 7.6) the factor of the non-uniformity is attributed according to the value obtained by the polynomial function.

On the right plot of Figure 7.10, the η non-uniformity needed to explain the measured constant term is plotted. In the barrel region ($|\eta| < 1$), on top of the measured ϕ non-uniformity an additional η non-uniformity of about 0.5% would be needed to explain the measured constant term. Moreover, in the transition region $|\eta| \approx 1.5$ an η non-uniformity of about 1.5% would be needed. In the other regions ($|\eta| \approx 1.0$ and $|\eta| \approx 2.0$) the ϕ non-uniformity explains the measured constant term.

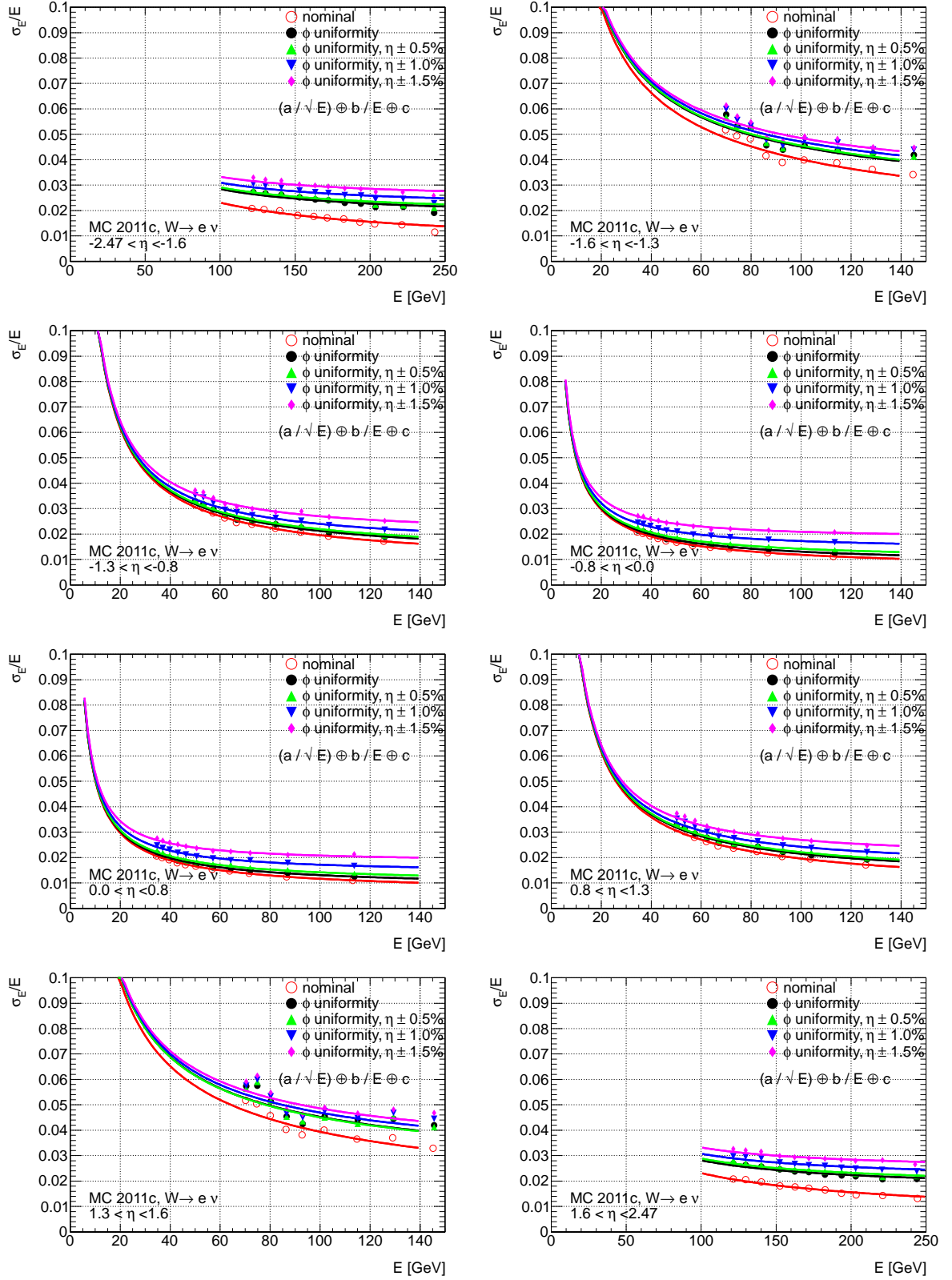


Figure 7.8: Fitting the resolution for different bins in η and extracting the constant term for different non-uniformities.

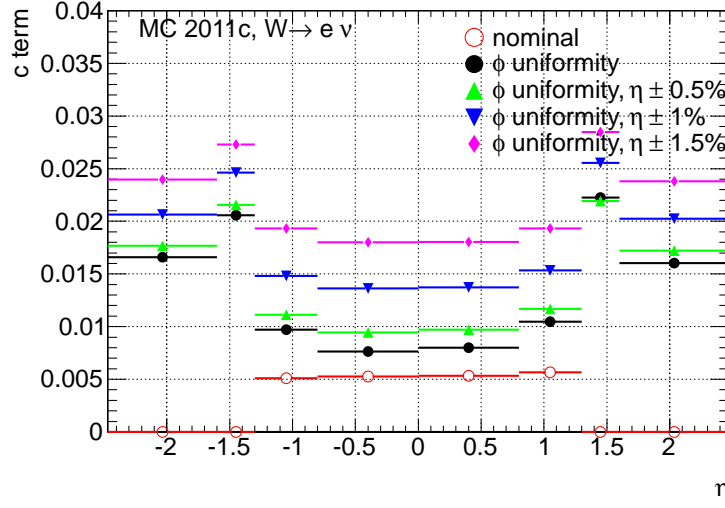


Figure 7.9: constant term for for the different injected non-uniformities along η . As expected, the constant term for nominal MC (red points) is 0.5% for $|\eta| < 1.37$. For the extraction of the constant term in nominal MC for $|\eta| > 1.37$ electrons with lower p_T would be needed for an accurate description.

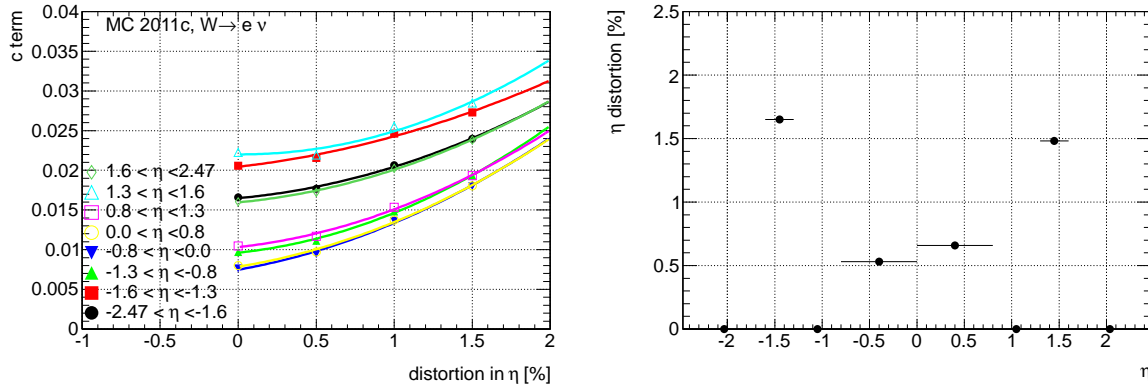


Figure 7.10: Left: constant terms for different η bins fitted with a polynomial function of a 2nd degree. Right: estimated percentage of η non-uniformity needed to explain constant term in 2011 data.

7.2.4 2D Uniformity in η and ϕ

To investigate the 2D uniformity, the energy response was calculated with E/p , normalized and compared to the normalized invariant mass of $Z \rightarrow e^+e^-$ events (see Figure 7.11).

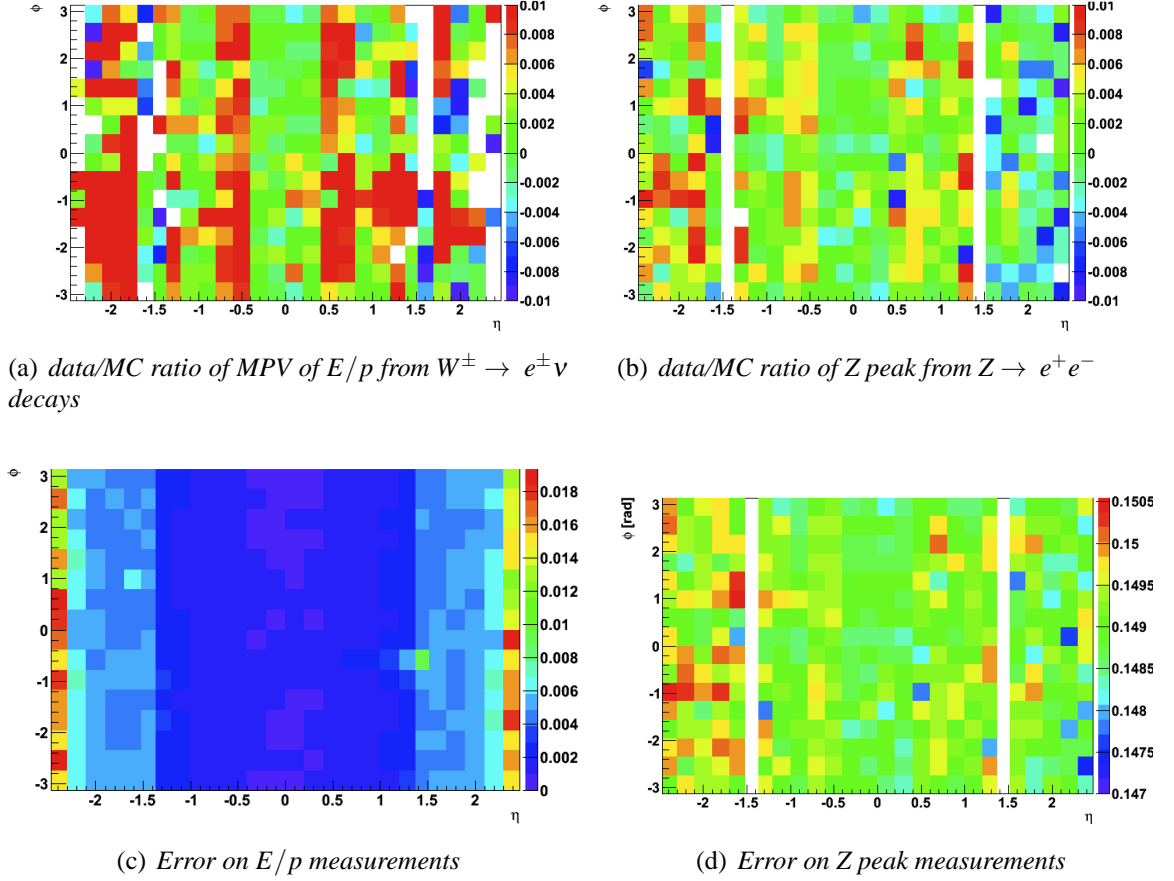


Figure 7.11: 2D uniformity extraction using the Z peak (Fig. (b)) and a Crystal Ball fit to the E/p distribution from $W^\pm \rightarrow e^\pm \nu$ decays (Fig. (a)). The color code represents the value of $(data/MC) - 1$ of both methods (in 16 η and 26 ϕ bins) as well as its error (Fig. (c) and (d))

Results for 2011 Data

The two methods are in good agreement taking into account the expected approximate factor of two. The following regions with different characteristics can be identified:

- $0.4 < |\eta|$, along ϕ good data/MC agreement for both methods
- $0.4 < |\eta| < 0.8$, along ϕ 0.8% deviations from data/MC ratio
- $0.8 < |\eta| < 1.3$, along ϕ and for positive η structures with a periodicity of $\pi/2$ can be observed. They seem to be less pronounced for negative η .
- $|\eta| > 1.57$, along ϕ : disagreement due to the larger errors on the MPV of the E/p distributions in the end-caps.

Results for 2012 Data

The normalized energy response parameter in two dimensions as an indicator for possible structures along η and ϕ is shown in Figure 7.12. Due to a larger number of electrons reconstructed in 2012 w.r.t. 2011 more bins in η were used.

Possible structures in ϕ around $|\eta| \approx 0.5; 1.5$ and $\phi : \pm \frac{\pi}{4}$ and $\pm \frac{3\pi}{4}$, can be observed. At $|\eta| = 1.7$ some material discrepancy was found and corrected after studies that focused on that region. For bins $|\eta| > 1.5$, the momentum measurement gets worse and the E/p distributions become larger. In these regions it is difficult to see a possible 2D structure using E/p .

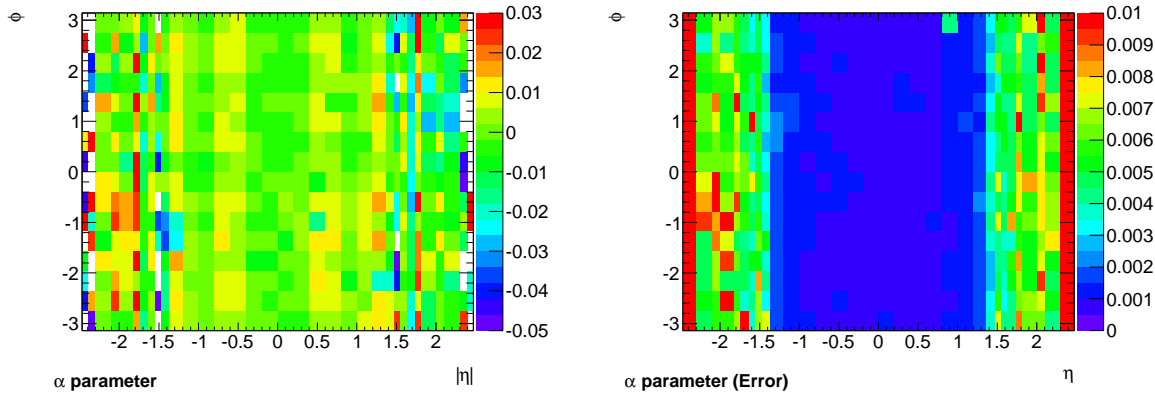


Figure 7.12: The figure on the left shows the 2012 2D uniformity of the data/MC ratio from $Z \rightarrow e^+e^-$ represented by the MPV extracted from a Crystal Ball fit to the E/p distribution. The color code represents the actual value $(\text{data/MC})-1$ for the MPV. η (x-axis) is fine binned ($\Delta \approx 0.2$) and ϕ (y-axis) in 16 bins. The error on the MPV can be found in the right plot. One can see possible structures in ϕ around $|\eta| \approx 0.5; 1.5$. As the momentum measurement gets worse in the end-caps ($|\eta| > 1.5$) the distributions become larger and the error on the MPV increases.

7.3 Stability

The stability of the EM calorimeter energy response as a function of time, the average number of interactions per bunch crossing, and the relative location in the bunch train is presented in the following. The extraordinarily high stability of the LAr EM calorimeter is an important ingredient to the physics performance of ATLAS.

7.3.1 Stability of Energy Response versus Relative Location in the Bunch Train in 2011 Data

In this subsection, the stability of the energy response with respect to the relative location of an event in the LHC bunch train structure is investigated.

The BCID (Bunch Crossing ID) variable indicates which LHC bunch collided to produce the considered electron candidate. A LHC cycle consists of 3564 bunch crossings, each uniquely identified by a BCID number, which are grouped together in so-called trains. The structure of the LHC beams necessitates an extra variable to study the energy response of the calorimeter. For the calorimetric energy response the relative position inside a train counts. The events from the first bunches do not receive the same out-of-time pile-up contributions than the later ones. Their in-time pile-up contribution is therefore not cancelled as is the case for later bunches in the train. The LAr pulse of about 500 ns is sampled every 25 ns (five samples in total) while the collisions occur every 50 ns. This means that each point of the LAr pulse receives an average contribution of several preceding collisions that cancel the in-time pile-up due to the zero integral over the pulse shape (see Chapter 2).

Figure 7.13 shows the energy response as a function of the position in the LHC bunch train. The red band corresponds to a large gap of 36 BCIDs (1800 ns). One sees that six trains have the the same sub-structure: they are composed of four sub-trains, separated by time intervals of eight BCIDs, corresponding to 400 ns. This clearly appears on the right plot, where these six trains are overlaid in order to increase the number of electrons per bin. The time interval of eight BCIDs is represented by a blue band. The rising of the $Z \rightarrow e^+e^-$ invariant mass (represented by the mean of the invariant mass of the two electrons) at each beginning of a new sub-train is clearly visible.

Due to this long gap of 36 BCIDs without any collision, the compensation for the integral of the LAr pulse shape is not complete, and more particularly the negative part of late events is not contributing anymore. Therefore there is an overestimation of the energy present for these early bunches in a train. This is the same for the small gaps, but with less impact on the energy. This plot also shows that this effect is properly described by the simulation which is used in the calibration procedure. In the offline reconstruction this baseline shift is corrected.

The FBX variable provides the bunch position within a train. More precisely, it counts the number of filled bunches before a given BCID, in a time range of 600 ns. Figure 7.14 (left) shows the dependence of the $Z \rightarrow e^+e^-$ invariant mass versus FBX showing that the energy

is larger for small FBX, due to a smaller negative contribution from the previous bunches. Figure 7.14 (right) shows the correction of the baseline shift for early bunches.

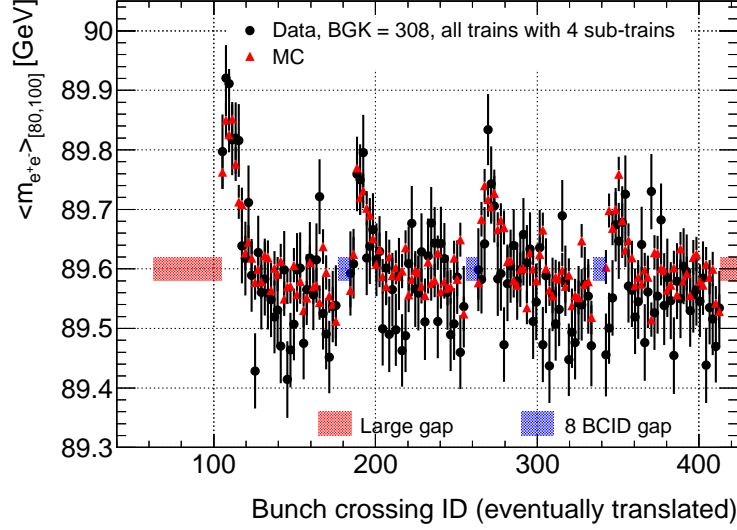


Figure 7.13: *Data-MC comparison of the $Z \rightarrow e^+e^-$ invariant mass (mean of the invariant mass of the two electrons) after overlaying six trains which have the same structure (in order to increase the number of reconstructed electrons). The mass rises at each beginning of a train or a sub-train, due to an incomplete compensation of the LAr ionisation pulse.*

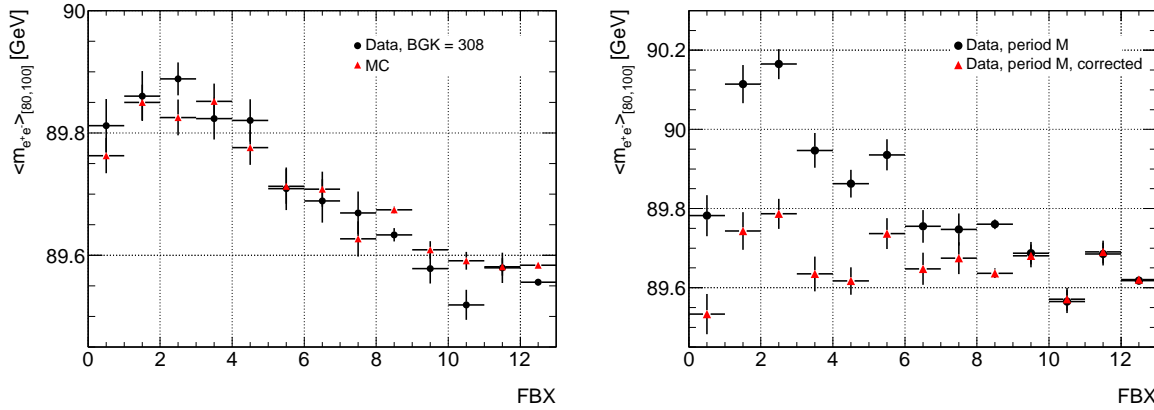


Figure 7.14: *The left figure represents the $Z \rightarrow e^+e^-$ invariant mass (mean of the invariant mass of the two electrons) as a function of FBX. The same feature is observed as in Figure 7.13: the mass rises for small FBX, which corresponds to the beginning of the trains. On the right side, the $Z \rightarrow e^+e^-$ invariant mass dependence with FBX is compared before and after the correction based on the prediction of the additional energy due to out-of-time pile-up.*

Figure 7.15 presents the final result for the stability of E/p and $Z \rightarrow e^+e^-$ invariant mass with respect to BCID for 4.9 fb^{-1} of 2011 data. As for the uniformity study, the results of the two methods (Z mass at around and E/p ratio around one) need to be normalized to their average

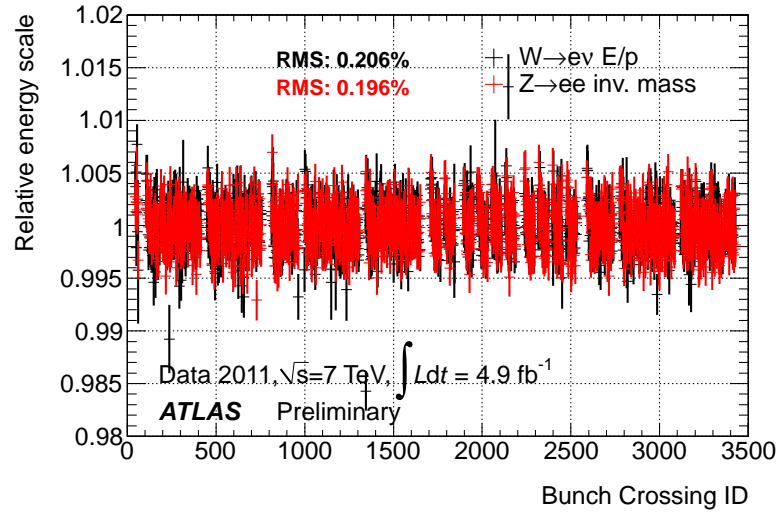


Figure 7.15: $Z \rightarrow e^+e^-$ invariant mass peak as well as the E/p MPV for $W^\pm \rightarrow e^\pm \nu$ events, normalized to their average value, as a function of BCID.

value to make them comparable.

The two methods are in good agreement and the instability versus this variable is not larger than 0.2%. For the 2011 dataset no correction of the energy due to the position in the bunch train was used. For the 2012 dataset a correction, based on the results of this analysis, is performed to remove the remaining BCID dependence. It uses the knowledge of the luminosity per FBX, and on the measured dependence with out-of-time pile-up. This correction is already applied at reconstruction level.

7.3.2 Stability of Energy Response versus Time and Pile-up

Using the two methods described in Section 7.2, the energy peak estimator is shown as a function of time and $\langle \mu \rangle$, the average number of interactions per bunch crossing (pile-up). In order to compare results for both methods, the different plots are normalized to their average value. The normalized relative energy scale versus time and pile-up is presented in Figure 7.16 for the 2011 and 2012 datasets. Within errors, the two methods agree well with each other and the obtained results show that the calorimeter energy scale is stable at the level of $\pm 0.03\%$. This exceptionally good result shows the impressive stability of the LAr calorimeter even in a harsh environment provided by the LHC. Equally impressive is the measured stability as a function of pile-up (RMS of 0.01%) for a wide range of pile-up (10-30 interactions per bunch crossing). It proves the efficient cancellation of the in-time pile-up by the out-of-time pile-up (negative tails of preceding signals).

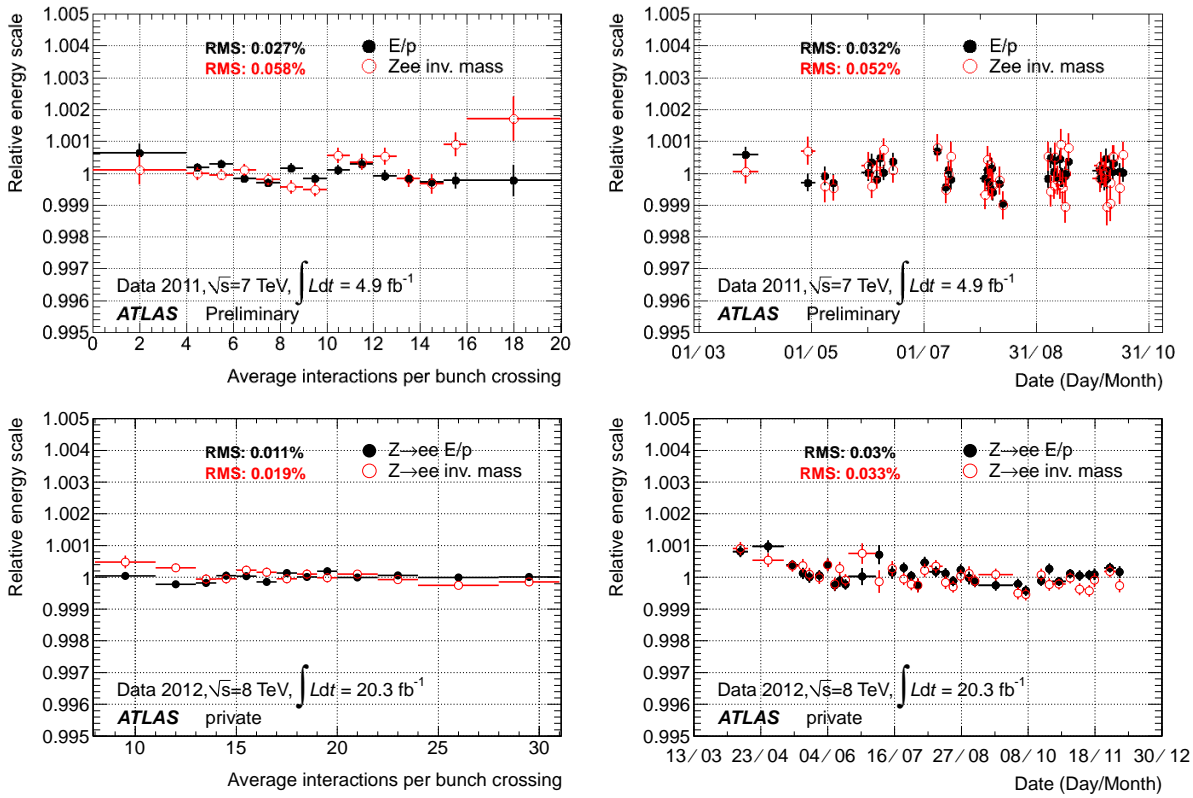


Figure 7.16: First and second row show quantities extracted respectively using the 2011 and 2012 datasets. The plots on the left present both the normalized $Z \rightarrow e^+e^-$ mass peak value and the normalised E/p MPV extracted from $W^\pm \rightarrow e^\pm \nu$ decays as functions of $\langle \mu \rangle$. The plots on the right show the same quantities as a function of time. Each point represents a recorded amount of data of around 100 pb^{-1} . Quoted RMS are the sum of statistical fluctuations and time (or $\langle \mu \rangle$) dependence, providing an upper bound on the energy response stability with time (or $\langle \mu \rangle$).

Figure 7.17 presents the electron energy response versus the number of primary vertices measured with the MPV of E/p extracted from $W^\pm \rightarrow e^\pm \nu$ with 13 fb^{-1} of integrated luminosity

of the 2012 dataset. As mentioned in Section 3.4.1, the average number of primary vertices in 2012 is a factor of about three larger than in 2011. An increase of the electromagnetic energy scale with the number of primary vertices can be observed since the in-time pile-up of the current bunch crossing is increasingly less compensated by the out-of-time pile-up produced by the preceding bunches. This increase of the electromagnetic energy scale with the number of primary vertices is due to the fact that the number of actual primary vertices has a “poisson-like” distribution and high numbers of primary vertices in one bunch crossing are usually above the average number of bunch crossings at that specific luminosity (the out-of-time pile-up is dictated by the average, however). The lower plot shows the data/MC ratio and proves that the increase of the energy scale with the number of primary vertices is very well described by the MC simulation (again on the sub-per-mill level).

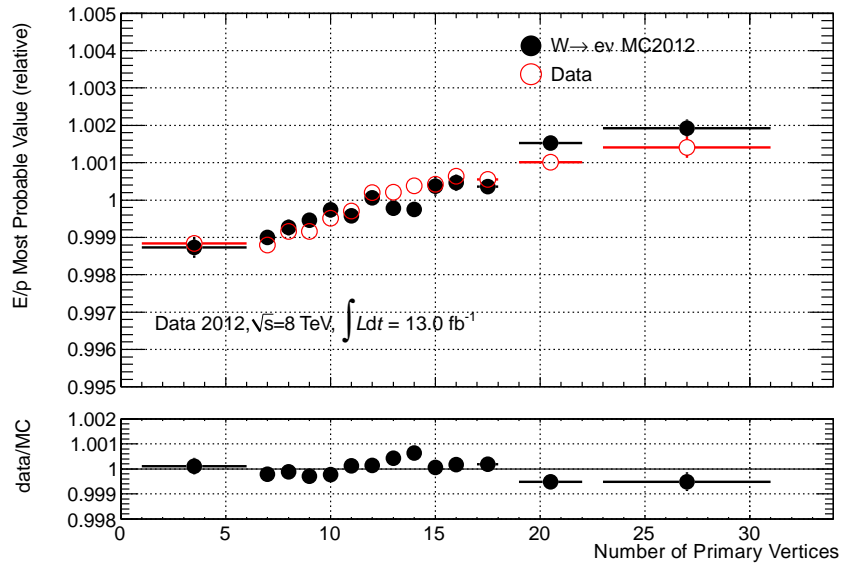


Figure 7.17: MPV extracted from E/p for electrons coming from $W^\pm \rightarrow e^\pm \nu$ decays versus the number of primary vertices in 2012 data (red points) compared to MC simulations (black points).

7.4 Summary

In the following section the summary for 2011 stability and uniformity measurements are given. Since the results for the 2012 uniformity measurements do not change only their difference (if present) is stated.

Table 7.7 summarizes the time dependence of the energy response, the stability against pile-up ($\langle \mu \rangle$ and number of primary vertices (NPV)), and the performance of the energy response as a function of the position in the LHC bunch train (BCID).

	data 2011		data 2012		data/MC (2012)
	E/p	Z peak	E/p	Z peak	E/p
BCID	0.206	0.196	N.A.	N.A.	N.A.
Time	0.032	0.053	0.03	0.033	N.A.
$\langle \mu \rangle$	0.027	0.058	0.011	0.019	N.A.
NPV	N.A.	N.A.	N.A.	N.A.	0.032

Table 7.7: *Summary table of stability measurements of the energy response as a function of BCID, time, pile-up and number of primary vertices. Results are given in percents.*

Table 7.8 and Figure 7.18 summarize the azimuthal uniformity in data given by the RMS of the energy response between the 16 calorimeter modules as a function of η . An agreement within the error bars between the two methods can be seen taking into account the expected factor of two. This factor two comes from the assumption that the second electron of the Z peak is evenly distributed in η .

For the barrel region ($\eta < 1.37$) the RMS is below 0.5% which is in agreement with the measured RMS in coarse η bins and fine bins in ϕ ($\sim 0.57\%$). The difference of about 0.07% comes from the fact that local non-uniformities in calorimeter cells are averaged, since the RMS is measured between calorimeter modules and not per cell in ϕ . The best results would be obtained from a measurement per cell in η and ϕ (or at least fine regions). This is not possible because a larger number of reconstructed electrons would be needed to obtain reliable fits (for both fitting methods, E/p and Z peak).

For the end-cap regions ($\eta > 1.52$) the error on the E/p measurement becomes larger due to a poor ID resolution. This worsens the E/p MPV and also increases the spread in ϕ , hence an artificially worse uniformity. An azimuthal uniformity of about 0.8% - 1% is assumed.

Since in most of the η -bins the ϕ -uniformity is at the 0.5% level (with some exceptions), which is acceptable for the present physics program, it was decided to perform the energy scale calibration of the electromagnetic calorimeter with the 1D (only η dependent) energy scale correction. The binning is dictated by the features observed here, as well as by the hardware and high-voltage structure of the calorimeter, namely:

$$\{0, 0.2, 0.4, 0.6, 0.8, 1.0, 1.2, 1.37, 1.47, 1.55, 1.63, 1.74, 1.82, 2.0, 2.1, 2.3, 2.4, 2.47\}$$

The binning is symmetrical in the negative η region.

η range	$RMS(E/p)$	$\langle \delta(E/p) \rangle$	$RMS(M_{ee})$	$\langle \delta(M_{ee}) \rangle$
$-2.47 < \eta < -2.3$	2.32	1.56	0.45	0.21
$-2.3 < \eta < -2.1$	0.90	0.61	0.23	0.17
$-2.1 < \eta < -1.9$	0.53	0.49	0.25	0.16
$-1.9 < \eta < -1.7$	0.81	0.49	0.28	0.15
$-1.7 < \eta < -1.52$	0.58	0.48	0.32	0.18
$-1.52 < \eta < -1.37$	1.06	0.49	-	-
$-1.37 < \eta < -1.2$	0.64	0.27	0.45	0.14
$-1.2 < \eta < -1.0$	0.24	0.19	0.21	0.12
$-1.0 < \eta < -0.8$	0.30	0.15	0.16	0.12
$-0.8 < \eta < -0.6$	0.21	0.12	0.14	0.11
$-0.6 < \eta < -0.4$	0.22	0.10	0.13	0.11
$-0.4 < \eta < -0.2$	0.16	0.09	0.11	0.11
$-0.2 < \eta < 0.0$	0.18	0.09	0.12	0.11
$0.0 < \eta < 0.2$	0.32	0.09	0.18	0.11
$0.2 < \eta < 0.4$	0.24	0.10	0.14	0.11
$0.4 < \eta < 0.6$	0.35	0.11	0.38	0.11
$0.6 < \eta < 0.8$	0.37	0.12	0.24	0.11
$0.8 < \eta < 1.0$	0.33	0.16	0.20	0.12
$1.0 < \eta < 1.2$	0.38	0.20	0.19	0.12
$1.2 < \eta < 1.37$	0.52	0.28	0.41	0.14
$1.37 < \eta < 1.52$	0.92	0.49	-	-
$1.52 < \eta < 1.7$	0.67	0.47	0.36	0.18
$1.7 < \eta < 1.9$	0.89	0.48	0.23	0.15
$1.9 < \eta < 2.1$	0.57	0.51	0.24	0.16
$2.1 < \eta < 2.3$	0.79	0.61	0.27	0.17
$2.3 < \eta < 2.47$	2.18	1.48	0.43	0.21

Table 7.8: Uniformity in ϕ versus η . For each η bin, the RMS along ϕ and the average error for all methods is quoted. Results are given in percents.

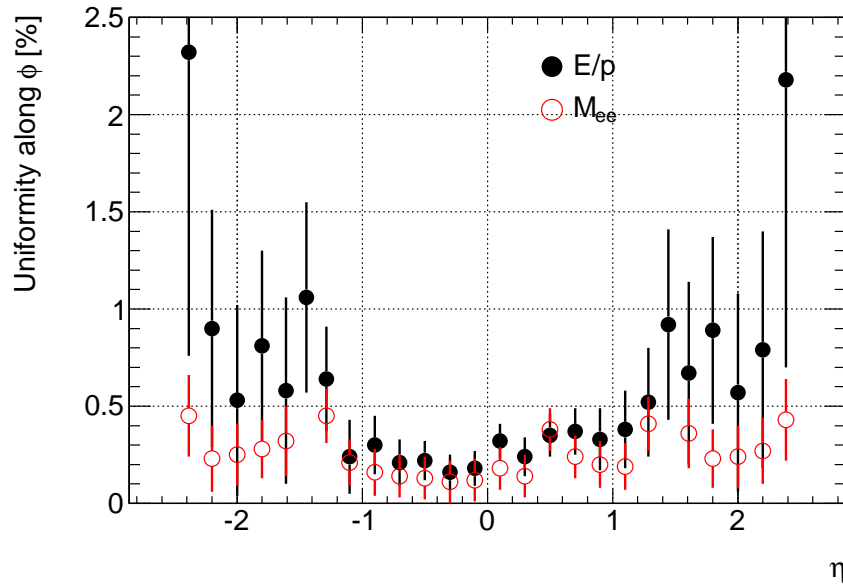


Figure 7.18: Uniformity along ϕ in different η bins visualizing Table 7.8. E/p results are given by the black points. The results of the Z peak method are in red.

Chapter 8

Linearity of Energy Response

8.1 Overview

A competitive measurement of the W boson mass is one of the most challenging physics goals of ATLAS. In order to achieve this goal, the energy scale of the electrons coming from W decays must be known with a precision of 10^{-4} . This very ambitious goal can be achieved when exploiting the full potential of the energy calibration using the decay of the Z boson. Its mass is known with a precision of $2 \cdot 10^{-5}$ and hence can be used to calibrate with the necessary accuracy. Since the p_T distribution of electrons from Z decays differs from those of W decays, the energy calibration must be extrapolated to different energies. The linearity of the calorimeter response is therefore of utmost importance.

This section describes the linearity of the calorimeter response measured with three independent methods

- using E/p for electrons from $W^\pm \rightarrow e^\pm \nu$:
 - Convolution Model
 - Crystal Ball Fits
 - Template Fits ¹
- $Z \rightarrow e^+ e^-$: energy scale extraction for different energy bins using the method explained in Appendix B

The linearity is expressed as an energy-dependent α parameter, following the usual convention:

$$\alpha(E_T) = \frac{E_{\text{DATA}}}{E_{\text{MC}}} - 1 \Big|_{E_T} \quad (8.1)$$

The energy scale extraction follows closely the methods described in Sections 5 and 6. The Monte Carlo samples used, are from the MC11c reprocessing produced in PYTHIA. The data used are from the full 2011 data set and contain a total integrated luminosity of 4.9 fb^{-1} and a

¹Different templates for E/p are generated based on the MC distributions. MC templates are applied to the data distribution and the best template in terms of χ^2 is used to estimate the scale correction α

total integrated luminosity of 12 fb^{-1} for the 2012 measurements. Periods and production tags are given in Appendix D.

Five bins in η and four in E_T were defined for the linearity measurement. The bins are defined in Table D.7. The larger binning in η gives a higher number of electrons per bin, which allows greater stability in the fits. The binning in E_T was chosen such that each bin contains approximately the same number of reconstructed electrons.

$ \eta $ boundaries	[0.0, 0.6, 1., 1.37, 1.82, 2.4]
E_T boundaries GeV	[25, 32, 40, 50, 100]

Table 8.1: Bin definition for Linearity measurement

8.2 Results

When plotting the scale correction α extracted for different bins in E_T as a function of energy, one can see that a significant non-linearity is observed in all η bins, with its magnitude depending on pseudorapidity. The order of the effect is reproduced by four different measurements using the methods mentioned above. Results for 2011 data are displayed in Figure 8.1. A non-linearity of a few per mill over different η ranges can be observed independent of the applied methods. In most η bins the 4 presented methods agree very well, larger discrepancies between the E/p and the Z peak methods for $1.0 < |\eta| < 1.37$ are however not understood.

For 2012 two results were obtained using E/p , namely measurements with the Convolution Model and Crystal Ball Fits. A summary and overlay with the 2011 linearity can be seen in Figure 8.2. The observed non-linearity of a few per mill over different η ranges is consistent for the 2011 and 2012 datasets.

This result is not expected, even though its amplitude is small and therefore its effect on the energy scale for e.g. Higgs boson searches and Higgs mass measurement was well covered in the used systematic errors. However, a full understanding of the case of those non-linearities and a way to correct for them would allow for a significant reduction of the systematic error and would lead to a more precise Higgs mass measurement.

To find the origin of the non-linearity shown in Figure 8.2 several investigations were performed and will be described in chapters 9 and 11. Different effects can lead to such a non-linearity, such as a miscalibration of calorimeter layer scales (Presampler and E_1, E_2 scales), passive material and lateral leakage. These effects will be studied in detail in the following chapters.

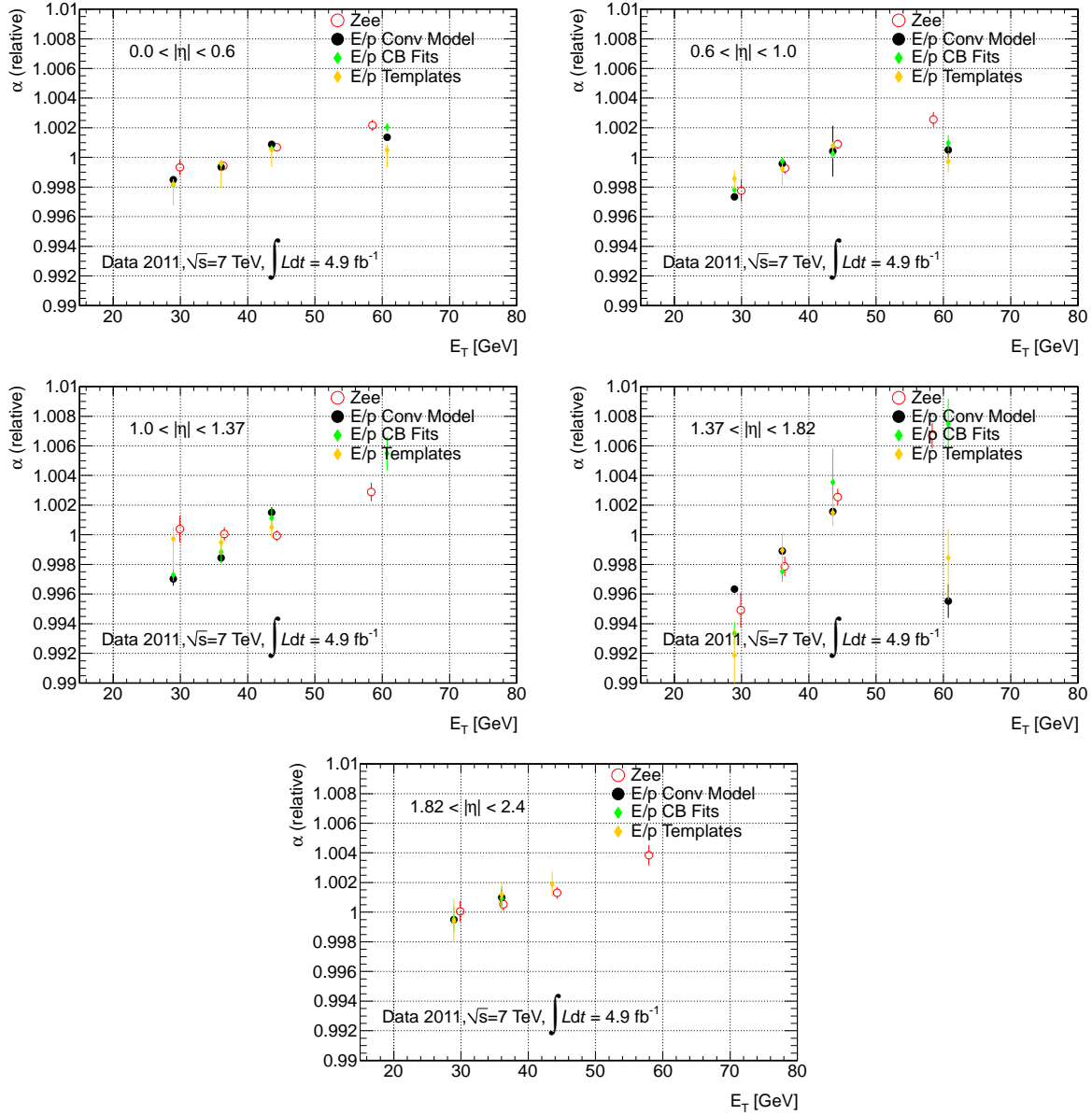


Figure 8.1: Measured linearity from E/p and $Z \rightarrow e^+e^-$ for the 2011 dataset. A non-linearity of a few per mill over the full η range can be observed. The different results are aligned such that the bin $E_T = 40[\text{GeV}]$ sits at 1. Only statistical errors are shown.

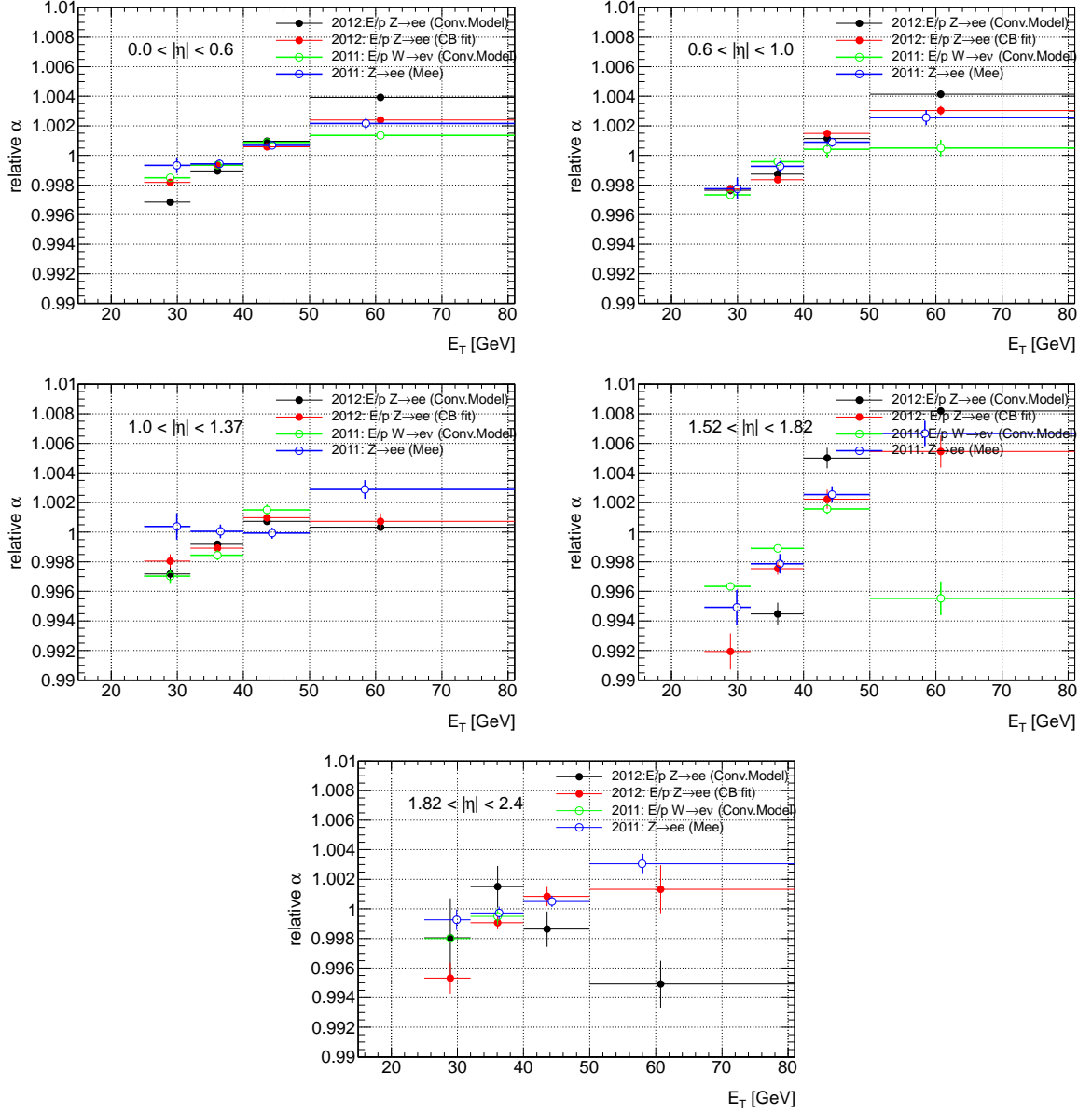


Figure 8.2: Measured linearity from E/p and $Z \rightarrow e^+e^-$ comparing the 2011 (open points) and 2012 (closed points) results. For 2011 the Convolution Model results are shown (green open points) and the results from the Z peak (blue open markers). For 2012 measurements coming from the two E/p methods, namely Convolution Model (black closed points) and Crystal Ball Fits (red closed points). The different graphs are aligned such that the value for $E_T = 40[\text{GeV}]$ is set to one. Only statistical errors are shown.

Chapter 9

Lateral Leakage

9.1 Overview

As already explained in Chapter 4, the energy of an electron is reconstructed based on the energy in cells in a cluster of 3×7 ($\eta \times \phi$) calorimeter cells (in the middle sampling) for $|\eta| < 1.52$ and 5×5 cells for $|\eta| > 1.52$ and the adjacent cells in the Presampler, strips and back layer. The lateral leakage (in η and ϕ) is the energy deposit in the EM calorimeter outside the cluster used for reconstruction. During the cluster calibration, the energy lost outside the cluster is being corrected based on the estimation of lateral leakage in MC. In the following a possible difference of the lateral leakage between data and MC coming from underestimated shower width in the MC is investigated. To estimate the lateral leakage, isolation cones are studied. For each reconstructed electron cones of different radii summing up the energy deposit within this cone are available (with the exception of the central 5×7 cells). The differences in MC and data using electron isolation cones information for different pile-up and η scenarios are studied.

9.2 Method description

Isolation cones are sums of cell energies around a given cell with

$$R^2 \leq \Delta\eta^2 + \Delta\phi^2, R \text{ being the cone radius.}$$

The central region of the cone ($\Delta\eta \times \Delta\phi = 5 \times 7$ cells)¹ is not added to the sum. In this way the cone contains the energy deposit around the cluster. Different cone sizes exist (see Table 9.2). This is done separately for MC and data in five bins of "Average Interaction Per Bunch Crossing" ($\langle \mu \rangle$) (see Table 9.1 and Figure 9.1) (and bins in E_T).

averageIntPerXing 2011 ($\langle \mu \rangle$)	[0,6,8,11,13,20]
averageIntPerXing 2012 ($\langle \mu \rangle$)	[0,18,27,32,36]

Table 9.1: *Binning in Average Interaction Per Bunch Crossing* ($\langle \mu \rangle$)

¹The size of one calorimeter cell in ϕ is 0.025 and for η $\frac{\pi}{128}$

Subsequently, the mean of MC is subtracted from its equivalent of data. Furthermore this " δ " in energy is calculated for each bin in $\langle \mu \rangle$ for different cone sizes (see Figure 9.2). For each $\langle \mu \rangle$ bin the points are plotted as a function of the cone area:

$$R^2 * \pi - 5 * 0.025 \times 7 * \frac{\pi}{128}$$

and linearly fitted. Whereas the slope of the fits can be interpreted as a data-MC difference of the pile-up contribution of the cells in the cone area, the offset (at cone-area = 0) is independent of pile-up and can be interpreted as the difference of the amount of *lateral leakage* between data and MC (see Figure 9.3).

For each bin in η the following factor is calculated:

$$\delta_{\text{cone}}^{\langle \mu \rangle} = \langle \text{data} \rangle_{\text{cone}}^{\langle \mu \rangle} - \langle \text{MC} \rangle_{\text{cone}}^{\langle \mu \rangle} \quad (9.1)$$

This study uses non calibrated electrons, particle identification: *tight* ++. The data used are from the full 2011 data set and contain a total integrated luminosity of 4.9 fb^{-1} and 12.0 fb^{-1} of the 2012 dataset.

9.3 Numbers of Bunches in Front - Out of Time Pile-Up

The read-out of the electromagnetic calorimeter is built in a way that in-time pile-up contributions are largely cancelled out by the out-of-time pile-up of preceding bunches. It is therefore necessary to take the out-of-time pile-up into account. In order to be sure that the in-time-pile-up is correctly balanced by the out-of-time pile-up from the preceding bunches, a cut on *FBX* is used, which reflects the position of each event in a LHC bunch train. The *D3PDBunchCrossingToolSA* tool was used to calculate *FBX* for each event.

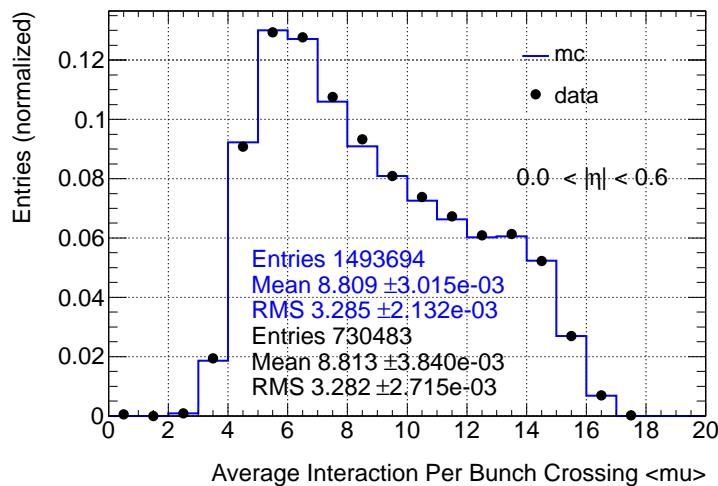


Figure 9.1: The good agreement between MC and data of the distribution of average interactions per bunch crossing ($\langle \mu \rangle$) after pile-up reweighting. The binning chosen can be found in Table 9.1.

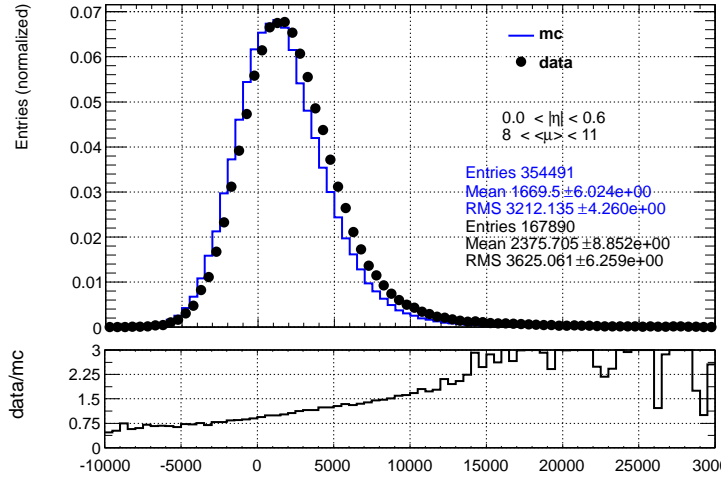


Figure 9.2: Energy distribution in an isolation cone, i.e. $el_etcone40$ (for MC and data), in the central barrel region $0.0 < |\eta| < 0.6$ and with an average interaction per bunch crossing $8 < \langle \mu \rangle < 11$ in the events. A larger energy deposit in the data sample can be seen, hence a significant data-MC disagreement is evident.

cone variable	number of cells (rounded, 5×7 subtracted)	area (5×7 subtracted)	R
$el_Etcone15$	80	0.0488	0.15
$el_Etcone20$	170	0.1038	0.2
$el_Etcone25$	285	0.1745	0.25
$el_Etcone30$	426	0.2609	0.3
$el_Etcone35$	593	0.3629	0.35
$el_Etcone40$	785	0.4808	0.4

Table 9.2: Cone variables used to estimate the leakage. For the effective cone size 5×7 cells need to be subtracted from the original, since they are not taken into account for the cone energy reconstruction. The area is calculated as follows: 1 cell = $0.025 \times \pi / 128$ in $\eta \times \phi$

After 600 ns inside a bunch train (12 filled bunches preceding), all bunches are considered equivalent. Plotting FBX vs a profile of the mass, one clearly can see the effect of the in-time pile-up that is insufficiently balanced by the out of time pile-up for early bunches in the train and hence shifting the measured values up (was already shown in Chapter 7). In this study, events where $FBX = 12$ ² (to avoid this effect) are selected.

² $FBX = 12$ contains all events coming from collisions of bunches that have at least 12 preceding bunches in the train.

9.4 Results

As one can see for 2011 data in Figure 9.3, the fits meet at one value at effective cone area = 0 (0,0) which indicates a leakage difference independent from pile-up. The mean and the RMS of the intersection of these lines with the abscissa is used in the following as an estimator for the pile-up independent out-of-cone difference, i.e. the lateral leakage. In Figure 9.4 one can see this value at effective cone area = 0 per cone variable as a function of the average number of interactions per bunch $\langle \mu \rangle$. This absolute data-MC difference per cone variable should be independent from pile-up, which is reflected by a straight line per isolation cone and seen in most of the bins. A non-flat behaviour is observed for isolation cones *el_Etcone35* and *el_Etcone40* and needs to be covered by a systematic error.

The method described above is repeated for different bins in E_T (see Table D.7) and for the 2012 dataset with a different binning in $\langle \mu \rangle$, as mentioned in Table 9.1, due to the higher pile-up in 2012.

Each value of the measured lateral leakage, i.e. the pile-up independent out-of-cone difference between data and MC obtained per E_T bin (and η bin), is divided by E_T to calculate its contribution to the non-linearity of the energy scale. The error is defined as the RMS of the spread of the different out-of-cone values per $\langle \mu \rangle$ bin.

A comparison of the lateral leakage and its contribution to the electron energy scale linearity between 2011 and 2012 can be found in Figure 9.5. One can see, that part of the non-linearity can be explained by the incorrect MC description of the lateral leakage. For energies $E_T < 50$ GeV one can see a slightly steeper turn-on in 2012 w.r.t. 2011. This small discrepancy is not understood at the moment and probably comes from pile-up.

The lateral leakage can certainly explain part of the non-linearity measured for the energy scale versus E_T (as explained in Chapter 8). Overlaying the results for the lateral leakage with the measured energy scales (see Figure 9.6) shows that the effect of the lateral leakage can explain part of the effect. However, other effects need to be looked at in greater detail, such as the Presampler scale, the energy scale of the first and second calorimeter layer and material effects. Those effects will be investigated in detail in the following chapters.

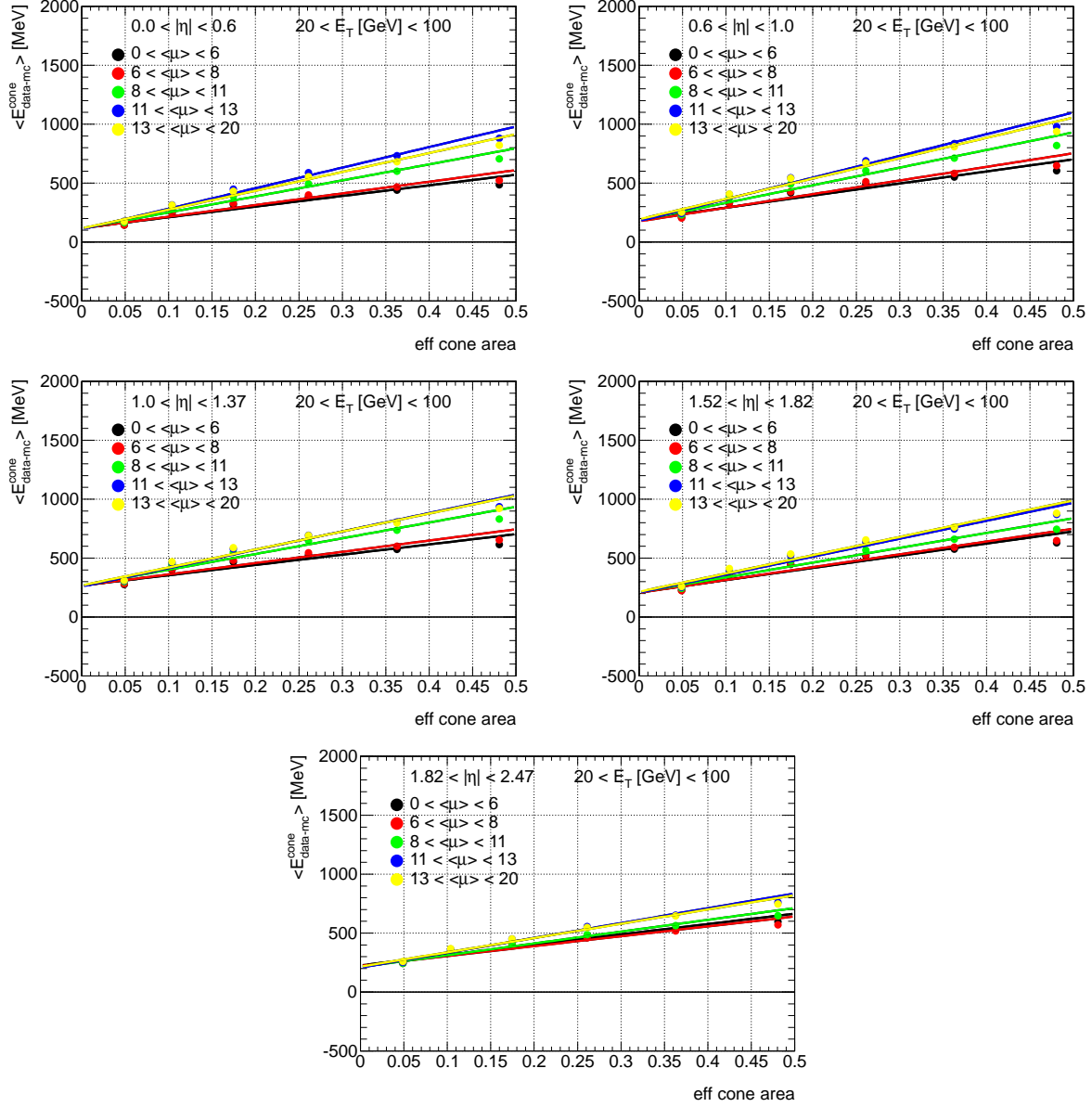


Figure 9.3: Absolute difference of data and MC (E_T integrated fits) [in MeV] versus the effective isolation cone size (subtracted 5x7 cells) for different $\langle \mu \rangle$ bins to estimate the offset at (0,0), which is the effective lateral leakage.

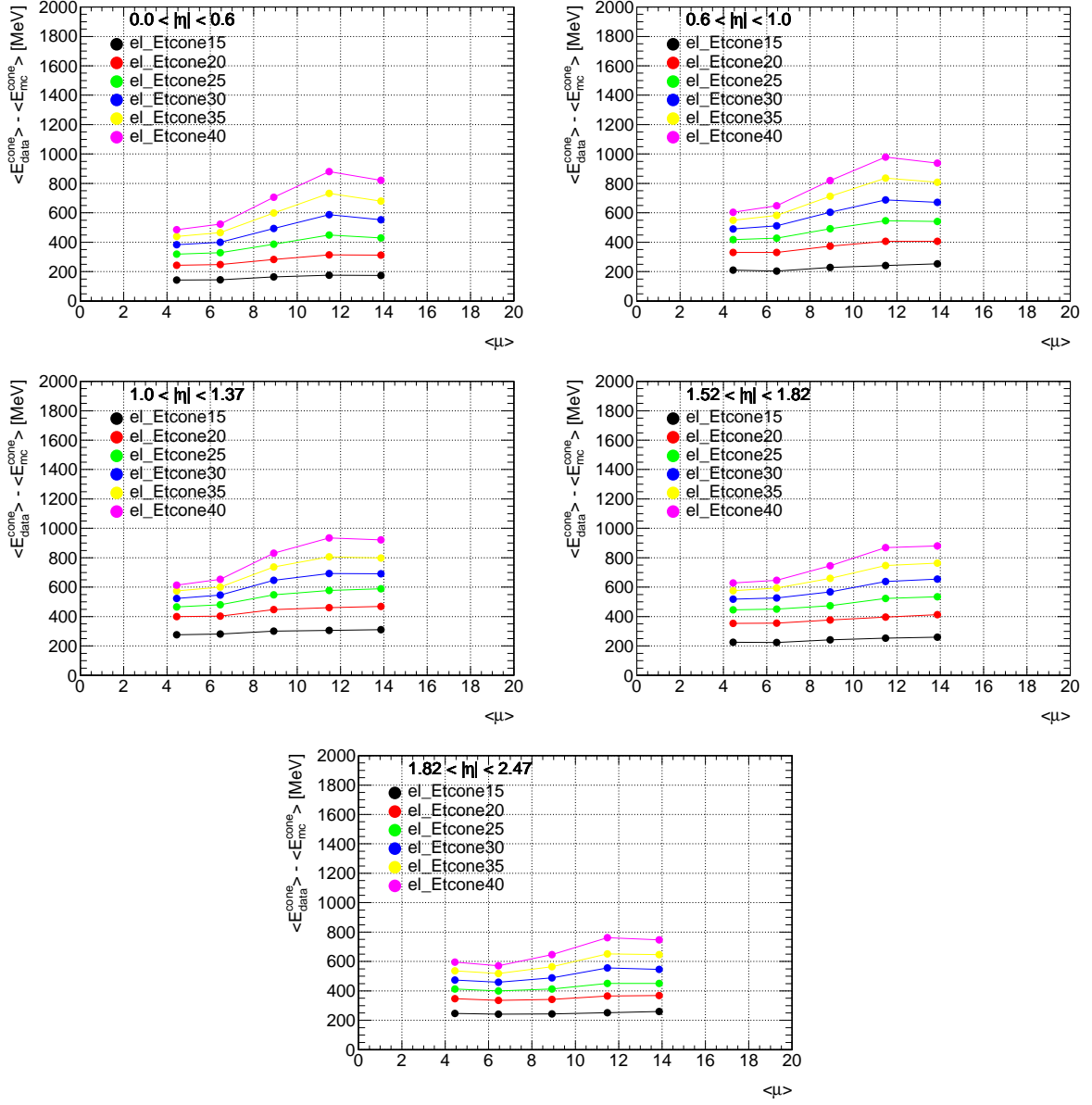


Figure 9.4: Absolute difference of data and MC (E_T integrated fits) [in MeV] versus number of $\langle \mu \rangle$ for different cone sizes. The x value for each point represents the "center-of-mass" for it's given bin in $\langle \mu \rangle$. The pile-up independence of the data-MC out-of-cone difference is reflected by a flat line.

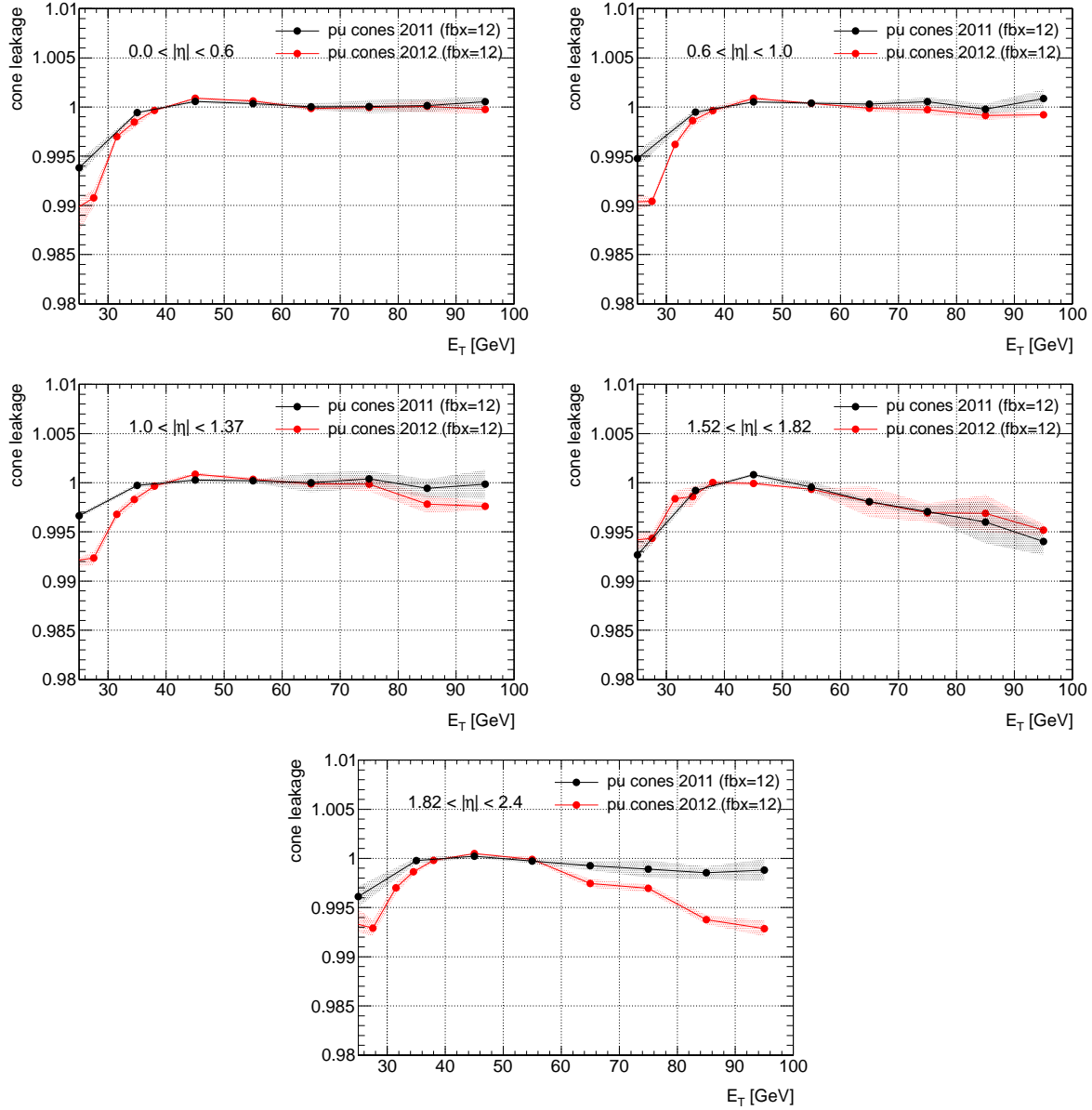


Figure 9.5: Estimated contribution of the lateral leakage to the non-linearity for two datasets. The black bullets show the points from 2011 and the red one from 2012. One can see a qualitative agreement for the two years over all η bins at higher E_T (> 50 GeV). At $E_T < 50$ GeV one can see a slight steeper turn in 2012 w.r.t. 2011 over most of the η bins (excluding $1.52 < |\eta| < 1.82$).

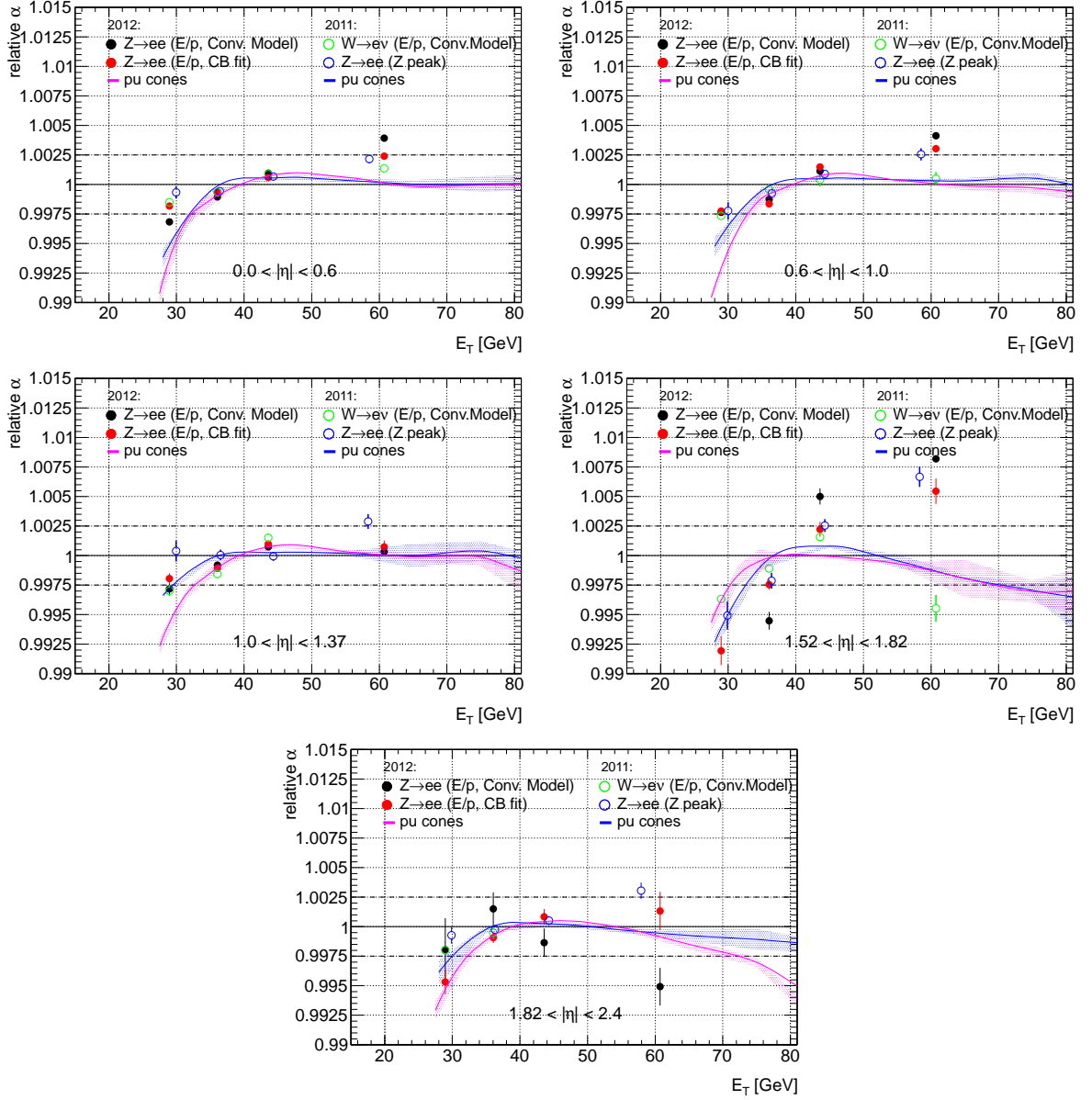


Figure 9.6: *Extracted scale correction (α) in coarse η bins and bins in E_T (open points 2011 and closed points 2012 measurements). The blue graph is the lateral leakage for 2011 as explained using the isolation cones. The purple graph is the lateral leakage measurement with 2012 data and MC. One can see that the lateral leakage has a turn-on of the same order of magnitude as the measured non-linearity. Side note: The average in-situ energy scale correction is subtracted and shifted to one for 40 GeV in E_T .*

Chapter 10

Passive Material Determination

10.1 Overview

Incomplete knowledge of material in front of the EM calorimeter has the potential to distort the electron energy measurement. Since the cluster based calibration (see Chapter 5, calibration hits) uses the energy deposit of MC simulated electrons in the passive material in front of the calorimeter to calculate the longitudinal weights of the PS and the accordion energies, any inaccuracy of the composition of material will translate into an inaccurate electron energy measurement. The amount of material in front of the EM calorimeter that is modeled in MC was already presented in Chapter 1 and shown in Figure 1.4.

The energy scale correction α as a function of η corrects the energy scale on average. Uncertainties of the passive material affect electrons with lower energy more severely than higher energetic electrons. Thus, there is a resulting energy dependent uncertainty that needs to be attributed to the electron energy scale. It is therefore important to minimize the uncertainty regarding the amount and composition of passive material.

As seen in Figure 10.1, the sensitivity to material for different particle types can be used to estimate material in front or inside the EM calorimeter: electrons and photons, which convert before the Presampler, can be used to measure material in the Inner Detector and the Cryostat. This chapter describes a way to estimate material in front of the electromagnetic calorimeter and to further improve the systematic uncertainties of the energy scale.

On the other hand, muons and photons converting after the Presampler are used to estimate material right after the Presampler and in the accordion. This will be further discussed in Chapter 11.

A method to measure the energy response with very fine granularity in η and ϕ exploiting periodicities in the ϕ coordinate will be explained in Section 10.2. This technique is used in some of the following studies to compare data-MC layer energies at cell granularity. It is needed to overcome a low number of reconstructed electrons in specific regions and to find ϕ repetitive effects.

The characteristics of the shower development (shower shape) can be used to study ef-

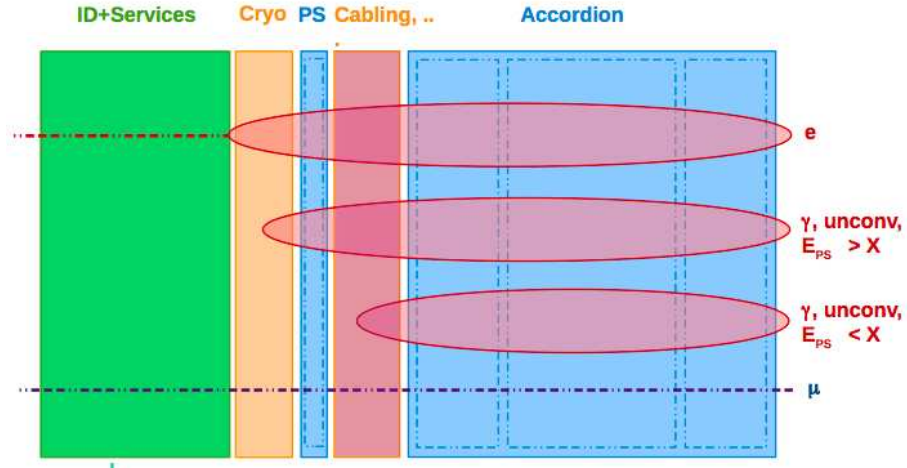


Figure 10.1: Schematic distribution of material shortly before and in the EM calorimeter. Different particle types are sensitive to different regions and hence can be used to measure different material. To measure material effects in late material (after the Presampler) with unconverted photons (γ unconv), the photons have to be chosen to deposit very little energy E_{PS} in the Presampler ($E_{PS} < X$, X denoting the energy threshold). It is therefore sure that these photons are not affected by the material upstream the Presampler. Taken from Ref. [46].

fects of passive material in front of the calorimeter. The ratio of the first sampling layer energy to the second sampling layer energy (E_1/E_2) is one figure of merit containing information of the longitudinal shower development and will be further explained in Section 10.3.

Tails in the E/p distribution are sensitive to material, too. By comparing these tails of MC simulation with data, defects in the MC material description can be localized (see Section 10.4).

During data taking in 2011 and 2012 a drop of efficiency was observed at $|\eta| \sim 1.7$. The influence of wrong material description was studied. The results are presented in Section 10.5.

Finally, the information gathered by the different material studies is summarized in Section 10.6. Recommendations for an improved MC material description for the upcoming Run 2 MC production are outlined.

10.2 Averaging using ϕ -Periodicity

In the following text, the way how this periodicity is exploited is explained. The measured quantity can be the MPV of E/p or the mean of E_1/E_2 or other variables.

Measuring, e.g. the average energy response (using for example the E/p distribution) for each cell in η and ϕ ($\Delta = 0.025$), with an adequate accuracy is difficult. MC simulation delivers not enough reconstructed electrons for such a fine granularity at the moment. However, when exploiting the symmetry of the calorimeter (e.g. module periodicity in ϕ), it is sufficient to keep the granularity in η , whilst averaging the ϕ direction with different periodicities.

The whole ϕ -coverage is divided into 2^n $n \in [0, 5]$ equal sections. Each of those sections is divided into 16 bins. The measured quantity of the first bins of all sections is averaged, as are those of all the other bins. The averaged resulting 16 bins will amplify any 2^n periodic characteristic. For different values of n , 2D-maps in η and averaged periodically in ϕ of several periodicities are created. These periodicities are from now on stated as modularities. For this material study, each bin in η and ϕ can contain different quantities such as the mean of shower shape variable E_1/E_2 or tailfractions of the E/p distribution.

10.3 Estimation of Passive Material Using Shower Shapes

The shower shape variable E_1/E_2 is sensitive to passive material in front of the calorimeter: an excess of passive material in data leads to earlier showers on average, increasing the mean value $\langle E_1/E_2 \rangle$. In addition, the energy response should decrease as a result of the increased energy fraction lost upstream.

The MC detector geometry variations used for these studies here are described in Chapter 3 and illustrated in Figure 3.5, taking as main references the nominal and distorted geometries (G'). The double ratios of $\langle E_1/E_2 \rangle_{data}$ in data to $\langle E_1/E_2 \rangle_{MC}$ of nominal MC as a function of η pinpoint to regions, where material is wrongly simulated. To translate this into X_0 , a comparison to the double ratio of $\langle E_1/E_2 \rangle_{G'}$ of the distorted geometry to $\langle E_1/E_2 \rangle_{MC}$ can be used (see Figure 10.2).

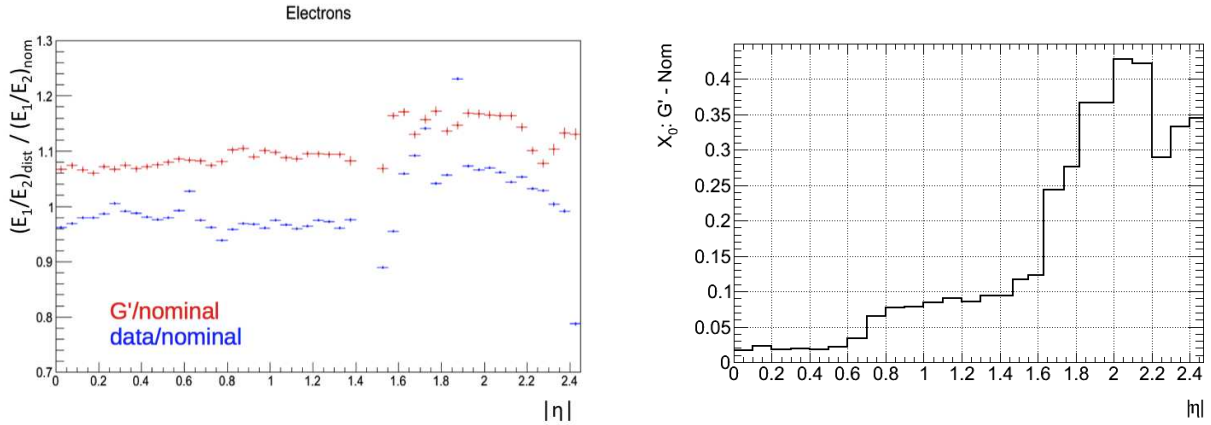


Figure 10.2: Left: $\langle E_1/E_2 \rangle$ as a function of η showing different defects in data/MC (blue). An estimation of missing material in nominal MC (in various η regions) is given by the ratio of distorted MC to nominal MC ($G'/nominal$). Right: distribution of the material added in distorted material MC w.r.t. nominal MC in terms of X_0 .

The global shift of the ratio of $\langle E_1/E_2 \rangle_{data}$ in data to $\langle E_1/E_2 \rangle_{MC}$ of nominal MC of about -3% for $0.0 < |\eta| < 1.37$ and about +8% for $1.37 < |\eta| < 2.47$ is as well observed with unconverted (up to the calorimeter) photons and hints to an imperfect modeling of

passive material between the Presampler and the accordion. This will be further discussed in Chapter 11.

The cuts taken for both years correspond to the general event selections as discussed in Chapter 3.5.3.

In the following, each interesting region in η with a local spike w.r.t. to the baseline will be discussed and further investigated along ϕ (see Figures 10.3, 10.4 and 10.5): $|\eta| = 0.25 - 0.3, 0.6 - 0.8, \sim 1.7, \sim 1.85$. For each region, corrections in terms of X_0 to the existing nominal MC will be proposed.

10.3.1 $0.25 < |\eta| < 0.3$

As seen in Figure 10.3 with a periodicity $n = 0$ a local $\Delta < E_1/E_2 > \sim 4\%$ from $\phi = -\pi/4$ to $-3\pi/4$ can be found. This translates, when compared to the distorted material sample G' , to a missing material of about $0.025 X_0$.

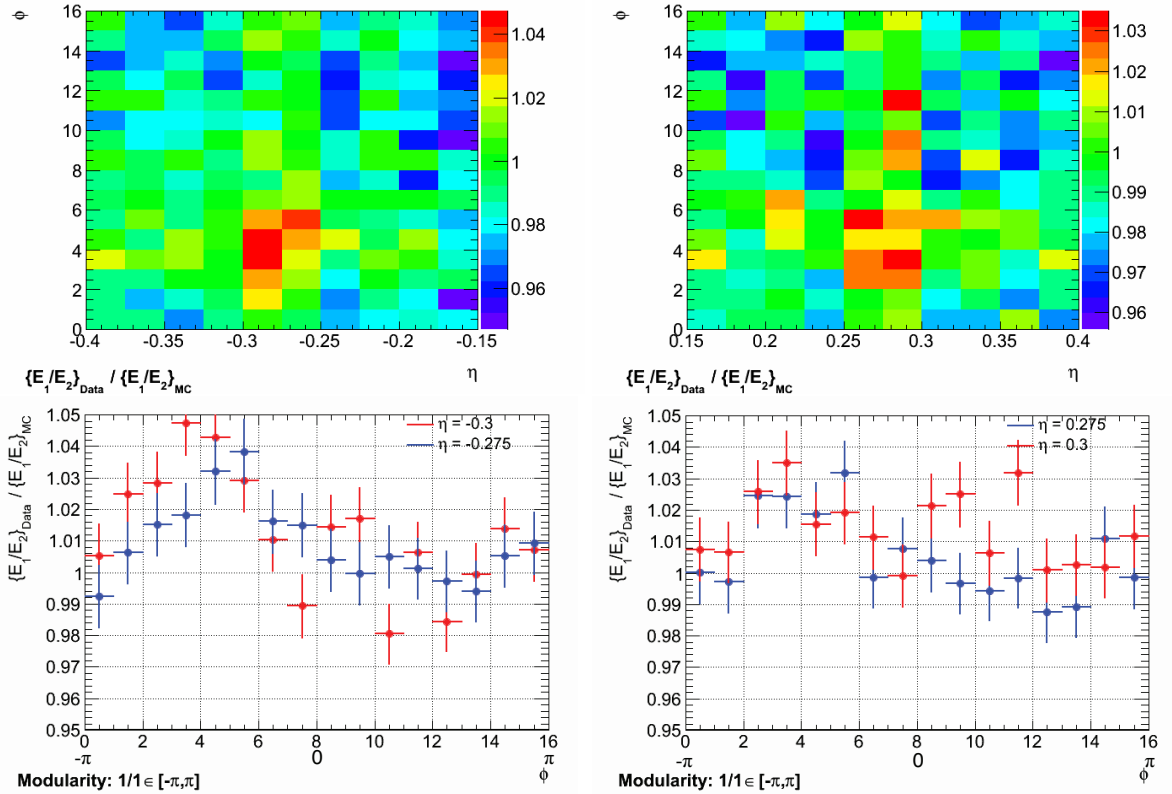


Figure 10.3: Left column upper plot: The obtained value (color code) by taking the ratio of $\langle E_1/E_2 \rangle_{\text{data}}$ to $\langle E_1/E_2 \rangle_{\text{MC}}$ in the negative η region at around -0.25 is shown, using no periodicity in ϕ where bin 0 represent $-\pi$, bin 8 equals 0 and bin 16 equals $+\pi$. The lower left plot shows two slices in ϕ for $\eta \sim -0.3$ and $\eta \sim -0.275$ (blues). The right column shows the same scenario but for positive η . A local change of about 3% in the mean values of $\langle E_1/E_2 \rangle$ in the data/MC ratio can be observed from $\phi = -\pi/4$ to $-3\pi/4$.

10.3.2 $0.6 < |\eta| < 0.8$

As seen in Figure 10.4, two local effects of about +8% at $\phi = -\pi/2$ and -8% at $\phi = \pi/2$ to the baseline can be seen (bin labeled 4 and 14). This would translate into additional $0.05 X_0$ at $|\eta| = 0.6$ and a decrease of about $0.05 X_0$ at $|\eta| = 0.8$.

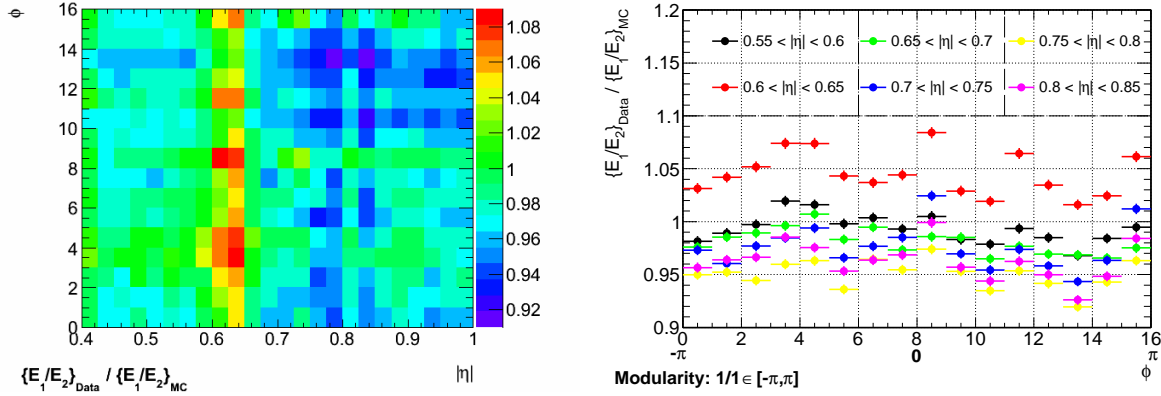


Figure 10.4: Left: $\langle E_1/E_2 \rangle$ for data over nominal MC. A clear structure of about $\pm 8\%$ in terms of $\langle E_1/E_2 \rangle$ can be seen along ϕ for $|\eta| \sim 0.6$ and $|\eta| \sim 0.8$. Right: $\langle E_1/E_2 \rangle$ slices in ϕ for interesting η regions distinguished by different colors: black ($0.55 < |\eta| < 0.6$); red ($0.6 < |\eta| < 0.65$); green ($0.65 < |\eta| < 0.7$); blue ($0.7 < |\eta| < 0.75$); yellow ($0.75 < |\eta| < 0.8$); purple ($0.8 < |\eta| < 0.85$)

10.3.3 $|\eta| \sim 1.7$

Large amount of material in front of the EM calorimeter exits in that region, such as SCT heaterpipes, Pixel cooling connectors and other ID services, as well as the end of the LAr barrel cryostat. In general, this material is also present in MC simulations. Nevertheless, a problem has manifested itself as missing data events in both the W and Z samples. A detailed description comes later Section 10.5.

10.3.4 $|\eta| \sim 1.85$

Various effects can be seen in Figure 10.5. An overall shift of about 8% to 10% in terms of $\langle E_1/E_2 \rangle$ can be observed, translating to a global need of $0.05 X_0$. For the region $\pi/2$, here labeled as bin 6-10, an additional shift of about 8% is seen. However, the most significant effect of $\sim 30\%$ compared to neighbouring cells can be seen in $\phi : 0 \pm \pi/16; 0 \pm 2\pi/16; \pi \pm \pi/16; \pi \pm 2\pi/16$ (labeled as bins 0-3 and 12-16). These numbers would translate into a need of $0.8 X_0$ at $|\eta| \sim 1.85$ and $\phi = 0; \pi$

10.4 Material Information in E/p Tailfractions

The E/p distribution is sensitive to material in front of the calorimeter. A Bremsstrahlung-loss due to material in front of the calorimeter can lead to an underestimation of the particle

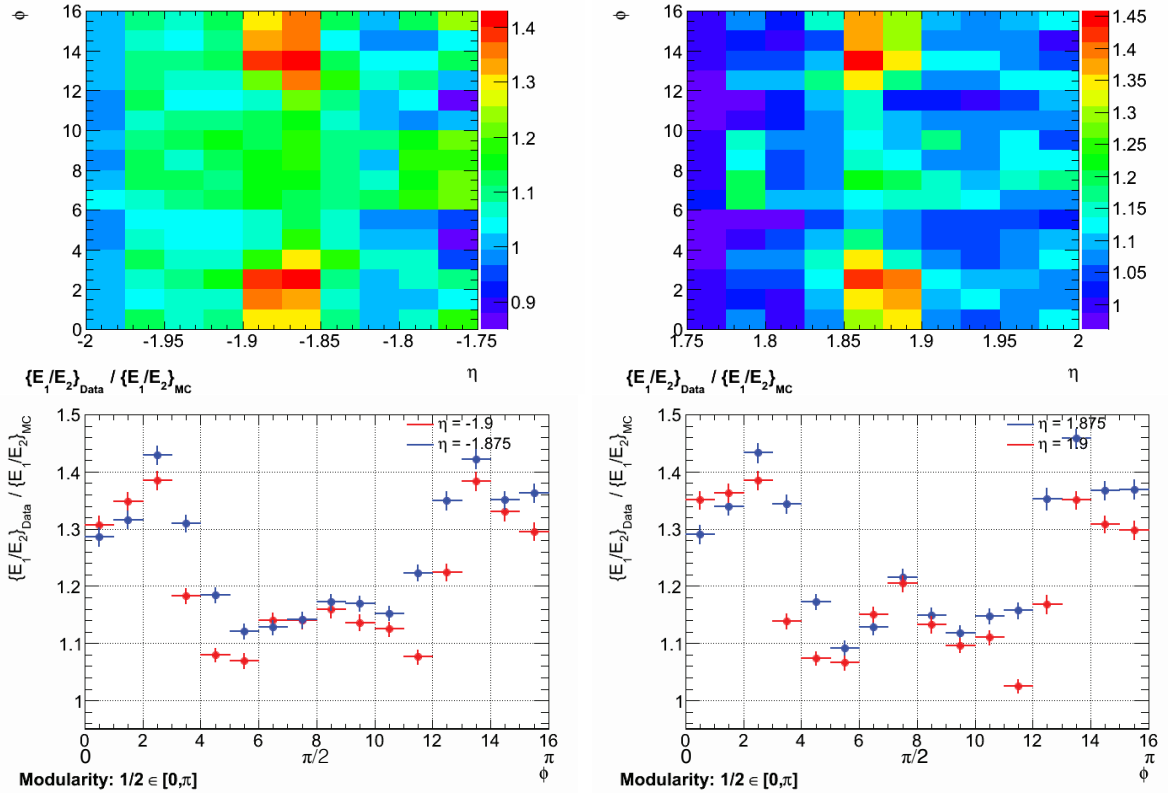


Figure 10.5: *Upper plots: 2D-maps of the data/MC ratio of $\langle E_1/E_2 \rangle$ for $|\eta| \sim 1.85$. The ϕ coordinate with a modularity of $[0, \pi]$. The color code represents the obtained value from the data/MC ratio. Lower plots: ϕ slices for two interesting regions. Several local effects are observed, as well as an overall baseline shift of data to MC of about 8%*

momentum. In 2012, a new reconstruction algorithm was introduced, where part of the Bremsstrahlung-loss is recovered by the GSF algorithm. However, the sensitivity of the E/p distribution to material remains (see Chapter 4).

This material dependent characteristics appear in the tail of the E/p distribution ($E/p > 1$), where events appear in which the electron traversing the inner detector is reconstructed with a lower momentum compared to the energy reconstruction. Comparing tails from MC simulations with tails from data can identify defaults in the material description upstream the calorimeter in MC simulation w.r.t. data.

The general shape of the E/p distribution is shown below. Two regions are distinguished depending on the material in front of the calorimeter (see Figure 10.6).

- $|\eta| < 1.5$: E/p centered at one (due to GSF as well) and small tails (Figure 10.6, left)
- $|\eta| > 1.5$: ID worse here \rightarrow positive tails become larger (as the error of the peak position) (Figure 10.6, right)

Two regimes can be defined:

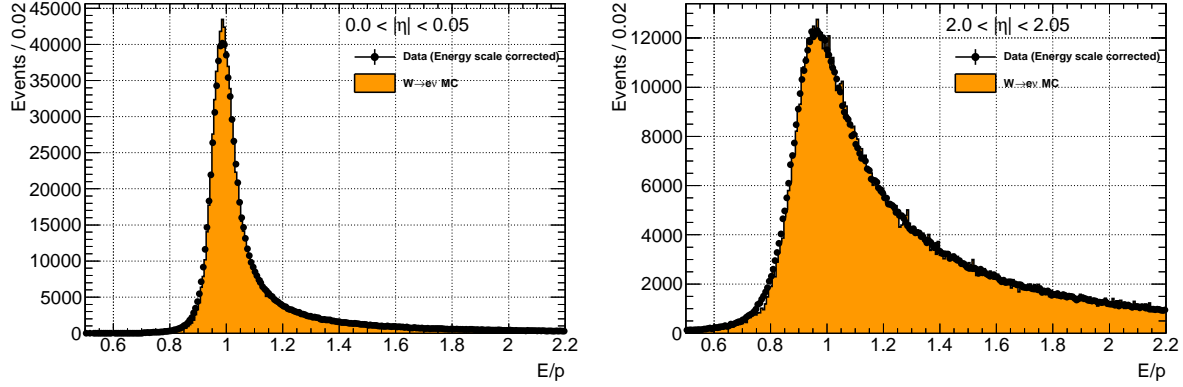


Figure 10.6: E/p distribution for different η regions. Left: one η bin in the central region of the detector. Right: in higher η regions the momentum measurement is worse compared to the energy measurement. Larger tails in E/p can be seen.

- The bulk of the distribution used to extract the MPV, which is sensitive to the calibration (see previous Chapter 6);
- The positive tail of the distribution, which is more sensitive to material inside the ID.

The E/p tailfraction N can be defined as:

$$N = \frac{\int_c^\infty f_e}{\int_0^c f_e}; c \dots \text{bulk-tail cut-off} \quad (10.1)$$

It was shown that for the tailfraction studies a cut-off parameter $c = 1.5$ is well suited. Hence, it will be used in all the studies presented here.

In order to separate material effects from calibration effects in the E/p tails, the scale correction α was used to rescale the cluster energy. To test if the tailfractions in data agree with them in MC simulations before and after energy calibration, a “pull” distribution (f_p) [63] is calculated:

$$f_p(a_N, b_N) = \frac{a_n - b_n}{\sqrt{\delta a_n^2 + \delta b_n^2}}; n \in [0, N] \quad (10.2)$$

where a_n (and its error δa_n) is one data bin and b_n (and its error δb_n) one MC bin. The distribution is filled for each bin n up until the total numbers of bins N . Pull distributions are expected to be standard Gaussian around zero. The width and the mean of the Gaussian reflect the agreement between the two probes (a_n, b_n).

In Figure 10.7, the behavior of the tailfractions of data before and after calibration w.r.t. to MC is shown. The RMS as well as the mean value improve in the calibrated case. Nevertheless, one can see that the E/p tailfractions do not agree well in any case. This might be partly due a wrong total material in the ID, but most likely comes from a discrepancy of the distribution of the material along the particle track.

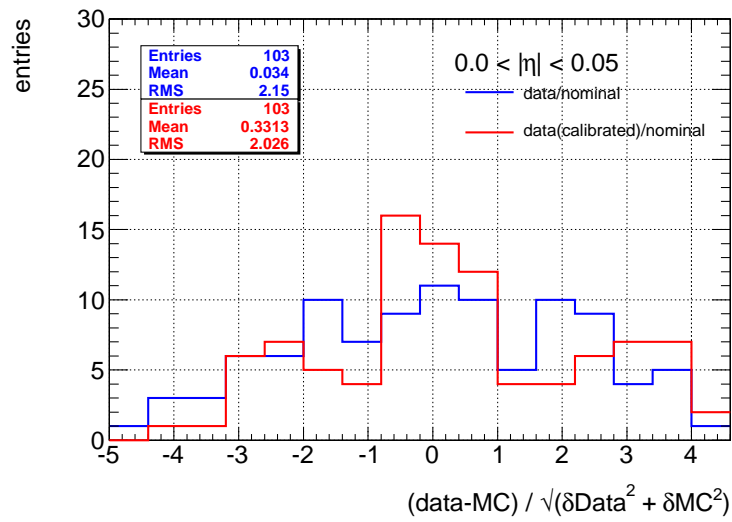


Figure 10.7: Pull distribution of the E/p tailfractions (using a cut-off parameter $c = 1.5$) comparing data-MC with data(calibrated)-MC for a the region $0.0 < |\eta| < 0.05$.

10.5 Efficiency Problem at $|\eta| \sim 1.7$

As already mentioned before, the region $|\eta| \sim 1.7$ is of special interest since - as seen in Figure 10.8 - a sudden drop between data and MC of about 30% can be observed.

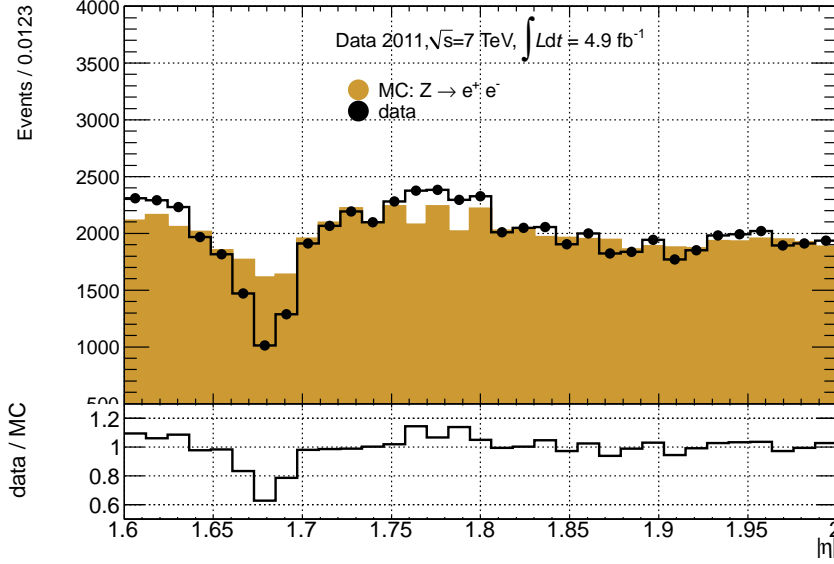


Figure 10.8: A drop of efficiency at $|\eta| \sim 1.7$ between data and MC in order of $\sim 40\%$ can be observed.

In this region, the most probable value (MPV) from a Crystal Ball fit to the E/p distribution, is extracted in 16 bins in ϕ with periodicity $n = 5$ and one bin per cell in η ($\Delta\eta = 0.025$). Building the ratio of the MPV obtained from data to the MPV obtained from MC, a 5% drop at $|\eta| \sim 1.7$ in three different regions in ϕ can be observed. Furthermore, a local spike of about 5% at $1.575 < |\eta| < 1.6$ can be observed (see Figure 10.9).

These local inhomogeneities in ϕ between data and MC affect also the overall energy scale extraction in this region. However, to measure material effects using E/p tailfractions, the official energy scale correction need to be applied. A residual miscalibration effect appears by comparing E/p from data with E/p from MC (Figure 10.10). This residual miscalibration is due to the fact that the energy scale correction α is averaged over a larger area in η and the energy scale changes quickly in this difficult region (see Figure 1.4).

To overcome this residual calibration effect, the E/p peak position in MC and data need to be re-aligned. A Gaussian function is fitted to the E/p bulk and the whole distributions (data, MC) are re-aligned by applying a correction factor, such that the Gaussian peaks are overlapping. The E/p tailfraction ratios of data over MC, for a $n = 5$ 32-fold periodicity ϕ coordinate, shows a difference in the order of about 20% along ϕ (see Figure 10.11).

This particular region in η was also investigated comparing longitudinal shower shapes (E_1/E_2)

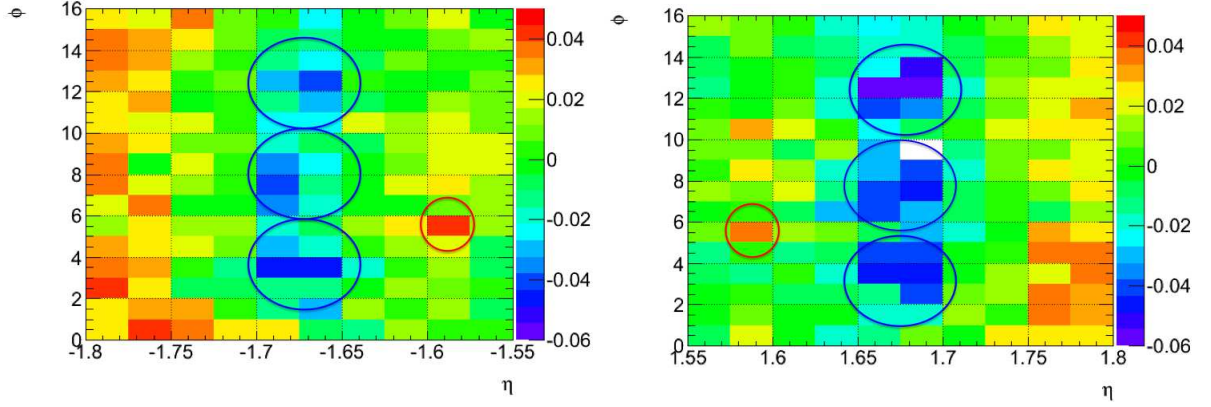


Figure 10.9: Ratio of the MPV of data to the MPV of MC obtained from a Crystal Ball fit to the E/p distribution showing a drop of about 5% in three different regions in ϕ and a local peak of about 5% w.r.t. the local baseline. Left: negative η , right: positive η . Periodicity $n = 0$.

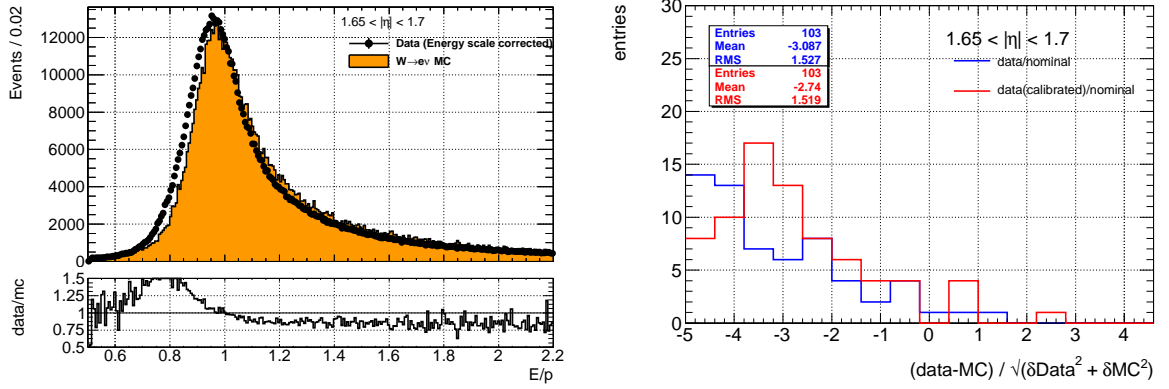


Figure 10.10: Left: E/p distribution for electrons coming from $W^\pm \rightarrow e^\pm \nu$ for the specific η bin. Right: Pull distribution for the events in E/p tails before and after calibration. A large data-MC discrepancy in the tails can still be seen.

in data and MC. A data-MC discrepancy of about 50% - 60% can be seen with a periodicity of $n = 5$ (32-fold) (Figure 10.12). Extrapolating from the double ratio of E_1/E_2 in nominal MC to G' as seen in Figure 10.2, this would translate into a need of about $1.2 X_0$ additional per module.

The investigations for the region $|\eta| \sim 1.7$ with the longitudinal shower shapes have led to rediscovering known material in the ID services, which were forgotten in MC simulation. TRT patch panels made out of steel and copper are located in this region having a granularity of $2\pi/32$. Close to $\phi = 0$ and π , there is less of this material because of the ID rails.

Regardless of all the effort of investigating additional material in that region, the reason for the drop in efficiency has not been completely resolved yet. Additional material will be added in the geometry description of MC simulation for Run 2. Once the new MVA based cluster calibration also uses this additional material information, the efficiency drop in region $|\eta| \sim 1.7$ should be again looked at. So far no additional correction in addition to the standard energy correction is applied for that region and the drop of efficiency is covered by the systematic error.

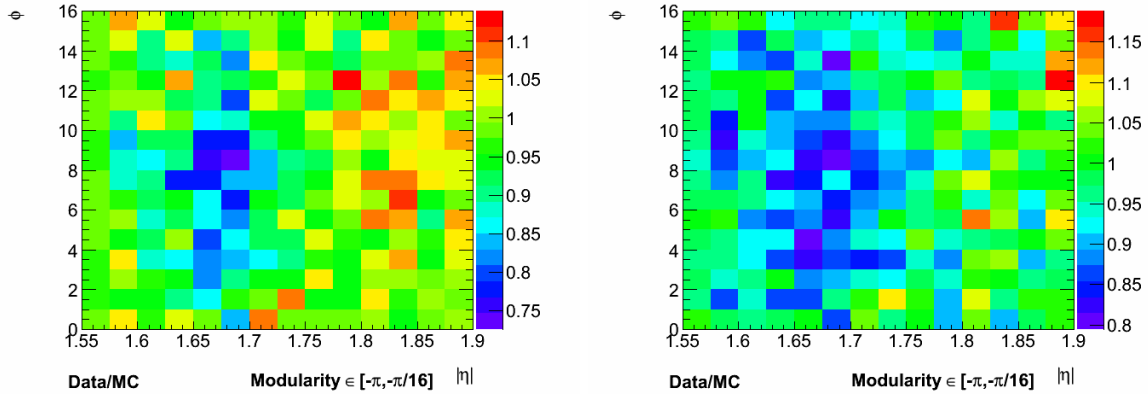


Figure 10.11: *Data-MC ratios of the tailfractions after the energy scale correction is applied on a 32-fold ϕ plane (1 module - 16 cells). Left: E/p peaks of MC and data were not aligned; Right: re-aligned MC and data E/p distributions.*

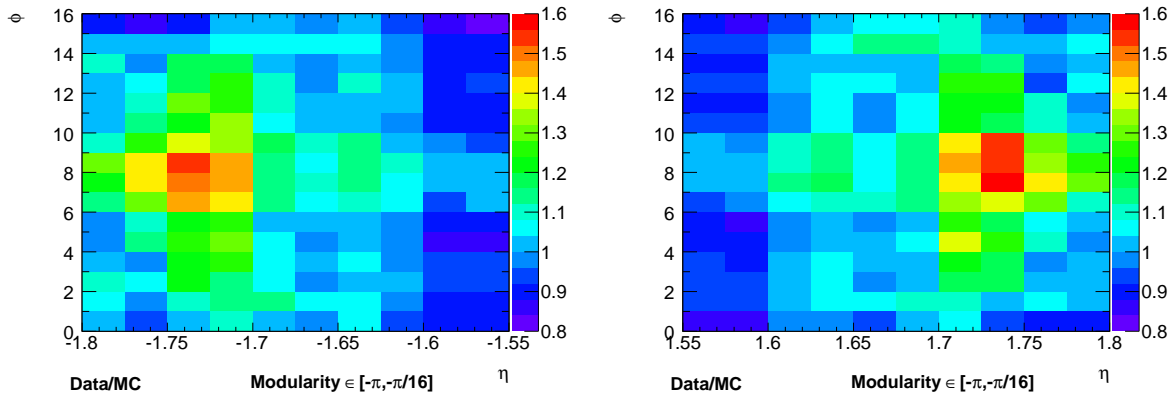


Figure 10.12: *Data-MC ratios for E_1/E_2 in the region $\eta \sim -1.7$ (left) and $\eta \sim 1.7$ (right) with a periodicity of $n = 5$ (32-fold) in the ϕ -coordinate. A data-MC discrepancy of 50% - 60% can be seen between $1.7 < \eta < 1.75$ and $-1.75 < \eta < 1.7$.*

10.6 Towards a Data-Driven Material Description

Several material defects in nominal MC w.r.t. to data along η were observed using the ratio of E_1/E_2 in data and MC. For each region in η additional material in terms of X_0 was proposed. The observed discrepancies are being summarized in Table 10.1.

$ \eta $	ϕ	X_0
[0.25, 0.3]	$[-3\pi/4, -\pi/4]$	+0.025
[0.6, 0.65]	$[-\pi/2]$	+0.05
[0.8, 0.85]	$[\pi/2]$	-0.05
[1.7, 1.75]	$[\pi/32 \times 32]$	+1.2
[1.85, 1.9]	$[-\pi, \pi]$	+0.05
[1.85, 1.9]	$[0, 0 \pm \pi/16], [\pi, \pi \pm \pi/16]$	+0.6
[1.85, 1.9]	$[0 \pm \pi/16, 0 \pm 2\pi/16],$ $[\pi \pm \pi/16, \pi \pm 2\pi/16]$	+0.4

Table 10.1: *Summary of the material effects observed, when comparing shower shapes from MC to data.*

In the region $|\eta| \sim 1.7$ the energy responses of MC and data, represented by the MPV extracted from a Crystal ball fit to the E/p distribution, were compared. A local difference between MC and data of about 5% was observed. The E/p tailfractions from MC and data were compared with each other. Even after calibrating the energy, the E/p distributions - for both, data and MC - had to be re-aligned, in order to overcome the difference in the peak position, which makes the results obtained from the E/p tailfraction unreliable. Mean values of E_1/E_2 ratios, on the cell level in η with a 32-fold periodicity in ϕ , between MC and data were compared. As discussed in Section 10.5, a data-MC discrepancy of 50% - 60% between $1.7 < \eta < 1.75$ and $-1.75 < \eta < -1.7$ has been observed, translating to a need of additional 1.2 X_0 .

In addition to the calorimeter based methods of mapping the material, in the ID tracking based methods are used, such as photon conversions or hadronic interactions. As described in Chapter 1 the ATLAS Inner Detector consists of a semi-conductor pixel detector, a semi-conductor microstrip (SCT) detector and a Transition Radiation Tracker (TRT), all of which are inside a 2 T solenoidal magnetic field.

Photons created in the primary interaction will transverse various material layers, e.g. beam pipe, Pixel and SCT layers or support structures. The radiation length of a localized amount of material is related to the fraction of photons that convert in it. Photon conversion candidates are then created by pairing oppositely-charged tracks. The number of photon conversions measured in a detector volume of known x/X_0 can be used as a normalization point to extract the amount of material at any other location inside the detector, by counting the relative number of conversions occurring in that portion. To obtain an unbiased map of the tracker material, it is necessary to correct the measured number of conversions by the conversion reconstruction efficiency. Several methods are being investigated to measure this efficiency from data, e.g. embedding Monte Carlo photon conversions in data or extracting it from the measure of decays.

Example of material maps obtained by photon conversions can be found in Figure 10.13.

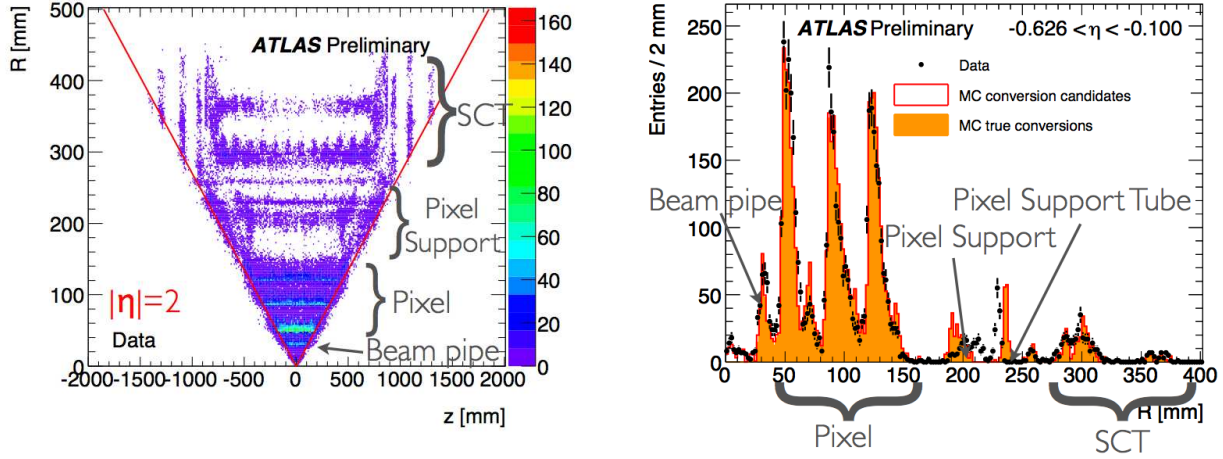


Figure 10.13: Example material mappings from photon conversions. Left: Mapping along Z (beam pipe direction) and R , showing precisely the different material layers. Right: Material mapping along R comparing MC with data. Generally, a good agreement between data and simulation can be seen, however pixel support structures and the support tube are shifted by ~ 1 cm in the simulation. Taken from Ref. [22].

Hadrons, on the other hand, created in the primary interaction will interact with the different material layers producing more than two outgoing particles. The way to map material with *hadronic interactions* is to find the vertices due to these secondary hadronic interactions in the Inner Detector. An inclusive vertex finding and fitting package is used to reconstruct these secondary vertices. Figure 10.14 shows the radius vs. z and x vs. y distribution of these secondary vertices.

Knowledge of the location and composition of the material is important for the physics performance of the detector. It is essential for the calibration of the EM calorimeter and important for the track reconstruction performance. To map material, either calorimeter based methods or track based methods were established.

The work presented within this thesis had major contributions to calorimeter based techniques, especially using shower shapes to determine any additional (or less) material in data w.r.t. to nominal MC simulations.

The goal is to put a new improved data driven MC geometry for Run 2 in place, based on material mappings and measurements using the 2011 and 2012 datasets.

Imperfect modeling of passive material in front of the EM calorimeter or between the Presampler and the accordion do also effect the linearity measurement, as described in Chapter 8, especially for low energetic electrons. The new data-driven MC description, as presented before, is in preparation for Run 2 and not used to estimate the effect of additional material in

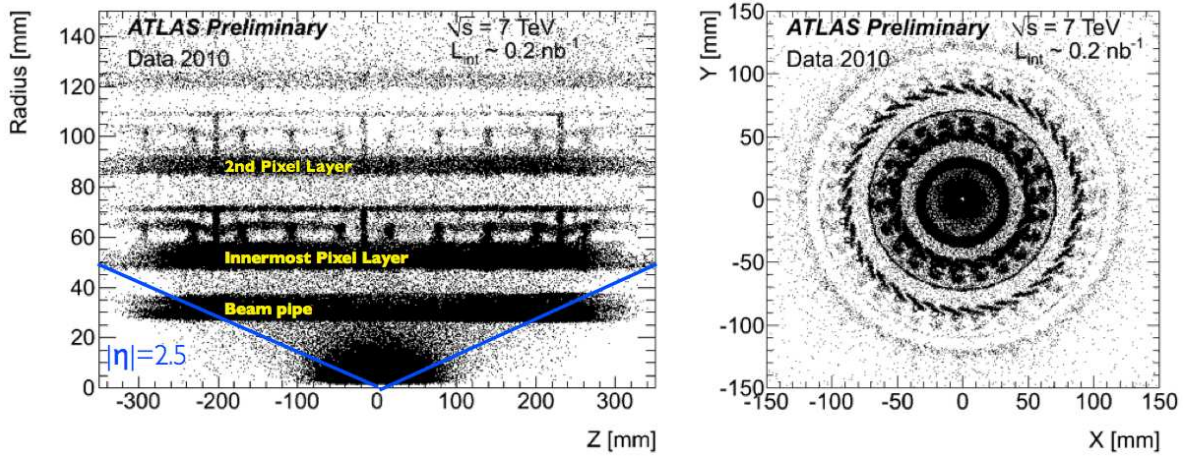


Figure 10.14: *Material mapping of hadronic interactions. Structure of the beam pipe, pixels layers and services are visible. Left: a view of the radius vs. z distribution of reconstructed vertices. Right: x vs. y . Taken from Ref. [22].*

front of the calorimeter on the energy scale correction. Currently, material effects need to be covered by a systematic error on the energy scale correction which is derived from the distorted geometry configuration G' and compared to nominal MC.

To derive this systematic error, the energy response as a function of η and E_T is calculated using the ratio $E_{\text{reco}}/E_{\text{truth}}$ (reconstructed energy over true energy). Since the cluster energy is calibrated with material information based on the nominal MC simulation, but the electron energy is reconstructed using the distorted geometry G' , the calculated energy response reflects the case having more material in data as in nominal MC simulation. A comparison of the obtained results with the linearity measurements of Chapter 8 can be seen in Figure 10.15. Due to limitations of reconstructed electrons in the distorted MC sample, only energies below 60 GeV are considered. In any case only electrons with low energies are expected to be sensitive to material defects. To extrapolate to energies above that value a fit, using the following function, was performed:

$$f(x) = a \cdot b \cdot \exp(-c \cdot x) \quad (10.3)$$

where a , b and c are free parameters in the fit. This function perfectly describes the turn-on for low energetic electrons and a saturation at higher energies. The largest effect can be observed in the region $1.52 < |\eta| < 1.82$ with a local change of material of about $0.8 X_0$ (see Figure 3.5) and with additional $0.15 X_0$ in the G' geometry. Since there is less additional material measured in data than given in the G' geometry, these results cover very well any imperfect modeling of passive material in front of the EM calorimeter. A systematic error will be defined and summarized in Chapter 12.

As already mentioned, imperfect modeling of passive material between the Presampler and the accordion will be further discussed in Chapter 11.

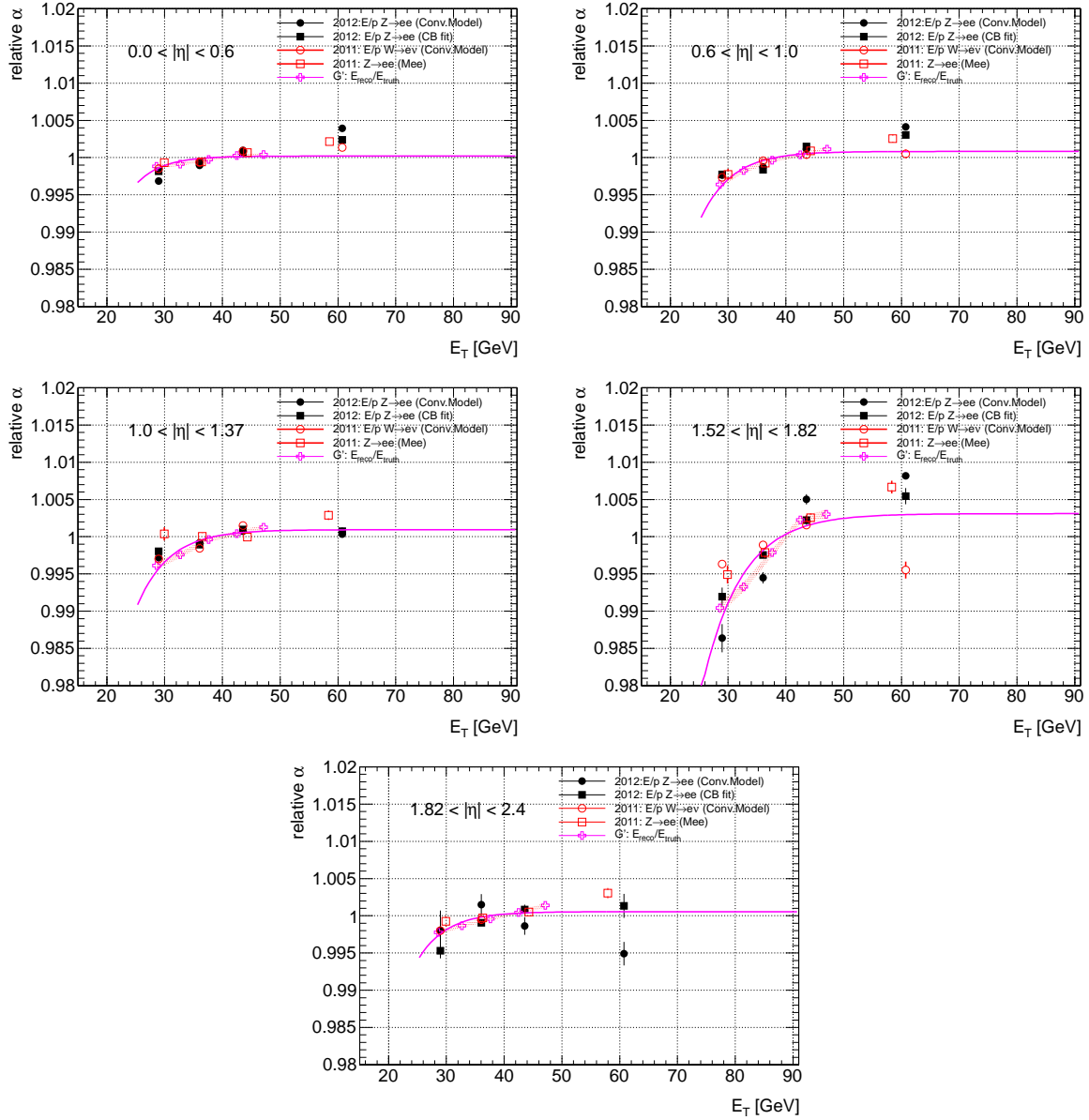


Figure 10.15: Measured linearity (Chapter 8) and comparison with additional material in front of the calorimeter obtained from a comparison of the energy response in nominal MC and distorted geometry G' (magenta points) - fitted with the function $f(x)$ according to Equation 10.3 (magenta). The open points are the measurements with 2011 data and the closed points are obtained with 2012 data. For a direct comparison the results are shifted to 1 for 40 GeV in E_T .

Chapter 11

Layer Calibration

11.1 Overview

As described in Chapter 2, the EM calorimeter is longitudinally segmented into a Presampler device ($|\eta| < 1.8$) and three sampling layers (E_1, E_2, E_3). The Presampler intends to correct for an energy loss in the dead material in front of the calorimeter. The calibration hits method calculates the weight of the Presampler in order to compensate for the energy lost upstream. This weight depends heavily on the material in front of the calorimeter and on the energy response of the Presampler itself. Since the in-situ calibration only fixes one overall scale, it cannot correct for any difference between the Presampler and the EM calorimeter energy scales. In this chapter, a method is presented to measure independently the Presampler scale and also the relative scales of the longitudinal calorimeter layers.

Any miscalibration between the sampling layers induces biases on E_1/E_2 and the total energy. Such a relative miscalibration does not change the energy if the sum of the layers is properly calibrated by scale correction α from $W^\pm \rightarrow e^\pm \nu$ and $Z \rightarrow e^+ e^-$. Nevertheless it induces a non-linearity in the energy response and problems for e to γ extrapolation.

Due to these properties, the layer inter-calibration is of major importance for the ATLAS physics program, in particular:

- $Z \rightarrow e^+ e^-$ invariant mass lineshape: a miscalibration of the Presampler energy scale has an impact on the $Z \rightarrow e^+ e^-$ mass tails and can therefore bias the in-situ energy scale extractions using the Z peak.
- Higgs mass measurement in di-photon channel: a miscalibration of one of the layers potentially leads to a bias on the total energy which is not perfectly corrected by the in-situ scale correction for photons.
- Any Standard Model precision measurement, such as the W mass measurement for example.

In this chapter, both the Presampler scale (Section 11.2) and the sampling layer scale calibration (Section 11.3) will be discussed.

11.2 Extraction of the Presampler Scale

The PS energy scale correction can be derived from the ratio of Presampler energy scales in data and MC, estimated from electrons from W and Z decays. It is important that the p_T distributions in data and MC are in good agreement (see Figure 6.1). However, these distributions are strongly influenced by the exact average starting point of the electromagnetic showers, which depends crucially on the amount of material in front of the EM calorimeter. This effect has therefore to be disentangled from the measurement of the layer energy scale.

Passive material effects are corrected exploiting the ratio of energy deposits in the front and middle compartments of the calorimeter, denoted E_1/E_2 or $E_{1/2}$ for short. This quantity is used because it is very sensitive to the amount of material upstream of the calorimeter: if there is extra material in the data compared to the simulation, this leads to an earlier shower development in data and then to a larger amount of energy deposited in the first sampling compared to the simulation (and the opposite when there is a deficit of material). When extra material is present, the ratio $E_{1/2}$ is then increasing in data. By comparing the observed ratio to the predictions from samples produced with nominal and distorted detector geometries, the total amount of passive material in front of the accordion can be estimated (see Figure 11.1).

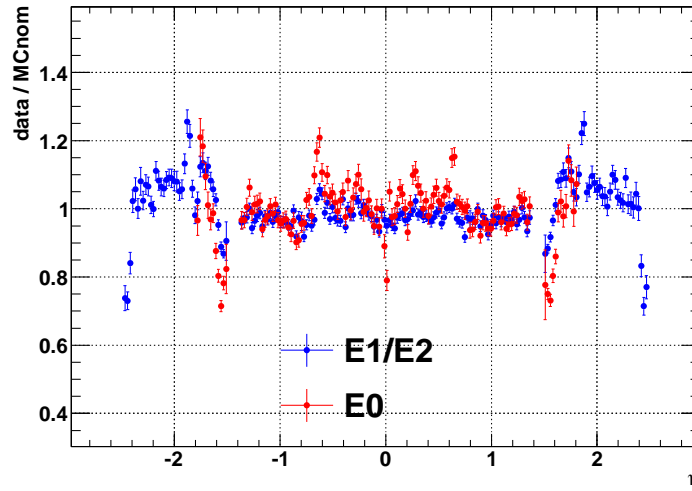


Figure 11.1: Data-MC ratios for E_0 (red points) and $E_{1/2}$ (blue points) using electrons from the 2012 $Z \rightarrow e^+e^-$ samples.

The linear relation between E_0 and $E_{1/2}$ due to passive material variations upstream of the calorimeter can be estimated using MC samples with different material variations. Samples with material variations upstream of the calorimeter follow a common trend (see Figure 11.2). One can also see that electrons from Z decays behave similarly as those from W decays, which indicates that the method is working regardless of the p_T distribution of the used electrons, as long as it is well modelled in MC. All points that do not follow this trend are from samples with additional material between the Presampler and the accordion.

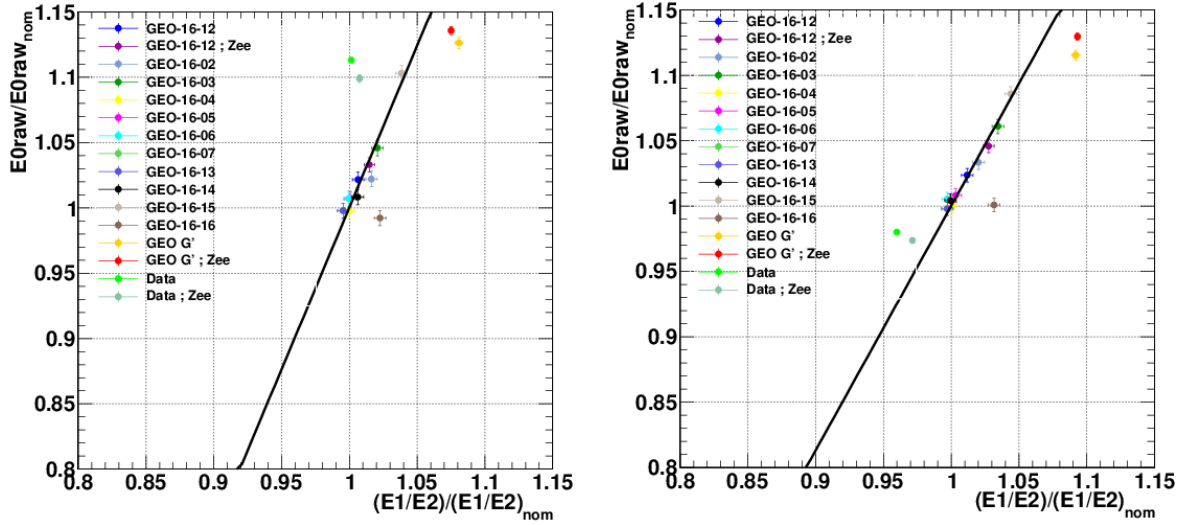


Figure 11.2: Example of the correlation between $E_0^{\text{data}}/E_0^{\text{MC}}$ and $E_{1/2}^{\text{data}}/E_{1/2}^{\text{MC}}$, obtained with electrons from $W^\pm \rightarrow e^\pm \nu$ decays in the regions $0.6 < |\eta| < 0.7$ (left) and $1.0 < |\eta| < 1.1$ (right). Different colors represent different geometry variations upstream of the calorimeter. The black line is a linear fit of these points passing through point (1,1). These fits are used to extract the slope $A(\eta)$.

The following linear parametrization summarizes the impact of passive material variations in front of the accordion on E_0 and $E_{1/2}$:

$$\frac{E_0^i(\eta)}{E_0^{\text{nom}}(\eta)} = 1 + A(\eta) \left(\frac{E_{1/2}^i(\eta)}{E_{1/2}^{\text{nom}}(\eta) b_{1/2}(\eta)} - 1 \right) \quad (11.1)$$

where the ratios are taken between predictions for a given geometry i and the nominal simulation. For geometry variations upstream of the calorimeter, A is a priori a function of η and is represented by the slope of the linear fit of the correlation between E_0 and $E_{1/2}$ (see Figure 11.2). The variable $b_{1/2}$ parametrizes a possible bias on the ratio $E_{1/2}$. Such a bias can reflect imperfect relative calibration of the calorimeter samplings, and/or imperfect modeling of the passive material between the Presampler and the accordion. This bias $b_{1/2}$ was measured using unconverted photons with inclusive and radiative photon samples, such as $Z \rightarrow l\bar{l}\gamma$. The photons in Figure 11.3 have been chosen to deposit very little energy in the Presampler ($E_0 < 0.5$ GeV). It is therefore sure that these photons are not affected by the material upstream the Presampler.

Based on the above parametrization, a material-corrected prediction for E_0 is derived using the relation

$$\frac{E_0^{\text{corr}}(\eta)}{E_0^{\text{nom}}(\eta)} = 1 + A(\eta) \left(\frac{E_{1/2}^{\text{data}}(\eta)}{E_{1/2}^{\text{nom}}(\eta) b_{1/2}(\eta)} - 1 \right) \quad (11.2)$$

where $E_0^{\text{corr}}(\eta)$ corresponds to the amount of expected Presampler energy in the simulation, after correction for the material-induced bias. The Presampler scale correction is then defined

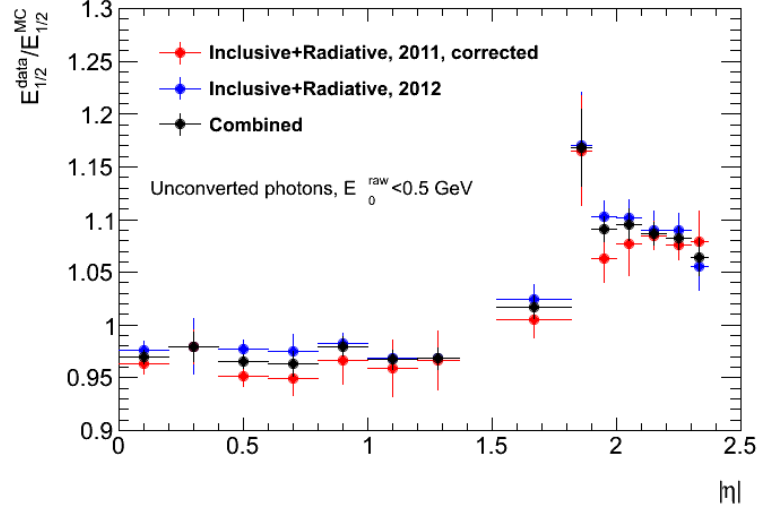


Figure 11.3: The data-MC ratio of the unconverted photon energy deposition (using the ratio of sampling 1 and sampling 2) along η is used to decouple calibration systematics from material effects close to the PS ($b_{1/2}$). $E_{1/2}$ is considered as independent of the upstream material, if the photon reaches the Presampler before it converts. A 3% bias can be seen in the barrel and up to 10% in the end-cap. This ratio is incorporated in Equation 11.1 and Equation 11.2 as $b_{1/2}(\eta)$.

by

$$\alpha_{\text{PS}}(\eta) = \frac{E_0^{\text{data}}(\eta)}{E_0^{\text{corr}}(\eta)} \quad (11.3)$$

incorporating Equation 11.2, leads to

$$\alpha_{\text{PS}}(\eta) = \frac{E_0^{\text{data}}(\eta)}{E_0^{\text{nom}}(\eta)} \cdot \left\{ 1 + A(\eta) \left(\frac{E_{1/2}^{\text{data}}(\eta)}{E_{1/2}^{\text{nom}}(\eta) b_{1/2}(\eta)} - 1 \right) \right\}^{-1} \quad (11.4)$$

The Presampler scale correction per η bin is defined by $\alpha_{\text{PS}}(\eta)$ and calculated using the above formula. In order to calculate $\alpha_{\text{PS}}(\eta)$, $A(\eta)$ is derived as described before and $b_{1/2}$ measured in different η regions. $\alpha_{\text{PS}}(\eta)$ is defined with a granularity reflecting the size of the Presampler modules, i.e. $\Delta\eta = 0.2$ for the barrel modules, and $\Delta\eta = 0.3$ for the end-cap module covering $1.5 < |\eta| < 1.8$. The final result of $\alpha_{\text{PS}}(\eta)$ is presented in Figure 11.4.

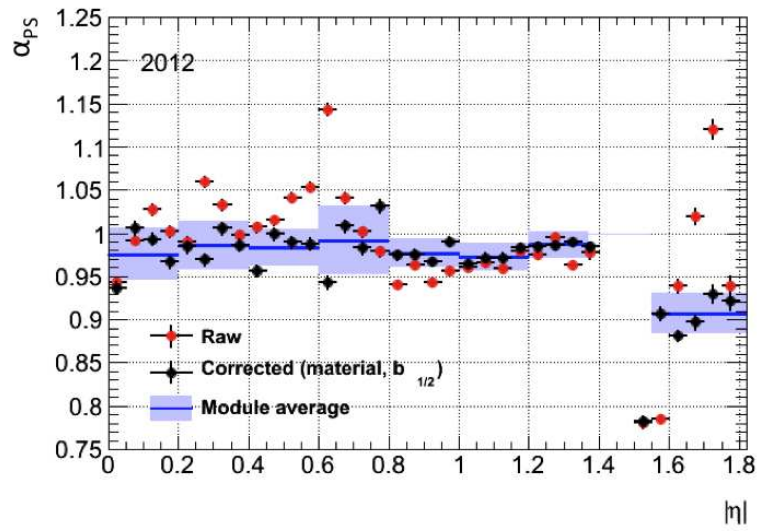


Figure 11.4: *Final Presampler scale correction and uncertainty, after all corrections. The red and black points represent the Presampler energy profiles before and after material corrections, respectively. The blue bands are averages over the data points performed in each Presampler module. The uncertainty gets contributions from the residual spread of the points within each module and from the uncertainty on the $b_{1/2}$ correction.*

11.3 Layer Calibration E_1 and E_2

Figure 11.3 shows that there is a significant disagreement between data and MC in the ratio of E_1/E_2 (3%) in the barrel. This disagreement, which is here shown for photons that didn't shower before the Presampler (and hence cannot be affected by material in front) can come either from the material between the Presampler and the accordion or from a different energy scale in E_1 and E_2 . To disentangle the two, the MPV of the E/p distribution was plotted as a function of E_1/E_2 . The same was done for nominal MC and for a MC sample with additional material.

To study this effect and calculate a scale correction, E/p of single electron energies is used to measure the energy response. Complementary, the position of the Z peak of two reconstructed electrons is used as a reference. The estimation of the Z peak position follows the scheme presented in Appendix A. As a further cross check the energy deposition of muons in the two sampling layers and its ratio is investigated.

11.3.1 Electrons

The basic $E_{1/2}$ distribution for electrons from $Z \rightarrow e^+e^-$ decays (for one bin in η) is shown in Figure 11.5. In this specific η bin it can be seen that $E_{1/2}$ peaks at 0.45, which means that the energy deposit in the first layer of the calorimeter (E_1) is 45% of the energy deposit in the second layer (E_2). The $E_{1/2}$ distribution is divided into bins of $\Delta 0.1$ and for each of these bins the E/p distributions are obtained in data and MC. The selection cuts follow the general selection criteria as presented in Section 3.5.3. The E/p distributions are fitted with a Crystal Ball function (as done in Section 6) to extract the MPV as a function of $E_{1/2}$.

In Figure 11.6 the MPV for different samples and its ratio to nominal MC as a function of $E_{1/2}$ is plotted (here one bin in η shown). Four different samples are compared with each other: firstly, the MPV is extracted for data recorded in 2012 using electrons from $Z \rightarrow e^+e^-$ to obtain the E/p distribution. Secondly, according to the results obtained in Section 11.2 a +3% bias in the barrel region on E_1 is added when reconstructing the total energy in data. The MPV is extracted for E/p distributions including that bias on E_1 in the total energy. Thirdly, the MPV is calculated for E/p distributions obtained from the 2012 $Z \rightarrow e^+e^-$ MC sample. Lastly, the MPV of E/p functions obtained from distorted geometry MC is extracted to eventually measure effects of additional material in front of the EM calorimeter.

As seen before, the MPV for these different cases along E_1/E_2 is not flat, neither is their ratio to nominal MC. An additional scale correction ($\alpha_{S1}(\eta)$) needs to be found such that the data/MC ratio of the MPV is independent of $E_{1/2}$.

To extract the scale correction $\alpha_{S1}(\eta)$, E_1 in the dataset is biased with a set of possible $1/\alpha_{S1}(\eta)$. The cluster energy (which is used in E/p) is recalculated with the set of $1/\alpha_{S1}(\eta)$. For these different biases, the E/p distribution is fitted for each bin in $E_{1/2}$ (and η bins) and the MPV is extracted. Furthermore, the ratio of the MPV from the biased data and MC is fitted

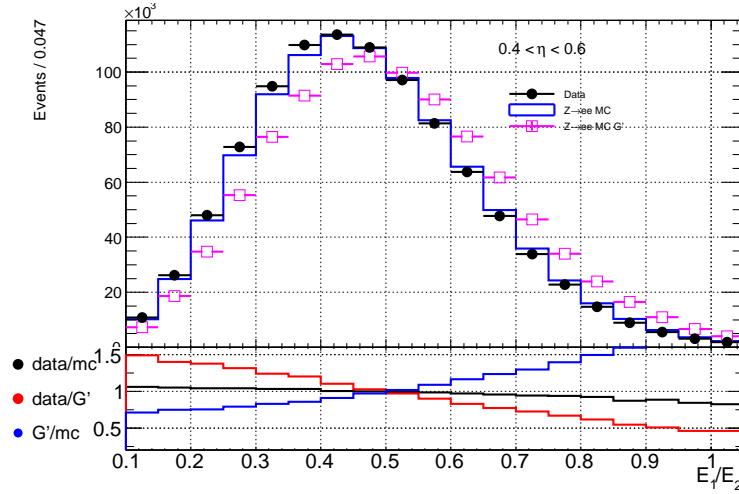


Figure 11.5: $E_{1/2}$ distribution for electrons coming from Z decay in data (black points), nominal MC (blue histogram) and distorted MC (magenta squares). The effect on $E_{1/2}$ of additional material upstream of the EM calorimeter can be seen when comparing nominal MC with distorted MC. The whole distribution is shifted to a higher mean in presence of additional material. In the bottom part three different ratios are shown. The data/MC (nominal) ratio shows that $E_{1/2}$ is differently modeled in MC as it is measured in data.

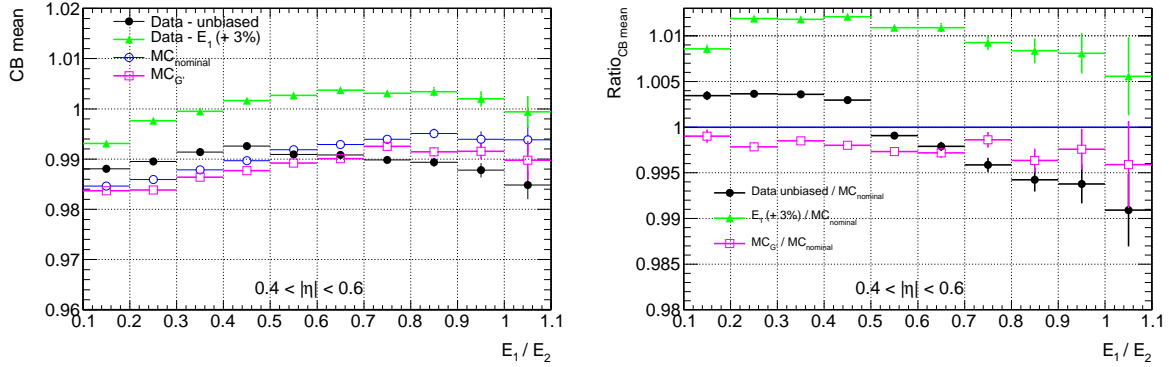


Figure 11.6: Left: the MPV of the E/p distribution (fitted with a Crystal Ball function) for different datasets plotted as a function of $E_{1/2}$. Right: the data-MC ratio of the MPV for different datasets as a function of $E_{1/2}$. The fitted mean (also the ratio to nominal MC) is not flat w.r.t $E_{1/2}$

with a horizontal (straight) line and a χ^2 [64] is assigned. A perfectly independent data/MC ratio of the MPV along E_1/E_2 would manifest itself in a horizontal line.

The different χ^2 values are plotted as a function of the bias applied on E_1 and then fitted with a parabola (see Figure 11.7). Consequently, the lowest point of the parabola determines the “best” $\alpha_{S1}(\eta)$.

To estimate $\alpha_{S1}(\eta)$ two possibilities are considered:

- $\alpha_{S1}(\eta)$ is determined, while the Presampler energy is not corrected with the factor α_{PS}
- $\alpha_{S1}(\eta)$ is determined, while the Presampler energy is calibrated using α_{PS} (Equation 11.2)

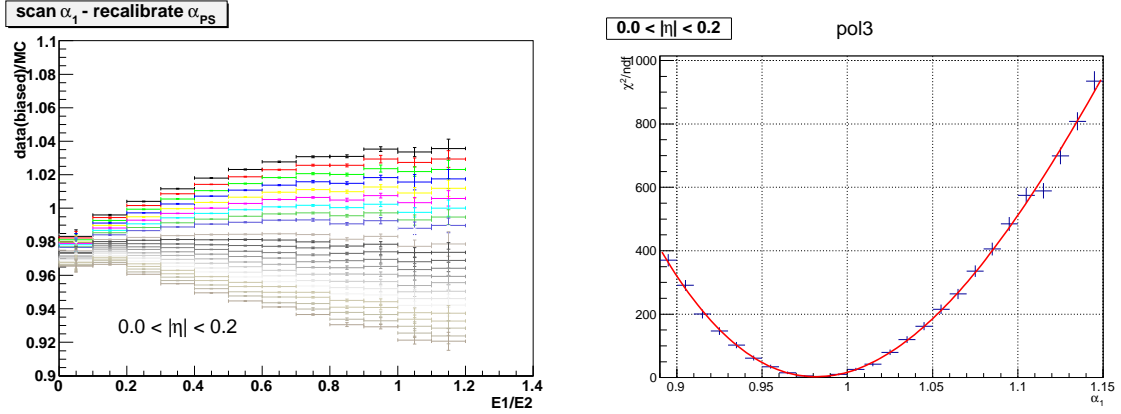


Figure 11.7: Left: a scan of the different data (biased)/MC ratios. Each of these ratios is fitted with a straight line. Right: the χ^2 of each fit. The line with the least χ^2 , i.e. the flattest, gives the scale correction $\alpha_{S1}(\eta)$ (for a specific η bin).

Figure 11.8 presents the results as a function of $|\eta|$. A 2% miscalibration of E_1 starting from the first $|\eta|$ bins up to 10% for $1.2 < |\eta| < 1.37$ is measured.

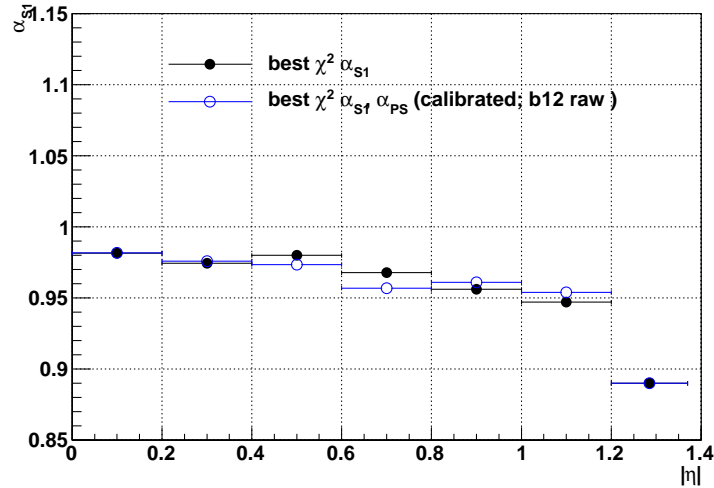


Figure 11.8: Results for the E/p cases; black points: without correcting for α_{PS} ; blue: correcting for α_{PS} (raw b_{12}), it follows the same pattern as non-corrected case and hence α_{PS} has not much influence on the layer calibration.

Unfortunately, E/p results are limited to the barrel ($|\eta| < 1.37$) only. The uncertainties of the momentum measurement get larger in end-caps, reflecting larger tails (for $E/p > 1$) and

a much broader width. Consequently, the extraction of the MPV is also affected by a larger uncertainty - in addition to the statistic uncertainty due to the binning in η and binning in $E_{1/2}$.

11.3.2 Muons

Only a small amount of the muon energy is deposited in the EM calorimeter, typically 20 MeV in the Presampler to about 250 MeV in the middle sampling and the signal to noise ratio is not very high. Nevertheless, due to the high number of reconstructed muons it is possible to measure its energy deposit in different η regions.

The mean energy deposit is very localised and muons behave almost as minimum ionizing particles. Moreover muons are highly insensitive to material in front of the calorimeter, hence they can be used as discriminators between calibration and material effects.

The most probable value for the energy loss (or dE/dx) is defined in the following section. The distribution of the individual muon energy deposits in the layer is parametrized with two approaches:

- Define a truncated mean, selecting the smallest intervals containing 30%-90% of data (see Figure 11.9)
- Fit the distribution with a convolution of a Landau with a Gaussian function and use the MPV.

The extracted most probable values for the muon energy loss are compared with MC and used to extract the energy scale (and its correction) as a function of η . The final results are presented in the next section, Figure 11.10.

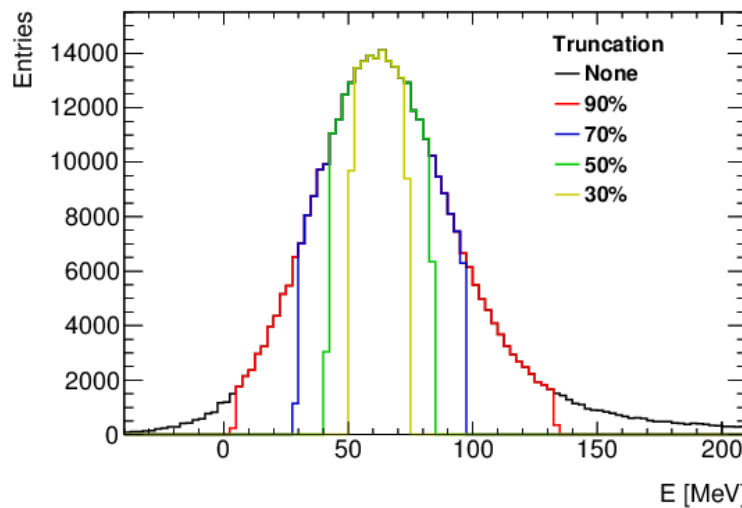


Figure 11.9: *Muon energy deposition in layer 1 for $0.1 < |\eta| < 0.2$, highlighting the intervals containing 30%-90% of data.*

11.4 Results

The comparison and the combination of the results for the different methods between electrons and muons are presented in Figure 11.10.

As seen above, for $|\eta| < 1.2$ and $|\eta| > 1.82$, the obtained scale corrections between the electron and muon methods agree very well with each other. In the region $1.2 < |\eta| < 1.82$, the results for muons and electrons diverge. The electron data, however, have large uncertainties in this region while the muon data tend to be more reliable.

For the final layer scale correction, the weighted average of all the four (three above $|\eta| = 1.4$) methods per bin in η is calculated. Consequently, the spread defines the error. A precision of 1% for $|\eta| < 1.2$ and $|\eta| > 1.82$ can be stated. In the transition region, the precision is worse, up to 3%.

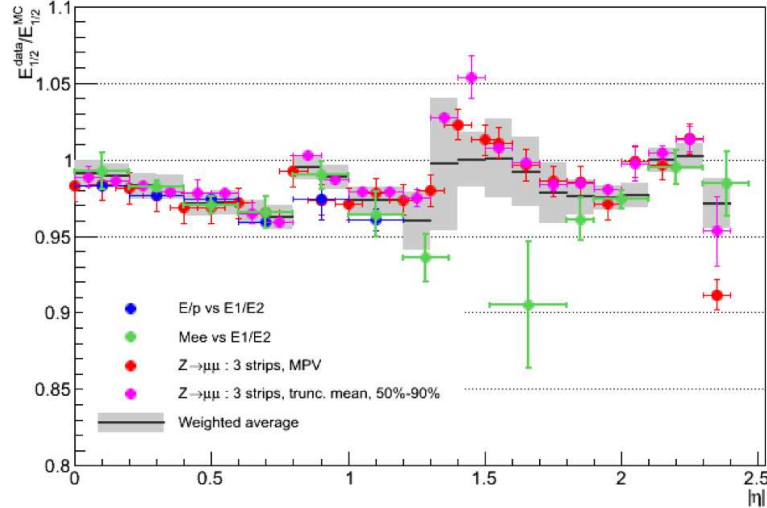


Figure 11.10: The four methods (two muon and two electrons) are compared. All results point to a data/MC disagreement of around -2% to -4% in the barrel. A discrepancy between the muon and the electron methods is visible $1.2 < |\eta| < 1.8$. For $|\eta| > 1.8$ muons and electrons are in a good agreement. The gray band is the weighted average of all the four (three) methods per bin in η , i.e. the final $E_{1/2}$ scale correction (α_{S1}) with error.

To find the origin of the measured non-linearity presented in Chapter 8 the impact of the EM calorimeter Presampler scale and layer scale calibration was investigated (see Figure 11.11). To predict the impact of the full layer calibration (including both, the Presampler scale and layer scale calibration), the ratio of the cluster energy with the “full layer calibrated” cluster energy is plotted as a function of E_T in different η bins. For $|\eta| < 1.0$ the miscalibration between the layers seems to be able to partly describe the effect of non-linearity, especially for energies $E_T \sim 40$ GeV. On the contrary, in the region $1.0 < |\eta| < 1.82$ the layer miscalibration seems to be able to explain pretty well the measured non-linearity (also for low energies). However, the measured non-linearity seems to be a superposition of several effects, such as the

here described layer (mis)calibration or the lateral leakage (see Chapter 9). In the next round of energy reconstruction both effects will be corrected and the residual non-linearity needs to be measured.

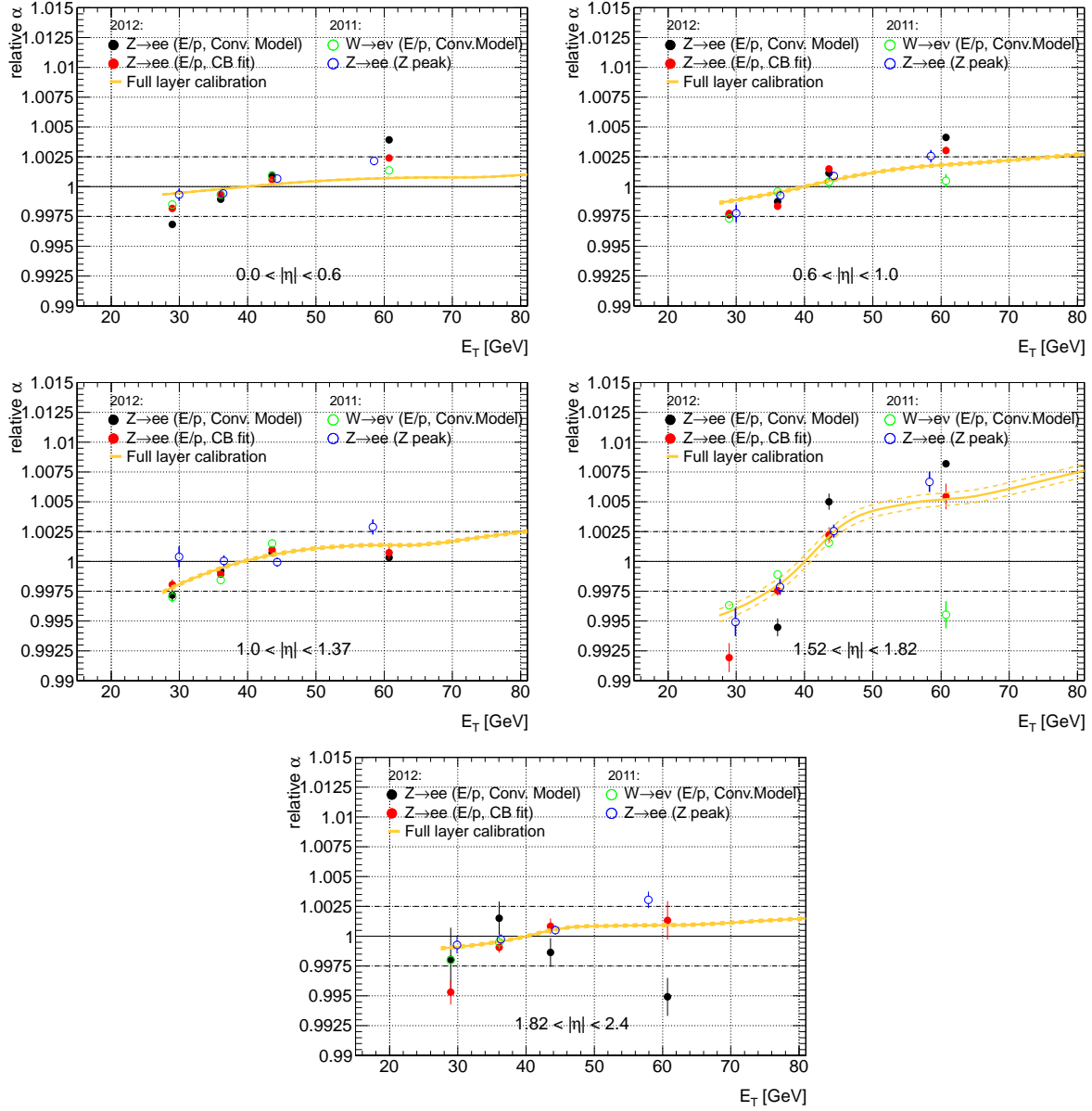


Figure 11.11: *Impact of the final layer calibration (α_{PS}, α_{S1}) on the measured linearity. The orange band is the ratio of the cluster energy (2012 dataset) with the layer energy corrected cluster energy - hence a prediction of the impact of the layer energy correction on the linearity. The open points are the linearity measurements of the 2011 dataset and the closed points the results of 2012.*

Chapter 12

Conclusion on the Final Energy Scale Correction

Due to the findings discussed in this thesis the scale correction $\alpha(\eta)$ (Equation 5.3), that was used to calibrate the electron energy scale for 2010 data [6], had to be supplemented by additional corrections.

In addition to the Z peak method, used to obtain results in 2010 [6], a new method extracting the energy scale from the ratio of the energy measured in the EM calorimeter to the momentum measured in the Inner Detector was introduced in Chapter 6.

However, before this method can be applied the different corrections discussed in the previous chapters have to be taken into account to obtain the best possible energy measurement. The scale correction $\alpha(\eta)$ that was extracted in Chapter 6 fixes the energy scale for electrons at a given η . Values of $\alpha(\eta)$ for the barrel obtained with 2012 data are summarized in Table 12.1.

$ \eta $	$\alpha(\eta)^{2012}$
0.0–0.2	$-0.28 \pm 0.011(\text{stat}) \pm 0.037(\text{non-closure})$
0.2–0.4	$-0.21 \pm 0.011(\text{stat}) \pm 0.053(\text{non-closure})$
0.4–0.6	$0.70 \pm 0.043(\text{stat}) \pm 0.072(\text{non-closure})$
0.6–0.8	$0.75 \pm 0.013(\text{stat}) \pm 0.073(\text{non-closure})$
0.8–1.0	$-0.05 \pm 0.020(\text{stat}) \pm 0.052(\text{non-closure})$
1.0–1.2	$0.64 \pm 0.023(\text{stat}) \pm 0.134(\text{non-closure})$
1.2–1.37	$1.03 \pm 0.013(\text{stat}) \pm 0.132(\text{non-closure})$

Table 12.1: $\alpha(\eta)$ for the 2012 dataset in the region $0.0 < |\eta| < 1.37$. Numbers are taken from Figure 6.15 in Chapter 6 and given in percent.

The mean energy of electrons coming from $Z \rightarrow e^+e^-$ and $W^\pm \rightarrow e^\pm \nu$ decays, used to calculate the scale correction, is about 40 GeV in E_T . This means that the energy scale for electrons with that specific energy is perfectly corrected. To measure the energy dependence of the scale correction above and below that energy, a scale correction for different values in E_T was extracted, as presented in Chapter 8. A non-linearity of about 0.5% per 10 GeV, on average in

η , was found.

Based on the findings of this thesis an overall scale correction needs to be defined including additional corrections, such as the lateral leakage (Chapter 9) as well as corrections due to material mismodeling (Chapter 10) and the Presampler energy and the layer energy calibration (Chapter 11). These additional scale corrections are derived as a function of η (the lateral leakage is also measured in E_T) with electrons of about ~ 40 GeV in E_T but as well energy dependent and hence contributing to the measured non-linearity. Their energy dependence needs to be extrapolated to energies below and above this energy with dedicated MC studies.

Taking the different corrections and their energy dependence into account an overall scale correction can be formulated:

$$\alpha_{\text{overall}}(E_T; \eta) = \alpha(\eta) + \sum_i \Delta\alpha_i(E_T; \eta), \quad (12.1)$$

$$i = \text{leak, mat, PS, S1}; \quad (12.2)$$

where $\alpha_{\text{overall}}(E_T; \eta)$ is the overall energy and η dependent energy scale correction, composed of the scale correction in η ($\alpha(\eta)$) obtained from the $Z \rightarrow e^+e^-$ and $W^\pm \rightarrow e^\pm \nu$ (E/p) samples and additional corrections $\alpha_i(E_T; \eta)$. For each additional correction, the scale correction averaged in η is subtracted at a transverse energy of about 40 GeV, to account for an absorption of effect i , written as $\Delta\alpha_i(E_T; \eta)$. The following additional corrections are currently considered:

1. $\Delta\alpha_{\text{leak}}(E_T; \eta)$ corrects for mismodeling of the electron energy fraction deposited outside the reconstructed electron cluster;
2. $\Delta\alpha_{\text{mat}}(E_T; \eta)$ accounts for passive material mismodeling;
3. $\Delta\alpha_{\text{PS}}(E_T; \eta)$ and $\Delta\alpha_{\text{S1}}(E_T; \eta)$ parametrize a potential miscalibration of the Presampler and the first calorimeter sampling relative to the second calorimeter sampling.

A schematic overview can be seen in Figure 12.1.

The transition region between the barrel and the end-caps ($1.37 < |\eta| < 1.52$) is not considered in the overall energy scale correction and excluded in most of the analyses using electrons. As explained in Section 6.5, from the calibration point of view a non-closure in MC simulation and a discrepancy in data between the E/p method and the Z peak is found.

The *final results* of the energy scale correction and its different energy dependent contributions can be seen in Figure 12.2 (compare with the uncertainties measured in 2010 shown for 2 regions in η in Figure 5.5) and are summarized in Table 12.2.

The contribution of the various corrections contribute differently depending on the region in η :

1. The data/MC difference of the *lateral leakage* provides a dominant contribution to the measured non-linearity throughout the pseudorapidity range. The difference between the two years is averaged and covered by the total uncertainty.

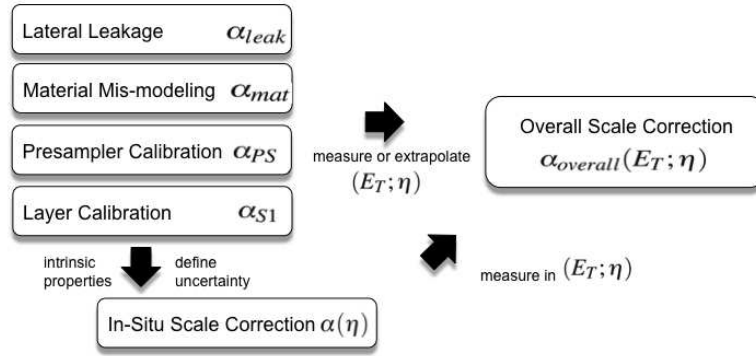


Figure 12.1: $\alpha(\eta)$ is extracted as a function of η with average electron energies of around 40 GeV. Four additional corrections need to be included: a lateral leakage correction (α_{leak}), a material correction (α_{mat}) and a Presampler (α_{PS}) and layer scale correction (α_{S1}). Their energy dependence is either extracted (as for the leakage correction) or needs to be extrapolated and compared to the measured non-linearity. All contributions result in an overall energy and η dependent energy scale correction: $\alpha_{overall}(E_T; \eta)$

2. The energy dependence of the *material corrections* is calculated with the distorted MC geometry configuration G' since the new data-driven MC description is currently in preparation (as described in Chapter 10). The G' material description is sufficient to estimate a conservative energy dependence due to a material mis-modeling. On average there is more additional material in the distorted material description w.r.t. the nominal MC as found in the data/MC comparison. A major contribution can be seen in the region $1.52 < |\eta| < 1.82$ where a local material increase from $0.1 X_0$ to $0.25 X_0$ is given in the G' geometry (see Figure 10.2 in Chapter 10).
3. The full *layer calibration* (including the Presampler energy and layer (E_1/E_2) energy calibration) contributes to the measured non-linearity at most in the region $1.52 < |\eta| < 1.82$, where the Presampler response is measured to be 10% lower in data than in the simulation.

The agreement between data and the energy dependent calibration effects (lateral leakage, material mis-modeling and full layer calibration) is typically within the range of the total uncertainty, except for a small number of outliers in the linearity measurements. In the future the calibration effects will be corrected already at the reconstruction level (updated material description in MC used for cluster calibration, corrected layer scales, corrected lateral leakage) and the residual non-linearity needs to be measured. This is being implemented at the moment and will be used for the final Higgs mass measurement and the W mass measurement.

	Lateral leakage	Material (G')	Full Layer Calibration ($\alpha_{\text{PS}}(\eta)$; $\alpha_{\text{S1}}(\eta)$)	Linearity (E/p; averaged)
$E_T \sim 40 \text{ GeV}$				
$0.0 < \eta < 0.6$	-1%	$0.025 X_0$	-2% ; -4%	-
$0.6 < \eta < 1.0$	-1%	$0.06 X_0$	-3% ; -3%	-
$1.0 < \eta < 1.37$	-0.7%	$0.09 X_0$	-3% ; -3%	-
$1.52 < \eta < 1.82$	-0.5%	$0.2 X_0$	-10% ; -1%	-
$1.82 < \eta < 2.47$	1%	$0.35 X_0$	- ; -1%	-
Effect per 10 GeV				
$0.0 < \eta < 0.6$	0.4%	0.2%	0.1%	0.3%
$0.6 < \eta < 1.0$	0.4%	0.3%	0.2%	0.3%
$1.0 < \eta < 1.37$	0.3%	0.4%	0.3%	0.4%
$1.52 < \eta < 1.82$	0.4%	1%	0.5%	0.9%
$1.82 < \eta < 2.47$	0.5%	0.3%	0.15%	0.4%

Table 12.2: Summary of the size of different extracted corrections (as measured in η and averaged) and its extrapolation to energies different than $E_T \sim 40 \text{ GeV}$. The extrapolations are given in the lower part of the table in percent per 10 GeV measured between 30 and 40 GeV and compared to the measured linearity in the rightmost column.

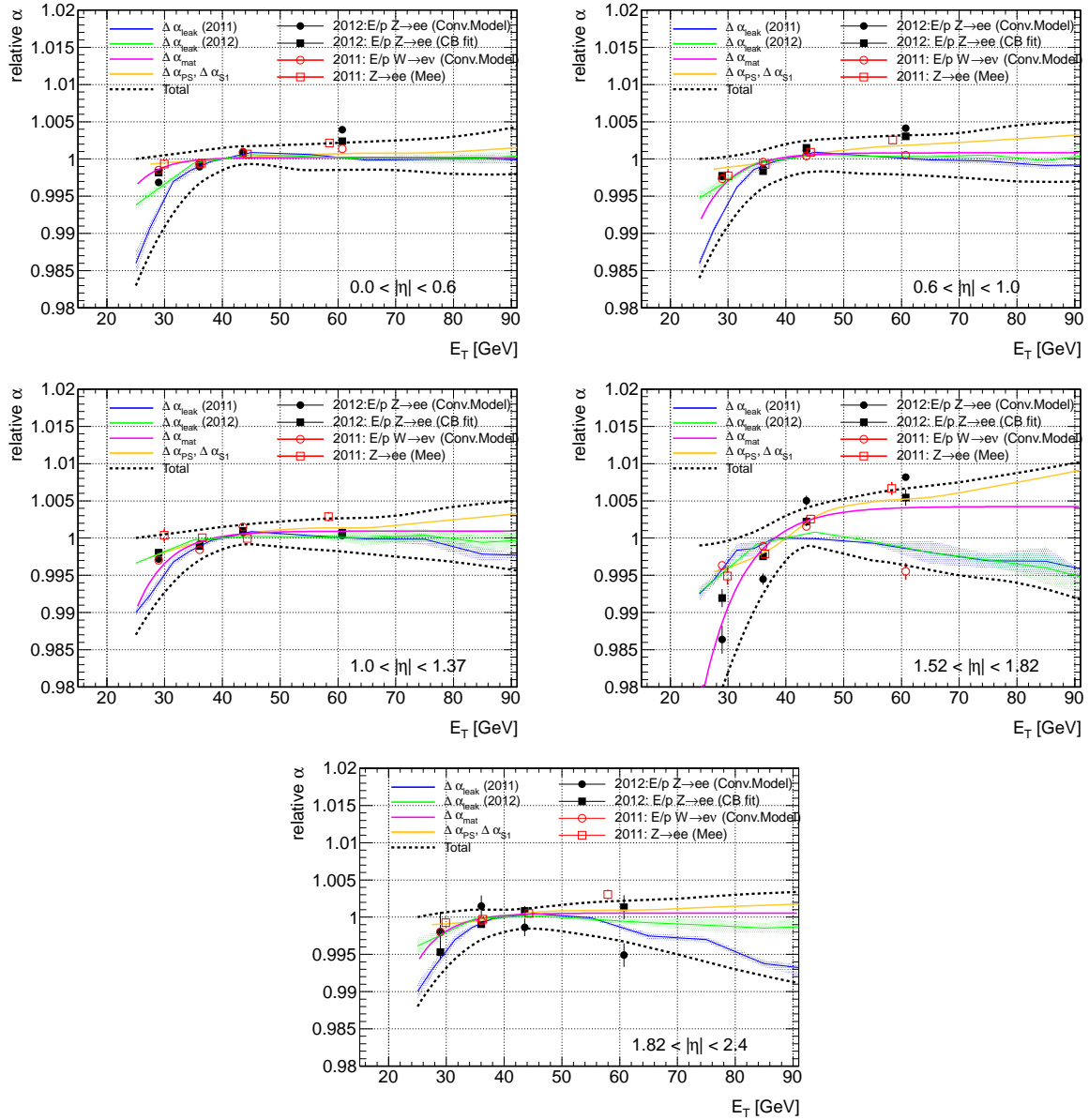


Figure 12.2: *Measured linearity (Chapter 8) and comparison with additional corrections based on the lateral leakage (α_{leak} , Chapter 9), passive material in front of the calorimeter (α_{mat} , Chapter 10) and the full layer calibration ($\alpha_{\text{PS}}, \alpha_{\text{S1}}$, Chapter 11). The open points are the measurements with 2011 data and the closed points are obtained with 2012 data. The average in-situ energy scale correction is subtracted and shifted to one for 40 GeV in E_T . The black dashed lines give the range of the total uncertainty of all corrections calculated with the quadratic sum of the individual uncertainties.*

Chapter 13

Measurement of the W Boson Mass

13.1 Overview

Improving the precision of Standard Model (SM) particle properties is one important part of the ATLAS physics program.

In the SM, quantum corrections to the mass of the W boson (M_W) are dominated by contributions depending on the mass of the top quark (M_{top}), the mass of the Higgs boson (M_H), and the fine-structure constant α [65]. A precise measurement of M_W and M_{top} therefore constrains M_H . Comparing this constraint with the mass of the recently discovered Higgs boson is a critical test of its nature and the consistency of the SM. The experimental precision on the measured M_W is currently the limiting factor on the constraints. Moreover, a precise measurement possibly diverging from predicted values could contribute to the discovery of new physics, since deviations break the inner consistency of the SM.

Amongst many precision measurements, the W boson mass is one of the experimentally most challenging, due to its nature of decay. Contrary to the Z mass, which can be easily measured in its decay channels into $e^+ e^-$ or $\mu^+ \mu^-$, the W boson dominantly decays into hadrons and into one lepton and one neutrino (ν). Since neutrinos escape without interacting with any of the sub-detector, they can only be characterized by missing energy reconstructed in the transverse plane (E_T^{miss} , see Section 4.6). Therefore it is impossible to obtain the W mass directly by reconstructing the invariant mass of the lepton and the neutrino. It must be measured using data-MC comparisons of kinematic variables such as the transverse mass $m_T^\ell = \sqrt{2p_T^\ell p_T^\nu (1 - \cos \Delta\phi)}$, where $\Delta\phi$ is the opening angle between the lepton and neutrino momenta in the plane transverse to the beam, the transverse momentum (p_T) or E_T^{miss} . One key aspect of the measurement is the correct calibration of the lepton energy scale.

The W boson mass has been measured by the CDF and D0 collaborations [66]. An unprecedented accuracy was achieved by the CDF measurement with 2.2 fb^{-1} of data in the electron and muon channels and by the D0 measurement in the electron channel using data corresponding to 4.3 fb^{-1} : $M_W = 80387 \pm 16 \text{ MeV}$, leading to a new world-average of $M_W = 80385 \pm 15 \text{ MeV}$. To further improve the accuracy of the W boson mass is a challenge for the two LHC experiments. Even though the higher integrated luminosity with respect

to CDF and D0 will help to further reduce statistical and systematic uncertainties, the much higher pile-up deteriorates dramatically the resolution of the E_T^{miss} measurement. The results of the last decades are summarized in Figure 13.1. The systematic uncertainties of the CDF measurement are summarized in Table 13.1.

The methodology of the W boson mass measurement will be outlined in Section 13.2. The impact of the non linearity measured in Chapter 8 will be discussed in Section 13.4 and conclusions on the findings will be drawn.

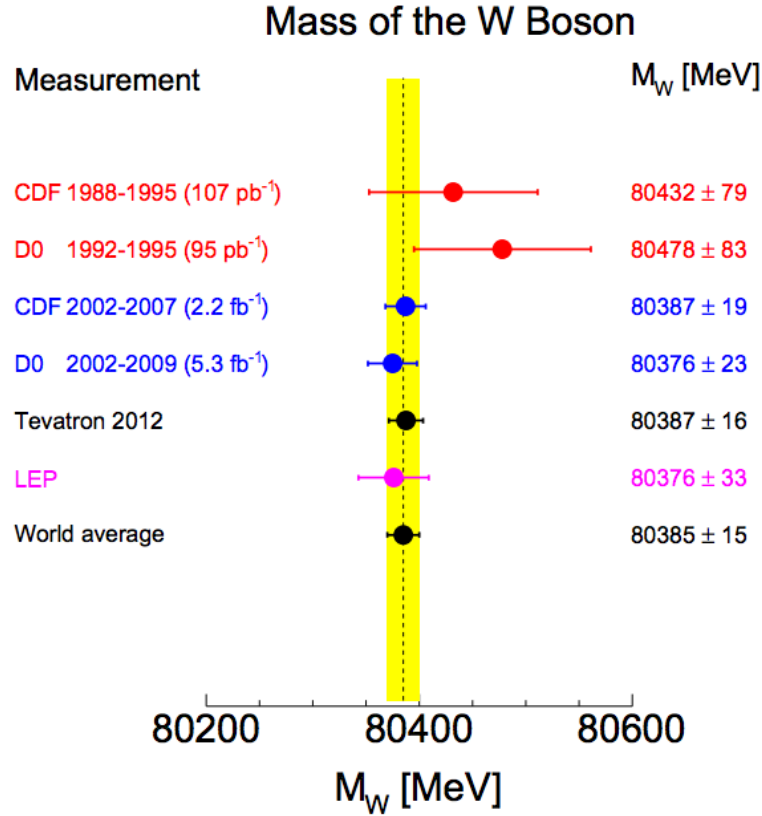


Figure 13.1: M_W measured by different experiments. The world-average is obtained by combining the Tevatron and LEP averages assuming no correlations between them. The world-average uncertainty (15 MeV) is indicated by the shaded band. Taken from Ref. [66].

13.2 The Templates Method

The W boson mass is extracted from so-called template fits. The distributions of five observables are predicted with MC simulations. These templates are produced for different kinematic observables for M_W and then compared to data using a χ^2 fit [64]. The best fitting template (per observable), determined by the smallest χ^2 between the template and the data distribution, is then associated with the input W mass. Observables used for the measurement are: transverse missing energy (E_T^{miss}), transverse mass (m_T), and the transverse momentum (p_T) of either the

Systematic uncertainty (MeV)	Electrons	Muons	Common
Lepton Energy Scale	10	7	5
Lepton Energy Resolution	4	1	0
Recoil Energy Scale	6	6	6
Recoil Energy Resolution	5	5	5
Lepton Removal	0	0	0
Backgrounds	3	5	0
$p_T(W)$ model	9	9	9
Parton Distributions	9	9	9
QED radiation	4	4	4
Total	19	18	16

Table 13.1: Break down of the different systematic uncertainties on the W mass measurement from the CDF collaboration (no statistical error incorporated). Taken from Ref. [67].

electron ($p_T^{e^-}$) or the positron ($p_T^{e^+}$) or without selection on the charge.

The template distributions for different values of M_W are produced by reweighting simulated events. These weights are determined by the Breit-Wigner-Probability density function for each of the generated value of M_W [68].

Once a template is generated, it is compared to the data or pseudo-data distribution with a χ^2 test (explained more detail in Section 13.4 and [64]). The obtained χ^2 values are plotted as a function of the W boson mass and then fitted with a parabola. Consequently, the minimum point of the parabola is the best template corresponding to the best fitted W mass. This procedure is illustrated in Figure 13.2.

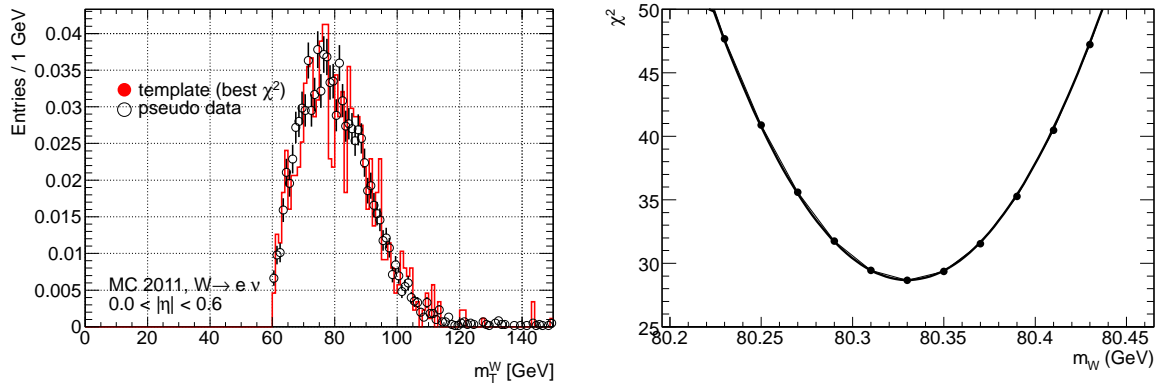


Figure 13.2: Left: Overlay of the generated template for m_T (red) with data (open black markers) for the best χ^2 . Right: Example of χ^2 values as function of the tested value of M_W . Each point represents a comparison between the data and the template distribution obtained for a given M_W . The curve is then fitted with a parabola. Taken from Ref. [69].

Monte Carlo simulations are used to predict the lineshape of the template distributions. These template predictions depend on a number of physics and detector effects constrained

by control samples or simulation. The important systematic uncertainties include lepton energy calibration, charge dependent corrections, momentum scale, resolution, reconstruction efficiency, trigger efficiency. From the physics point of view the following systematic effects need to be considered as well: hadronic recoil¹, all possible backgrounds, Next-to-Next-To-Leading-Order (NNLO) corrections. The simulated samples need to have next-to-leading-order (NLO) precision and need to include electroweak corrections.

The muon momentum calibration, the hadronic recoil calibration as well as the systematic uncertainties coming from physics processes are not subject to this thesis, therefore they are not explained here in detail. Further information is given in [70].

13.3 Event Selection

For this study the official nominal ATLAS MC simulation, with a value of $M_W = 80399 \pm 23$ MeV at generator level, is used. To study the effect of the measured non-linearity on the W mass, the results obtained in Chapter 12 are implemented in the electron energy reconstruction. The MC sample is split in half, one half serves as pseudo data and the other half is used to generate the templates. The datasets that have been used are summarized in the Appendix D. The final selections are summarized in Table 13.2.

Selection	cut
Electron Author	1 or 3 (to avoid electrons from conversions)
Acceptance	$ \eta < 2.4$ $ \eta < 1.37$ or $ \eta > 1.52$
Object Quality	pass
ID menu	<i>tight</i> ++
Electron p_T	$p_T^{\text{el}} > 30$ GeV
W mass	$m_T^W > 60$ GeV
Missing Energy	$E_T^{\text{miss}} > 30$ GeV
Jet Cleaning	<i>loose</i>

Table 13.2: $W^\pm \rightarrow e^\pm \nu$ selection cuts.

13.4 Impact of Non-Linearity on the W mass measurement

Based on the findings in Chapter 8 only events for $|\eta| < 1.37$ are considered. To estimate the effect of the non linearity measured with 2011 data, the W mass is fitted for two cases:

¹The hadronic recoil is the vector sum of transverse energy over all calorimeter towers, where the towers associated with the leptons are explicitly removed from the calculation. The response of the calorimeter to the recoil is described by a response function which scales the true recoil magnitude to simulate the measured magnitude. The hadronic resolution receives contributions from initial state radiation (ISR) jets and the underlying event.

- MC closure: templates are generated with the nominal MC and compared to a statistically independent set of pseudo-data also obtained from nominal MC.
- Linearity: templates are generated with the nominal MC and the non-linearities based on 2011 data are incorporated to pseudo-data. The same sample is used for the templates and the pseudo-data, hence the statistical errors are 100% correlated.

Three different types of templates are generated (transverse mass (m_T), and transverse momentum (p_T) of the electron and the positron) with ten deviations from the W mass in nominal MC in per-cent:

$$\{-0.1, -0.07, -0.05, -0.03, -0.01, 0, 0.01, 0.03, 0.05, 0.07, 0.1\}$$

As already mentioned, the impact of the non linearity is, amongst others, a systematic contribution to the final W mass measurement. This effect was tested incorporating the measured non-linearity of 2011 data in pseudo data, while generating the templates from nominal MC.

For each of the ten variations of the W mass a template is generated (in different η regions and variables) and compared by a χ^2 test to pseudo data distributions, either from nominal MC or MC with a non linear energy response according to the measured non linearity in 2011. An example of a parabola fit to different χ^2 values for one template variable can be seen in Figure 13.3.

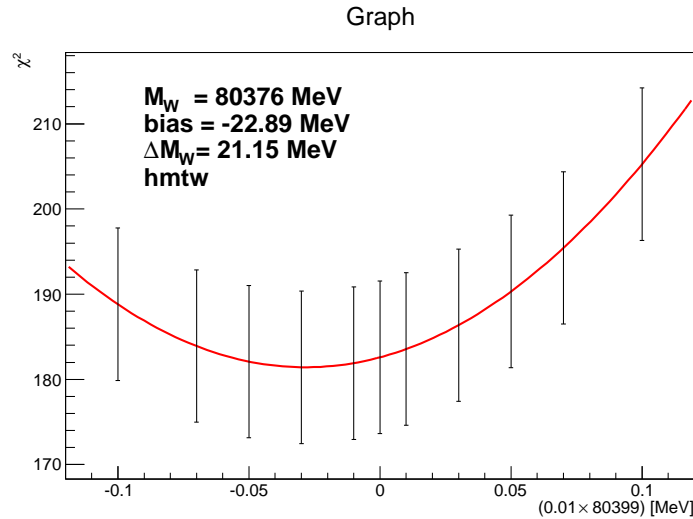


Figure 13.3: Example parabola fit of the variable m_T for different χ^2 values obtained from the templates generated with nominal MC and tested on pseudo-data (MC with incorporated (measured) non-linearity). The x-axis shows the variation of the W mass in per-cent of its nominal value, the y-axis the obtained χ^2 per variation. A non-linearity of the energy scale in pseudo-data manifests itself in large values of χ^2 .

For the above procedure to work in practice, three variables in one η -region are used: m_T , $p_T^{e^-}$, $p_T^{e^+}$. The best χ^2 as a function of the W mass for three templates is obtained by a parabola fit. To estimate the systematic effect of the template generation, a MC closure test is performed. The MC sample is split into two parts, where one half was used to generate the template distributions while the other half served as pseudo-data. As seen in Figure 13.4 (left) a very good closure is obtained. When incorporating the non-linearity from Chapter 8 the results presented in Figure 13.4 (right) are obtained.

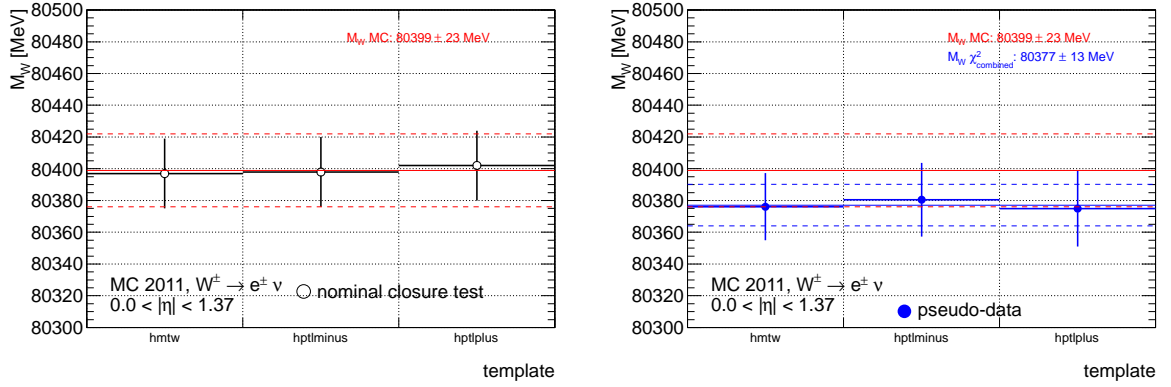


Figure 13.4: M_W calculated for $|\eta| < 1.37$ from the best χ^2 (parabola fit) for three templates: m_T (hmtw), $p_T^{e^-}$ (hptminus), $p_T^{e^+}$ (hptplus). Left: Results of a MC closure test in black. The red straight line is M_W for MC simulation on generator level. The dashed line is its associated error. Right: the measured non linearity of 2011 data is incorporated in pseudo-data (blue points). The blue line is the obtained M_W of the global χ^2 fit and the dashed blue lines are its error. The non-linearity induces a downwards shift of about 22 MeV w.r.t. the generated mass. Red: value of M_W in MC simulation on generator level.

To obtain an estimation of the W mass with all the three observables combined a global χ^2 fit is used. For each variation on the W mass the obtained χ^2 values (and its errors) are summed up and fitted with a parabola. The minimum of this parabola and (its error) gives the combined-overall W mass. As seen in Figure 13.4 (right), a non-linearity as measured with 2011 and 2012 data (compare to Chapter 8) induces a systematic shift of 22 MeV on the measurement of the W mass. Although the value of M_W is measured here with a statistical error of 13 MeV the measurement of the shift between perfect linearity and assumed non-linearity is much more precise since the shift was extracted with the same statistical sample. The statistical uncertainties of M_W with and without non-linearity are therefore 100% correlated.

To avoid this systematic effect on the W boson mass measurement, the non-linearity has to be corrected. The measurements presented in Chapter 12 will be used for the final W boson mass measurement and all other precision measurements. Without correcting the non-linearity, the measured W boson mass is off by 22 MeV and the uncertainty on the measurement would be too large to compete with the latest results measured by the Fermilab Tevatron Collider.

Chapter 14

Conclusions

For the calibration of the energy of the electromagnetic calorimeter I developed a method that allows to intercalibrate the energy scale of the electromagnetic calorimeter with the momentum scale of the Inner Detector by deriving a scale correction. This method uses the E/p distributions of electrons and positrons from $W^\pm \rightarrow e^\pm \nu$ and $Z \rightarrow e^+ e^-$ decays. The final result is obtained by a fit to the E/p distribution with a function which is a convolution of the detector response functions of the calorimeter and the Inner Detector.

The energy scale correction (in addition to the Z calibration) for the 2011 and 2012 dataset in 1D (binned in η) was obtained with the described “Convolution Model”. The scale correction was found to be precise on the per mill level (depending on the region) and in very good agreement with other calibration procedures. I estimated systematic errors coming from the description of the energy response in the calorimeter and included the systematics of the measured momentum of the ID. Apart from many other checks, Monte Carlo datasets with an artificially distorted material description were used to estimate any bias of a wrong material description on the energy scale extraction. To this end, additional material in front of the detector during detector simulation was added.

By extracting the E/p scale correction (using the developed “Convolution Model”) I was able to measure the linearity of the calorimeter energy response in the energy range of 20 to 100 GeV for the first time in ATLAS. Ultimately, four different methods measuring the calorimeter’s linearity in five regions of the detector (bins in η) were compared. Very good agreement between the different methods was obtained. Different causes such as the Presampler energy scale, residual Inner Detector misalignment ($1/p$), material effects using distorted MC samples and systematic uncertainties of the Convolution Model were studied and compared to the measured non-linearity.

One possible cause of the measured non-linearity was identified to be the inadequate simulation of the out-of-cluster energy deposit (lateral leakage). Therefore, I undertook a study comparing shower shapes in data and MC to investigate any difference which could result in the measured non-linearity. To estimate the lateral leakage (coming from underestimated shower width in MC), isolation cones were studied. The differences between MC and data using the information of electron isolation cones for different pile-up and η bins were studied to extract the pile-up

independent lateral leakage. This lateral leakage shows an underestimation of the shower widths in the MC simulation and can therefore partially explain the measured non-linearity.

I investigated the stability and uniformity of the energy response as a function of time and pile-up for the whole 2011 and 2012 datasets using E/p of electrons coming from $W^\pm \rightarrow e^\pm \nu$. For the stability measurement, the E/p distribution was binned in time and fitted with a Crystal Ball function. The extracted most probable value was then compared to the stability of the Z peak, and again very good agreement was found. I also showed that the energy response with pile-up is stable within a few per mill, which showcases the very good performance of the LAr calorimeter and the calibration (especially for 2012, where pile-up of up to 30 events has been observed). It was shown that the energy response was stable within 0.02% over the whole year of 2012. The uniformity was investigated in fine η and ϕ regions (on the cell level) to measure any residual effect on the effective constant term. Again, the E/p distribution was fitted with a Crystal Ball function and the extracted most probable value was then compared to the uniformity of the Z peak. For the 2011 dataset the two methods were in a very good agreement with each other. Inhomogeneities in different regions of the energy response were found, such as the Inter Module Widening effect.

The overall goal was a calibration of the energy scale and linearity to better than 0.1%. The extensive work on the calibration of the EM calorimeter will translate into an exceptionally small EM energy scale uncertainty for many precision measurements. This thesis contributed to a very large extent to this achievement and hence will be an important ingredient for many physics measurements within ATLAS. To correct the energy scale, the non-linearity and the non-uniformities, packages were added to the official `ElectronPhotonFourMomentumCorrection` tool (formerly known as the `EnergyRescalerTool`), used throughout the ATLAS analyses groups to correct the electron energy in data and smear the resolution in MC. This tool was used to calibrate the electron energy for the mass measurement of the newly discovered Higgs boson. The systematic uncertainty on the mass of the Higgs particle comes mainly from the electron energy scale uncertainties. These uncertainties were estimated with results obtained within this thesis.

I contributed to the W mass precision measurement (with 2011 data), where the goal is to reach an accuracy comparable or better than that of the Tevatron, i.e. better than 0.02%. To measure the mass of the W boson amongst many other effects, the linearity of the electron energy measurement in a region of 20 to 80 GeV is crucial. I used the derived energy scale and linearity from the E/p distribution and studied their impact with MC simulated pseudo data. The effect of the non-corrected (non-) linearity on the W mass was estimated to be around 22 MeV.

Appendix A

The $Z \rightarrow e^+e^-$ Invariant Mass Peak

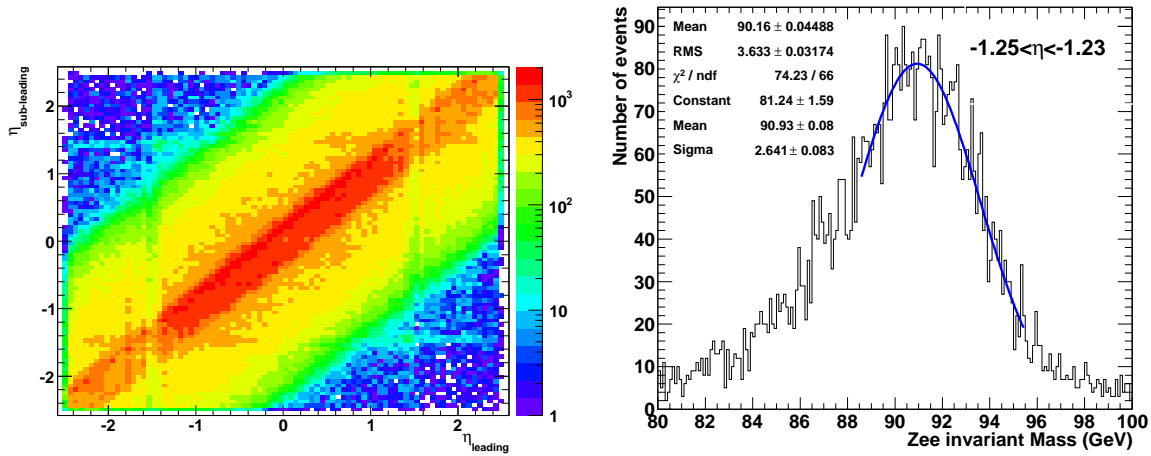


Figure A.1: Left plot shows the η correlations of the two electrons coming from $Z \rightarrow e^+e^-$ events. The right plot shows an example of a $Z \rightarrow e^+e^-$ distribution and its peak fit with a gaussian in η region: $-1.25 < \eta < -1.23$.

In this method, the leading electron (higher momentum) is selected in the region of interest whereas no selection is done on the sub-leading one. Hence, the sub-leading will be from any random region of the whole calorimeter acceptance. As shown on Figure A.1, due to the kinematic correlations between the two electrons from $Z \rightarrow e^+e^-$ decays, this is in reality not an uniform average. In fact, the Z often is boosed and the two electrons tends to be both either in the positive η region or in the negative one. Events selected for this study follow the baseline cuts of the calibration ntuples for the $Z \rightarrow e^+e^-$ events (see Table 6.1). Additionally, the crack regions ($1.37 < |\eta| < 1.52$) are removed and a cut on the di-electron invariant mass is applied to enrich the sample with real Z decay events: only events with $80 < m_{ee} < 100$ GeV are selected.

To define the invariant mass peak of $Z \rightarrow e^+e^-$ events two methods are used:

1. the mean value M in a given mass range (i.e. $[80 - 100 \text{ GeV}]$) is taken as an estimator of the peak. This method is sensitive to the tails of the distribution.

2. a gaussian fit to the peak in a window $[M - 0.5 \sigma, M + 1.5 \sigma]$ gives another estimation of the mass peak position being less sensitive to tails. (see Figure A.1).

The energy correction factor α_{Mee} is defined as:

$$\alpha_{Zee} = \frac{M_{data}}{M_{MC}} - 1 \quad (\text{A.1})$$

Appendix B

Energy Scale from the $Z \rightarrow e^+e^-$ Lineshape

The invariant mass of a reconstructed $Z \rightarrow e^+e^-$ candidate is computed as :

$$M = \sqrt{2E_1E_2(\cosh(\eta_1 - \eta_2) - \cos(\phi_1 - \phi_2))} \quad (\text{B.1})$$

where E_1 and E_2 are the energies of the two electrons measured by the calorimeter and $\eta_1, \phi_1, \eta_2, \phi_2$ the electron angles measured by the tracker. Differences between the energy calibration in data and simulation are parameterized in the following way:

$$E^{data} = E^{MC}(1 + \alpha_i) \quad (\text{B.2})$$

where E^{data} and E^{MC} are the electron energies in data and simulation, and α_i represents the electron scale factors, in a range in pseudorapidity labeled i . Neglecting second-order terms and supposing that the angle between the two electrons is perfectly known, the effect on the di-electron invariant mass is:

$$M_{ij}^{data} \simeq M_{ij}^{MC} \left(1 + \frac{\alpha_i + \alpha_j}{2}\right) \equiv M_{ij}^{MC} (1 + \beta_{ij}) \quad (\text{B.3})$$

Both methods described below categorize the event sample according to (η_1, η_2) and determine the corresponding β_{ij} corrections. The following linear system is then solved:

$$\beta_{ij} = (\alpha_i + \alpha_j)/2, \quad (\text{B.4})$$

yielding the α_i . The first method to determine the $\beta_{i,j}$ consists in minimizing the following unbinned log-likelihood:

$$-\ln L_{\text{tot}} = \sum_{k=1}^{N_{\text{events}}} -\ln L_{ij} \left(\frac{M_k}{1 + \beta_{i,j}} \right) \quad (\text{B.5})$$

where $0 < i, j < N_\eta$, N_η is the number of regions considered for the calibration, N_{events} is the total number of selected events and $L_{ij}(M)$ is the probability density function (PDF) quantifying the compatibility of an event with the expected Z boson line shape at the reconstruction level, when the two electrons fall in regions i and j . The PDF is obtained from the MC simulation, which takes into account experimental and theoretical effects defining the Z line-shape. Histograms are built from the simulation in the range $70 < M_{ee} < 110$ GeV. The $L_{ij}(M)$

are produced separately for each (η_i, η_j) . The fit is performed in the range $80 < M_{ee} < 100$ GeV.

The second method is well described in [71, 69]. A set of template histograms are first created for each (η_i, η_j) from the simulation, adding scale perturbations to the reconstruction-level quantities, with a range covering the expected uncertainty and in narrow steps. As for the lineshape fit method described above, templates are built separately for the various electron pseudorapidity configurations.

Analog distributions are built from data. A set of χ^2 tests is performed between data and the corresponding templates, resulting in a function of the injected energy scales. The function is parabolic near its minimum, and the parameters of the parabola determine β_{ij} and its uncertainty for this configuration.

Both methods are illustrated in Figure B.1, for example (η_i, η_j) categories.

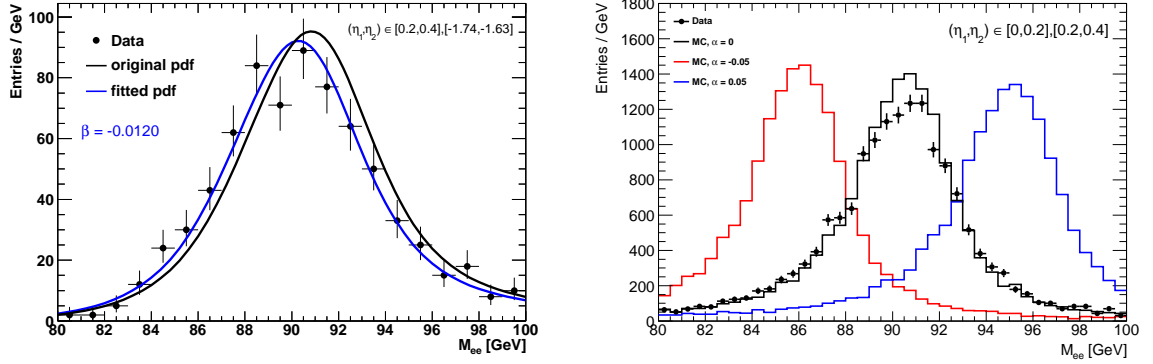


Figure B.1: Left : example likelihood fit for $(\eta_i, \eta_j) = ([0.2, 0.4], [-1.74, -1.63])$. Right : data and example energy scale templates for $(\eta_i, \eta_j) = ([0.2, 0.4], [0.2, 0.4])$.

Appendix C

Intermodule Widening Effect

In Figure C.1 the most probable value of the variable E/p is drawn as a function of the azimuth of the electron probe. To increase the statistical precision, the periodicity of the modules of the barrel calorimeter is used. The ϕ -bin size is $2\pi/1024$, in order to see more precisely any cell-structure. The positive and negative azimuths are separated.

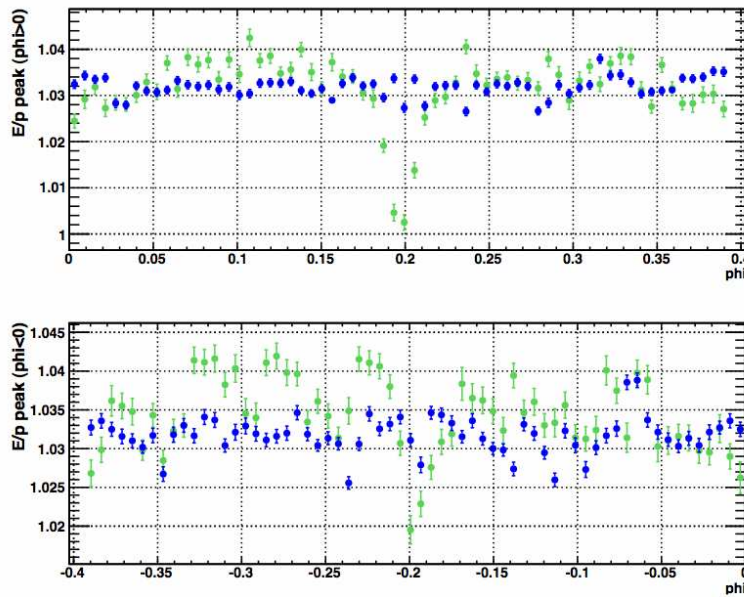


Figure C.1: *Evolution of the E/p most probable value for positive (top) or negative (bottom) azimuths for the data (green) and nominal MC (blue) as a function of ϕ in barrel calorimeter when all 16 modules are averaged.*

The data and MC disagree in the region $\phi \sim 0.2$, both in positive and negative ϕ . The size of the discrepancy is different: $\sim 3.5\%$ (resp. $\sim 1.5\%$) for $\phi > 0$ (resp. $\phi < 0$). The drop in E/p follows the typical inter-modules localization, and this suggests a loss of energy in data due larger LAr gaps between the modules.

The gap size uniformity has been probed with the measurement of the electron drift time in the liquid argon from cosmic events and found to be good along pseudorapidity [72]. The

uniformity of the drift time along the azimuthal angle has also been checked with cosmic muons and collision data [73]. A similar periodical ϕ asymmetry has been found.

The ϕ -dependence observed in Figure C.1 is further investigated. The barrel is divided in four parts each containing four modules: $\pi/4 < \phi < 3\pi/4$ (top), $-3\pi/4 < \phi < -\pi/4$ (bottom), $-\pi/4 < \phi < \pi/4$ (right) and $-3\pi/4 < \phi < 3\pi/4$ (left). The E/p most probable value extracted in these four regions for the data is shown in Figure C.2.

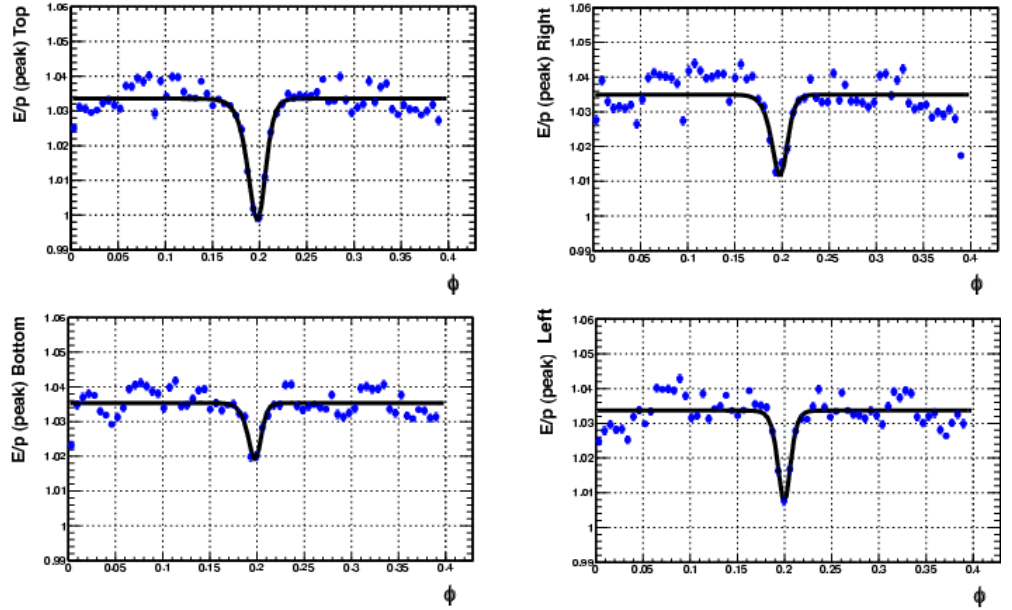


Figure C.2: Evolution of E/p MPV value for the data (blue points) as a function of ϕ in the barrel calorimeter. 4 modules averaged in each plot: $\pi/4 < \phi < 3\pi/4$ (top), $-3\pi/4 < \phi < -\pi/4$ (bottom), $-\pi/4 < \phi < \pi/4$ (right) and $-3\pi/4 < \phi < 3\pi/4$ (left). The black line corresponds to the Double Fermi-Dirac fit on the data (see text).

The top and bottom parts of the calorimeter have the maximal ($\sim 3.5\%$) and minimal ($\sim 1.5\%$) deviations, respectively in the inter-modules, whereas the two sides have intermediate deviations ($\sim 2.5\%$). This is interpreted as a widening of the barrel inter-module gaps, modulated by a mechanical sagging effect. The top part of the calorimeter has larger gaps because the sagging of the absorbers under gravity tends to widen them.

A correction for this effect has been derived, using the E/p variable. The holes observed in data

are fitted with a Double Fermi-Dirac (DFD) function:

$$f(\phi) = A - B \cdot \frac{1}{1 + e^{C \cdot (\phi - 0.2)}} \cdot \frac{1}{1 + e^{-D \cdot (\phi - 0.2)}} \quad (\text{C.1})$$

with A the averaged value on either sides of the hole, B the hole depth and C and D the hole width. This provides four sets of coefficients (A, B, C, D). The result of the fit is seen in Figure C.2, in black line.

The electron energy is corrected with this function $f(\phi)$, and the correction size in GeV as a function of ϕ is illustrated in Figure C.3 for electrons with $p_T = 40$ GeV. The corrected uniformity measurements (as presented in Chapter 7) are shown in Figure C.4.

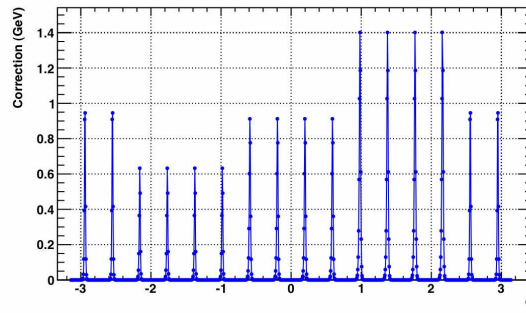


Figure C.3: *Size of the correction of the energy in GeV as a function of ϕ , for an electron with $p_T = 40$ GeV.*

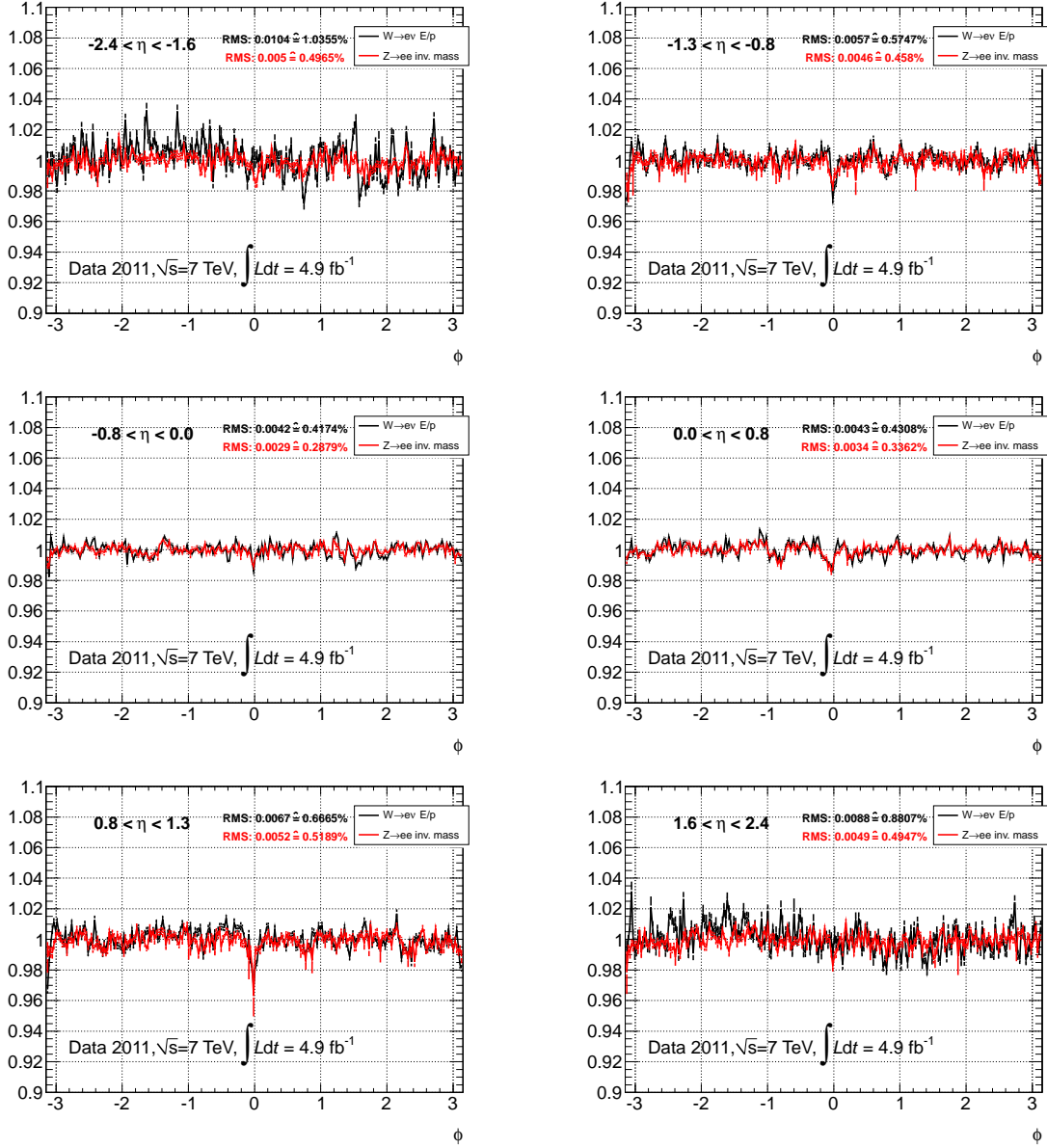


Figure C.4: Uniformity in data in narrow ϕ bins after Intermodule Widening effect correction. This effects only affects a region in $0 < |\eta| < 1.3$. Both methods follow very similar shapes of inhomogeneities although some are not completely understood. The quoted RMS show that these effects have not a large contribution to the constant term.

Appendix D

Event Selection and Used Tags

D.1 Monte Carlo Sample Generation

A summary of the events generated for both years can be found in Table D.1. The tags used for the MC production in 2011 and 2012, as found in the ATLAS database, can be found in Table D.2.

D.2 Data Sample

An overview of the different data taking tags and calibration ntuples versions are given in Table D.3.

D.3 General Selection Cuts

In order to reduce the background, clean up the signal electrons and be consistent with the current Standard Model analyses different cuts on the electron selection were used. A general

Geometry	Process	Statistics	Generator	Dataset Number
2011				
nominal	$W \rightarrow e\nu$	MC11a: 20M; MC11b,c: 40M	PYTHIA	106043
nominal	$Z \rightarrow ee$	MC11a,c: 10M; MC11b: 1M	PYTHIA	106046
2012				
nominal	$W^+ \rightarrow e^+\nu$	23 000 000	PYTHIA/POWHEG	147800
nominal	$W^- \rightarrow e^-\nu$	17 000 000	PYTHIA/POWHEG	147803
nominal	$Z \rightarrow ee$	10 000 000	PYTHIA/POWHEG	147806
distorted	$W^+ \rightarrow e^+\nu$	3 000 000	PYTHIA/POWHEG	147800
distorted	$W^- \rightarrow e^-\nu$	2 000 000	PYTHIA/POWHEG	147803
distorted	$Z \rightarrow ee$	5 000 000	PYTHIA/POWHEG	147806

Table D.1: Summary of the MC samples (nominal and distorted) used in this thesis mentioning the generator and the number of events on the generator level.

	Simulation	Reco+Digi	AOD Merging
MC11a (nom)	s1299	r2732 (tight trigger) or r2729 (loose trigger)	r2700
MC11b (nom)	s1299 or s1310	r2934 (tight trigger) or r2935 (loose trigger)	r2900
MC11c (nom)	s1272, s1274, s1299 or s1310	r3043 (tight trigger) or r3044 (loose trigger)	r2993
MC11a (dist)	s1356 or s1353	r2732 (tight trigger) or r2729 (loose trigger)	r2780
MC11b (dist)	s1356 or s1353	r2934 (tight trigger) or r2935 (loose trigger)	r2900
MC11c (dist)	s1356 or s1353	r3043 (tight trigger) or r3044 (loose trigger)	r2993
MC12 (nom)	s1468, s1469 or s1479	r3542, r3658 and r3754	r3549
MC12 (dist)	s1472, s1482, s1486 or s1479	r3542 and r3658	r3549

Table D.2: Summary of the different tags for reconstruction and simulation of the MC samples for the years 2011 and 2012. Remark: in 2011 three MC productions were done (MC11a,b,c).

Calib Ntuple	Run Number	Reconstruction Tag	Period
2011 (<i>data11.7TeV</i>)			
v12 / v17	177986 - 187815	from <i>r2603_p659_p768</i> to <i>r2713_p705_p768</i>	A - K
v12 / v17	188902 - 191933	from <i>f403_m975_p768</i> to <i>f415_m1025_p768</i>	L - M
2012 (<i>data12.8TeV</i>)			
v17	200804 - 209899	from <i>f437_m1126_p1032_p1033</i> to <i>f475_m1223_p1032_p114</i>	A - E (HCP dataset)
v18	200804 - 213314	<i>r4065_p1278_p1344_p1345</i>	A - H
v18	213479 - 216432	from <i>f482_m1238_p1344_p1345</i> to <i>f507_m1271_p1344_p1345</i>	I - M
v18_19	200804 - 201556	<i>r4644_p1517_p1562</i>	A (reprocessed)

Table D.3: Data samples used for both years (2011 and 2012) mentioning the different data collection periods and tags.

cut-flow, which most of the studies in this thesis follow is presented here. In Table D.4 general selections for electrons coming from $W^\pm \rightarrow e^\pm \nu$ decays can be seen. Table D.5 shows selection criteria on electrons coming from $Z \rightarrow e^+ e^-$.

cut1	Trigger	if run < 186873: <i>EF_e20_medium</i>
	Trigger	if run < 188902: <i>EF_e22_medium</i>
	Trigger	else <i>EF_e22vh_medium1</i> or <i>EF_e45_medium1</i>
cut1	Trigger	if run > 200804: <i>EF_e22vh_medium1</i>
	Trigger	if run > 200804: <i>EF_e45_medium1</i>
	Trigger	if run > 200804: <i>EF_e24vhi_medium1</i>
	Trigger	if run > 200804: <i>EF_e60_medium1</i>
cut2	Electron Object Quality (<i>el_OQ</i>) applied	
cut3	Electron author: 1 or 3 for W	
cut4	<i>el_et</i> > 25 GeV	
cut5	Electron ID: <i>medium</i> ++	
cut6	<i>MET</i> (LocHadTopo) > 25 GeV	
cut7	<i>M_T</i> > 40 GeV	
cut1	GRL	
cut2	<i>el_Etcone30_pt_corrected</i> < 6 GeV	
cut3	<i>el_et</i> > 30 GeV	
cut4	<i>el_trackpt</i> > 30 GeV	
cut5	<i>MET_LocHadTopo_et</i> > 30 GeV	
cut6	<i>m_T</i> > 60 GeV	
cut7	<i>el_cl_eta</i> > 2.47	
cut8	Electron ID: <i>tight</i> ++	

Table D.4: General $W^\pm \rightarrow e^\pm \nu$ selection cuts performed in 2 steps.

cut1	Trigger	if run < 186873: <i>EF_e20_medium</i>
	Trigger	if run < 188902: <i>EF_e22_medium</i>
	Trigger	else <i>EF_e22vh_medium1</i> or <i>EF_e45_medium1</i>
cut1	Trigger	if run > 200804: <i>EF_e22vh_medium1</i>
	Trigger	if run > 200804: <i>EF_e45_medium1</i>
	Trigger	if run > 200804: <i>EF_e24vhi_medium1</i>
	Trigger	if run > 200804: <i>EF_e60_medium1</i>
cut2	Electron Object Quality (<i>el_OQ</i>) applied	
cut3	Electron author: 1 or 3 for W	
cut4	<i>el_pt</i> > 7 GeV	
cut5	Electron ID: <i>medium</i> ++	
cut6	Electron pairs: opposite charge	
cut7	<i>M_{ee}</i> > 50 GeV	
cut1	GRL	
cut2	80 GeV < <i>M_{ee}</i> < 100 GeV	
cut3	<i>el_trackpt</i> > 37 GeV	
cut4	<i>el_cl_eta</i> > 2.47	
cut5	Electron ID: <i>medium</i> ++	

Table D.5: General $Z \rightarrow e^+ e^-$ selection cuts performed in 2 steps.

D.4 Ratio of Calorimeter Energy and Inner Detector momentum, E/p

- Pythia identifier: 106043 (Wenu), production tags: `e815_s1272_s1274_r3043_r2993_p833`
- $5.6 \cdot 10^6 W^\pm \rightarrow e^\pm \nu$ events after all cuts
- Boson- p_T , Vertex and Pile-up reweighting on MC events are applied

This covers the following data periods and production tags:

- Data periods: B-M, production tag: p768

	MC	data
overall events	$40 \cdot 10^6$	–
after cut step 1	$11.2 \cdot 10^6$	$32.01 \cdot 10^6$
after cut step 2	$5.62 \cdot 10^6$	$13.92 \cdot 10^6$

Table D.6: Number of residual $W^\pm \rightarrow e^\pm \nu$ events after applying the cuts mentioned before for the 2011 dataset and MC simulation.

D.5 Linearity of Energy Response

- ATLAS MC: `mc11_7TeV`, PYTHIA identifier: 106046 ($Z \rightarrow e^+ e^-$), 106043 ($W^\pm \rightarrow e^\pm \nu$), production tags: `e815_s1272_s1274_r3043_r2993_p833`
- Data periods: B-M, production tag: p768

The 2012 Monte Carlo samples are produced in PYTHIA and POWHEG. The HCP dataset is used, containing a total integrated luminosity of 12 fb^{-1} . Periods and production tags are reminded below:

- ATLAS MC: `mc12_8TeV`, Generator identifier: 147806 ($Z \rightarrow e^+ e^-$), 147800 ($W^+ \rightarrow e^+ \nu$), 147803 ($W^- \rightarrow e^- \nu$), production tags: `e1169_s1469_s1470_r3542_r3549_p1196`
- Data periods: A-E, production tag: p1032

D.6 Lateral Leakage

This covers the following data periods and production tags:

- ATLAS MC: `mc11_7TeV`, PYTHIA identifier: 106046 ($Z \rightarrow e^+ e^-$), production tag: `e815_s1272_s1274_r3043_r2993_p833`

- Data periods: B-M, production tag: p768

For the 2012 results, a dataset of 12 fb^{-1} of total integrated luminosity (HCP dataset) are used. This covers the following data periods and production tags:

- ATLAS MC: $mc12.8TeV$, PYTHIA identifier: 147806 ($Z \rightarrow e^+e^-$), production tag: e1169_s1469_s1470_r3542_r3549_p1344
- Data periods: A-E, production tag: r4065_p1278_p1344_p1345

5 bins in η and 9 in E_T were defined for the linearity measurement. The bins are defined in Table D.7. This binning was chosen to compare with the linearity measurements.

$ \eta $ range	[0.0, 0.6, 1., 1.37, 1.82, 2.4]
E_T range [GeV]	[10,20,30,40,50,60,70,80,90,100]

Table D.7: *This table shows the binning used in this study in η and E_T*

D.7 W Mass Measurement

- ATLAS MC: $mc11.7TeV$
- 108297 PowHegWplusenuPythia
- 108300 PowHegWminenuPythia
- Generation/Simulation/Reconstruction tags: e825_s1272_s1274_r3043_r2993_p833

Bibliography

- [1] Brüning, O. and others. *LHC design report*. CERN-2004-003-V-1, CERN-2004-003-V-2, CERN-2004-003-V-3. Geneva, 2004. URL: {<http://cdsweb.cern.ch/record/782076>}, {<http://cdsweb.cern.ch/record/815187>}, {<http://cdsweb.cern.ch/record/823808>}.
- [2] J.J. Goodson. *Gallery - ATLAS/LHC Figures*. URL: {<http://www.jetgoodson.com/thesisGallery.html>}.
- [3] ATLAS Collaboration. *A Torroidial LHC Apparatus - Technical Design Report*. 1996.
- [4] Kate Metropolis. *Understanding luminosity through 'barn', a unit that helps physicists count particle events*. URL: {<http://news.stanford.edu/news/2004/july21/femto barn-721.html>}.
- [5] ATLAS Collaboration. *The ATLAS Inner Detector Technical Design Report*. CERN/LHCC/97-16, Apr. 1997. ISBN: 92-9083-102-2.
- [6] ATLAS Collaboration. "Electron performance measurements with the ATLAS detector using the 2010 LHC proton-proton collision data". In: *Eur.Phys.J.* C72 (2012), p. 1909. DOI: 10.1140/epjc/s10052-012-1909-1. arXiv:1110.3174 [hep-ex].
- [7] ATLAS Collaboration. *ATLAS Liquid Argon Calorimeter - Technical Design Report*. CERN-LHCC-96-041, 1996.
- [8] ATLAS Collaboration. *ATLAS Muon Spectrometer Technical Design Report*. CERN-LHCC-97-22, May 1997. ISBN: 92-9083-108-1.
- [9] K. Kordas et al. "The ATLAS Data Acquisition and Trigger: concept, design and status". In: (Aug. 2007).
- [10] Sheldon L. Glashow. "Partial-symmetries of weak interactions". In: *Nuclear Physics* 22.4 (1961), pp. 579–588. ISSN: 0029-5582. DOI: [http://dx.doi.org/10.1016/0029-5582\(61\)90469-2](http://dx.doi.org/10.1016/0029-5582(61)90469-2). URL: <http://www.sciencedirect.com/science/article/pii/0029558261904692>.
- [11] Steven Weinberg. "A Model of Leptons". In: *Phys. Rev. Lett.* 19 (21 Nov. 1967), pp. 1264–1266. DOI: 10.1103/PhysRevLett.19.1264. URL: <http://link.aps.org/doi/10.1103/PhysRevLett.19.1264>.
- [12] P.W. Higgs. "Broken symmetries, massless particles and gauge fields". In: *Physics Letters* 12.2 (1964), pp. 132–133. ISSN: 0031-9163. DOI: [http://dx.doi.org/10.1016/0031-9163\(64\)91136-9](http://dx.doi.org/10.1016/0031-9163(64)91136-9). URL: <http://www.sciencedirect.com/science/article/pii/0031916364911369>.

- [13] L. Evans and P. Bryant. “LHC Machine”. In: *JINST* 3 (2008), S08001.
- [14] The LEP Working Group for Higgs boson searches et al. “Search for the standard model Higgs boson at LEP”. In: *Physics Letters B* 565.61 (2003). DOI: [http://dx.doi.org/10.1016/S0370-2693\(03\)00614-2](http://dx.doi.org/10.1016/S0370-2693(03)00614-2).
- [15] CDF Collaboration. “Combined search for the standard model Higgs boson decaying to a $b\bar{b}$ pair using the full CDF data set”. In: *Phys. Rev. Lett.* (2012). eprint: arXiv:1207.1707 [hep-ex]. URL: <http://arxiv.org/abs/1207.1707>.
- [16] Victor Mukhamedovich Abazov et al. “Combined search for the standard model Higgs boson decaying to $b\bar{b}$ using the D0 Run II data set”. In: *Phys.Rev.Lett.* 109 (2012), p. 121802. DOI: 10.1103/PhysRevLett.109.121802. arXiv:1207.6631 [hep-ex].
- [17] T. Aaltonen et al. “Evidence for a particle produced in association with weak bosons and decaying to a bottom-antibottom quark pair in Higgs boson searches at the Tevatron”. In: *Phys.Rev.Lett.* 109 (2012), p. 071804. DOI: 10.1103/PhysRevLett.109.071804. arXiv:1207.6436 [hep-ex].
- [18] S. Chatrchyan et al. “Combined results of searches for the standard model Higgs boson in pp collisions at $\sqrt{s}=7$ TeV”. In: *Physics Letters B* 710.1 (2012), pp. 26–48. ISSN: 0370-2693. DOI: <http://dx.doi.org/10.1016/j.physletb.2012.02.064>. URL: <http://www.sciencedirect.com/science/article/pii/S0370269312002055>.
- [19] ATLAS Collaboration. “Combined search for the Standard Model Higgs boson in pp collisions at $\sqrt{s}=7$ TeV with the ATLAS detector”. In: *Phys. Rev. D* 86 (3 Aug. 2012), p. 032003. DOI: 10.1103/PhysRevD.86.032003. URL: <http://link.aps.org/doi/10.1103/PhysRevD.86.032003>.
- [20] ATLAS Collaboration. “Observation of a new particle in the search for the Standard Model Higgs boson with the ATLAS detector at the LHC”. In: *Physics Letters B* 716.1 (2012), pp. 1–29. ISSN: 0370-2693. DOI: <http://dx.doi.org/10.1016/j.physletb.2012.08.020>. URL: <http://www.sciencedirect.com/science/article/pii/S037026931200857X>.
- [21] ATLAS Collaboration. “Search for new phenomena in final states with large jet multiplicities and missing transverse momentum at $\sqrt{s}=8$ TeV proton-proton collisions using the ATLAS experiment”. In: (2013). arXiv:1308.1841 [hep-ex].
- [22] ATLAS Collaboration. *ATLAS public results*. URL: <https://twiki.cern.ch/twiki/bin/view/AtlasPublic/>.
- [23] ATLAS Collaboration. *Measurement of the Top Quark Mass in Dileptonic Top Quark Pair Decays with $\sqrt{s}=7$ TeV ATLAS Data*. Tech. rep. ATLAS-CONF-2013-077. Geneva: CERN, June 2013.
- [24] ATLAS Collaboration. “Measurement of the high-mass Drell–Yan differential cross-section in pp collisions at $\sqrt{s}=7$ TeV with the ATLAS detector”. In: *Phys.Lett.* B725 (2013), pp. 223–242. DOI: 10.1016/j.physletb.2013.07.049. arXiv:1305.4192 [hep-ex].
- [25] ATLAS Collaboration. “Search for microscopic black holes in a like-sign dimuon final state using large track multiplicity with the ATLAS detector”. In: (2013). arXiv:1308.4075 [hep-ex].

- [26] ATLAS Collaboration. “Observation of a Centrality-Dependent Dijet Asymmetry in Lead-Lead Collisions at $\sqrt{s_{NN}} = 2.76$ TeV with the ATLAS Detector at the LHC”. In: *Phys. Rev. Lett.* 105 (25 Dec. 2010), p. 252303. DOI: 10.1103/PhysRevLett.105.252303. URL: <http://link.aps.org/doi/10.1103/PhysRevLett.105.252303>.
- [27] Richard Wigmans. *Calorimetry - Energy Measurement in Particle Physics*. Oxford: Clarendon Press, 2000. ISBN: 0 19 850296 6.
- [28] H.-C. Schulz-Coulon and J. Stachel. *Lecture on 'The Physics of Particle Detectors'*. Oct. 2013. URL: http://www.kip.uni-heidelberg.de/~coulon/Lectures/Detectors/Free_PDFs/.
- [29] J. Beringer et al. (Particle Data Group). *The Review of Particle Physics*. Vol. D86. 2012. eprint: {010001(2012)}.
- [30] Janos Kirz. *X-Ray Data Booklet: Section 3.1 SCATTERING of X-RAYS from ELECTRONS and ATOMS*. Oct. 2013. URL: http://xdb.lbl.gov/Section3/Sec_3-1.html.
- [31] Ian C. Brock. *Physics of and with Leptons WS 05/06 - Feynman Graphs*. Oct. 2013. URL: http://www-zeus.physik.uni-bonn.de/~brock/feynman/vtp_ws0506/.
- [32] E. Longo and I. Sestili. Vol. 128. 1975.
- [33] ATLAS Collaboration. “The ATLAS Experiment at the CERN Large Hadron Collider”. In: *Journal of Instrumentation* 3.08 (2008), S08003. URL: <http://stacks.iop.org/1748-0221/3/i=08/a=S08003>.
- [34] M. Aharrouche et al. “Energy linearity and resolution of the ATLAS electromagnetic barrel calorimeter in an electron testbeam”. In: ().
- [35] P. Calafiura, W. Lavrijsen, C. Leggett, M. Marino and D. Quarrie. *The athena control framework in production, new developments and lessons learned*. In *Interlaken 2004, Computing in high energy physics and nuclear physics* 456-458. URL: {<http://indico.cern.ch/materialDisplay.py?contribId=108&sessionId=6&materialId=paper&confId=0>}.
- [36] R. Brun and F. Rademakers. *The ROOT system*. URL: {<http://root.cern.ch/>}.
- [37] ATLAS Collaboration. *The ATLAS Core Software*. URL: {<https://twiki.cern.ch/twiki/bin/viewauth/AtlasComputing/CoreSoftware>}.
- [38] CERN. *Worldwide LHC Computing Grid*. URL: {<http://wlcg.web.cern.ch/>}.
- [39] P. Skands et al. *A Brief Introduction to PYTHIA*. URL: {<http://home.thep.lu.se/~torbjorn/Pythia.html>}.
- [40] S. Alioli et al. *The POWHEG BOX*. URL: {<http://powhegbox.mib.infn.it/>}.
- [41] Elisabetta Barberio, Bob van Eijk, and Zbigniew Was. “PHOTOS: A Universal Monte Carlo for QED radiative corrections in decays”. In: *Comput.Phys.Commun.* 66 (1991), pp. 115–128. DOI: 10.1016/0010-4655(91)90012-A.
- [42] Allison, J. et al. *Geant4 is a toolkit for the simulation of the passage of particles through matter*. URL: {<http://geant4.cern.ch/>}.

- [43] ATLAS Collaboration. “Measurement of the inclusive W^\pm and Z/γ^* cross sections in the e and μ decay channels in pp collisions at $\sqrt{s} = 7\text{TeV}$ with the ATLAS detector”. In: *Phys. Rev. D* 85 (7 Apr. 2012), p. 072004. DOI: 10.1103/PhysRevD.85.072004. URL: <http://link.aps.org/doi/10.1103/PhysRevD.85.072004>.
- [44] *Inclusive W/Z cross section at 8 TeV*. Tech. rep. CMS-PAS-SMP-12-011. Geneva: CERN, 2012.
- [45] ATLAS Collaboration. *ATLAS public results - Data Quality Information*. URL: {<https://twiki.cern.ch/twiki/bin/view/AtlasPublic/RunStatsPublicResults2010>}.
- [46] Bocci, A et al. *ATLAS electron γ TWiki*. URL: {<https://twiki.cern.ch/twiki/bin/viewauth/AtlasProtected/ElectronGamma>}.
- [47] T Cornelissen et al. *Concepts, design and implementation of the ATLAS new tracking (NEWT)*. Tech. rep. ATL-SOFT-PUB-2007-007. Geneva: CERN, Mar. 2007.
- [48] Frühwirth, R. “Application of Kalman filtering to track and vertex fitting”. In: *Nucl. Instrum. Methods Phys. Res., A* 262. HEPHY-PUB-503 (1987), 444. 19 p.
- [49] T. G. Cornelissen et al. “The global χ^2 track fitter in ATLAS”. In: *Journal of Physics: Conference Series* 119.3 (2008), p. 032013. ISSN: 1742-6596.
- [50] ATLAS Collaboration. “Improved electron reconstruction in ATLAS using the Gaussian Sum Filter-based model for bremsstrahlung”. In: ATL-CONF-2012-047 (May 2012).
- [51] W Lampl et al. *Calorimeter Clustering Algorithms: Description and Performance*. Tech. rep. ATL-LARG-PUB-2008-002. ATL-COM-LARG-2008-003. Geneva: CERN, Apr. 2008.
- [52] “Performance of the Missing Transverse Energy Reconstruction and Calibration in Proton-Proton Collisions at a Center-of-Mass Energy of 7 TeV with the ATLAS Detector”. In: (2010).
- [53] W.E. Cleland and E.G. Stern. “Signal processing considerations for liquid ionization calorimeters in a high rate environment”. In: *Nucl. Instr. and Meth. in Phys. Res. A* 338 (1994), pp. 467–497.
- [54] D Banfi, L Carminati, and L Mandelli. *Calibration of the ATLAS electromagnetic calorimeter using calibration hits*. Tech. rep. ATL-LARG-PUB-2007-012. ATL-COM-LARG-2007-007. Geneva: CERN, 2007.
- [55] Maarten Boonekamp et al. *EGamma Calibration overview and endorsement*. URL: {<https://indico.cern.ch/conferenceDisplay.py?confId=285146>}.
- [56] CERN Document Server. *4th July 2012, Seminar at CERN*. URL: {<http://cds.cern.ch/record/1459513?ln=de>}.
- [57] *Study of alignment-related systematic effects on the ATLAS Inner Detector tracking*. Tech. rep. ATLAS-CONF-2012-141. Geneva: CERN, Oct. 2012.
- [58] M Aleksa et al. “Measurement of the ATLAS solenoid magnetic field”. In: *Journal of Instrumentation* 3.04 (2008), P04003. URL: <http://stacks.iop.org/1748-0221/3/i=04/a=P04003>.

- [59] J. Gaiser. “Charmonium Spectroscopy From Radiative Decays of the J/ψ and ψ' ”. In: (1982).
- [60] E Abat et al. “Combined performance studies for electrons at the 2004 ATLAS combined test-beam”. In: *Journal of Instrumentation* 5.11 (2010), P11006. URL: <http://stacks.iop.org/1748-0221/5/i=11/a=P11006>.
- [61] M. Aharrouche et al. “Response uniformity of the ATLAS liquid argon electromagnetic calorimeter”. In: *Nuclear Instruments and Methods in Physics Research Section A: Accelerators, Spectrometers, Detectors and Associated Equipment* 582.2 (2007), pp. 429–455. ISSN: 0168-9002. DOI: <http://dx.doi.org/10.1016/j.nima.2007.08.157>. URL: <http://www.sciencedirect.com/science/article/pii/S0168900207018591>.
- [62] M. Aharrouche et al. “Energy linearity and resolution of the ATLAS electromagnetic barrel calorimeter in an electron test-beam”. In: *Nuclear Instruments and Methods in Physics Research Section A: Accelerators, Spectrometers, Detectors and Associated Equipment* 568.2 (2006), pp. 601–623. ISSN: 0168-9002. DOI: <http://dx.doi.org/10.1016/j.nima.2006.07.053>. URL: <http://www.sciencedirect.com/science/article/pii/S0168900206013222>.
- [63] L. Demortier and L. Lyons. “Everything you always wanted to know about pulls”. In: *CDF Note 5776* (2002).
- [64] Weisstein, Eric W. *Chi-Squared Test*. URL: <http://mathworld.wolfram.com/Chi-SquaredTest.html>.
- [65] Ashutosh V. Kotwal and Jan Stark. “Measurement of the W Boson Mass at the Tevatron”. In: *Annual Review of Nuclear and Particle Science* 58.1 (2008), pp. 147–175. DOI: 10.1146/annurev.nucl.58.110707.171227. eprint: <http://www.annualreviews.org/doi/pdf/10.1146/annurev.nucl.58.110707.171227>. URL: <http://www.annualreviews.org/doi/abs/10.1146/annurev.nucl.58.110707.171227>.
- [66] CDF Collaboration and D0 Collaboration. “Combination of CDF and D0 W-Boson mass measurements”. In: *Phys. Rev. D* 88 (5 2013), p. 052018. DOI: 10.1103/PhysRevD.88.052018. URL: <http://link.aps.org/doi/10.1103/PhysRevD.88.052018>.
- [67] CDF Collaboration. “Precise Measurement of the W-Boson Mass with the CDF II Detector”. In: *Phys. Rev. Lett.* 108 (15 Apr. 2012), p. 151803. DOI: 10.1103/PhysRevLett.108.151803. URL: <http://link.aps.org/doi/10.1103/PhysRevLett.108.151803>.
- [68] T H V Nguyen, N Besson, and M Boonekamp. E_T^{miss} from the reconstruction and calibration of the hadronic recoil. Tech. rep. ATL-PHYS-INT-2010-039. Geneva: CERN, Apr. 2010.
- [69] Nathalie Besson et al. “Re-evaluation of the LHC potential for the measurement of m_W ”. In: *Eur.Phys.J. C* 57 (2008), pp. 627–651. DOI: 10.1140/epjc/s10052-008-0774-4. arXiv:0805.2093 [hep-ex].
- [70] A Belloni et al. *Measurement of the W Boson Transverse Momentum using Muons and Electrons in proton-proton collisions at $\sqrt{s} = 7$ TeV with the ATLAS detector*. Tech. rep. ATL-COM-PHYS-2011-251. Geneva: CERN, Mar. 2011.

- [71] N Besson and M Boonekamp. “Determination of the Absolute Lepton Scale Using Z Boson Decays: Application to the Measurement of M_W ”. In: ATL-PHYS-PUB-2006-007. ATL-COM-PHYS-2005-072 (2005).
- [72] ATLAS Collaboration. “Readiness of the ATLAS Liquid Argon Calorimeter for LHC Collisions”. In: *Eur. Phys. J. C* 70 (2010), p. 723. arXiv:0912 . 2642 [physics.ins-det].
- [73] X Ruan et al. *Drift Time Measurement in the ATLAS Liquid Argon Barrel Electromagnetic Calorimeter using Collision Events*. Tech. rep. ATL-COM-LARG-2011-039. Geneva: CERN, Oct. 2011.

CURRICULUM VITAE

Florian Teischinger

Personal Details

Birth October 20, 1981
Address 1211 Geneve 23, E28700
Phone +41 76 74120
Mail florian.teischinger@cern.ch

Experience

2011 - 2013	CERN PhD Student in the ATLAS Calorimeter Group, CERN and Vienna University of Technology
2010	Research Assistant in the CMS B Physics Analysis Group, Institute of High Energy Physics, Vienna
2009	Graduation in Technical Physics, DI
2008 - 2009	Diploma Student in the CMS Level-1 Trigger Group, Institute of High Energy Physics and Vienna University of Technology
2006 - 2007	Internship in the Nuclear Particle Physics Group, Institute of Atomic and Subatomic Physics, Vienna University of Technology
2004 - 2006	Project Associate at the Institute of Wood Science and Technology, University of Natural Resources and Life Sciences, Vienna
2001	Diploma Studies in Technical Physics, Vienna University of Technology
2001	Military Service, Pioneer Company, Leibnitz
1992 - 2000	Federal grammar school, Bundes- und Bundesrealgymnasium Weiz, Specialization: Latin and French

Skills

Languages	German (mother tongue), English (fluent), French (fluent)
Software	C++, PYTHON, JAVA, MATLAB, FORTRAN, ROOT, GEANT 4, L ^A T _E X